

A Joint Analysis of Gross Primary Production and Evapotranspiration of Australia Using Eddy Covariance, Remote Sensing and Land Surface Modelling Approaches

Hao Shi

February 2017

*A thesis submitted in fulfillment of the requirements
for the degree of Doctor of Philosophy*

*School of Life Sciences
University of Technology Sydney*

Certificate of original authorship

I certify that the work in this thesis has not previously been submitted for a degree nor has it been submitted as part of requirements for a degree except as fully acknowledged within the text. I also certify that the thesis has been written by me. Any help that I have received in my research work and the preparation of the thesis itself has been acknowledged. In addition, I certify that all information sources and literature used are indicated in the thesis.

Signature

Date 2017-02-15

Acknowledgements

I have experienced an amazing period in the University of Technology Sydney during the past four years. I am grateful to have a chance to work with distinguished scholars in this world on terrestrial ecosystem functioning.

I am deeply and sincerely appreciative for the guidance and support from my supervisors Prof. Derek Eamus and Dr. Longhui Li. Longhui was the first to set up this PhD project and has always encouraged me in continuing this work. Derek has taught me how to focus on the scientific questions. His suggestions have greatly helped me in developing and structuring my work.

I would like to thank Prof. Qiang Yu. Qiang is professional in ecosystem modelling and even in chats with him I learned a lot in ecosystem mechanisms and modelling. Talks with Qiang are enjoyable and many ideas are inspired.

Many thanks goes to Prof. Alfredo Huete and Dr. James Cleverly. Alfredo is a distinguished scientist in remote sensing and gave me amounts of advice in developing this thesis. Besides, Alfredo is always kind even though I had not much knowledge of remote sensing when being a beginner. James gave me a number of suggestions on writing and always patiently corrected the grammar errors in my manuscripts.

I also sincerely thank all my friends and office buddies for their support and accompany. I am most happy to share a period with them. Many thanks to all my collaborators for their valuable comments on my work. Special thanks to Dr. Xingjie Lu at CIRSO for sharing meteorological forcing data and Mike Lake at UTS for assistance in using UTS HPC.

I would also like to acknowledge the financial support from the Australian Research Council Scholarship and the UTS International Research Scholarship. Without these funding, I could

not have completed this work. Many thanks to UTS staff from the School of Life Sciences and the Graduate Research School.

The biggest thanks to my family who always support me and have scarified for me so much, especially my wife. I love you all!

Preface

Accurate estimation of gross primary production (GPP) through vegetation photosynthesis and its coupled evapotranspiration (ET) process is critical for the Earth's life support system. This thesis aims to understand the mechanisms underlying the GPP and ET processes and thus to improve the estimation of them across various spatio-temporal scales. The thesis consists of seven chapters with Chapters two to six written as journal articles. Chapters two to five focus on one of different methods such as eddy covariance, remote sensing and land surface modelling. Chapter six integrates eddy covariance observations, remote sensing products and land surface modelling to investigate the deficits existing in current models. These chapters have been published, submitted or in preparation. This thesis is compiled from above chapters with guidance and support from my supervisors and collaborators from other institutes. The details are as the following:

Chapter 2: Shi, H., L. Li, D. Eamus, J. Cleverly, A. Huete, J. Beringer, Q. Yu, E. v. Gorsel, and L. Hutley (2014), Intrinsic climate dependency of ecosystem light and water-use-efficiencies across Australian biomes, *Environmental Research Letters*, 9(10), 104002.

Chapter 3: Shi, H., L. Li, D. Eamus, A. Huete, J. Cleverly, X. Tian, Q. Yu, S. Wang, L. Montagnani, V. Magliulo, E. Rotenberg, M. Pavelka, and A. Carrara (2017), Assessing the ability of MODIS EVI to estimate terrestrial ecosystem gross primary production of multiple land cover types, *Ecological Indicators*, 72, 153-164.

Chapter 4: Shi, H., W. Zhuang, L. Li, J. Beringer, J. Cleverly, J. Dong, D. Eamus, Q. Guo, and Q. Yu (2016), Remote estimation of evapotranspiration for Australian seasonally water-limited ecosystems within an evapotranspiration-vegetation index framework, *Remote Sensing Letters*, submitted.

Chapter 5: Shi, H., L. Li, Y.-P. Wang, J. Beringer, J. Cleverly, L. Cheng, D. Eamus, L. He, X. Lu, L. Zhang, and Q. Yu (2016), Identifying and optimizing key above- and below-ground processes for carbon assimilation and evapotranspiration in the CABLE model across Australian vegetation types, *Journal of Geophysical Research*, internal review.

Chapter 6: Shi, H., L. Li, D. Eamus, X. Lu, Y.-P. Wang, J. Cleverly, J. Beringer, and Q. Yu (2016), Benchmarking the CABLE model using remote sensing GPP and ET products across Australia, *Journal of Hydrometeorology*, in prep.

Other coauthored papers include:

1. Bai, J., J. Wang, X. Chen, G. Luo, H. Shi, L. Li, and J. Li (2015), Seasonal and inter-annual variations in carbon fluxes and evapotranspiration over cotton field under drip irrigation with plastic mulch in an arid region of Northwest China, *Journal of Arid Land*, 7(2), 272-284.
2. L.H. Li, Y.P. Wang, D. Eamus, V.K. Arora, H. Shi, L. Cheng, J. Cleverly, T. Hajima, D.Y. Ji, C. Jones, M. Kawamiya, W.P. Li, J. Tjiputra, A. Wiltshire, T.W. Wu, Q. Yu, and L. Zhang (2015), Benchmarking global land surface models in CMIP5: analysis of ecosystem water- and light-use efficiencies within a Budyko framework, *Journal of Climate*, under review.
3. L.H. Li, Y.P. Wang, J. Beringer, H. Shi, D. Eamus, A. Huete, J. Cleverly (2015), Coherent and positive response of gross primary production to precipitation across Australian arid and semi-arid biomes, *Scientific Reports*, under review.
4. X.L. Yuan, L.H. Li, X. Chen, H. Shi (2015), Effects of Precipitation Intensity on NDVI-Based Grass Change over Northern China During the Period from 1982 to 2011, *Remote Sensing*, vol. 7, no. 8, doi:10.3390/rs70810164

Contents

Certificate of original authorship	i
Acknowledgements	ii
Preface	iv
Abstract	1
Chapter 1. Introduction.....	2
1.1 GPP and ET	2
1.1.1 GPP.....	2
1.1.2 Evapotranspiration (ET).....	3
1.2 Main approaches for measurements and estimation of GPP and ET	4
1.2.1 Eddy covariance method	4
1.2.2 Remote sensing techniques	5
1.2.3 Land surface models.....	6
1.3 Progress on estimation of GPP and ET	7
1.3.1 GPP estimation	7
1.3.2 ET estimation.....	9
1.4 Study area	12
1.5 Aims and overview	13
Chapter 2: Intrinsic climate dependency of ecosystem light and water-use-efficiencies across Australian biomes.....	26
Abstract.....	26
2.1 Introduction.....	26
2.2 Methods	29
2.2.1 Sites and data processing.....	29
2.2.2 Wavelet aggregation method	34
2.3 Results.....	36
2.3.1 GPP responses to PAR and ET	36

2.3.2 Relationships of eLUE and eWUE with climate	38
2.3.3 Relationships of eLUE and eWUE to SWC and LAI	41
2.3.4 Behavior of eLUE and eWUE in summer and winter	45
2.4 Discussion	47
2.4.1 Relationships between GPP, PAR and ET	47
2.4.2 Climate dependence of eLUE and eWUE among biomes	48
2.4.3 Seasonal patterns of eLUE and eWUE across biomes	49
2.5 Conclusions	50
Chapter 3. Assessing the ability of MODIS EVI to estimate terrestrial ecosystem gross primary production of multiple land cover types	58
Abstract	58
3.1 Introduction	59
3.2 Data and Methods	62
3.2.1 Eddy covariance and meteorological data	62
3.2.2 Benchmark dataset	64
3.2.3 Satellite data	65
3.2.4 Statistical analyses	69
3.3 Results	70
3.3.1 The overall relationship between GPP and iEVI without biomes categorization	70
3.3.2 Biome-specific relationships between GPP and iEVI	71
3.3.3 Global application of biome-specific GPP-iEVI relationships	76
3.3.3 LAI and precipitation effects on biome-specific GPP-iEVI relationships	80
3.4 Discussion	81
3.4.1 Uncertainty analysis	81
3.4.2 Relationships between EVI and GPP	83
3.4.3 Environmental constraints on the ability of EVI to estimate GPP	84
3.5 Conclusions	86

Chapter 4: Remote estimation of evapotranspiration for Australian seasonally water-limited ecosystems within an evapotranspiration-vegetation index framework.....	101
Abstract.....	101
4.1 Introduction.....	101
4.2 Data and Methods	103
4.2.1 Data	103
4.2.2 Development of the ET-EVI Framework	108
4.2.3 A Simple EVI-Based ET Model	109
4.3 Results.....	112
4.3.1 Performance of the TG-SM Model across Sites.....	112
4.3.2 Performance of the TG-SM Model within Sites.....	113
4.3.3 Performance of the TG-SM Model at the Regional Scale.....	116
4.4 Discussion and conclusions	119
Chapter 5. Identifying and optimizing key above- and below-ground processes for carbon assimilation and evapotranspiration in the CABLE model across Australian vegetation types	128
Abstract.....	128
5.1 Introduction	129
5.2 Data and Methods	132
5.2.1 Sites and Measurements	132
5.2.2 The CABLE Model	134
5.2.3 Sensitivity Analysis	138
5.2.4 Parameter Optimization.....	141
5.2.5 Statistical Metrics	144
5.3 Results.....	144
5.3.1 Important Parameters for GPP and Qle	144
5.3.2 Distribution of Optimized Parameters.....	146
5.3.3 Performance of Optimization at the Hourly Time-scale	148

5.3.4 Simulated SWC, GPP and ET at the Daily Time-scale	152
5.3.5 Seasonal Responses of Simulated GPP and Qle to Water Deficits	155
5.3.6 Effects of Optimization on GPP and ET at Different Time-scales	157
5.4 Discussion.....	159
5.4.1 Key Parameters and Processes for GPP and ET.....	159
5.4.2 Applications of the Model-data Fusion Framework.....	163
5.4.3 Further Model Uncertainties	164
5.5 Conclusions.....	165
Chapter 6. Benchmarking the CABLE model using remote sensing GPP and ET products across Australia.....	174
Abstract.....	174
6.1 Introduction.....	175
6.2 Data and Methods	177
6.2.1 Flux sites.....	177
6.2.2 Spatial data	178
6.2.3 Remote sensing GPP models.....	181
6.2.4 Remote sensing ET models	181
6.2.5 The CABLE Model	182
6.2.6 Data-driven product.....	183
6.2.7 Statistical metrics	183
6.3 Results.....	184
6.3.1 Temporal benchmarking.....	184
6.3.2 Spatial benchmarking	188
6.4 Discussion.....	198
6.5 Conclusions.....	201
Chapter 7. General discussion and conclusions	209
7.1 General discussion	209

7.1.1 Coupling of GPP and ET across Australian biomes	209
7.1.2 EVI-based GPP model.....	209
7.1.3 TG-SM ET model.....	210
7.1.4 Optimization of the CABLE model.....	211
7.1.5 Benchmarking CABLE using remote sensing products.....	212
7.2 Future research.....	212

List of Figures

Figure 1.1. Spatial distribution of 13 OzFlux sites. The IGBP land cover types in Australia are also shown. The acronyms WAT, ENF, EBF, DBF, MF, CSH, OSH, WSA, SAV, GRA, WET, CRO, URB, CNM, SNO and BRN denote water, evergreen needleleaf forest, evergreen broadleaf forest, deciduous broadleaf forest, mixed forest, closed shrublands, open shrublands, woody savannas, savannas, grasslands, wetlands, croplands, urban and built-up, cropland/natural vegetation mosaic, snow and ice and barren or sparsely vegetated, respectively.	13
Figure 1.2. Framework of this thesis. The horizontal axis indicates time-scale while the vertical axis indicates spatial scale. The box for thesis step represents the spatio-temporal scales at which the research is conducted. The solid arrow lines indicate methods used in the chapter while the dashed arrow lines indicate output of the chapter into following steps.	14
Figure 2.1. Average annual precipitation contour map of Australia in 30 years from 1976 to 2005 (statistics by Bureau of Meteorology, Australia), spatial distribution of selected sites and average monthly climate over the respective observation periods for each site. T indicates temperature, Prcp indicates precipitation, PAR indicates photosynthetically active radiation, and VPD indicates the vapor pressure deficit.	32
Figure 2.2. eWUE reconstruction at hourly, daily, monthly, seasonal and yearly scales using the wavelet transform at the Howard Springs site from 2004 to 2008. The reconstructed time series removes the higher frequency information in lower scales.	36
Figure 2.3. Relationships between (left) daily (GPP_d), eight day (GPP_{8d}), monthly (GPP_m) GPP and PAR and between (right) GPP and ET for seven sites. Ellipses (left) indicate 95% confidence boundaries of GPP. Bars indicate one standard deviation of annual eLUE or eWUE at each site. Also shown is the linear fit between GPP and ET (right). Annual eLUE($eLUE_{yr}$) and eWUE($eWUE_{yr}$) were calculated from annual GPP, PAR and ET.	37
Figure 2.4. Relationships between (left) daily ($eLUE_d$), eight day ($eLUE_{8d}$), monthly ($eLUE_m$) eLUE and VPD and between (right) daily ($eWUE_d$), eight day ($eWUE_{8d}$), monthly ($eWUE_m$) eWUE and VPD for seven sites. Ellipses indicate 95% confidence boundaries of eLUE and eWUE. Bars indicate one standard deviation of annual eLUE, eWUE or VPD at each site. Also shown are logarithmically fitted functions, coefficients of determination (R^2) and p values.	40

Figure 2.5. Relationships between (left) daily ($eLUE_d$), eight day ($eLUE_{8d}$), monthly ($eLUE_m$) $eLUE$ and SWC and between (right) daily ($eWUE_d$), eight day ($eWUE_{8d}$), monthly ($eWUE_m$) $eWUE$ and SWC for seven sites. Ellipses indicate 95% confidence boundaries of $eLUE$ and $eWUE$. Bars indicate one standard deviation of annual $eLUE$, $eWUE$ or SWC at each site. Also shown are logarithmically fitted functions, coefficients of determination (R^2) and p values.....	42
Figure 2.6. Relationships between (left) eight day ($eLUE_{8d}$), monthly ($eLUE_m$) and yearly ($eLUE_{yr}$) $eLUE$ and mean maximum LAI (LAI_{max}) and between (right) eight day ($eWUE_{8d}$), monthly ($eWUE_m$) and yearly ($eWUE_{yr}$) $eWUE$ and LAI_{max} for seven sites. Bars indicate standard one standard deviation of annual $eLUE$, $eWUE$ or LAI_{max} . Also shown are logarithmically or linearly fitted functions, coefficients of determination (R^2) and p values. .	44
Figure 2.7. Logarithmical relationships between (top two) monthly LUE ($eLUE_m$) and VPD and between monthly WUE ($eWUE_m$) and VPD in summer and winter, respectively. Comparisons of (bottom two) average seasonal $eLUE$ ($eLUE_{season}$) and $eWUE$ ($eWUE_{season}$) for seven sites are also shown in summer and winter, respectively. Error bars indicate the standard deviations of seasonal $eLUE$ or $eWUE$ at each site. “****”, “***”, and “*” above the error bars of each site indicate significance at 0.001, 0.01, and 0.05 levels, while “ns” represents not significant, based on t -test statistics, and these symbols above the horizontal lines represent significance at biome level.....	46
Figure 3.1. Geographical distribution of flux towers overlaid onto the 2001 MODIS IGBP land cover map at a $0.5^\circ \times 0.5^\circ$ resolution.	64
Figure 3.2. Relationship between derived annual GPP from iEVI (GPP_{iEVI}) and eddy covariance tower measured GPP (GPP_{EC}) since 2000 based on all sites and across 12 different biomes. The inset shows \ln -transformed annual GPP_{EC} and annual iEVI for all site-years. The solid line represents the least squares regression line. The dashed line represents the 1:1 line.	71
Figure 3.3. Biome-specific relationships between tower-estimated annual GPP (GPP_{EC}) and iEVI. Solid lines represent GPP-iEVI relationships derived from the $\ln(GPP_{EC}) \sim \ln(iEVI)$ formulas within each biome. Coefficient of determination (R^2) represents the fit goodness of the $\ln(GPP_{EC}) \sim \ln(iEVI)$ relationship, and the root mean squared error (RMSE) represents the bias between GPP estimated using iEVI and GPP_{EC} . All relationships are statistically significant.	73

Figure 3.4. Linear correlations between observed GPP anomaly and iEVI anomaly within each biome. The anomaly is calculated as the variable values subtracting their mean.	74
Figure 3.5. Comparison of modelled annual GPP (GPP_{iEVI}) using biome-specific GPP-iEVI relationships with eddy covariance tower measured GPP (GPP_{EC}). The solid line represents the linear regression line. The dashed line represents the 1:1 line.	76
Figure 3.6. Comparison between modelled average annual GPP using iEVI (GPP_{iEVI}) (2000-2013) and the benchmark GPP (GPP_{MTE}) (1982-2008) at a grid level (left) and a biome level (right) across the globe. The red solid line represents the linear regression line and the black dashed line represents the 1:1 line. Horizontal and vertical error bars (right) indicate standard deviations of mean annual biome GPP_{iEVI} (2000-2013) and GPP_{MTE} (1982-2008), respectively.	77
Figure 3.7. Spatial comparison of (A) the mean annual GPP from iEVI (GPP_{iEVI} , $g\ C\ m^{-2}\ yr^{-1}$) (2000-2013) with (B) the benchmark GPP (GPP_{MTE} , $g\ C\ m^{-2}\ yr^{-1}$) (1982-2008) and the distribution of (C) the residual ($g\ C\ m^{-2}\ yr^{-1}$) between GPP_{iEVI} and GPP_{MTE} within the 5-95% quantile.	78
Figure 3.8. Latitudinal patterns (0.5° bands) of mean annual GPP by iEVI (GPP_{iEVI} , 2000-2013) and the benchmark (GPP_{MTE} , 1982-2008), respectively. The red shaded area represents the standard deviation of all GPP_{iEVI} values of cells along the latitude. The grey shaded area represents the standard deviation of all GPP_{MTE} values of cells along the latitude.	79
Figure 3.9. Strength (R^2) and slopes of relationships between $\ln(GPP_{EC})$ and $\ln(iEVI)$ for each biome as a function of either mean annual precipitation (Prcp, inset) or mean annual maximum LAI in each biome. Black lines represent the segmented linear regression line. The dashed vertical line indicates the breakpoint of the segmented linear relationship. The shaded area represents 95% confidence band.	80
Figure 4.1. Spatial distribution of eight OzFlux sites. The IGBP land cover types in Australia are also shown. The acronyms WAT, ENF, EBF, DBF, MF, CSH, OSH, WSA, SAV, GRA, WET, CRO, URB, CNM, SNO and BRN denote water, evergreen needleleaf forest, evergreen broadleaf forest, deciduous broadleaf forest, mixed forest, closed shrublands, open shrublands, woody savannas, savannas, grasslands, wetlands, croplands, urban and built-up, cropland/natural vegetation mosaic, snow and ice and barren or sparsely vegetated, respectively.	106

Figure 4.2. Scatterplots of measured monthly ET versus scaled monthly EVI across eight seasonally water- limited ecosystems in Australia. The inset is a conceptual diagram [Feddes <i>et al.</i> , 1978; Seneviratne <i>et al.</i> , 2010] defining energy-limited and water-limited ET regimes as a function of soil moisture (θ). θ_{wilt} is the “soil wilting point” and θ_{crit} is a critical soil moisture value. The black line represents a three-segment regression line. The coefficients of determination (R^2) and the significance values (p) for the stage 1 in water-limited domain and energy-limited domain are shown in black. The blue line is the linear regression line between ET and scaled EVI. The related regression equation and statistical values are shown in blue color.	109
Figure 4.3. Regulation effects of land surface temperature (LST, a) and soil moisture (SM, b) on ecosystem observed ET across eight Australian seasonally water-limited sites.	111
Figure 4.4. Comparison of predicted ET by TG-SM models fitted within each site with in-situ measured ET across all eight sites in Australia on a monthly basis.	113
Figure 4.5. Comparison of predicted ET and measured ET across (top) and within (bottom) eight sites. (a) Performance of the model parametrized across all sites, (b) performance of the model parametrized in only the energy-limited domain, (c) performance of the model parametrized in only the extremely water-limited domain, and (d, e and f) coefficients of determination (R^2), RMSE (mm month^{-1}) and fitted slopes of TG-SM, CABLE or MOD16A2 predicted ET against measured ET at each site on a monthly time-scale. At AU-Cap, MOD16A2 ET was not significantly correlated with observed ET. At AU-Da2, CABLE ET was correlated with observed ET at a significant level of $p < 0.05$. All correlations between estimated and observed ET were significant with $p < 0.01$ except for the CABLE model at AU-Da2 ($p < 0.05$).	114
Figure 4.6. The performance of the CABLE model at each of the eight flux sites at a monthly time-scale.....	115
Figure 4.7. The performance of MOD16A2 ET product at each of the eight flux sites at a monthly timescale.....	116
Figure 4.8. Spatial comparisons of mean annual TG-SM ET (a) and mean annual MOD16A2 ET (b) against mean annual ET-MTE (c) during 2001-2011. Figure 4.8d is the probability density distributions of spatial mean values. The red, blue and green dashed lines indicate spatial mean annual values for TG-SM, MOD16A2 and ET-MTE, respectively. Figures 4.8e, 4.8f and 4.8g are determination coefficients (R^2), RMSE and significant values of monthly	

TG-SM ET against monthly ET-MTE at the pixel level and Figure 4.8h is the probability density distribution of R^2 between TG-SM ET and ET-MTE. Figures 4.8i, 4.8j and 4.8k are determination coefficients, RMSE and significant values of monthly MOD16A2 ET against monthly ET-MTE at the pixel level and Figure 4.8l is the probability density distribution of R^2 between MOD16A2 ET and ET-MTE. Black dashed lines in Figures 4.8h and 4.8l indicate mean values of R^2 118

Figure 5.1. Sensitivities of key parameters identified by the Morris method for gross primary productivity (GPP, Figure 5.1a) and latent heat (Q_{le} , Figure 5.1b) over the study periods across ten flux sites, covering crops (CRO), evergreen broad-leaf forests (EBF), C4 grasslands (GRA), open shrublands (OSH), savannas (SAV) and woody savannas (WSA). Bars tending to be red indicate parameters involved in above-ground processes whereas bars tending to be blue indicate parameters involved in below-ground processes. 146

Figure 5.2. Boxplots of optimized values of key above-ground (red) and below-ground (blue) parameters at ten flux sites. Black cross symbols represent default values of parameters. Boxplots show first quartile, median and third quartile (box) as well as the total range of values. 147

Figure 5.3. Average diurnal cycles for net ecosystem carbon exchange (NEE) as calculated from the observations (Obs, open circles) and modeled by CABLE using default parameters (Def, black line), optimized above-ground parameters alone (Abv, blue line) and optimized parameters (Opt, red line), respectively. The shaded area represents standard deviation of the mean observed NEE. 149

Figure 5.4. Average diurnal cycles for gross primary productivity (GPP) as calculated from the observations (Obs, open circles) and modeled by CABLE using default parameters (Def, black line), optimized above-ground parameters alone (Abv, blue line) and optimized parameters (Opt, red line), respectively. The shaded area represents standard deviation of the mean observed GPP. 150

Figure 5.5. Average diurnal cycles for latent heat (GPP) as calculated from the observations (Obs, open circles) and modeled by CABLE using default parameters (Def, black line), optimized above-ground parameters alone (Abv, blue line) and optimized parameters (Opt, red line), respectively. The shaded area represents standard deviation of the mean observed Q_{le} 151

Figure 5.6. Statistical metrics for CABLE performance at the hourly time-scale using default

parameters (Def), optimized above-ground parameters alone (Abv) and optimized parameters (Opt) at ten sites. Figures 5.6a, 5.6b and 5.6c indicate coefficient of determination (R^2) and Figures 5.6d, 5.6e and 5.6f indicate agreement index (d).	152
Figure 5.7. Mean daily soil water content (SWC) at depth 5 cm as calculated from the observations (Obs, open circles) and modeled by CABLE at depth 5.8 cm using default parameters (Def, black line), optimized above-ground parameters alone (Abv, blue line) and optimized parameters (Opt, red line), respectively.....	153
Figure 5.8. Mean daily gross primary productivity (GPP) as calculated from the observations (Obs, open circles) and modeled by CABLE using default parameters (Def, black line), optimized above-ground parameters alone (Abv, blue line) and optimized parameters (Opt, red line), respectively.	154
Figure 5.9. Mean daily evapotranspiration (ET) as calculated from the observations (Obs, open circles) and modeled by CABLE using default parameters (Def, black line), optimized aboveground parameters alone (Abv, blue line) and optimized parameters (Opt, red line), respectively.....	155
Figure 5.10. Monthly gross primary productivity (GPP) as calculated from the observations (Obs, open circles) and modeled by CABLE using default parameters (Def, black line), optimized above-ground parameters alone (Abv, blue line) and optimized parameters (Opt, red line), respectively. The shaded area denotes the dry season.	156
Figure 5.11. Monthly evapotranspiration (ET) as calculated from the observations (Obs, open circles) and modeled by CABLE using default parameters (Def, black line), optimized aboveground parameters alone (Abv, blue line) and optimized parameters (Opt, red line), respectively. The shaded area denotes the dry season.	157
Figure 5.12. Performance of the optimized CABLE at different time-scales. Model parameters are optimized targeted at observed hourly GPP, Q_{le} and NEE. Coefficient of determination (R^2 , solid line) and agreement index (d , dashed line) are shown at hourly (black), daily (blue) and monthly (red) time-scales. Both GPP (Figure 5.12a) and Q_{le} (Figure 5.12b) are ordered by mean annual precipitation across the ten sites.....	158
Figure 5.13. Coupling of gross primary productivity (GPP) and evapotranspiration (ET) at the annual time-scale across ten sites as calculated from the observations (Obs, dark green) and modeled by CABLE using default parameters (Def, black line), optimized above-ground parameters alone (Abv, blue line) and optimized parameters (Opt, red line), respectively. The	

solid line represents the linear regression and the dashed line indicates the linear regression using observation data. 159

Figure 6.1. Comparison of MCD12C1 biomes and the CABLE biomes. Acronyms WAT, ENF, EBF, DBF, MF, CSH, OSH, WSA, SAV, GRA, WET, CRO, URB, CNM, SNO and BRN denote water, evergreen needleleaf forest, evergreen broadleaf forest, deciduous broadleaf forest, mixed forest, closed shrublands, open shrublands, woody savannas, savannas, grasslands, wetlands, croplands, urban and built-up, cropland/natural vegetation mosaic, snow and ice and barren or sparsely vegetated, respectively. 177

Figure 6.2. Monthly gross primary production (GPP), leaf area index (LAI) and photosynthetic capacity (PC, the ratio of GPP over LAI) of different models across Australia from 2001 to 2011. The gray line indicates the product of PC-CABLE and LAI-MOD. 186

Figure 6.3. Monthly evapotranspiration (ET) and surface soil water content (SWC) of different models across Australia from 2001 to 2011. 188

Figure 6.4. Average monthly gross primary production (GPP) calculated from different models from 2001 to 2011. The unit is $\text{gC m}^{-2} \text{ month}^{-1}$ 189

Figure 6.5. The spatial distribution of per-pixel correlations and RMSE between GPP-EVI, GPP-TG, GPP-CABLE and GPP-MTE. The cross symbols indicate the correlation is not statistically significant at a p level of 0.05. 190

Figure 6.6. Average monthly photosynthetic capacity (GPP/LAI) calculated from different models from 2001 to 2011. The unit is $\text{gC LAI}^{-1} \text{ month}^{-1}$ 191

Figure 6.7. The spatial distribution of per-pixel correlations and RMSE between PC-EVI, PCTG, PC-CABLE and PC-MTE. The cross symbols indicate the correlation is not statistically significant at a p level of 0.05. 192

Figure 6.8. Average monthly leaf area index (LAI) calculated from the MCD12C1 product and the CABLE estimation during the period of 2001 to 2011. 193

Figure 6.9. The spatial distribution of per-pixel correlations and RMSE between estimated LAI and SWC by the CABLE model with LAI-MOD and SWC-ECV products. The RMSE between SWC-CABLE and SWC-ECV is multiplied by 40. The cross symbols indicate the correlation is not statistically significant at a p level of 0.05. 194

Figure 6.10. Average monthly evapotranspiration (ET) calculated from different models from 2001 to 2011. The unit is mm month^{-1} 196

Figure 6.11. The spatial distribution of per-pixel correlations and RMSE between ET-TGSM, ET-MOD, ET-CABLE and ET-MTE. The cross symbols indicate the correlation is not statistically significant at a p level of 0.05.	197
Figure 6.12. Average monthly soil water content (SWC) at soil surface layer calculated from the ECV product and the CABLE estimation during the period of 2001 to 2011.....	198

List of Tables

Table 2.1. La Thuile code, site name, latitude (Lat), longitude (Long), year of observations, altitude (Alt), biomes (Evergreen Broadleaf Forests, EBF; Savannas, Savn; Grasslands, Grass), mean maximum annual temperature (T_{\max}), mean minimum annual temperature (T_{\min}), mean annual precipitation (MAP), mean annual minimum leaf area index (LAI_{\min}) and mean annual maximum LAI (LAI_{\max}) during observation intervals for the study sites.	31
Table 2.2. Coefficients of determination (R^2) between LUE, WUE and T_a , PAR, VPD, SWC or LAI_{\max} by logarithmic/exponential (Log/Exp) and linear (Lin) fitting, respectively. ***, **, *, and NULL indicates significant relationship at $p < 0.001$, 0.01, 0.05 and not significant, respectively. Monthly(S) and Monthly(W) indicate monthly variables in summer (December, January, and February) and winter (June, January, and August).	39
Table 3.1. Summary of number of sites and site-years used for each biome. CNM: cropland/natural vegetation mosaic; CRO: croplands; CSH: closed shrublands; DBF: deciduous broadleaf forest; DNF: deciduous needle-leaf forest; EBF: evergreen broadleaf forest; ENF: evergreen needle-leaf forest; GRA: grasslands; MF: mixed forest; OSH: open shrublands; SAV: savannas; WET: permanent wetlands; WSA: woody savannas.	64
Table 3.2. Summary of the raw and leave-one-out cross-validation (CV) performance measures (coefficients of determination, R^2 ; root mean squared error, RMSE) of $\ln(GPP)-\ln(iEVI)$ models for all data points and each biome, respectively.	75
Table 4.1. Brief description of the eight flux tower sites used to develop and validate the TG-SM model, including site identifier (ID), site name (Site), latitude (Lat, °S), longitude (Long, °E), biome type (IGBP), data period, mean annual temperature (MAT, °C), mean annual precipitation (MAP, mm yr ⁻¹) and mean annual radiation (Rad, W m ⁻² s ⁻¹). SAV denotes savannas; OSH denotes open shrublands; WSA denotes woody savannas; and GRA denotes grasslands.	104
Table 5.1. Eddy covariance data used in this study. Information includes site name (Site), latitude (Lat), longitude (Lon), vegetation type (IGBP), data observed period, mean annual temperature (MAT, °C), mean annual radiation (MAR, W m ⁻²), mean annual precipitation (MAP, mm y ⁻¹) and reference citation	133
Table 5.2. Definitions and ranges of CABLE parameters in sensitivity analysis.....	141
Table 6.1. Eddy covariance data used in this study. Information includes site name (Site),	

latitude (Lat), longitude (Lon), vegetation type (IGBP), data observed period and reference citation	178
Table 6.2. Comparison of input data for various GPP and ET models. FAPAR indicates the fraction of absorbed photosynthetic active radiation (APAR), LWDown and SWDown indicate downward long- and short-wave radiation, respectively	180
Table 6.3. Key parameters used in CABLE for evergreen broad-leaf forests (EBF), open shrublands (OSH), C4 grasslands/savannas/woody savannas (C4 GRA/SAV/WSA), C3 croplands (C3 CRO), C3 grasslands (C3 GRA) and barren soils (BRN). Soil 1 is coarse sand/loamy sand, soil 2 is medium clay loam/silty clay loadm/silt loam, and soil 3 is coarse-medium sandy loam/loam. V_{cmax} is the maximum RuBP carboxylation rate at canopy top at a leaf temperature of 25 °C, a_1 is an empirical parameter in leaf stomatal model, α is the initial slope of leaf response curve of potential electron transport rate to absorbed quantum flux, G_0 is the stomatal conductance for water when leaf net photosynthesis is 0, β_r is a parameter for estimating vertical root mass distribution in soil, and ν is an empirical parameter in hydraulic conductivity function	184
Table 6.4. Statistical metrics for the performance of models on estimating GPP, ET, LAI and SWC. For spatial statistics, the significance level is calculated as the percent of pixels with significant correlations against object data at a p level of 0.05.....	187

Abstract

The aim of this thesis is to analyze the patterns of gross primary production (GPP) and evapotranspiration (ET) across Australian biomes in combination of eddy covariance, remote sensing and land surface model (LSM) methods, taking advantage of their respective applicability on different space and time scales. To do this, I (1) used the wavelet method to decompose eddy covariance observed half-hourly GPP and ET into different frequencies from hourly to annual to investigate the coupling of GPP and ET and their interactions with climate and vegetation variability over hourly to annual time-scales, (2) established GPP-EVI relationships across multiple biomes using observed GPP and MODIS EVI and applied them to the global scale, (3) developed an pure remote sensing ET model (TG-SM) in combination of MODIS EVI, LST and microwave soil moisture data, (4) identified and optimized key above- and below-ground processes of GPP and ET in the CABLE model across 10 Australian flux sites, and (5) benchmarked the CABLE model across the whole Australia through integrative use of remote sensing products of GPP and ET predicted by both my own remote sensing models and other available products.

Each chapter provides new insights into the popular approach for estimating GPP or ET, while together they form a strong example in joint analysis of GPP and ET across various spatio-temporal scales.

Chapter 1. Introduction

The problem of pattern and scale is a core issue in ecology [Levin, 1992]. Ecosystems can show varied patterns from fine to broad scales of space and time. Carbon assimilation (i.e., gross primary production, GPP) and evapotranspiration (ET) are two fundamental functions of terrestrial ecosystems and are critical for the sustainability of the Earth's life-support system [Costanza *et al.*, 1997]. Responses of both GPP and ET to environmental variability are typically regulated by scales of either space or time. For example, short-scale (hourly) variability of meteorological forcing can effectively influence fast processes such as GPP whereas it has only small impact on long-term (inter-annual) variability of carbon and water fluxes [Paschalis *et al.*, 2015]. The well-known Budyko's curve [Budyko, 1974] can operate well at basin to global spatial scales and long-term time-scales but fails in estimating ET at local scales and short-term time-scales [Brooks *et al.*, 2011; Pappas *et al.*, 2015]. Therefore, the scale issue constitutes a major challenge in recognizing patterns and estimating of GPP and ET and this is particularly true when considering the heterogeneity of ecosystems. This is because different plant function types have differed functioning and adaptation strategies in responding to various environmental changes or stresses [Allen and Breshears, 1998; Bréda *et al.*, 2006; Holdo and Brocato, 2015; Paschalis *et al.*, 2015]. The importance, approaches and research gaps of GPP and ET are outlined in the following sections.

1.1 GPP and ET

1.1.1 GPP

GPP is the amount of carbon captured from the atmosphere by land vegetation through the photosynthesis process, and thus is a key component of the terrestrial carbon balance [Beer *et al.*, 2007; Xiao *et al.*, 2005]. It is of fundamental importance to human society because plant

production provides most of our food, fiber and wood supply and creates environments suitable for human inhabitation [Melillo *et al.*, 1993; Xiao *et al.*, 2005; Zhao *et al.*, 2005]. Climate changes (e.g., aridity, droughts, changes in precipitation patterns) are expected to profoundly affect the GPP of terrestrial ecosystems [Ciais *et al.*, 2005; Piao *et al.*, 2008] and accurate monitoring and estimation of GPP continuously are the bases for addressing the carbon related issues such as the size of the terrestrial carbon sink, vegetation phenology, vegetation dynamics, and management of forests and grasslands [Ciais *et al.*, 2005; Ma *et al.*, 2013; Sims *et al.*, 2006b].

1.1.2 Evapotranspiration (ET)

ET is the sum of soil evaporation, canopy evaporation, and canopy transpiration transferred to the atmosphere. It is a major link between the global energy budgets and hydrological cycles [Smith and Choudhury, 1990] and accounts for over half of the total water loss from most terrestrial vegetated ecosystems [Zhang *et al.*, 2001]. Accurate estimates of ET are of remarkable importance to proper and sound management of water resource, particularly in semi-arid and arid regions, where water resource supply is limited for human and environmental needs. At catchment scales, ET is closely linked with vegetation characteristics and climate [Zhang *et al.*, 2001]. Specifically, rainfall interception, net radiation, advection, turbulent transport, canopy resistance, leaf area, and plant available water can affect ET [Zhang *et al.*, 2001]. In long-term period, for a large area, ET is mainly controlled by water and energy availability and by land surface characteristics to a minor extent [Milly, 1994; Zhang *et al.*, 2001; Zhang *et al.*, 2004].

1.2 Main approaches for measurements and estimation of GPP and ET

1.2.1 Eddy covariance method

The eddy covariance method, originating from micrometeorological field, directly measures the net carbon and water fluxes across a horizontal plane between vegetated canopies and the atmosphere [Aubinet *et al.*, 2000; Baldocchi *et al.*, 2001]. At an individual EC site, a fast-response, three-dimensional wind sensor (sonic anemometer) is installed to obtain the orthogonal wind components and the speed of sound (to derive air temperature). An infrared gas analyzer is used to obtain water vapor density and CO₂ concentration. Carbon, water, and heat fluxes are determined by measuring the covariance between fluctuations in vertical velocity and the mixing ratio of trace gases of interest [Aubinet *et al.*, 2000; Baldocchi, 2008]. The EC method can measure mass and energy fluxes over the flux footprint around the tower (100 to 2000 m) [Schmid, 1994] across timescales of seconds, hours, days, weeks, seasons and years with negligible disturbance to the underlying vegetation.

Networks of EC systems have been deployed across continents (e.g. AmeriFlux, EuroFlux, AsiaFlux, OzFlux) and yield a global network FLUXNET, which includes more than 850 sites. With this network, valuable data sets of ecological and hydrological variables for the first time have been obtained across a spectrum of biomes and climate zones worldwide, with excellent coverage in Europe and North America [Baldocchi, 2008; Baldocchi *et al.*, 2001; Wang and Dickinson, 2012]. To provide consistent gap-filled and partitioned flux data, FLUXNET has made effort to unify methodology for EC data processing [Mauder *et al.*, 2008; Reichstein *et al.*, 2005]. FLUXNET aims to integrate flux measurements, remote sensing and land surface modeling to assess the interactions between terrestrial biosphere and the atmosphere [Baldocchi *et al.*, 2001]. The data produced by FLUXNET provide the opportunity to evaluate the effects of disturbances (e.g. droughts, aridity), complex terrain, and land use change, and

to develop and test remote sensing methods and LSMs [Baldocchi *et al.*, 2001; Cleugh *et al.*, 2007].

The EC method has its own weakness. It requires that atmospheric conditions are steady, the underlying terrain is relatively flat and the vegetation extends horizontally about 100 times the sampling height [Baldocchi *et al.*, 2001]. Also it is argued that the EC method can only measure small eddies while large eddies are not in steady state and thus cannot be measured with the EC technique [Foken, 2008; Franssen *et al.*, 2010]. Nevertheless, the advantages of the EC method far outweigh its weakness and the measurements are relatively accurate for a variety of common situations [Baldocchi *et al.*, 2001; Wang and Dickinson, 2012].

1.2.2 Remote sensing techniques

Remote sensing techniques can take digital images of surface features through measuring electromagnetic energy reflected or emitted by objects [Lillesand *et al.*, 2014]. According to the wavelength regions of these energy signals in the electromagnetic spectrum, remote sensing can be partitioned into optical, infrared, microwave, etc. Depending on the structural, chemical and physical properties of material, different objects have different spectrum characteristics, which enables detection and discrimination of them [Lillesand *et al.*, 2014]. Remote sensing vegetation indices (VIs) alone [e.g., Sims *et al.*, 2006c; Yebra *et al.*, 2013] or together with land surface temperature (LST) or meteorological variables are common in estimating GPP [e.g., Sims *et al.*, 2008; Wu *et al.*, 2010; Xiao *et al.*, 2004a; Xiao *et al.*, 2004b; Zhao *et al.*, 2005] and ET [e.g., Wang *et al.*, 2007; Yang and Shang, 2013]. VIs *per se* are spectral transformations of two or more bands to enhance the signal of vegetation properties [Huete *et al.*, 2002]. NDVI and EVI are two most famous “greenness” indices:

$$NDVI = \frac{\rho_{NIR} - \rho_{red}}{\rho_{NIR} + \rho_{red}} \quad (1.1)$$

$$EVI = G \frac{\rho_{NIR} - \rho_{red}}{\rho_{NIR} + C_1 \times \rho_{red} - C_2 \times \rho_{blue} + L} \quad (1.2)$$

where ρ_{NIR} , ρ_{red} and ρ_{blue} are atmospherically corrected or partially corrected surface near-infrared (NIR), red and blue spectral reflectances, G is the gain factor, L is the canopy background adjustment, and C_1 , C_2 are the coefficients of the aerosol resistance term, which uses the blue band to correct for aerosol influences in the red band. The NDVI is successful in serving as a surrogate of vegetation NPP or above-ground NPP (ANPP), coverage fraction and fraction of APAR (fAPAR), and is also an important parameter to general and biogeochemical models [Carlson and Ripley, 1997; Huete et al., 2002; Potter et al., 1999]. The major advantage of NDVI than EVI is that NDVI has been obtained globally since 1980s via the NOAA-AVHRR (Advanced Very High Resolution Radiometer onboard the National Oceanic and Atmospheric Administration polar-orbiting satellites) mission while the EVI global product is only traced back to the Moderate Resolution Imaging Spectroradiometer (MODIS) launch in early 2000. The MODIS NDVI is also referred to as the “continuity index” to the AVHRR-NDVI [Huete et al., 2002].

1.2.3 Land surface models

Land surface models (LSMs) are important for understanding and predicting mass and energy exchange between the terrestrial biosphere and atmosphere. LSMs integrate the key processes in land surface such as photosynthesis, respiration, evapotranspiration [Williams et al., 2009]. Generally, LSMs are a critical component of large domain models, for example, global carbon cycle models and global circulation models [Li et al., 2012; Williams et al., 2009]. The output

results of LSMs influence climate system through the control of greenhouse gas exchanges, energy balance and partitioning of sensible and latent heat fluxes.

The Australian Community Atmosphere-Biosphere-Land Exchange (CABLE) model consists of radiation, canopy micrometeorology, surface flux, soil and snow, and ecosystem respiration sub-models [Wang and Leuning, 1998]. The radiation sub-model calculates the PAR, NIR radiation and thermal radiation absorbed by sunlit and shaded leaves. The canopy micrometeorology sub-model calculates canopy roughness length and aerodynamic transfer resistance. The surface flux sub-model calculates net photosynthesis, water extraction and ground heat fluxes. The soil and snow sub-model calculates soil temperature and moisture in the rooting zone, snow age, snow density and depth, and snow covered surface albedo. The ecosystem respiration sub-model calculates the non-leaf plant respiration, soil respiration and net ecosystem CO₂ exchange.

In a recent improvement of CABLE model, a dynamic root water uptake function and a hydraulic redistribution function were incorporated for better simulating the responses of vegetation to seasonal droughts or changes in soil moisture content [Li *et al.*, 2012]. The root water uptake function was firstly developed by [Lai and Katul, 2000] assuming that root water uptake efficiency varies with rooting depth.

1.3 Progress on estimation of GPP and ET

1.3.1 GPP estimation

For decades, several methods have been developed to estimate GPP over a wide range of spatial and temporal scales. The eddy covariance (EC) technique is suited to derive GPP on a local scale from half-hourly to annual scales [Baldocchi *et al.*, 2001; Reichstein *et al.*, 2007], but observations are limited both on a global-scale and in a long-term perspective.

Production efficiency models (PEMs) incorporate remote sensing data to estimate GPP or net primary production (NPP) of terrestrial ecosystems over the stand to global scales [Running *et al.*, 2004; Xiao *et al.*, 2005; Yuan *et al.*, 2007]. Thus:

$$GPP(NPP) = \varepsilon_g(\varepsilon_n) \times FAPAR \times PAR \quad (1.3)$$

where ε_g and ε_n are light-use-efficiencies for calculation of GPP and NPP, respectively, PAR is photosynthetically active radiation, and FAPAR is fraction of absorbed PAR. ε_g or ε_n is a function of plant-function-type (PFT), specific apparent quantum yield or maximum light use efficiency (ε_0) down-regulated by temperature, soil water content, vapor pressure deficit (VPD), or leaf phenology [Xiao *et al.*, 2005; Yuan *et al.*, 2007]. The deficiencies inherent in PEMs are the coarse spatio-temporal resolutions of weather inputs and the generally long intervals between successive satellite observations. In addition, ε_0 varies significantly across biomes and with climate [Polley *et al.*, 2011; Rahman *et al.*, 2005; Turner *et al.*, 2003], thus the use of plant function type specific ε_0 in PEMs can introduce significant errors to modeled GPP or NPP [Rahman *et al.*, 2005; Turner *et al.*, 2003; Zhao *et al.*, 2005]. To overcome the obstacles, satellite-based vegetation indices (VIs) are employed to directly estimate GPP or NPP based entirely on remote sensing data. Normalized difference vegetation index (NDVI) shows strong relationships with carbon flux in some ecosystems over one or two weeks [Sims *et al.*, 2006a; Wylie *et al.*, 2003]. The disadvantages of NDVI are the inherent nonlinearity of ratio-based indices, the influence of additive noise effects, saturation over high biomass, and sensitivity to high background brightness [Huete, 1988; Huete *et al.*, 2002]. The enhanced vegetation index (EVI) was developed to improve sensitivity in high biomass regions and to decouple the canopy background signal with reduction in atmosphere influences [Huete *et al.*, 2002]. Thus EVI was regressed to GPP and it was found to be better correlated with GPP than NDVI in evergreen [Xiao *et al.*, 2004a] and deciduous [Xiao *et al.*,

2004b] forest sites. A strong overall relationship between EVI and GPP was also found across 10 AmeriFlux tower sites representing a wide range of vegetation types [Rahman *et al.*, 2005]. However, relationships between GPP and NDVI, and GPP and EVI have not been validated across enough different biomes and the temporal resolution (weekly or 16-day) is quite coarse to detect the short-time (hours to days) fluctuations in GPP [Sims *et al.*, 2006b].

Process-based ecosystem models estimate global GPP from leaf photosynthesis equations, which are up-scaled to continents and the globe [Beer *et al.*, 2007]. These models need dozens of PFT specific physiological parameters and climate data or concurrent remote sensing data to drive. The benefit is that these models enable prediction of GPP from very short time periods (minutes to hours) to long term periods (years to decades) over canopy to global spatial scales. However, such modeled GPP need independent data-driven estimation to increase the reliability [Beer *et al.*, 2007]. Therefore, there is considerable interest in integrating and comparing the three methods of eddy covariance technique, remote sensing, and ecosystem modeling to estimate GPP in a consistent way.

1.3.2 ET estimation

Sapflow and eddy covariance methods estimate ET at high temporal resolution and are regarded as the most accurate at stand scales (0.1 to 1 km) [Nagler *et al.*, 2005a; Sun *et al.*, 2011]. However, these two methods only perform well in relatively uniform ecosystems and are less reliable in complex stands [Barker *et al.*, 2009; Sun *et al.*, 2008]. In addition, similar to GPP, the ET observations using sapflow and eddy covariance methods are still very limited for the large area (regional to global) and a long-term time scale (years to decades). Directly extrapolating data from flux towers to larger spatial scales can lead to significant biases due to the limited samplings of a whole biome [Wylie *et al.*, 2003].

Remote sensing based models or models coupled with remote sensing thus are highly

recommended to predict ET from regional to global scales continuously [Verstraeten *et al.*, 2005]. These models can be partitioned into mass and energy balance based biophysical models and empirical models that regress ET against remote sensing VIs and land surface climate variables. Among biophysical models, the resistance energy balance method is widely applied [e.g., Hall *et al.*, 1992; Kalma and Jupp, 1990] but is shown to be unreliable in a regional experiment due to the inherent non-linearity in the governing heat transfer equation and the lack of energy-balance constraint on the sensible flux derived from the radiative surface temperature [Cleugh *et al.*, 2007]. The Penman-Monteith model (Equation 1.4 [Monteith, 1965]) provides a more robust method to estimate land surface ET but requires several meteorological forcing data and aerodynamic and surface resistances, which are usually unavailable for large areas [Cleugh *et al.*, 2007]. Thus,

$$\lambda E = \frac{\Delta \cdot (R_n - G) + \rho C_p \cdot [e_s(T_a) - e] / r_h}{\Delta + (1 + r_c / r_h) \cdot \gamma} \quad (1.4)$$

where λ is the latent heat of vaporization, E is the evapotranspiration, Δ is the derivative of the saturated vapor pressure (e_s) with respect to the air temperature (T_a), R_n is the net radiation, G is the ground heat flux, ρ is the density of air, C_p is the specific heat of air, e is the air vapor pressure, r_h is the aerodynamic resistance, r_c is the canopy resistance, and γ is the psychrometric constant [Monteith, 1965]. To overcome the difficulties, remotely-sensed leaf area index (LAI) and NDVI were used to estimate the surface conductance [Cleugh *et al.*, 2007]. The Budyko-type models, assuming ET as a function of precipitation and available energy, can adequately predict long-term ET at regional scale [Zhang *et al.*, 2004]. However, it is still challenging to estimate ET of vegetated surfaces at fine spatial and temporal scales [Sun *et al.*, 2011]. The empirical models use remote sensing to extrapolate eddy covariance water flux to regional scales. Empirical relationship between ET

and EVI and air temperature data was developed for cottonwood and salt cedar stands on the Middle Rio Grande and on western U.S. rivers [Nagler *et al.*, 2005a; Nagler *et al.*, 2005b]. This method offers a simple statistical approach to estimate ET over quite a short time scale (weekly to 16-day) in a large area. The disadvantage is that it is not known whether such a relationship generally exist across a large variety of biomes.

Land surface models (LSMs), basically based on Monin-Obukhov similarity theory estimate latent heat flux (λE) and sensible heat flux (H) from measurements of near-surface winds, temperature, and humidity [Monin and Obukhov, 1954], are capable of estimating ET across multiple spatial and temporal scales (stands to globe, hourly to decades). LSMs need meteorological forcing inputs, PFT coverage, vegetation status (e.g. LAI) information [Ghilain *et al.*, 2012; Williams *et al.*, 2009]. Parameterization in a specific PFT is calibrated and evaluated using site-level ground observations, literature, or laboratory experiments and then up-scaled to coarse grids [Chen and Zhang, 2009; Williams *et al.*, 2009]. However, field measurements suggest that parameters vary significantly over different environmental conditions, even within a PFT [Wright *et al.*, 2004]. The erroneous partitioning of ET between transpiration and soil or canopy evaporation limits the capability of LSMs to predict the sensitivities of ET to precipitation deficits and land cover change [Lawrence and Chase, 2009; Wang and Dickinson, 2012]. Furthermore, the partitioning of ET into canopy transpiration and evaporation affects the simulated GPP [Bonan *et al.*, 2011]. Soil water availability for canopy transpiration, such as an unrealistic default root depth, also reduces the accuracy of ET estimation using LSMs, particularly over drought periods [Beer *et al.*, 2010; Li *et al.*, 2012; Schlosser and Gao, 2010; Tanaka *et al.*, 2008]. Additional issues on LSMs are described in detail in several excellent reviews, for example, Wang and Dickinson [2012] and Overgaard *et al.* [2006]. Providing the advantages and disadvantages of ET estimation methods above, the efforts of quantifying ET continuously and accurately will obviously benefit from

inter-comparing ET estimates using eddy covariance, remote sensing data and land surface models.

1.4 Study area

This study mainly focus on biomes across Australia (except Chapter 3), covering evergreen broadleaf forests (EBF), open shrublands (OSH), C4 grasslands (GRA), C3 crops (CRO), wetlands (WET), savannas (SAV) and woody savannas (WSA). The eddy covariance flux towers are from the OzFlux network (<http://www.ozflux.org.au/>), including Adelaide River (AU-Ade), Alice Springs (AU-Asm), Calperum (AU-Cap), Daly Pasture (AU-Da1), Daly Uncleared (AU-Da2), Dry River (AU-Dry), Fogg Dam (AU-Fog), Howard Springs (AU-How), Yanco (AU-JXA), Sturt Plains (AU-Stp), Tumbarumba (AU-Tum), Wallaby Creek (AU-Wac) and Wombat (AU-Wom). These sites include major biomes in Australia and are dominated by a spectrum of climate regimes such as temperate, sub-tropical and tropical (Figure 1.1). Detailed information on these sites can be found in following chapters. It is noted that whether a site is included in a chapter is determined by the objective of the study. In Chapter 3, I extended the research into the global scale to get enough eddy covariance data and include biomes that do not naturally occur in Australia, such as deciduous needle-leaved forests and evergreen needle-leaved forests.

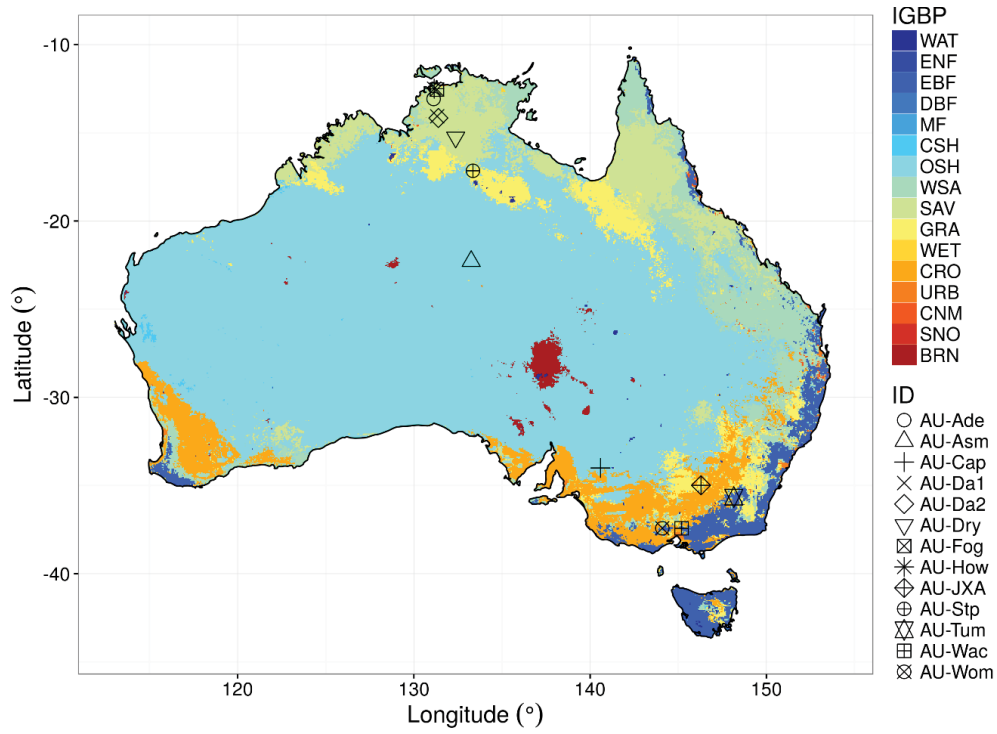


Figure 1.1. Spatial distribution of 13 OzFlux sites. The IGBP land cover types in Australia are also shown. The acronyms WAT, ENF, EBF, DBF, MF, CSH, OSH, WSA, SAV, GRA, WET, CRO, URB, CNM, SNO and BRN denote water, evergreen needleleaf forest, evergreen broadleaf forest, deciduous broadleaf forest, mixed forest, closed shrublands, open shrublands, woody savannas, savannas, grasslands, wetlands, croplands, urban and built-up, cropland/natural vegetation mosaic, snow and ice and barren or sparsely vegetated, respectively.

1.5 Aims and overview

This study aims to integrate eddy covariance method, remote sensing techniques, and land surface modeling to quantify GPP and ET across Australian terrestrial biomes and their responses to climate change over a range of time scales. In chapter 2 to 5, I use one of the three approaches in a novel way to address scientific questions on the coupling or estimation of GPP and ET and produce available GPP and ET products (Figure 1.2). In Chapter 6,

outputs by previous chapters are integrated into a comprehensive assessment of patterns and underlying mechanisms of GPP and ET in Australia (Figure 1.2). Hypotheses and specific aims for each chapter are listed as the following:

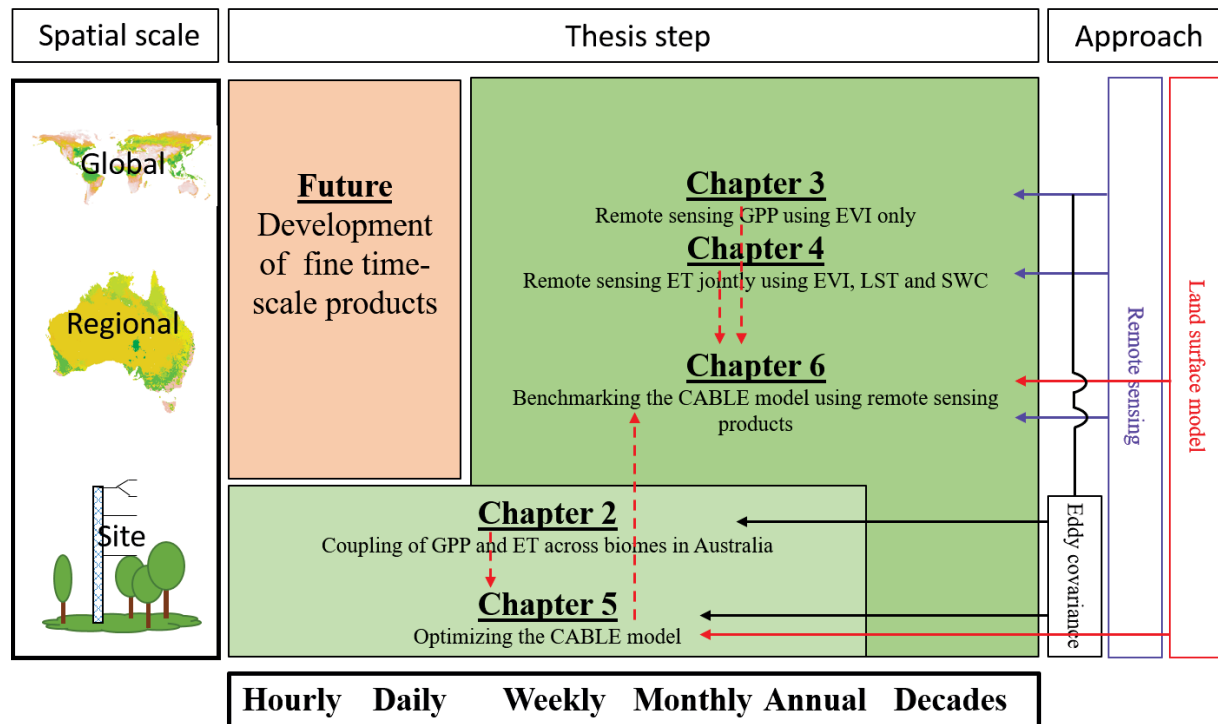


Figure 1.2. Framework of this thesis. The horizontal axis indicates time-scale while the vertical axis indicates spatial scale. The box for thesis step represents the spatio-temporal scales at which the research is conducted. The solid arrow lines indicate methods used in the chapter while the dashed arrow lines indicate output of the chapter into following steps.

(1) In Chapter 2, I assume that the sensitivities of GPP to energy and water resources (represented as ET) across biomes, i.e., ecosystem light-use efficiency (eLUE) and ecosystem water-use efficiency (eWUE), are closely related with climate variables. The lack of consensus on controlling factors of eLUE and eWUE at multiple temporal scales and across biomes reflects the complexity of interactions between terrestrial ecosystems and climate. The eddy covariance technique provides an opportunity to examine this because it includes

simultaneous measurements of solar radiation, carbon and water fluxes, VPD and soil moisture content, thereby generating an extensive time series of eLUE and eWUE from hourly to annual time-scales. Seven OzFlux sites along a precipitation gradient were used. The novelty of this study lies in the application of the wavelet-aggregation method in decomposing half-hourly flux data into different frequencies.

(2) In Chapter 3, I examined the ability of EVI alone to estimate GPP across biomes. Previous studies have shown that the EVI holds the potential to estimate GPP across biomes. However, this capacity of EVI has never been validated or developed against biomes distributed globally. The FLUXNET and MODIS EVI data set offer the opportunity to explore the relationship between annual GPP and annual EVI and thus can provide long-term monitoring of GPP to compare with modeled GPP by LSMs.

(3) In Chapter 4, I aim to develop a pure remote sensing model of ET. Thermal or physical based remote sensing models are limited by the accuracy of land surface temperature, complex parameterization and coarse resolution of global meteorological inputs. The novelty of this study is that within a sophisticated hydrological framework of ET regimes, energy and water constraints on ET are represented by multi-source remote sensed variables, including optical EVI, thermal LST and microwave soil water content (SWC).

(4) In Chapter 5, the Bayesian Monte Carlo Markov Chain method is used to identify and optimize key processes for GPP and ET in the CABLE model. Different from previous studies focusing on above- or below-ground processes only, I investigated both simultaneously through an improved version of CABLE, which incorporates a dynamic root water uptake function and a hydrologic redistribution function.

(5) In Chapter 6, GPP estimated by EVI alone, ET estimated in Chapter 4 and other remote sensing products of GPP and ET are jointly used to benchmark the optimized CABLE model

across Australia. The specific aims are to find the deficits of LSMs in utilizing available information included in inputs and investigate the performance of LSMs at a large spatial scale with a variety of vegetation types and climate regimes.

(6) In Chapter 7, findings and their implications in previous chapters are discussed as well as priority research directions in future.

References

- Allen, C. D., and D. D. Breshears (1998), Drought-induced shift of a forest–woodland ecotone: rapid landscape response to climate variation, *Proceedings of the National Academy of Sciences*, 95(25), 14839-14842.
- Aubinet, M., A. Grelle, A. Ibrom, Ü. Rannik, J. Moncrieff, T. Foken, A. Kowalski, P. Martin, P. Berbigier, and C. Bernhofer (2000), Estimates of the annual net carbon and water exchange of forests: the EUROFLUX methodology, *Advances in ecological research*, 30, 113-175.
- Baldocchi, D. (2008), 'Breathing' of the terrestrial biosphere: lessons learned from a global network of carbon dioxide flux measurement systems, *Australian Journal of Botany*, 56(1), 1-26.
- Baldocchi, D., E. Falge, L. Gu, R. Olson, D. Hollinger, S. Running, P. Anthoni, C. Bernhofer, K. Davis, and R. Evans (2001), FLUXNET: A new tool to study the temporal and spatial variability of ecosystem-scale carbon dioxide, water vapor, and energy flux densities, *Bulletin of the American Meteorological Society*, 82(11), 2415-2434.
- Barker, C. A., B. D. Amiro, H. Kwon, B. E. Ewers, and J. L. Angstrom (2009), Evapotranspiration in intermediate-aged and mature fens and upland black spruce boreal forests, *Ecohydrology*, 2(4), 462-471.
- Beer, C., M. Reichstein, P. Ciais, G. Farquhar, and D. Papale (2007), Mean annual GPP of

- Europe derived from its water balance, *Geophysical Research Letters*, 34(5), L05401.
- Beer, C., M. Reichstein, E. Tomelleri, P. Ciais, M. Jung, N. Carvalhais, C. Rödenbeck, M. A. Arain, D. Baldocchi, and G. B. Bonan (2010), Terrestrial gross carbon dioxide uptake: global distribution and covariation with climate, *Science*, 329(5993), 834-838.
- Bonan, G. B., P. J. Lawrence, K. W. Oleson, S. Levis, M. Jung, M. Reichstein, D. M. Lawrence, and S. C. Swenson (2011), Improving canopy processes in the Community Land Model version 4 (CLM4) using global flux fields empirically inferred from FLUXNET data, *Journal of Geophysical Research: Biogeosciences* (2005–2012), 116(G2).
- Bréda, N., R. Huc, A. Granier, and E. Dreyer (2006), Temperate forest trees and stands under severe drought: a review of ecophysiological responses, adaptation processes and long-term consequences, *Annals of Forest Science*, 63(6), 625-644.
- Brooks, P. D., P. A. Troch, M. Durcik, E. Gallo, and M. Schlegel (2011), Quantifying regional scale ecosystem response to changes in precipitation: Not all rain is created equal, *Water Resources Research*, 47(10).
- Budyko, M. I. (1974), Climate and Life, *Academic Press*, 508 p.
- Carlson, T. N., and D. A. Ripley (1997), On the relation between NDVI, fractional vegetation cover, and leaf area index, *Remote Sensing of Environment*, 62(3), 241-252.
- Chen, F., and Y. Zhang (2009), On the coupling strength between the land surface and the atmosphere: From viewpoint of surface exchange coefficients, *Geophysical Research Letters*, 36(10).
- Ciais, P., M. Reichstein, N. Viovy, A. Granier, J. Ogée, V. Allard, M. Aubinet, N. Buchmann, C. Bernhofer, and A. Carrara (2005), Europe-wide reduction in primary productivity caused by the heat and drought in 2003, *Nature*, 437(7058), 529-533.
- Cleugh, H. A., R. Leuning, Q. Mu, and S. W. Running (2007), Regional evaporation estimates

- from flux tower and MODIS satellite data, *Remote Sensing of Environment*, 106(3), 285-304.
- Costanza, R., R. d'Arge, R. De Groot, S. Faber, M. Grasso, B. Hannon, K. Limburg, S. Naeem, R. V. O'Neill, and J. Paruelo (1997), The value of the world's ecosystem services and natural capital.
- Foken, T. (2008), The energy balance closure problem: An overview, *Ecological Applications*, 18(6), 1351-1367.
- Franssen, H., R. Stöckli, I. Lehner, E. Rotenberg, and S. Seneviratne (2010), Energy balance closure of eddy-covariance data: A multisite analysis for European FLUXNET stations, *Agricultural and Forest Meteorology*, 150(12), 1553-1567.
- Ghilain, N., A. Arboleda, G. Sepulcre-Cantò, O. Batelaan, J. Ardö, and F. Gellens-Meulenberghs (2012), Improving evapotranspiration in a land surface model using biophysical variables derived from MSG/SEVIRI satellite, *Hydrology and Earth System Sciences*, 16(8), 2567-2583.
- Hall, F. G., K. F. Huemmrich, S. J. Goetz, P. J. Sellers, and J. E. Nickeson (1992), Satellite remote sensing of surface energy balance: Success, failures, and unresolved issues in FIFE, *Journal of Geophysical Research: Atmospheres* (1984–2012), 97(D17), 19061-19089.
- Holdo, R. M., and E. R. Brocato (2015), Tree–grass competition varies across select savanna tree species: a potential role for rooting depth, *Plant Ecology*, 216(4), 577-588.
- Huete, A. (1988), A soil-adjusted vegetation index (SAVI), *Remote Sensing of Environment*, 25(3), 295-309.
- Huete, A., K. Didan, T. Miura, E. P. Rodriguez, X. Gao, and L. G. Ferreira (2002), Overview of the radiometric and biophysical performance of the MODIS vegetation indices, *Remote Sensing of Environment*, 83(1), 195-213.

- Kalma, J., and D. Jupp (1990), Estimating evaporation from pasture using infrared thermometry: evaluation of a one-layer resistance model, *Agricultural and Forest Meteorology*, 51(3), 223-246.
- Lai, C.-T., and G. Katul (2000), The dynamic role of root-water uptake in coupling potential to actual transpiration, *Advances in Water Resources*, 23(4), 427-439.
- Lawrence, P. J., and T. N. Chase (2009), Climate impacts of making evapotranspiration in the Community Land Model (CLM3) consistent with the Simple Biosphere Model (SiB), *Journal of Hydrometeorology*, 10(2), 374-394.
- Levin, S. A. (1992), The problem of pattern and scale in ecology: the Robert H. MacArthur award lecture, *Ecology*, 73(6), 1943-1967.
- Li, L., Y. Wang, Q. Yu, B. Pak, D. Eamus, J. Yan, E. van Gorsel, and I. Baker (2012), Improving the responses of the Australian community land surface model (CABLE) to seasonal drought, *Journal of Geophysical Research*, 117, G04002.
- Lillesand, T., R. W. Kiefer, and J. Chipman (2014), *Remote sensing and image interpretation*, John Wiley & Sons.
- Ma, X., A. Huete, Q. Yu, N. R. Coupe, K. Davies, M. Broich, P. Ratana, J. Beringer, L. Hutley, and J. Cleverly (2013), Spatial patterns and temporal dynamics in savanna vegetation phenology across the North Australian Tropical Transect, *Remote Sensing of Environment*, 139, 97-115.
- Mauder, M., T. Foken, R. Clement, J. Elbers, W. Eugster, T. Grünwald, B. Heusinkveld, and O. Kolle (2008), Quality control of CarboEurope flux data? Part 2: Inter-comparison of eddy-covariance software, *Biogeosciences*, 5(2), 451-462.
- Melillo, J. M., A. D. McGuire, D. W. Kicklighter, B. Moore, C. J. Vorosmarty, and A. L. Schloss (1993), Global climate change and terrestrial net primary production, *Nature*, 363(6426), 234-240.

- Milly, P. (1994), Climate, soil water storage, and the average annual water balance, *Water Resources Research*, 30(7), 2143-2156.
- Monin, A., and A. Obukhov (1954), Basic laws of turbulent mixing in the surface layer of the atmosphere, *Contrib. Geophys. Inst. Acad. Sci. USSR*, 151, 163-187.
- Monteith, J. (1965), Evaporation and environment, paper presented at Symp. Soc. Exp. Biol.
- Nagler, P. L., R. L. Scott, C. Westenburg, J. R. Cleverly, E. P. Glenn, and A. R. Huete (2005a), Evapotranspiration on western US rivers estimated using the Enhanced Vegetation Index from MODIS and data from eddy covariance and Bowen ratio flux towers, *Remote sensing of environment*, 97(3), 337-351.
- Nagler, P. L., J. Cleverly, E. Glenn, D. Lampkin, A. Huete, and Z. Wan (2005b), Predicting riparian evapotranspiration from MODIS vegetation indices and meteorological data, *Remote Sensing of Environment*, 94(1), 17-30.
- Overgaard, J., D. Rosbjerg, and M. Butts (2006), Land-surface modelling in hydrological perspective? a review, *Biogeosciences*, 3(2), 229-241.
- Pappas, C., S. Fatichi, S. Rimkus, P. Burlando, and M. O. Huber (2015), The role of local-scale heterogeneities in terrestrial ecosystem modeling, *Journal of Geophysical Research: Biogeosciences*, 120(2), 341-360.
- Paschalis, A., S. Fatichi, G. G. Katul, and V. Y. Ivanov (2015), Cross-scale impact of climate temporal variability on ecosystem water and carbon fluxes, *Journal of Geophysical Research: Biogeosciences*, 120(9), 1716-1740.
- Piao, S., P. Ciais, P. Friedlingstein, P. Peylin, M. Reichstein, S. Luyssaert, H. Margolis, J. Fang, A. Barr, and A. Chen (2008), Net carbon dioxide losses of northern ecosystems in response to autumn warming, *Nature*, 451(7174), 49-52.
- Polley, H. W., R. L. Phillips, A. B. Frank, J. A. Bradford, P. L. Sims, J. A. Morgan, and J. R. Kiniry (2011), Variability in light-use efficiency for gross primary productivity on Great

- Plains grasslands, *Ecosystems*, 14(1), 15-27.
- Potter, C. S., S. Klooster, and V. Brooks (1999), Interannual variability in terrestrial net primary production: Exploration of trends and controls on regional to global scales, *Ecosystems*, 2(1), 36-48.
- Rahman, A., D. Sims, V. Cordova, and B. El-Masri (2005), Potential of MODIS EVI and surface temperature for directly estimating per-pixel ecosystem C fluxes, *Geophysical Research Letters*, 32(19), L19404.
- Reichstein, M., E. Falge, D. Baldocchi, D. Papale, M. Aubinet, P. Berbigier, C. Bernhofer, N. Buchmann, T. Gilmanov, and A. Granier (2005), On the separation of net ecosystem exchange into assimilation and ecosystem respiration: review and improved algorithm, *Global Change Biology*, 11(9), 1424-1439.
- Reichstein, M., D. Papale, R. Valentini, M. Aubinet, C. Bernhofer, A. Knohl, T. Laurila, A. Lindroth, E. Moors, and K. Pilegaard (2007), Determinants of terrestrial ecosystem carbon balance inferred from European eddy covariance flux sites, *Geophysical Research Letters*, 34(1).
- Running, S. W., R. R. Nemani, F. A. Heinsch, M. Zhao, M. Reeves, and H. Hashimoto (2004), A continuous satellite-derived measure of global terrestrial primary production, *Bioscience*, 54(6), 547-560.
- Schlosser, C. A., and X. Gao (2010), Assessing evapotranspiration estimates from the second Global Soil Wetness Project (GSWP-2) simulations, *Journal of Hydrometeorology*, 11(4), 880-897.
- Schmid, H. (1994), Source areas for scalars and scalar fluxes, *Boundary-Layer Meteorology*, 67(3), 293-318.
- Sims, D. A., H. Luo, S. Hastings, W. C. Oechel, A. F. Rahman, and J. A. Gamon (2006a), Parallel adjustments in vegetation greenness and ecosystem CO₂ exchange in response to

- drought in a Southern California chaparral ecosystem, *Remote Sensing of Environment*, 103(3), 289-303.
- Sims, D. A., A. F. Rahman, V. D. Cordova, B. Z. El-Masri, D. D. Baldocchi, L. B. Flanagan, A. H. Goldstein, D. Y. Hollinger, L. Misson, and R. K. Monson (2006b), On the use of MODIS EVI to assess gross primary productivity of North American ecosystems, *Journal of Geophysical Research: Biogeosciences* (2005–2012), 111(G4).
- Sims, D. A., A. F. Rahman, V. D. Cordova, B. Z. El-Masri, D. D. Baldocchi, P. V. Bolstad, L. B. Flanagan, A. H. Goldstein, D. Y. Hollinger, and L. Misson (2008), A new model of gross primary productivity for North American ecosystems based solely on the enhanced vegetation index and land surface temperature from MODIS, *Remote Sensing of Environment*, 112(4), 1633-1646.
- Sims, D. A., et al. (2006c), On the use of MODIS EVI to assess gross primary productivity of North American ecosystems, *Journal of Geophysical Research: Biogeosciences*, 111(G4), G04015.
- Smith, R., and B. Choudhury (1990), Relationship of multispectral satellite data to land surface evaporation from the Australian continent, *International Journal of Remote Sensing*, 11(11), 2069-2088.
- Sun, G., A. Noormets, J. Chen, and S. McNulty (2008), Evapotranspiration estimates from eddy covariance towers and hydrologic modeling in managed forests in Northern Wisconsin, USA, *Agricultural and Forest Meteorology*, 148(2), 257-267.
- Sun, G., K. Alstad, J. Chen, S. Chen, C. R. Ford, G. Lin, C. Liu, N. Lu, S. G. McNulty, and H. Miao (2011), A general predictive model for estimating monthly ecosystem evapotranspiration, *Ecohydrology*, 4(2), 245-255.
- Tanaka, N., T. Kume, N. Yoshifuji, K. Tanaka, H. Takizawa, K. Shiraki, C. Tantasirin, N. Tangtham, and M. Suzuki (2008), A review of evapotranspiration estimates from tropical

- forests in Thailand and adjacent regions, *Agricultural and Forest Meteorology*, 148(5), 807-819.
- Turner, D. P., S. Urbanski, D. Bremer, S. C. Wofsy, T. Meyers, S. T. Gower, and M. Gregory (2003), A cross-biome comparison of daily light use efficiency for gross primary production, *Global Change Biol.*, 9(3), 383-395.
- Verstraeten, W. W., F. Veroustraete, and J. Feyen (2005), Estimating evapotranspiration of European forests from NOAA-imagery at satellite overpass time: Towards an operational processing chain for integrated optical and thermal sensor data products, *Remote Sensing of Environment*, 96(2), 256-276.
- Wang, K., and R. E. Dickinson (2012), A review of global terrestrial evapotranspiration: Observation, modeling, climatology, and climatic variability, *Reviews of Geophysics*, 50(2).
- Wang, K., P. Wang, Z. Li, M. Cribb, and M. Sparrow (2007), A simple method to estimate actual evapotranspiration from a combination of net radiation, vegetation index, and temperature, *Journal of Geophysical Research: Atmospheres*, 112(D15), D15107.
- Wang, Y. P., and R. Leuning (1998), A two-leaf model for canopy conductance, photosynthesis and partitioning of available energy I: Model description and comparison with a multi-layered model, *Agricultural and Forest Meteorology*, 91(1), 89-111.
- Williams, M., A. Richardson, M. Reichstein, P. Stoy, P. Peylin, H. Verbeeck, N. Carvalhais, M. Jung, D. Hollinger, and J. Kattge (2009), Improving land surface models with FLUXNET data, *Biogeosciences*, 1341-1359.
- Wright, I. J., P. B. Reich, M. Westoby, D. D. Ackerly, Z. Baruch, F. Bongers, J. Cavender-Bares, T. Chapin, J. H. Cornelissen, and M. Diemer (2004), The worldwide leaf economics spectrum, *Nature*, 428(6985), 821-827.
- Wu, C., Z. Niu, and S. Gao (2010), Gross primary production estimation from MODIS data

- with vegetation index and photosynthetically active radiation in maize, *Journal of Geophysical Research: Atmospheres* (1984–2012), 115(D12).
- Wylie, B. K., D. A. Johnson, E. Laca, N. Z. Saliendra, T. G. Gilmanov, B. C. Reed, L. L. Tieszen, and B. B. Worstell (2003), Calibration of remotely sensed, coarse resolution NDVI to CO₂ fluxes in a sagebrush–steppe ecosystem, *Remote Sensing of Environment*, 85(2), 243-255.
- Xiao, X., Q. Zhang, D. Hollinger, J. Aber, and B. Moore III (2005), Modeling gross primary production of an evergreen needleleaf forest using MODIS and climate data, *Ecological Applications*, 15(3), 954-969.
- Xiao, X., D. Hollinger, J. Aber, M. Goltz, E. A. Davidson, Q. Zhang, and B. Moore III (2004a), Satellite-based modeling of gross primary production in an evergreen needleleaf forest, *Remote Sensing of Environment*, 89(4), 519-534.
- Xiao, X., Q. Zhang, B. Braswell, S. Urbanski, S. Boles, S. Wofsy, B. Moore III, and D. Ojima (2004b), Modeling gross primary production of temperate deciduous broadleaf forest using satellite images and climate data, *Remote Sensing of Environment*, 91(2), 256-270.
- Yang, Y., and S. Shang (2013), A hybrid dual-source scheme and trapezoid framework–based evapotranspiration model (HTEM) using satellite images: Algorithm and model test, *Journal of Geophysical Research: Atmospheres*, 118(5), 2284-2300.
- Yebra, M., A. Van Dijk, R. Leuning, A. Huete, and J. P. Guerschman (2013), Evaluation of optical remote sensing to estimate actual evapotranspiration and canopy conductance, *Remote Sensing of Environment*, 129, 250-261.
- Yuan, W., S. Liu, G. Zhou, G. Zhou, L. L. Tieszen, D. Baldocchi, C. Bernhofer, H. Gholz, A. H. Goldstein, and M. L. Goulden (2007), Deriving a light use efficiency model from eddy covariance flux data for predicting daily gross primary production across biomes, *Agricultural and Forest Meteorology*, 143(3), 189-207.

- Zhang, L., W. Dawes, and G. Walker (2001), Response of mean annual evapotranspiration to vegetation changes at catchment scale, *Water resources research*, 37(3), 701-708.
- Zhang, L., K. Hickel, W. Dawes, F. H. Chiew, A. Western, and P. Briggs (2004), A rational function approach for estimating mean annual evapotranspiration, *Water Resources Research*, 40(2).
- Zhao, M., F. A. Heinsch, R. R. Nemani, and S. W. Running (2005), Improvements of the MODIS terrestrial gross and net primary production global data set, *Remote sensing of Environment*, 95(2), 164-176.

Chapter 2: Intrinsic climate dependency of ecosystem light and water-use-efficiencies across Australian biomes

Abstract

The sensitivity of ecosystem gross primary production (GPP) to availability of water and photosynthetically active radiation (PAR) differs among biomes. Here I investigated variations of ecosystem light-use-efficiency (eLUE: GPP/PAR) and water-use-efficiency (eWUE: $GPP/evapotranspiration$) among seven Australian eddy covariance sites with contrasting annual precipitation, species composition and temperature regimes. Changes to both eLUE and eWUE were primarily correlated with atmospheric vapor pressure deficit (VPD) at multiple temporal scales across biomes, with minor additional correlations observed with soil moisture and temperature. The effects of leaf area index on eLUE and eWUE were also relatively weak compared to VPD, indicating an intrinsic dependency of eLUE and eWUE on climate. Additionally, the influence of eLUE and eWUE were statistically different for biomes between summer and winter, except eWUE for savannas and the grassland. These findings will improve our understanding of how light- and water-use traits in Australian ecosystems may respond to climate change.

2.1 Introduction

Climate imposes important but often contrasting limitations on productivity in most vegetated biomes [Churkina and Running, 1998]. Among climate factors, solar radiation provides the energy source for photosynthesis, while water availability alters leaf-scale photosynthesis via modulations of plant stomatal conductance [Beer *et al.*, 2009] and canopy-scale photosynthesis via changes in leaf area index [Eamus *et al.*, 2001]. Ecosystem

light-use-efficiency (eLUE) and water-use-efficiency (eWUE) are two critical traits of terrestrial ecosystems that characterize the sensitivity of biomass production to solar irradiance and water supply [Beer *et al.*, 2007; Hu *et al.*, 2008; Ponton *et al.*, 2006; Turner *et al.*, 2003]. eLUE and eWUE differ substantially in value and vary with environmental stress and vegetation structure within and across biomes [Farquhar *et al.*, 1989; Law *et al.*, 2002; Schwalm *et al.*, 2006]. The values of both eLUE and eWUE exhibit time-scale dependence in the sense that their primary environmental controls vary temporally [Campos *et al.*, 2013; Schwalm *et al.*, 2006; Turner *et al.*, 2003].

Historically, eLUE (ϵ) has been defined as the ratio of net primary production (NPP, aboveground or total, ϵ_n) or gross primary production (GPP, ϵ_g) to incident photosynthetically active radiation (PAR) or absorbed PAR (APAR) [Gower *et al.*, 1999]. Based upon evolutionary and physiological theory, ϵ_n and ϵ_g are expected to converge across biomes [Goetz and Prince, 1999]. However, values of each are dependent on plant function type [Gower *et al.*, 1999; Schwalm *et al.*, 2006; Turner *et al.*, 2003]. The biophysical, biochemical and meteorological controls of eLUE among biomes at multiple time-scales are not well understood, resulting in imprecise estimates of NPP and GPP and uncertainties in the responses of eLUE to climate change [Kanniah *et al.*, 2011]. For example, in one study, daily ϵ_g decreased with increasing APAR but was poorly correlated with vapor pressure deficit (VPD) or air temperature (T_a), while the relative values of ϵ_g across biomes were influenced by relative nitrogen availability [Turner *et al.*, 2003]. In contrast, Schwalm *et al.* [2006] observed that changes in daily ϵ_g were driven by variation in light and temperature with no correlation to water availability or foliar nitrogen, while annual ϵ_g varied across biomes as a function of mean annual temperature (MAT) and leaf area index (LAI). Additionally, annual ϵ_g can increase with increasing total annual precipitation and decreasing potential evapotranspiration [Polley *et al.*, 2011] or MAT [Lafont *et al.*, 2002].

eWUE reflects a trade-off between carbon gain and water loss from leaves and ecosystems [Baldocchi, 1994], and is important for ecosystem productivity and resilience [Campos *et al.*, 2013; Huxman *et al.*, 2004]. At the leaf-scale, eWUE is expressed as the ratio of net photosynthesis to transpiration but at the ecosystem-scale, eWUE is defined as the ratio of either NEE or GPP to ET or canopy transpiration [Beer *et al.*, 2009; Niu *et al.*, 2011]. To quantify the role of water limitation on above-ground NPP, rain-use-efficiency (RUE, the ratio of above-ground NPP to rainfall) is widely used [Huxman *et al.*, 2004]. Alternatively, inherent water-use-efficiency (IWUE, $GPP \cdot VPD / ET$) can be used to normalize the effect of VPD on ET [Beer *et al.*, 2009; Eamus *et al.*, 2013]. Daily eWUE is negatively correlated with VPD during the time of peak GPP activity [Ponton *et al.*, 2006] and so is monthly eWUE across a large range of biomes [Law *et al.*, 2002]. In contrast, annual eWUE tends to be similar across biomes except for tundra vegetation [Law *et al.*, 2002]. Across a grassland transect in China, LAI is considered as the primary determinant of seasonal eWUE [Hu *et al.*, 2008]. Annual eWUE of grasslands may decrease [Li *et al.*, 2008] or increase [Niu *et al.*, 2011] with increasing annual precipitation whilst eWUE may differ between wet and dry years [Campos *et al.*, 2013; Huxman *et al.*, 2004] or wet and dry seasons [Eamus *et al.*, 2013], and varies with soil moisture and LAI [Beer *et al.*, 2009].

The lack of consensus on the relative importance of different controlling factors of eLUE and eWUE across biomes at multiple temporal scales reflects the complexity of interactions between terrestrial ecosystems and climate. Therefore, a key issue to resolve is the relationships of eLUE and eWUE to climatic drivers. The eddy covariance (EC) technique provides an opportunity to examine the potential relationships through simultaneous measurements of solar radiation, carbon and water fluxes, VPD and soil water content (SWC), thereby generating an extensive time series of eLUE and eWUE from hourly to multi-annual time-scales. Concurrent measurement of meteorological variables with fluxes can be used to

quantify limitations on eLUE and eWUE and the interaction of climate variables as determinants of eLUE and eWUE. Thus, the current study used eddy covariance data from seven contrasting ecosystems in Australia for examining the magnitude, spatial patterns, and environmental regulation of eLUE and eWUE at multiple time-scales (hourly, daily, 8-day, monthly, and yearly). These seven EC sites encompass a range of biomes along a large precipitation, species compositional and temperature gradient, thereby providing further insights into coupling between ecosystems and climate. I aimed to identify variations in eLUE and eWUE of Australian major ecosystems over different time-scales and their key climatic drivers among biomes. This will allow for a better understanding of the coupling of carbon and water cycles and the effects of climate change on ecosystem carbon budgets and water use.

2.2 Methods

2.2.1 Sites and data processing

2.2.1.1 Sites information

Seven sites were selected for this study in Australia. These sites include four contrasting savannas (Savn, AU-Ade, AU-Asm, AU-Dry and AU-How sites), two different evergreen broadleaf forests (EBF, AU-Tum and AU-Wac sites), and one grassland (Grass, AU-Stp site) (Table 2.1; Figure 2.1). The dominant woody species differ among the sites. The AU-How and AU-Dry sites are *Eucalyptus tetrodonta*/*Eucalyptus miniata* dominated savannas (tree height *ca* 12 m), which are widely distributed across tropical Australia [Hutley *et al.*, 2011]. The AU-Ade site is dominated by *Eucalyptus tectifica* and *Corymbia latifolia* (tree height *ca* 16 m) as a result of the finer textured and poorly drained soils. The canopy dominant tree species at the AU-Asm site is the N₂ fixing species *Acacia aneura*, which is 6.5 m tall on average. Each of these sites (AU-How, AU-Dry, AU-Ade and AU-Asm) are classified as savanna, a

biome defined by a discontinuous tree canopy with a grassy understory [Eamus *et al.*, 2001] experiencing seasonality in rainfall. The grassland AU-Stp is dominated by Mitchell grass within an extensive tussock grassland ecosystem that occurs on heavily cracking clay soils. The AU-Tum site is classified as a wet sclerophyllous forest and is dominated by *Eucalyptus delegatensis* (tree height *ca* 40 m). The AU-Wac site is an 300-year-old growth stand dominated by *Eucalyptus regnans* (tree height *ca* 75 m) with a temperate rainforest understory consisting of *Pomaderris aspera* and *Olearia argophylla* (tree height 10-18 m) [Kilinc *et al.*, 2013a]. Bioclimatic classifications of these sites range from tropical wet-dry in northern Australia, through tropical semi-arid in central Australia to cool temperate mesic in southeastern. Mean annual precipitation (MAP) is smallest in central Australia and largest in far northern monsoonal Australia. All sites show seasonal patterns in precipitation, temperature and VPD that interact with large fluctuations in water availability. Seasonal variability in temperature and PAR was larger at the two forests in southeastern Australia than at the grassland and savanna sites. Conversely, seasonal variability in VPD and rainfall was larger in the northern and central sites, where a distinct dry season occurs during Australian winter (Figure 2.1).

Table 2.1. La Thuile code, site name, latitude (Lat), longitude (Long), year of observations, altitude (Alt), biomes (Evergreen Broadleaf Forests, EBF; Savannas, Savn; Grasslands, Grass), mean maximum annual temperature (T_{\max}), mean minimum annual temperature (T_{\min}), mean annual precipitation (MAP), mean annual minimum leaf area index (LAI_{\min}) and mean annual maximum LAI (LAI_{\max}) during observation intervals for the study sites.

La code	Thuile	Site name	Lon	Lat	Year	Alt (m)	Biome s	T_{\max} (°C)	T_{\min} (°C)	MAP (mm)	LAI_{\min} - LAI_{\max} (m ² /m ²)
AU-How		Howard Springs	131.15 E	12.50 S	2004- 2008	64	Savn	39.3	12.2	1201	1.23-2.16
AU-Ade		Adelaide River	131.12 E	13.08 S	2007- 2009. 05	90	Savn	38.0	11.7	1852	0.73-2.04
AU-Dry		Dry River	132.37 E	15.26 S	2009- 2012. 09	175	Savn	40.6	8.9	995	1.03-1.66
AU-Stp		Sturt Plains	133.35 E	17.15 S	2008- 2012	250	Grass	42.7	6.2	695	0.38-1.03
AU-Asm		Alice Springs	133.25 E	22.28 S	2010. 09-20 13.09	606	Savn	40.8	0.2	335	0.27-0.47
AU-Tum		Tumbarum ba	148.15 E	35.66 S	2008- 2012	120 0	EBF	29.3	-2.9	1000	4.06-5.58
AU-Wac		Wallaby Creek	145.19 E	37.43 S	2006- 2008	720	EBF	33.1	-0.1	1595	0.98-5.01

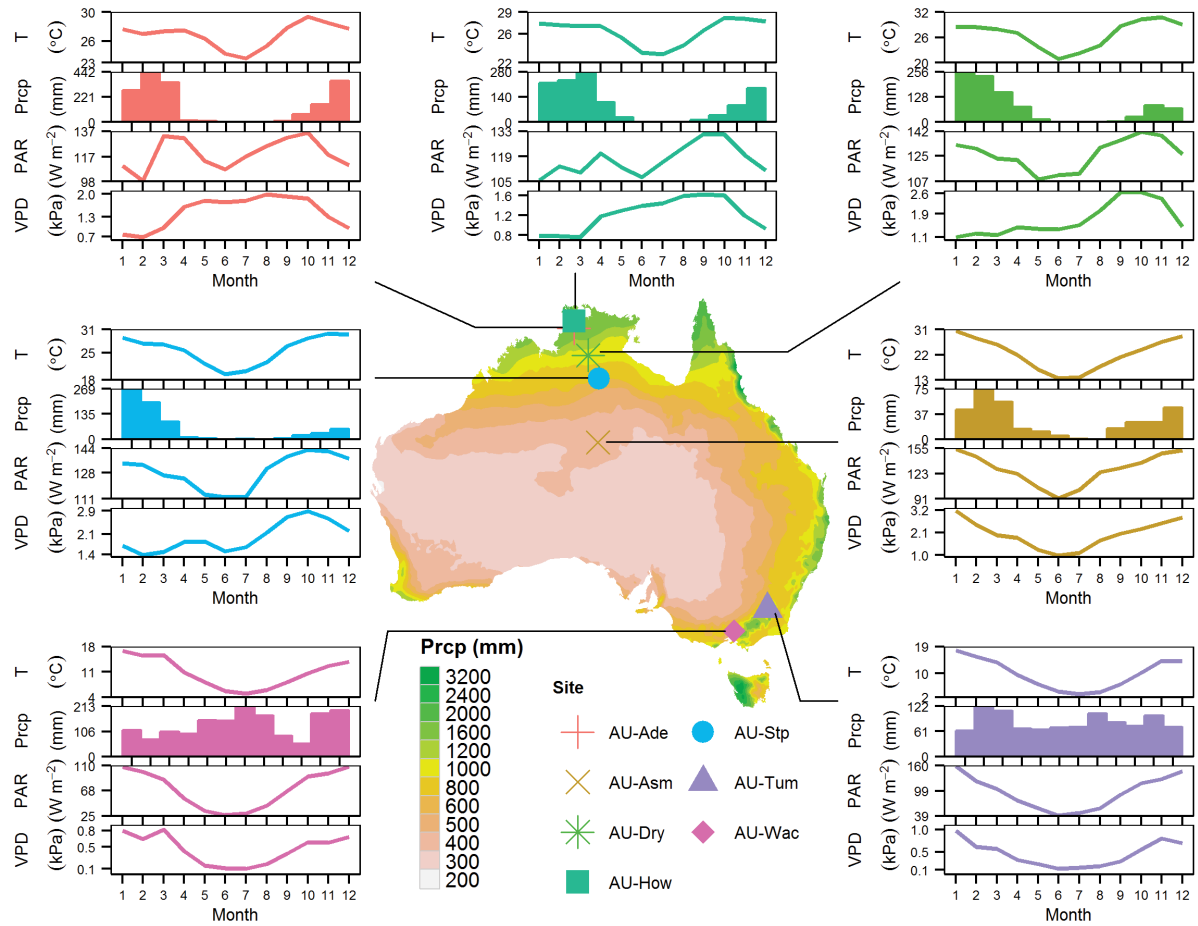


Figure 2.1. Average annual precipitation contour map of Australia in 30 years from 1976 to 2005 (statistics by Bureau of Meteorology, Australia), spatial distribution of selected sites and average monthly climate over the respective observation periods for each site. T indicates temperature, Prctp indicates precipitation, PAR indicates photosynthetically active radiation, and VPD indicates the vapor pressure deficit.

2.2.1.2 Data processing

At each site, LAI data were derived from the space-borne MODIS (Moderate Resolution Imaging Spectroradiometer) sensor (500 m spatial resolution and 8 day temporal resolution). The MODIS images are spatially similar to the footprint size of the EC data used. A central 3×3 window was used to extract the flux tower LAI time series. This sampling strategy can effectively reduce the error due to the scale mismatch between the tower footprint and MODIS pixels [Rahman *et al.*, 2005; Xiao *et al.*, 2005]. Then the LAI data series were smoothed using the TIMESAT tool [Jönsson and Eklundh, 2004]. Mean maximum LAI (LAI_{max}) for each site were aggregated at 8-day, monthly and yearly scales.

Half-hourly carbon and water fluxes, rainfall, air and soil temperature, soil water content, absolute humidity, downward shortwave radiation and net radiation were measured using an eddy covariance system and associated meteorological and soil moisture sensors installed at each site. PAR and ET were calculated as downward shortwave radiation (unit: W m^{-2}) times 0.5 and latent heat flux (unit: W m^{-2}) divided by the latent heat of vaporization ($2450 \text{ J g H}_2\text{O}^{-1}$), respectively. Water and CO_2 fluxes were processed through OzFlux level 2 (i.e., QA/QC) and level 3 (e.g. rotation, correction for frequency attenuation, and density-flux (WPL) corrections) using standardized methodology [Eamus *et al.*, 2013]. The post processing of the quality controlled data to fill gaps in meteorology, soil moisture and fluxes as well as partitioning NEE into GPP and ecosystem respiration was performed using the Dynamic INtegrated Gap filling and partitioning for Ozflux (DINGO) system. The system was coded in Python and consisted of modules to gap fill meteorological variables (air temperature, specific humidity, wind speed and barometric pressure) using nearby Bureau of meteorology (www.bom.gov.au) automatic weather stations that were correlated and corrected to tower observations. All radiation streams were gap-filled using a combination of MODIS albedo products (MCD43 BRDF-Albedo suite) and Bureau of Meteorology (BoM)

gridded global solar radiation and gridded daily meteorology from the Australian Water Availability Project data set (BoM AWAP) [Jones *et al.*, 2009]. Precipitation was gap-filled using either nearby BoM stations or BoM AWAP. Soil temperature and moisture were filled using the BIOS2 land surface model [Haverd *et al.*, 2013] run for each site forced with BoM AWAP data. Gap filling of fluxes were performed using an Artificial Neural Network (ANN) model using a multilayer network of full connectivity following Beringer *et al.* [2007]. Training was done using gradient information in a truncated Newton algorithm. NEE and the fluxes of sensible, latent and ground heat fluxes were modelled using the ANN with incoming solar radiation, VPD, soil moisture content, soil temperature, wind speed and MODIS EVI as inputs. The Ustar threshold for each site was determined following [Reichstein *et al.*, 2005] and night time observations below the μ^* (the wind friction velocity) threshold were replaced with ANN modelled values of ecosystem respiration using soil moisture content, soil temperature, air temperature and MODIS EVI as inputs. The ANN model for ecosystem respiration was applied to daylight periods to estimate daytime respiration and GPP was calculated as the difference between net ecosystem exchange and ecosystem respiration.

2.2.2 Wavelet aggregation method

Half-hourly eLUE and eWUE were defined as ratios of GPP to PAR and GPP to ET, respectively. For eLUE, using incident PAR as the denominator instead of absorbed PAR (APAR) can couple carbon and energy budgets directly at the ecosystem level rather than merely focusing on the biological mechanisms that drive photosynthesis [Schwalm *et al.*, 2006]. When large disturbances occurred (for example, fire or extensive insect-induced defoliation), flux and LAI data were excluded from all analyses to minimize the introduction of bias arising from the inclusion of short-term episodic large-scale fluctuations in these data. To analyze multi-scale interactions between eLUE/eWUE and forcing variables, measured

carbon and water fluxes, meteorological variables, SWC and LAI were resolved using the wavelet transformation [Ding *et al.*, 2013; Stoy *et al.*, 2005; Torrence and Compo, 1998]. The wavelet transformation can be used to analyze time series such as eddy covariance fluxes [Scanlon and Albertson, 2001] that contain non-stationary power at different frequencies [Daubechies, 1990]. Here a continuous wavelet transformation with the Morlet basis was employed. The Morlet mother wavelet function can be represented as:

$$\psi_0(\eta) = \pi^{-1/4} e^{i\omega_0\eta} e^{-\eta^2/2} \quad (3.1)$$

where ω_0 is the frequency and is taken as 6 to make above function have zero mean and be localized in both time and frequency space. To ensure the wavelet transform at different scales are comparable to each other and the transforms of other time series, the $\psi_0(\eta)$ wavelet function at each scale s is normalized as:

$$\psi(\eta) = \left(\frac{\delta t}{s} \right)^{1/2} \psi_0(\eta) \quad (3.2)$$

where δt is the time step of the time series. Then the continuous wavelet transform of a discrete time series x_n is the convolution of x_n with a scaled and translated Morlet mother wavelet:

$$W_n(s) = \sum_{t=0}^{N-1} x_t \psi^* \left[\frac{(t-n)\delta t}{s} \right] \quad (3.3)$$

where n indicates the localized time index, N is the number of x_n and $(*)$ indicates the complex conjugate. The scale s is usually given as fractional powers of two:

$$s_j = s_0 2^{j\delta j}, j = 0, 1, \dots, J \quad (3.4)$$

where s_0 is the smallest resolvable scale and generally taken to be $2\delta t$, δj indicates the scale sampling step and given to be 1/12 here and $J = \delta j^{-1} \log(2, N\delta t/s_0)$ indicates the number of scales. Then the reconstructed time series at scale k is the sum of the real part of

the wavelet transform over k to J scales:

$$x_{n,k} = \frac{\delta j \delta t^{1/2}}{C_\delta \psi_0(0)} \sum_{j=k}^J \frac{R\{W_n(s_j)\}}{s_j^{1/2}} \quad (3.5)$$

where R indicates the real part of complex and C_δ is a constant of 0.776.

Using the wavelet method, half-hourly carbon and water fluxes and environmental factors were transformed, reconstructed and then aggregated at hourly, daily, 8-day, monthly, seasonal and yearly time-scales, respectively. eLUE and eWUE were concurrently calculated at each time-scale. Figure 2.2 gives an example of this method at the Howard Springs site.

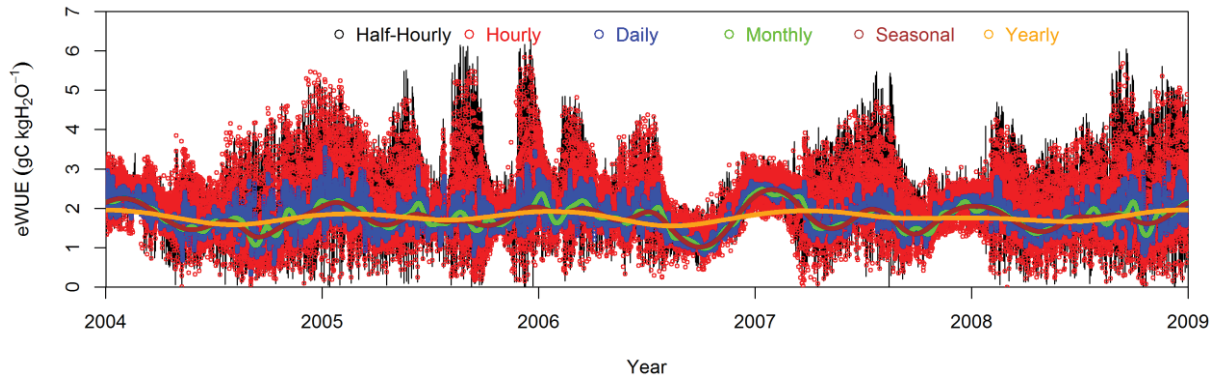


Figure 2.2. eWUE reconstruction at hourly, daily, monthly, seasonal and yearly scales using the wavelet transform at the Howard Springs site from 2004 to 2008. The reconstructed time series removes the higher frequency information in lower scales.

2.3 Results

2.3.1 GPP responses to PAR and ET

Figure 2.3 shows the multi-temporal (i.e. at daily to yearly time-scales) responses of GPP to variations in PAR and ET across the various ecosystems. GPP and PAR were significantly correlated only at the two temperate forest sites ($R^2 = 0.88$ – 0.97 , $p < 0.001$ and $R^2 = 0.67$ – 0.98 , $p < 0.001$ at AU-Tum and AU-Wac, respectively) (Figure 2.3). Generally, GPP exhibited a significant linear correlation with ET (R^2 from 0.48 to 0.96, $p < 0.001$) at all sites

across daily to monthly time-scales. Across the three biomes, average eLUE and eWUE were largest in forests, intermediate in savannas, and smallest in the grassland. Among the savannas, eLUE and eWUE were largest at AU-How and AU-Ade (tropical savannas) and smallest at AU-Asm (semi-arid savanna).

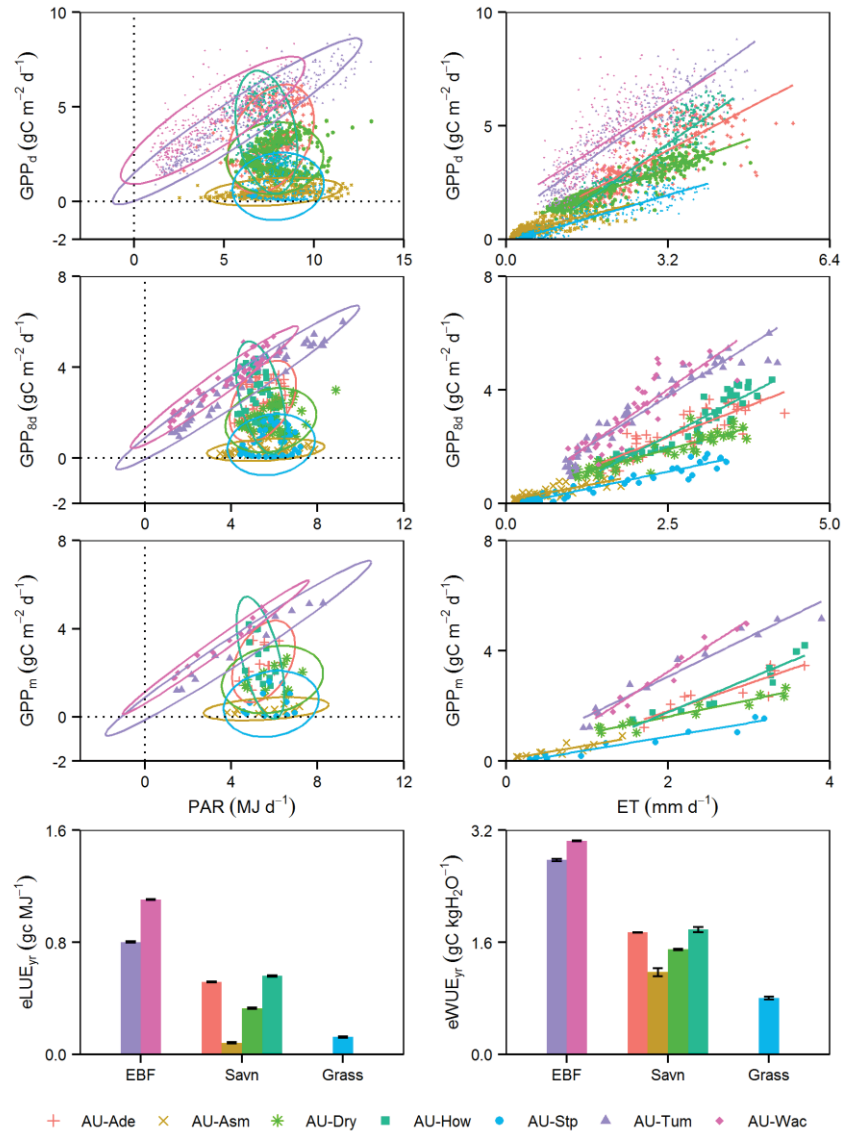


Figure 2.3. Relationships between (left) daily (GPP_d), eight day (GPP_{8d}), monthly (GPP_m) GPP and PAR and between (right) GPP and ET for seven sites. Ellipses (left) indicate 95% confidence boundaries of GPP. Bars indicate one standard deviation of annual eLUE or eWUE at each site. Also shown is the linear fit between GPP and ET (right). Annual eLUE(eLUE_{yr}) and eWUE(eWUE_{yr}) were calculated from annual GPP, PAR and ET.

2.3.2 Relationships of eLUE and eWUE with climate

eLUE was significantly correlated with air temperature and PAR, and eWUE was significantly correlated with PAR. However, these correlations across biomes became much weaker at shorter time-scales, especially at the hourly time-scale and in the summer when light is less limiting (Table 2.2). PAR explained less variation in eLUE than VPD at all time-scales, and air temperature was less correlated with eWUE than VPD at all time-scales except the hourly time-scale. Henceforth, of climate factors I mainly focus on the relationships between eLUE/eWUE and VPD, but this does not mean the effects of PAR on eLUE and air temperature on eWUE were not important. Across all sites, eLUE and eWUE followed a negative logarithmic relationship with VPD (Table 2.2; Figure 2.4). The goodness-of-fit increased as the time-scale increased. However, within a given ecosystem, a significant relationship between eLUE or eWUE and meteorology was, on occasion, absent. For example, at the AU-How site, eWUE was very weakly or not correlated with VPD (Figure 2.4). Likewise, at the AU-Asm site, eLUE was very weakly or not correlated with VPD (Figure 2.4). This suggests that the factors driving eLUE and eWUE can differ within and across biomes.

Table 2.2. Coefficients of determination (R^2) between LUE, WUE and Ta, PAR, VPD, SWC or LAI_{max} by logarithmic/exponential (Log/Exp) and linear (Lin) fitting, respectively. ***, **, *, and NULL indicates significant relationship at $p < 0.001$, 0.01, 0.05 and not significant, respectively. Monthly(S) and Monthly(W) indicate monthly variables in summer (December, January, and February) and winter (June, January, and August).

	Scale	Hourly		Daily		8-day		Monthly	
	Model	Log/Exp	Lin	Log/Exp	Lin	Log/Exp	Lin	Log/Exp	Lin
eLUE	Ta	0.34***	0.35***	0.41***	0.41***	0.43***	0.43***	0.44***	0.44***
	PAR	0.20***	0.21***	0.52***	0.43***	0.46***	0.39***	0.46***	0.41***
	VPD	0.43***	0.34***	0.71***	0.62***	0.76***	0.71***	0.78***	0.75***
	SWC	0.59***	0.49***	0.63***	0.67***	0.63***	0.74***	0.64***	0.76***
	LAI _{max}					0.48***	0.33***	0.53***	0.38***
eWUE	Ta	0.52***	0.52***	0.62***	0.63***	0.62***	0.65***	0.64***	0.67***
	PAR	0.05***	0.11***	0.51***	0.46***	0.44***	0.41***	0.46***	0.44***
	VPD	0.49***	0.34***	0.71***	0.57***	0.74***	0.65***	0.78***	0.72***
	SWC	0.44***	0.45***	0.50***	0.56***	0.53***	0.62***	0.55***	0.66***
	LAI _{max}					0.50***	0.47***	0.55***	0.52***

(Continued)

	Scale	Monthly(S)		Monthly(W)		Annual	
	Model	Log/Exp	Lin	Log/Exp	Lin	Log/Exp	Lin
eLUE	Ta	0.38**	0.39**	0.52***	0.51**	0.59*	0.56
	PAR	0.40**	0.35**	0.77***	0.70***	0.82**	0.84**
	VPD	0.90***	0.83***	0.76***	0.74***	0.89**	0.94***
	SWC	0.63***	0.61***	0.65***	0.84***	0.70*	0.84**
	LAI _{max}	0.81***	0.58***	0.36**	0.20*	0.83**	0.68*
eWUE	Ta	0.65***	0.67***	0.63***	0.59***	0.75*	0.71*
	PAR	0.22*	0.19*	0.73***	0.69***	0.82**	0.85**
	VPD	0.83***	0.69***	0.79***	0.78***	0.95***	0.96***
	SWC	0.51***	0.60***	0.60***	0.77***	0.70*	0.81**
	LAI _{max}	0.82***	0.73***	0.49***	0.36**	0.84**	0.80**

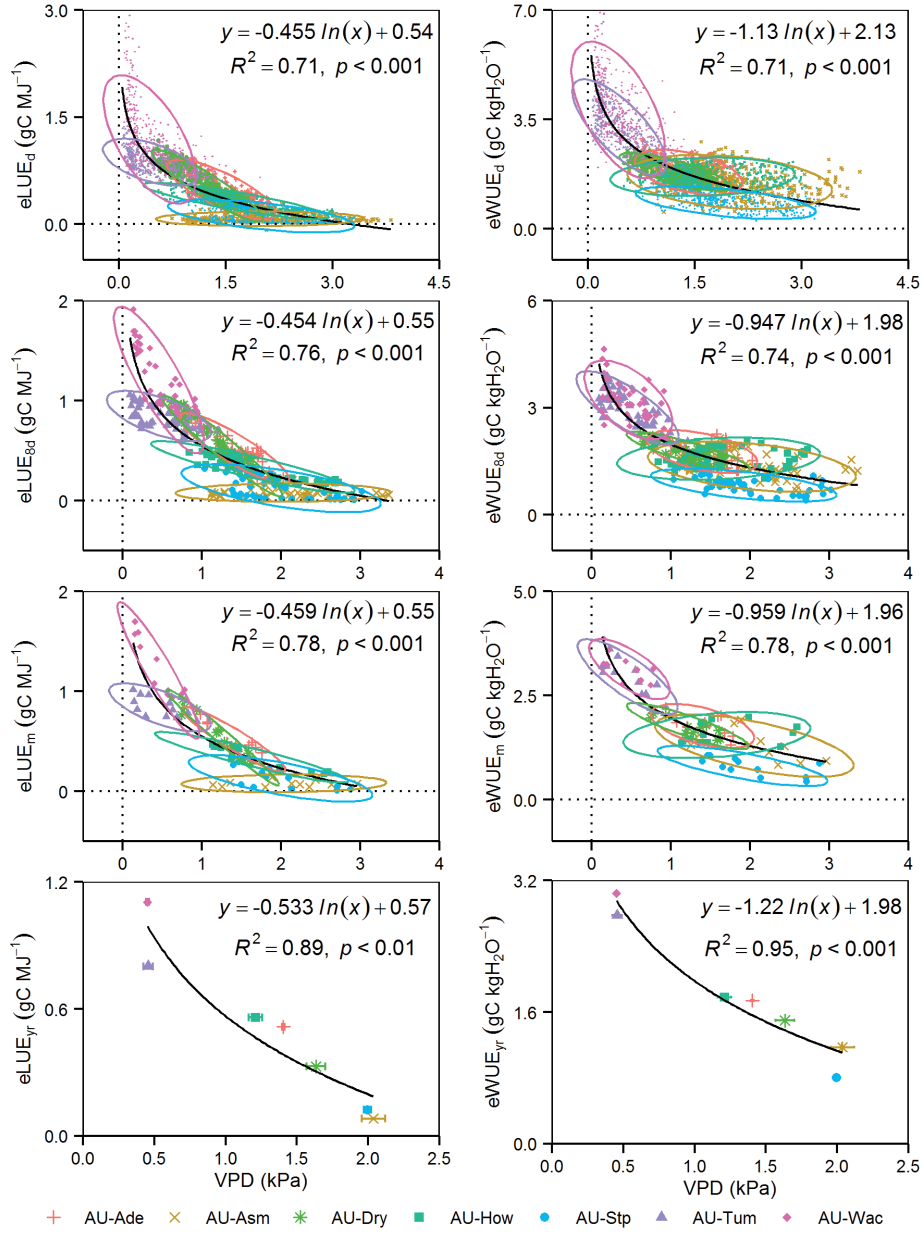


Figure 2.4. Relationships between (left) daily (eLUE_d), eight day (eLUE_{8d}), monthly (eLUE_m) eLUE and VPD and between (right) daily (eWUE_d), eight day (eWUE_{8d}), monthly (eWUE_m) eWUE and VPD for seven sites. Ellipses indicate 95% confidence boundaries of eLUE and eWUE. Bars indicate one standard deviation of annual eLUE, eWUE or VPD at each site. Also shown are logarithmically fitted functions, coefficients of determination (R^2) and p values.

2.3.3 Relationships of eLUE and eWUE to SWC and LAI

Significant positive correlations between eLUE/eWUE and SWC were observed across all time-scales (Table 2.2; Figure 2.5). The strength of these correlations increased with increasing time-scale. SWC showed a slightly better relationship with eLUE at hourly time-scale than VPD (Table 2.2), while at other time-scales, the influence of SWC was consistently and slightly weaker than VPD. Across all time-scales, SWC was less correlated with eWUE than VPD. Specifically, SWC explained much less compared to VPD in variation of eLUE in summer. Considering the seven ecosystems together, a spatial pattern emerged whereby ecosystems with high annual average SWC also had large eLUE and eWUE. This was consistent with the response of eLUE/eWUE to VPD because of the inverse relationship between SWC and VPD. However, the relationships between eLUE/eWUE and SWC varied from site to site. Notably, at the AU-How site, eLUE increased with SWC whereas eWUE appeared to decrease as SWC increased (Figure 2.5).

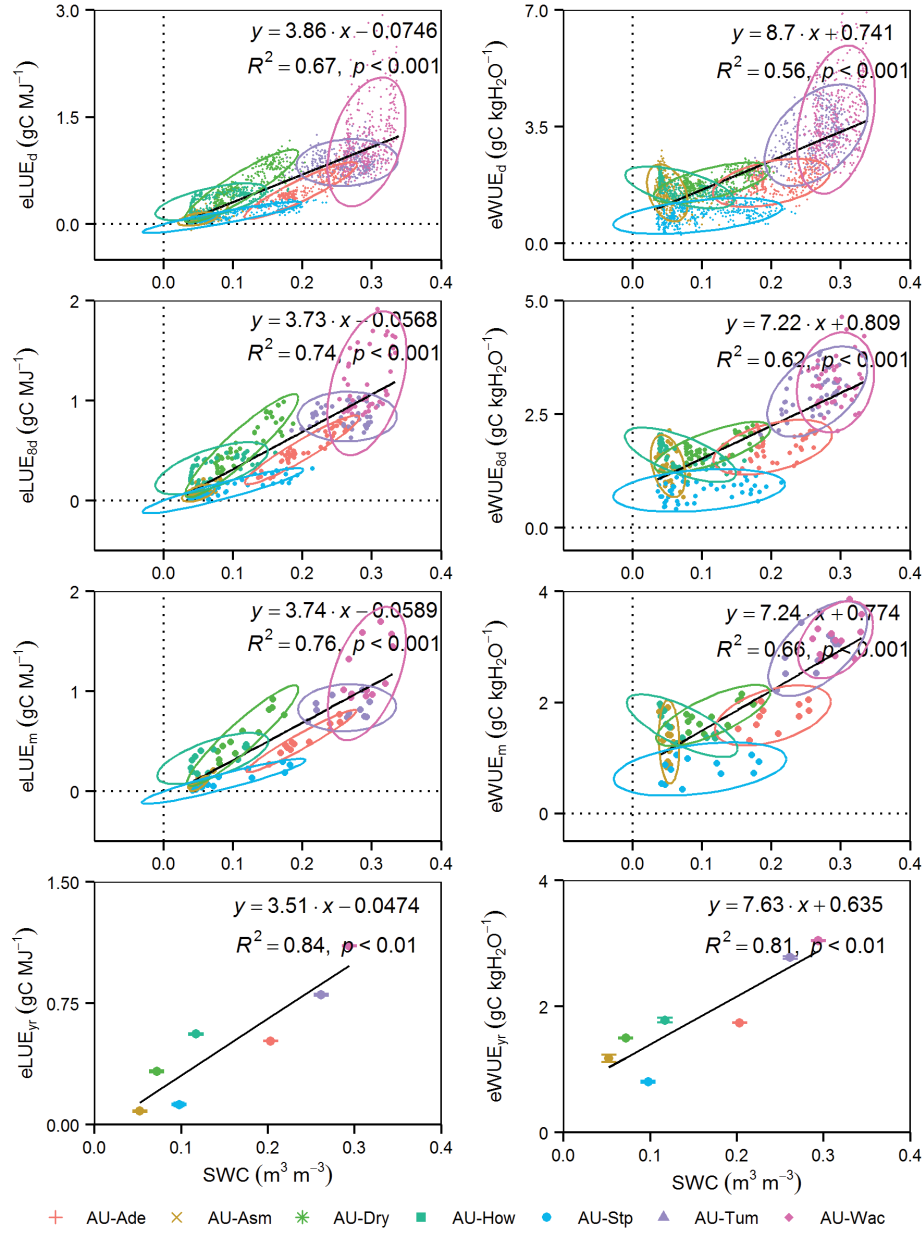


Figure 2.5. Relationships between (left) daily (eLUE_d), eight day (eLUE_{8d}), monthly (eLUE_m) eLUE and SWC and between (right) daily (eWUE_d), eight day (eWUE_{8d}), monthly (eWUE_m) eWUE and SWC for seven sites. Ellipses indicate 95% confidence boundaries of eLUE and eWUE. Bars indicate one standard deviation of annual eLUE, eWUE or SWC at each site. Also shown are logarithmically fitted functions, coefficients of determination (R^2) and p values.

There were significant positive correlations between eLUE or eWUE and LAI_{max} at 8-day, monthly and annual time-scales (Table 2.2; Figure 2.6). Correlations between LAI_{max} with eLUE and eWUE among biomes were not found within all sites. In contrast, for example, there was a significant decrease in eLUE and eWUE with LAI_{max} increasing at AU-Wac site. Similar to climate variables, the correlation among biomes became stronger as time-scale increased. However, these relationships were much weaker than those between eLUE/eWUE and VPD. Specifically, in winter, eLUE and eWUE were moderately or weakly correlated with LAI_{max} . In contrast, eLUE and eWUE in summer showed strong correlation with LAI_{max} .

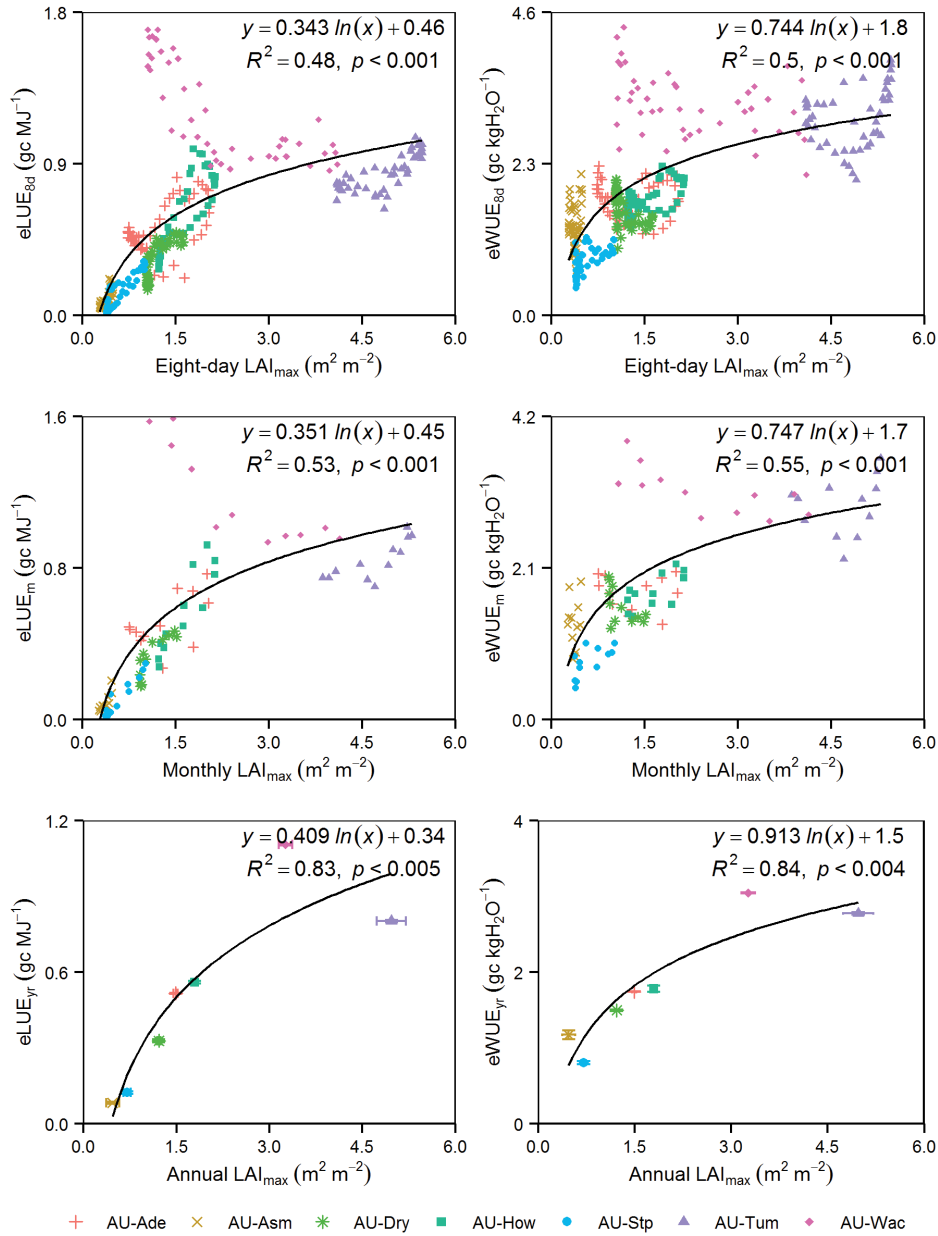


Figure 2.6. Relationships between (left) eight day (eLUE_{8d}), monthly (eLUE_m) and yearly (eLUE_{yr}) eLUE and mean maximum LAI (LAI_{max}) and between (right) eight day (eWUE_{8d}), monthly (eWUE_m) and yearly (eWUE_{yr}) eWUE and LAI_{max} for seven sites. Bars indicate standard one standard deviation of annual eLUE, eWUE or LAI_{max}. Also shown are logarithmically or linearly fitted functions, coefficients of determination (R^2) and p values.

2.3.4 Behavior of eLUE and eWUE in summer and winter

Monthly eLUE and eWUE in summer and winter showed responses to climate variables consistent with the daily/8-day to annual time-scales (Table 2.2; Figure 2.7) but the correlation between eLUE/eWUE *versus* SWC in summer became relatively weak compared with VPD and LAI (Table 2.2). During summer, the VPD dependence of eLUE and eWUE were more apparent than dependence on other climate variables and SWC (Table 2.2). By contrast in winter, variations in eLUE and eWUE were less sensitive to VPD (i.e. the fitted slopes in Figure 2.7). Notably, SWC explained slightly more variability in eLUE during winter, than climatic variables in summer, suggesting different controlling factors and/or mechanisms regulating eLUE in contrary hydrothermal conditions.

Seasonal eLUE differed between summer and winter at all sites except three savannas sites (Figure 2.7). Notably, difference of eLUE between summer and winter was significantly large ($p < 0.001$) at the AU-How savannas site. Contrary to AU-How and the grassland, the two EBF sites showed higher eLUE in winter. There was no significant difference of seasonal eWUE at biome scale except EBF. Similar to eLUE, eWUE at the two EBF sites was lower in summer than that in winter.

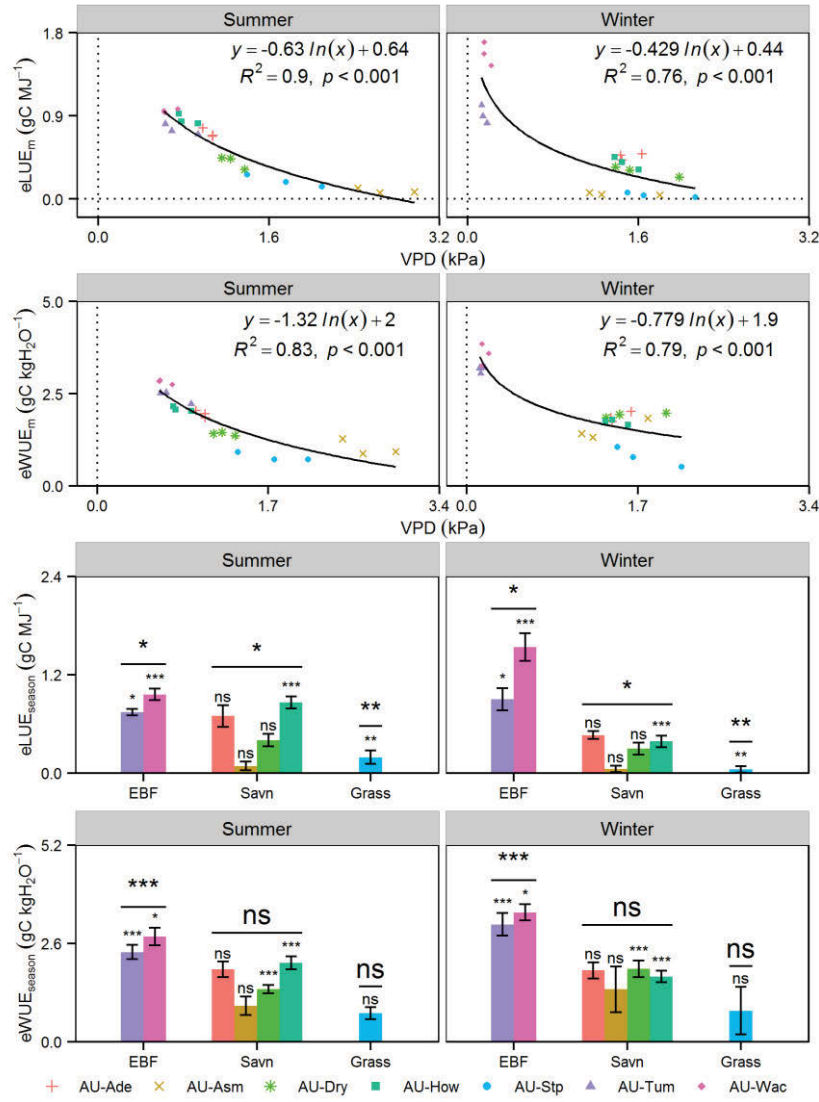


Figure 2.7. Logarithmical relationships between (top two) monthly LUE (eLUE_m) and VPD and between monthly WUE (eWUE_m) and VPD in summer and winter, respectively. Comparisons of (bottom two) average seasonal eLUE (eLUE_{season}) and eWUE (eWUE_{season}) for seven sites are also shown in summer and winter, respectively. Error bars indicate the standard deviations of seasonal eLUE or eWUE at each site. “****”, “***”, and “**” above the error bars of each site indicate significance at 0.001, 0.01, and 0.05 levels, while “ns” represents not significant, based on *t*-test statistics, and these symbols above the horizontal lines represent significance at biome level.

2.4 Discussion

2.4.1 Relationships between GPP, PAR and ET

Canopy photosynthesis can be linearly related with PAR [McMurtrie and Wang, 1993] or show a hyperbolic response function [Ramier *et al.*, 2009]. Hyperbolic responses of canopy photosynthesis to PAR are expected in biomes with low photosynthetic capacity or low LAI [Baldocchi and Amthor, 2001], where self-shading within canopies is relatively small, in contrast to biomes with large LAI where light saturation of photosynthesis does not occur so frequently in the lower canopy. Thus, the significant linear correlation of GPP with PAR at EBF sites can be explained by their relatively large LAI (Table 2.1; Figure 2.3). Consequently, these sites are primarily light limited during the period of measurement. In savannas and the grassland, GPP was not correlated with variations in PAR at these northern tropical sites (Figure 2.3) due to relatively small intra-annual variations in daily average PAR (arising from their lower latitude) (Figures 2.1 and 2.3). Seasonal variation in GPP primarily responded to large changes in LAI arising from senescence of the grassy understory as driven by seasonal monsoonal rainfall [Whitley *et al.*, 2011]. Thus it is light interception rather than light supply that limits GPP at these sites.

Coupling of GPP to ET has been observed in many studies [Baldocchi, 1994; Beer *et al.*, 2009], and stems from the intrinsic link between carbon and water fluxes via stomatal conductance at the leaf level [Beer *et al.*, 2009]. In contrast to reported convergence of annual eWUE across multiple biomes (except for tundra vegetation) [Law *et al.*, 2002], I only observed similar eWUE values (that is, functional convergence of eWUE) within the savannas (Figure 2.3). Similarly, Ponton *et al.* [2006] identified differing eWUE among Douglas-fir forest, aspen forest and grassland within a growing season. However, it is noteworthy that the regression slope of GPP against ET in savannas during the dry season (when ET is minimal)

was similar to that of forests (Figure 2.3). This is likely to be because ET is driven by C3 trees in the dry season following senescence of the annual C4 grasses. At larger rates of ET during the wet season, C4 grasses dominate the understory and have a larger WUE than C3 plants. Thus, there is some evidence that the eucalypt species examined across temperature and tropical biomes in the current study converged to a common WUE. This result is consistent with the results of *O'Grady et al.* [2009], who observed convergence of rates of tree water use within an arid-zone woodland in Australia. Apparent divergence of eWUE between seasons in wet-dry tropical biomes is therefore driven by changes in the relative contributions of upper (C3) and lower (C4) canopies to ET and GPP, rather than changes in functional behavior of the biomes *per se*.

2.4.2 Climate dependence of eLUE and eWUE among biomes

Variations of eLUE were best explained by VPD and SWC while variations of eWUE were best explained by VPD across all time-scales but also well correlated with SWC (Table 2.2). This suggested that VPD co-varied with SWC and water availability was the most influential factor for eLUE/eWUE. Rapid ecosystem transitions that include changes in ecosystem productivity, structure and water cycling can result from long-term climate variations, such as variability in inter-annual precipitation and seasonality of precipitation [*Grimm et al.*, 2013]. Over northern savannas in Australia and the grassland, rainfall is the primary environmental controlling factor such that vegetation structure (i.e. tree height and LAI) has adapted to the available resources [*Cook et al.*, 2002]. In contrast, PAR, VPD and air temperature which usually strongly co-vary, were the major drivers of variation in ecosystem productivity in the two temperate forests [*Cleverly et al.*, 2013; *Kanniah et al.*, 2011; *van Gorsel et al.*, 2013]. Therefore, climate variables are critical factors that essentially regulate eLUE and eWUE through their long-term influence on ecosystem structure and functioning. Consequently, the

results presented here showed a robust intrinsic dependence of eLUE and eWUE on climate across all time-scales.

Several explanations exist for the strong link between eLUE/eWUE and climate. Generally, climatic control of ET and GPP lies somewhere along a continuum between either severe water or energy limitation [*Budyko*, 1974; *Whitley et al.*, 2011], although temperature also limits productivity in many low latitude ecosystems [*Churkina and Running*, 1998]. Deficits of radiation, temperature or water that cause a decrease in GPP will lead to lower canopy conductance and ET [*Beer et al.*, 2009]. Most sites in the present study, and particularly the tropical ones that experience a distinct dry season, did not show evidence of energy supply limitation (as inferred from PAR) at any temporal scales because the range in daily PAR was too small (Figure 2.3). VPD represents atmospheric evaporative demand and is responsive to patterns of water availability. Increasing VPD leads to reduced GPP through smaller stomatal conductance [*Beer et al.*, 2009], hence eLUE and eWUE decline with increasing VPD because at low and moderate values of VPD, increasing VPD causes increased ET [*Eamus et al.*, 2008; *Thomas and Eamus*, 1999; *Wharton et al.*, 2009] but reduced GPP (Table 2.2; Figure 2.7).

2.4.3 Seasonal patterns of eLUE and eWUE across biomes

eLUE and eWUE showed significant difference between summer and winter at several sites (Figure 2.7). Seasonal changes in climate variables, soil water content and vegetation structure (e.g. LAI_{max}) can explain these seasonal similarity or difference. At the EBF sites during winter, GPP increased with PAR. During winter neither temperature nor VPD were supra-optimal for GPP. In contrast, in the summer, increasing PAR was accompanied by either temperature or VPD attaining supra-optimal values, thereby limiting the response of

GPP to increased PAR and leading to a smaller eLUE in summer. A similar phenomenon was also found in eWUE. At the EBF sites, both GPP and ET decreased in winter. However, in summer, high VPD and temperature imposed larger limiting effects on GPP than ET, which caused a smaller eWUE in summer. This limiting effect was especially obvious at the AU-Wac site because VPD became increasingly important for GPP during summer compared to winter [Kilinc *et al.*, 2013b]. Meanwhile, since both GPP and LAI_{max} at AU-Wac were larger in summer whereas the corresponding eLUE was relatively smaller ($p < 0.01$), eLUE was negatively correlated with LAI_{max} (Figure 2.6) as with VPD. At the grassland site, dry winter (Figure 2.1) caused SWC and LAI to decline significantly compared to summer (data not shown), which decreased canopy photosynthesis and transpiration and further decreased eLUE substantially but not significantly affected eWUE. At AU-How, as a combination of trees and seasonal grass, savannas have larger LAI in summer resulting in a larger GPP. Meanwhile, PAR in winter at AU-How was comparable to that in summer. Consequently, eLUE in summer at this site was larger than that in winter ($p < 0.001$). Similarly, both GPP and ET in winter significantly decreased resulting from senescence of C4 grass and effects of meteorological variables, but the decrease in GPP was stronger than the decrease in ET at AU-How, leading to a smaller eWUE. Contrarily, at AU-Dry the decrease in ET exceeded the decrease in GPP resulting in a larger eWUE in winter. This asynchronous response of GPP and ET to climatic variables or LAI and thus variations of eWUE are in good agreement with previous findings in China [Yu *et al.*, 2008].

2.5 Conclusions

Climate drivers are critical in regulating water cycling (and consequently soil water content) and LAI through their long term influences on ecosystem structure and functioning [Kanniah *et al.*, 2011]. Understanding the spatial patterns of eLUE and eWUE at multiple time-scales

and their underlying environmental control mechanisms is of great significance for estimating ecosystem carbon budgets and water carrying capacity under changing hydrothermal conditions (i.e., climate change) [Yu *et al.*, 2008]. In this study, I investigated the relationships between eLUE and eWUE *versus* climate factors, soil water content and vegetation dynamics across diverse climatic regimes across environmental gradients. Across biomes, eLUE and eWUE were tightly and coherently correlated with climate drivers, particularly VPD (and consequently SWC), at multiple time-scales. For any specific biome, eLUE and eWUE were significantly different between summer and winter except eWUE for savannas and the grassland. LAI played an important role in influencing eLUE and eWUE in summer season. Our results provide valuable information for predicting the spatial pattern of eLUE and eWUE at multiple time-scales across Australian biomes. Also this study improves understanding of the responses of ecosystem functional traits to gradients in water availability and temperature, which in turn enables improvements of estimating carbon and water fluxes on a large spatial scale.

Acknowledgements

This research was supported by an Australian Research Council Discovery Early Career Research Award (project number DE120103022).

References

- Baldocchi, D. (1994), A comparative study of mass and energy exchange rates over a closed C₃ (wheat) and an open C₄ (corn) crop: II. CO₂ exchange and water use efficiency, *Agricultural and Forest Meteorology*, 67(3), 291-321.
- Baldocchi, D., and J. Amthor (2001), Canopy photosynthesis: history, measurements, and models, in *Terrestrial global productivity*, edited by J. Roy, B. Saugier and H. A. Mooney,

- pp. 9-31, Academic Press, San Diego.
- Beer, C., M. Reichstein, P. Ciais, G. Farquhar, and D. Papale (2007), Mean annual GPP of Europe derived from its water balance, *Geophysical Research Letters*, 34(5), L05401.
- Beer, C., P. Ciais, M. Reichstein, D. Baldocchi, B. Law, D. Papale, J.-F. Soussana, C. Ammann, N. Buchmann, and D. Frank (2009), Temporal and among-site variability of inherent water use efficiency at the ecosystem level, *Global Biogeochemical Cycles*, 23(2), GB2018.
- Beringer, J., L. B. Hutley, N. J. Tapper, and L. A. Cernusak (2007), Savanna fires and their impact on net ecosystem productivity in North Australia, *Global Change Biology*, 13(5), 990-1004.
- Budyko, M. I. (1974), *Climate and life*, Academic Press, New York.
- Campos, G. E. P., M. S. Moran, A. Huete, Y. Zhang, C. Bresloff, T. E. Huxman, D. Eamus, D. D. Bosch, A. R. Buda, and S. A. Gunter (2013), Ecosystem resilience despite large-scale altered hydroclimatic conditions, *Nature*, 494(7437), 349-352.
- Churkina, G., and S. W. Running (1998), Contrasting climatic controls on the estimated productivity of global terrestrial biomes, *Ecosystems*, 1(2), 206-215.
- Cleverly, J., N. Boulain, R. Villalobos-Vega, N. Grant, R. Faux, C. Wood, P. G. Cook, Q. Yu, A. Leigh, and D. Eamus (2013), Dynamics of component carbon fluxes in a semi-arid Acacia woodland, central Australia, *Journal of Geophysical Research: Biogeosciences*, 118(3), 1168-1185.
- Cook, G. D., R. J. Williams, L. Hutley, A. O'Grady, and A. C. Liedloff (2002), Variation in vegetative water use in the savannas of the North Australian Tropical Transect, *Journal of Vegetation Science*, 13(3), 413-418.
- Daubechies, I. (1990), The wavelet transform, time-frequency localization and signal analysis, *Information Theory, IEEE Transactions on*, 36(5), 961-1005.

- Ding, R., S. Kang, R. Vargas, Y. Zhang, and X. Hao (2013), Multiscale spectral analysis of temporal variability in evapotranspiration over irrigated cropland in an arid region, *Agricultural Water Management*, 130, 79-89.
- Eamus, D., L. B. Hutley, and A. P. O'Grady (2001), Daily and seasonal patterns of carbon and water fluxes above a north Australian savanna, *Tree Physiology*, 21(12-13), 977-988.
- Eamus, D., D. T. Taylor, C. M. Macinnis-Ng, S. Shanahan, and L. De Silva (2008), Comparing model predictions and experimental data for the response of stomatal conductance and guard cell turgor to manipulations of cuticular conductance, leaf-to-air vapour pressure difference and temperature: feedback mechanisms are able to account for all observations, *Plant, Cell & Environment*, 31(3), 269-277.
- Eamus, D., J. Cleverly, N. Boulain, N. Grant, R. Faux, and R. Villalobos-Vega (2013), Carbon and water fluxes in an arid-zone Acacia savanna woodland: An analyses of seasonal patterns and responses to rainfall events, *Agricultural and Forest Meteorology*, 182, 225-238.
- Farquhar, G. D., J. R. Ehleringer, and K. T. Hubick (1989), Carbon isotope discrimination and photosynthesis, *Annual Review of Plant Biology*, 40(1), 503-537.
- Goetz, S., and S. D. Prince (1999), Modelling terrestrial carbon exchange and storage: evidence and implications of functional convergence in light-use efficiency, *Advances in Ecological Research*, 28, 57-92.
- Gower, S. T., C. J. Kucharik, and J. M. Norman (1999), Direct and indirect estimation of leaf area index, f_{APAR} , and net primary production of terrestrial ecosystems, *Remote Sensing of Environment*, 70(1), 29-51.
- Grimm, N. B., et al. (2013), The impacts of climate change on ecosystem structure and function, *Frontiers in Ecology and the Environment*, 11(9), 474-482.
- Haverd, V., M. R. Raupach, P. R. Briggs, J. G. Canadell, P. Isaac, C. Pickett-Heaps, S. H.

- Roxburgh, E. van Gorsel, R. A. Viscarra Rossel, and Z. Wang (2013), Multiple observation types reduce uncertainty in Australia's terrestrial carbon and water cycles, *Biogeosciences*, 10(3), 2011-2040.
- Hu, Z., G. Yu, Y. Fu, X. Sun, Y. Li, P. Shi, Y. Wang, and Z. Zheng (2008), Effects of vegetation control on ecosystem water use efficiency within and among four grassland ecosystems in China, *Global Change Biology*, 14(7), 1609-1619.
- Hutley, L. B., J. Beringer, P. R. Isaac, J. M. Hacker, and L. A. Cernusak (2011), A sub-continental scale living laboratory: Spatial patterns of savanna vegetation over a rainfall gradient in northern Australia, *Agricultural and Forest Meteorology*, 151(11), 1417-1428.
- Huxman, T. E., M. D. Smith, P. A. Fay, A. K. Knapp, M. R. Shaw, M. E. Loik, S. D. Smith, D. T. Tissue, J. C. Zak, and J. F. Weltzin (2004), Convergence across biomes to a common rain-use efficiency, *Nature*, 429(6992), 651-654.
- Jönsson, P., and L. Eklundh (2004), TIMESAT—A program for analyzing time-series of satellite sensor data, *Computers & Geosciences*, 30(8), 833-845.
- Jones, D. A., W. Wang, and R. Fawcett (2009), High-quality spatial climate data-sets for Australia, *Australian Meteorological and Oceanographic Journal*, 58(4), 233.
- Kanniah, K. D., J. Beringer, and L. Hutley (2011), Environmental controls on the spatial variability of savanna productivity in the Northern Territory, Australia, *Agricultural and Forest Meteorology*, 151(11), 1429-1439.
- Kilinc, M., J. Beringer, L. B. Hutley, N. J. Tapper, and D. A. McGuire (2013a), Carbon and water exchange of the world's tallest angiosperm forest, *Agricultural and forest meteorology*, 182, 215-224.
- Kilinc, M., J. Beringer, L. Hutley, N. J. Tapper, and D. A. McGuire (2013b), Carbon and water exchange of the world's tallest angiosperm forest, *Agricultural and Forest Meteorology*,

182, 215-224.

- Lafont, S., L. Kergoat, G. Dedieu, A. Chevillard, U. Karstens, and O. Kolle (2002), Spatial and temporal variability of land CO₂ fluxes estimated with remote sensing and analysis data over western Eurasia, *Tellus B*, 54(5), 820-833.
- Law, B., E. Falge, L. v. Gu, D. Baldocchi, P. Bakwin, P. Berbigier, K. Davis, A. Dolman, M. Falk, and J. Fuentes (2002), Environmental controls over carbon dioxide and water vapor exchange of terrestrial vegetation, *Agricultural and Forest Meteorology*, 113(1), 97-120.
- Li, S. G., W. Eugster, J. Asanuma, A. Kotani, G. Davaa, D. Oyunbaatar, and M. Sugita (2008), Response of gross ecosystem productivity, light use efficiency, and water use efficiency of Mongolian steppe to seasonal variations in soil moisture, *Journal of Geophysical Research: Biogeosciences (2005–2012)*, 113(G1), G01019.
- McMurtrie, R., and Y. P. Wang (1993), Mathematical models of the photosynthetic response of tree stands to rising CO₂ concentrations and temperatures, *Plant, Cell & Environment*, 16(1), 1-13.
- Niu, S., X. Xing, Z. Zhang, J. Xia, X. Zhou, B. Song, L. Li, and S. Wan (2011), Water-use efficiency in response to climate change: from leaf to ecosystem in a temperate steppe, *Global Change Biology*, 17(2), 1073-1082.
- O'Grady, A., P. Cook, D. Eamus, A. Duguid, J. Wischusen, T. Fass, and D. Worldege (2009), Convergence of tree water use within an arid-zone woodland, *Oecologia*, 160(4), 643-655.
- Polley, H. W., R. L. Phillips, A. B. Frank, J. A. Bradford, P. L. Sims, J. A. Morgan, and J. R. Kiniry (2011), Variability in light-use efficiency for gross primary productivity on Great Plains grasslands, *Ecosystems*, 14(1), 15-27.
- Ponton, S., L. B. Flanagan, K. P. Alstad, B. G. Johnson, K. Morgenstern, N. Kljun, T. A. Black, and A. G. Barr (2006), Comparison of ecosystem water-use efficiency among Douglas-fir

- forest, aspen forest and grassland using eddy covariance and carbon isotope techniques, *Global Change Biology*, 12(2), 294-310.
- Rahman, A., D. Sims, V. Cordova, and B. El-Masri (2005), Potential of MODIS EVI and surface temperature for directly estimating per-pixel ecosystem C fluxes, *Geophysical Research Letters*, 32(19), L19404.
- Ramier, D., N. Boulain, B. Cappelaere, F. Timouk, M. Rabanit, C. R. Lloyd, S. Boubkraoui, F. Métayer, L. Descroix, and V. Wawrzyniak (2009), Towards an understanding of coupled physical and biological processes in the cultivated Sahel–1. Energy and water, *Journal of Hydrology*, 375(1), 204-216.
- Reichstein, M., E. Falge, D. Baldocchi, D. Papale, M. Aubinet, P. Berbigier, C. Bernhofer, N. Buchmann, T. Gilmanov, and A. Granier (2005), On the separation of net ecosystem exchange into assimilation and ecosystem respiration: review and improved algorithm, *Global Change Biology*, 11(9), 1424-1439.
- Scanlon, T. M., and J. D. Albertson (2001), Turbulent transport of carbon dioxide and water vapor within a vegetation canopy during unstable conditions: identification of episodes using wavelet analysis, *Journal of Geophysical Research: Atmospheres (1984–2012)*, 106(D7), 7251-7262.
- Schwalm, C. R., T. A. Black, B. D. Amiro, M. A. Arain, A. G. Barr, C. P.-A. Bourque, A. L. Dunn, L. B. Flanagan, M.-A. Giasson, and P. M. Lafleur (2006), Photosynthetic light use efficiency of three biomes across an east–west continental-scale transect in Canada, *Agricultural and Forest Meteorology*, 140(1), 269-286.
- Stoy, P. C., G. G. Katul, M. B. Siqueira, J.-Y. Juang, H. R. McCarthy, H.-S. Kim, A. C. Oishi, and R. Oren (2005), Variability in net ecosystem exchange from hourly to inter-annual time scales at adjacent pine and hardwood forests: a wavelet analysis, *Tree Physiology*, 25(7), 887-902.

- Thomas, D., and D. Eamus (1999), The influence of predawn leaf water potential on stomatal responses to atmospheric water content at constant C_i and on stem hydraulic conductance and foliar ABA concentrations, *Journal of Experimental Botany*, 50(331), 243-251.
- Torrence, C., and G. P. Compo (1998), A practical guide to wavelet analysis, *Bulletin of the American Meteorological society*, 79(1), 61-78.
- Turner, D. P., S. Urbanski, D. Bremer, S. C. Wofsy, T. Meyers, S. T. Gower, and M. Gregory (2003), A cross-biome comparison of daily light use efficiency for gross primary production, *Global Change Biol.*, 9(3), 383-395.
- van Gorsel, E., *et al.* (2013), Primary and secondary effects of climate variability on net ecosystem carbon exchange in an evergreen Eucalyptus forest, *Agricultural and Forest Meteorology*, 182–183, 248 - 256.
- Wharton, S., M. Schroeder, K. Bible, and M. Falk (2009), Stand-level gas-exchange responses to seasonal drought in very young versus old Douglas-fir forests of the Pacific Northwest, USA, *Tree physiology*, 29(8), 959-974.
- Whitley, R. J., C. M. O. Macinnis-Ng, L. B. Hutley, J. Beringer, M. Zeppel, M. Williams, D. Taylor, and D. Eamus (2011), Is productivity of mesic savannas light limited or water limited? Results of a simulation study, *Glob. Change Biol.*, 17(10), 3130-3149.
- Xiao, X., Q. Zhang, D. Hollinger, J. Aber, and B. Moore III (2005), Modeling gross primary production of an evergreen needleleaf forest using MODIS and climate data, *Ecological Applications*, 15(3), 954-969.
- Yu, G., X. Song, Q. Wang, Y. Liu, D. Guan, J. Yan, X. Sun, L. Zhang, and X. Wen (2008), Water-use efficiency of forest ecosystems in eastern China and its relations to climatic variables, *New Phytologist*, 177(4), 927-937.

Chapter 3. Assessing the ability of MODIS EVI to estimate terrestrial ecosystem gross primary production of multiple land cover types

Abstract

Terrestrial ecosystem gross primary production (GPP) is the largest component in the global carbon cycle. The enhanced vegetation index (EVI) is strongly correlated with annual GPP within several biomes. However, the annual GPP-EVI relationship and associated environmental regulations have not yet been comprehensively investigated across biomes at the global scale. Here I explored relationships between annual integrated EVI (iEVI) and annual GPP observed at 155 eddy flux sites, where GPP was predicted with a log-log model: $\ln(GPP) = a \times \ln(iEVI) + b$. iEVI was computed from MODIS monthly EVI products following removal of values affected by snow or cold temperature and without calculating growing season duration. Through categorization of flux sites into 12 land cover types, the ability of iEVI to estimate GPP was considerably improved (R^2 from 0.62 to 0.74, RMSE from 454.7 to 368.2 g C m⁻² yr⁻¹). The biome-specific GPP-iEVI formulae generally showed a consistent performance in comparison to a global benchmarking dataset ($R^2 = 0.79$, RMSE = 387.8 g C m⁻² yr⁻¹). Specifically, iEVI performed better in cropland regions with high productivity but poorer in forests. The ability of iEVI in estimating GPP was better in deciduous biomes (except deciduous broadleaf forest) than in evergreen biomes due to the large seasonal signal in iEVI in deciduous biomes. Likewise, GPP estimated from iEVI was in a closer agreement to global benchmarks at mid and high-latitudes, where deciduous biomes are more common and cloud cover has a smaller effect on remote sensing retrievals. Across biomes, a significant and negative correlation ($R^2 = 0.37$, $p < 0.05$) was observed between the

strength (R^2) of GPP-iEVI relationships and mean annual maximum leaf area index (LAI_{max}), and the relationship between the strength and mean annual precipitation followed a similar trend. LAI_{max} also revealed a scaling effect on GPP-iEVI relationships. These results suggest that iEVI provides a very simple but robust approach to estimate spatial patterns of global annual GPP whereas its effect is comparable to various light-use-efficiency and data-driven models. The impact of vegetation structure on accuracy and sensitivity of EVI in estimating spatial GPP provides valuable clues to improve EVI-based models.

3.1 Introduction

Terrestrial gross primary production (GPP) is the amount of carbon captured from the atmosphere through vegetation photosynthesis [Beer *et al.*, 2010]. Vegetation GPP is a key component of the terrestrial carbon balance and is of fundamental importance to human society because plants provide food, fiber and wood supply and also contribute to the production of environmental conditions suitable for human habitation [Melillo *et al.*, 1993; Xiao *et al.*, 2005; Zhao *et al.*, 2005]. Therefore, continuous monitoring and accurate estimation of GPP is required to ensure the long term security of terrestrial ecosystem services and to address issues pertaining to the global carbon cycle, including determination of the size of the terrestrial carbon sink, prediction of vegetation dynamics, and management of forests and grasslands [Ciais *et al.*, 2005; Ma *et al.*, 2013; Sims *et al.*, 2006b].

GPP can be calculated as the sum of vegetation assimilated carbon flux, partitioned from net carbon exchange measured at eddy covariance (EC) tower sites [Baldocchi *et al.*, 2001; Reichstein *et al.*, 2007], but such observations are limited, both temporally and spatially. Remote sensing technique provides a promising approach to overcome these limitations. Various diagnostic models taking advantage of spatially extensive remote sensing and

meteorological data have been developed to estimate GPP across stand-to-global scales for a relatively long period [e.g., *Jung et al.*, 2008; *Running et al.*, 2004; *Sims et al.*, 2008; *Xiao et al.*, 2005]. These models can be generally partitioned into three categories: light-use-efficiency (LUE) models, machine learning algorithms and simple empirical models [*Verma et al.*, 2014]. The LUE theory was first proposed by *Monteith* [1972], in which GPP is generally represented as the product of LUE, photosynthetically active radiation (PAR), the fraction of PAR absorbed by vegetation (fAPAR), and environmental scalars. fAPAR is a strong function of vegetation greenness, as measured by vegetation indices (VIs), such as the normalized difference vegetation index [NDVI; e.g., *Goward and Huemmrich*, 1992] and the enhanced vegetation index [EVI; e.g., *Xiao et al.*, 2004a; *Xiao et al.*, 2004b]. However, it is difficult to estimate LUE, which varies among plant functional types, and it can be down-regulated by temperature, soil water content, vapour pressure deficit (VPD), and leaf phenology [*Xiao et al.*, 2005]. Another deficiency of LUE models is the coarse resolution of climate inputs, which are often only available at large scales. This may introduce significant errors to estimations of GPP [*Heinsch et al.*, 2006; *Zhao et al.*, 2005] and hinder the acquisition of fine-resolution GPP estimates at large scales. Machine learning algorithms, such as artificial neural networks [*Papale and Valentini*, 2003], support vector machines [*Yang et al.*, 2007], and model tree ensembles [*Jung et al.*, 2009], predict GPP based on the non-functional patterns extracted in training data sets. Obviously, the accuracy of machine learning algorithms relies on the abundance and representativeness of input information including remotely sensed vegetation properties, meteorological, and land cover data [*Jung et al.*, 2011]. Therefore, the use of machine learning algorithms is also limited by the coarse resolution of meteorological data. Moreover, in many cases machine learning algorithms show no better performance than LUE models in specific ecosystems [e.g., *Yang et al.*, 2007]. Consequently, simple empirical models utilizing remote sensing proxies of vegetation

photosynthesis activity (with or without meteorological data) enjoy consistent interest in estimating both spatial and temporal variations of GPP [e.g., *Jung et al.*, 2008; *Rahman et al.*, 2005; *Sims et al.*, 2006b].

The growing season NDVI and EVI show strong relationships with vegetation production over one or two week intervals [e.g., *Mao et al.*, 2014; *Rahman et al.*, 2005; *Sims et al.*, 2006a; *Sims et al.*, 2006b; *Wylie et al.*, 2003]. Vegetation indices *per se* are transformations of two or more spectral bands to enhance the signal derived from vegetation properties [*Huete et al.*, 2002]. Both NDVI and EVI employ surface bidirectional reflectances of red and near-infrared spectral bands that are sensitive to leaf chlorophyll content [*Huete et al.*, 2002], which converts light to photosynthetic carbon fixation. NDVI is limited due to its saturation over dense vegetation and large sensitivity to canopy background brightness [*Huete et al.*, 2002], whereas EVI can improve performance in regions of high biomass through a decoupling of the canopy and background signals and a reduction in the influence of atmospheric conditions using a blue spectral reflectance [*Huete et al.*, 2002]. This makes EVI more responsive to canopy structural variations and thus EVI is better correlated with GPP than NDVI in evergreen [*Xiao et al.*, 2004a] and deciduous [*Xiao et al.*, 2004b] forests as well as in croplands [*Xiao et al.*, 2005]. Compared to LUE models, the growing season EVI or EVI-based models [e.g., Temperature-Greenness model; *Sims et al.*, 2008] provide a comparable or better estimation of GPP at both the 16-day [*Sims et al.*, 2008; *Sims et al.*, 2006b] and annual [*Verma et al.*, 2014] time-scales. As well as EVI, cumulative growing season fAPAR with separate functions for herbaceous plants, evergreen forests and all other vegetation types has been used to predict annual GPP in Europe [*Jung et al.*, 2008]. The disadvantage of selecting fAPAR against EVI is subtle: fAPAR consists of fractional absorbance of PAR absorbed by both chlorophyll and by non-photosynthetic pigments [*Zhang et al.*, 2005], while EVI is much closer to the fraction of PAR absorbed by chlorophyll.

Moreover, fAPAR shows no significant correlation with GPP in deciduous broadleaf forests [Jung *et al.*, 2008]. Therefore, the use of EVI should be favored over fAPAR in correlating to GPP. However, current studies on EVI-GPP relationships or EVI-based models have been focused within only a limited number of biomes and these EVI-based models generally need to compute the start and end or the length of the growing season period [Jung *et al.*, 2008; Sims *et al.*, 2008; Sims *et al.*, 2006b; Verma *et al.*, 2014], which constitutes an extra source of uncertainty. Simultaneously, environmental influences on the ability of EVI to estimate GPP across a wide spectrum of biomes have not yet been investigated [Sims *et al.*, 2006b; Sjöström *et al.*, 2011].

In this study, I used the annual integral of MODIS EVI (iEVI), which only needs removal of those values that have been affected by cold temperature or snow and subtracting the soil background signal, to regress with annual eddy covariance measured GPP across 12 land cover types. The developed set of formulae were then applied at the global scale and compared with a widely used GPP benchmark dataset to evaluate the effectiveness and robustness of iEVI, thereby determining whether iEVI can serve as a reference for other GPP models over a fine-to-coarse resolution. The impacts of environmental conditions on iEVI in estimating GPP were further investigated across biomes, to improve our understanding of the underlying mechanistic processes that differentiate responses of vegetation photosynthetic activity to remote sensing spectral measurements among biomes.

3.2 Data and Methods

3.2.1 Eddy covariance and meteorological data

The eddy covariance method is a micrometeorological technique that directly measures net carbon, water and energy fluxes across a horizontal plane between vegetation canopies and

the atmosphere [Aubinet *et al.*, 2000; Baldocchi *et al.*, 2001]. In the present study a total of 155 sites (Appendix Table A3.1) were selected, consisting of 624 site-years of data and representing a worldwide spectrum of biomes and climate regimes with excellent coverage in North America, Eurasia and Oceania [Table 3.1, Figure1; Baldocchi, 2008; Baldocchi *et al.*, 2001; Wang and Dickinson, 2012].

The flux data were obtained from three sources: (1) a small fraction (mainly high-latitude and wetland sites) was collected directly from published studies, which only included annual values of flux and meteorological forcing; (2) a larger fraction was contributed directly from participating site researchers; and (3) the majority were from FLUXNET level 2 or level 4 products that were downloaded from the database. Of the latter two categories, only site-years with small gaps (i.e., individual gaps in NEE of less than 5% of the entire annual record) were selected except in certain ecosystems of the boreal region where only growing season data were available. Carbon and water fluxes and meteorological variables in all selected site-years were then processed through gap-filling and flux partitioning routines. If the principal investigator at each site had already performed these processes, the already gap-filled and partitioned GPP dataset was aggregated from a half-hourly time-step to an annual time-scale (GPP_{EC}). Otherwise, half-hourly GPP derived using one of the two FLUXNET standard methods, either the marginal distribution sampling [MDS, a local method; Reichstein *et al.*, 2005] or a feed-forward artificial neural network [ANN, trained on an annual dataset; Papale and Valentini, 2003], were obtained from the FLUXNET products to calculate annual GPP. Both partitioning methods show good performance according to previous studies [Papale and Valentini, 2003; Reichstein *et al.*, 2005]. For sites with neither investigator's decomposition nor standardized flux partitioning, the publicly available online MDS tool [<http://www.bgc-jena.mpg.de/~MDIwork/eddyproc/index.php>; Reichstein *et al.*, 2005] was used to gap-fill and partition NEE. The derived half-hourly GPP, temperature, precipitation

and vapour pressure deficit (VPD) of all site-years were screened for outliers and linearly interpolated in bins representing the measurement hour of the day before aggregation into the annual scale.

Table 3.1. Summary of number of sites and site-years used for each biome. CNM: cropland/natural vegetation mosaic; CRO: croplands; CSH: closed shrublands; DBF: deciduous broadleaf forest; DNF: deciduous needle-leaf forest; EBF: evergreen broadleaf forest; ENF: evergreen needle-leaf forest; GRA: grasslands; MF: mixed forest; OSH: open shrublands; SAV: savannas; WET: permanent wetlands; WSA: woody savannas.

Biome	CRO	CSH	DBF	DNF	EBF	ENF	GRA	MF	OSH	SAV	WET	WSA
Sites	16	4	18	4	13	40	24	8	7	7	9	5
Site-years	61	11	83	6	55	190	76	28	21	24	34	35

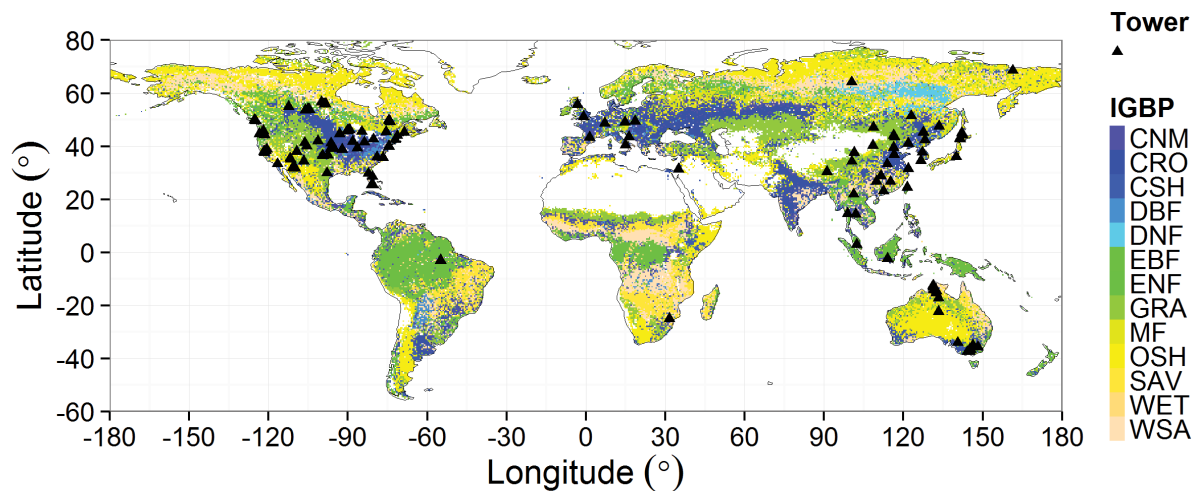


Figure 3.1. Geographical distribution of flux towers overlaid onto the 2001 MODIS IGBP land cover map at a $0.5^\circ \times 0.5^\circ$ resolution.

3.2.2 Benchmark dataset

The model tree ensemble (MTE) approach was used to empirically up-scale FLUXNET

measurements of fluxes (hereafter GPP_{MTE}) to the global scale. Explanatory variables for the model consisted of meteorological variables, the biophysical state of the vegetation, and vegetation types [Jung *et al.*, 2009; Jung *et al.*, 2011]. GPP_{MTE} constitutes a benchmark for global FLUXNET up-scaling that has been used as a baseline for evaluating land surface models and estimating global CO_2 uptake [e.g., Beer *et al.*, 2010; Bonan *et al.*, 2011]. However, GPP_{MTE} has its own weakness, specifically for estimates of GPP in high-production croplands [Guanter *et al.*, 2014]. Mean annual GPP_{MTE} was calculated at a spatial resolution of 0.5° for the years 1982-2008. The same grid was also applied in our global GPP estimation.

3.2.3 Satellite data

3.2.3.1 EVI data

EVI is widely used as a proxy of canopy “greenness” to address spatial and temporal variations in terrestrial photosynthetic activity [e.g., Huete *et al.*, 2002; Ma *et al.*, 2013]. EVI is defined as [Huete *et al.*, 1997]:

$$EVI = G \frac{\rho_{NIR} - \rho_{red}}{\rho_{NIR} + C_1 \times \rho_{red} - C_2 \times \rho_{blue} + L} \quad (5.1)$$

where ρ_{NIR} , ρ_{red} and ρ_{blue} are atmospherically corrected, either fully or partially, values of surface near-infrared (NIR, 841-876 nm), red (620–670 nm) and blue (459-479 nm) spectral reflectance, respectively; G is the gain factor (set at 2.5); L (set at 1.0) is the canopy background adjustment; and C_1 (set at 6) and C_2 (set at 7.5) are the coefficients of the aerosol resistance term, which uses the blue band to correct for the influence of aerosols in the red band.

MODIS monthly VI products (MOD13A3.005) for February 2000 to 2013 were obtained from the USGS repository (<http://e4ftl01.cr.usgs.gov/MOLT/MOD13A3.005/>). This dataset is

produced globally over land at 1-km resolution and monthly compositing periods from atmospherically corrected surface reflectances. The compositing algorithm is based on a constrained-view angle-maximum value composite (CV-MVC) to minimize atmospheric and bidirectional reflectance distribution function (BRDF) influences [Huete *et al.*, 2002].

It is difficult to precisely co-locate the pixels that directly correspond to the footprint of an EC tower [Sims *et al.*, 2006b]. Fluctuations in flux tower footprint size and shape, due to the underlying topography, vegetation, wind speed and other factors, may induce a footprint mismatch between the tower and MODIS [Jung *et al.*, 2009; Sims *et al.*, 2006b; Sjöström *et al.*, 2011]. Where the landscape is homogenous, the scale mismatch is not a serious problem and the MODIS pixels can adequately represent flux site conditions. Discrepancies are typically observed at grassland and cropland sites, likely due to the fragmentation of these landscapes [Cescatti *et al.*, 2012]. However, sub- and inter-pixel heterogeneity is unavoidable in most cases and thus introduces additional bias. Consequently, a central 3×3 km window surrounding the flux tower was used to extract mean EVI time series. The 3×3 km window has been found to reduce scale mismatch relative to a centrally located 1 km pixel or window sizes of 5×5 or 7×7 km [e.g., Ma *et al.*, 2013; Rahman *et al.*, 2005; Sims *et al.*, 2006b; Sjöström *et al.*, 2011; Xiao *et al.*, 2005]. At sites with spatially varying amounts of mixed vegetation types, averaging across the MODIS window is equivalent to averaging across time in flux measurements [Sims *et al.*, 2006b].

3.2.3.2 Smoothing method of EVI

To reduce noise and uncertainties in the MODIS EVI time series at each site, the singular spectrum analysis (SSA) was employed. SSA is a data adaptive, non-parametric analysis approach based on embedding a time series $\{X(t): t=1, N\}$ in a vector space of dimension

M and it works well in the analysis of non-linear dynamics in geophysical datasets [Kondrashov and Ghil, 2006; Ma et al., 2013; Wang and Liang, 2008]. The SSA technique consists of two complementary stages: decomposition and reconstruction [Hassani, 2007]. The one-dimensional time series $\{X(t): t=1, N\}$ is first embedded into a trajectory matrix $X = [X_1, \dots, X_K] = (x_{ij})_{i,j=1}^{L,K}$, where $K = t - L + 1$. Next, singular value decomposition (SVD) is applied to X :

$$X = \sum_{j=1}^d \sqrt{\lambda_j} U_j V_j^T, V_j = X' / \sqrt{\lambda_j} \quad (5.2)$$

where λ_j is the j th eigenvalue of XX' , U_j is the j th eigenvector of XX' , and d is the rank of X . The reconstruction includes the eigentriple grouping and diagonal averaging (i.e., Hankelization of a matrix), to produce a length N time series from the matrix X . The SSA method is more robust to outliers than linear filtering because it conducts a global reconstruction (i.e., convolution) of the whole time series as with Fourier methods [Alexandrov, 2009].

Key parameters in SSA are the decomposition window length L and the number of leading components in reconstruction. In the monthly EVI time series, a window length of 37 (i.e. 37 months) and 6 leading components best captured the periodicity and simultaneously reduced random noises during reconstruction. The missing EVI value in January 2000 was extrapolated, thereby yielding a complete set of 14 years of EVI data. Since bare soil yields an EVI value of $0.08 \sim 0.10$, around which GPP is zero [Sims et al., 2008; Sims et al., 2006b], monthly values of EVI reconstructed from SSA were corrected by offsetting 0.10 to remove the background signal. EVI data are also contaminated by snow effects in mid- and high latitudes that result in a false positive signal [Huete et al., 2002]. To minimise the contamination, the snow/ice flag in MOD13A3 VI quality assurance field was first used to

remove the snow-covered EVI values; and then EVI values were further screened for effects of cold temperature [daytime land surface temperature below -2°C ; *Tan et al.*, 2011; *Zhang et al.*, 2004] using the MODIS land surface temperature product (MOD11C3). Finally, positive values of monthly EVI during non-snow and non-cold temperature periods were summed into annual, integrated values (iEVI) to regress against annual GPP calculated at each flux site. In our global GPP estimation, the 1 km EVI data were re-gridded into 0.5° resolution to compare with global GPP_{MTE} and then processed the same way as the site level analysis.

3.2.3.3 Leaf area index data

The MOD15A2.005 leaf area index (LAI) product is composited every 8 days at 1 km resolution and is available at the USGS repository (<http://e4ftl01.cr.usgs.gov/MOLT/MOD15A2.005>). LAI is retrieved through a three-dimensional radiative transfer model that requires land cover classification [*Knyazikhin et al.*, 1998]. By applying a procedure similar to that used for EVI, a central 3×3 km window was used to extract LAI time series from 2000 to 2013, and SSA was applied to smooth the series. At each site, peak LAI values in individual site-years were averaged to represent the mean annual maximum LAI (LAI_{max}) of the site and then the site LAI values within a land cover type were averaged to get the mean LAI for each of the land cover classifications except wetlands, which have no observed values in MOD15A2.005. In this analysis a mean LAI value of $6.3 (\pm 2.3)$ was assigned for the 6 wetland sites, obtained from a global synthesis of LAI observations [*Asner et al.*, 2003].

3.2.3.4 Land cover types

The MCD12Q1.005 land cover type product provides options of five global land cover

classification systems. The IGBP land cover scheme was used which includes 17 land cover classes: water, evergreen needle-leaf forest (ENF), evergreen broadleaf forest (EBF), deciduous needle-leaf forest (DNF), deciduous broadleaf forest (DBF), mixed forest (MF), closed shrublands (CSH), open shrublands (OSH), woody savannas (WSA), savannas (SAV), grasslands (GRA), permanent wetlands (WET), croplands (CRO), urban and built-up, cropland/natural vegetation mosaic (CNM), snow and ice, barren or sparsely vegetated. The IGBP land cover map in 2001 was obtained from ORNL DAAC (http://webmap.ornl.gov/wcsdown/wcsdown.jsp?dg_id=10004_1). The product has a spatial resolution of 500 m. In our global GPP estimation, this map was resampled into 0.5° resolution to match the GPP_{MTE} product. Four land cover types were excluded (water, urban and built-up, snow and ice, and barren or sparsely vegetated), and CNM was classed with CRO. The GPP_{MTE} product and spatial EVI data were overlaid using the IGBP map.

3.2.4 Statistical analyses

Annual GPP calculated for each site in each year was correlated with the corresponding annual iEVI using log-log regressions following [Campos *et al.*, 2013]. Since the goodness-of-fit for intra-annual GPP-EVI correlations may differ across biomes [Rahman *et al.*, 2005; Sims *et al.*, 2006b; Wu *et al.*, 2010], the GPP-iEVI relationship was further investigated within each biome. The performance of these GPP-iEVI models within each biome was evaluated based on leave-one-out cross-validations (CV), which can test the practical accuracy of these models. The GPP-iEVI models based on biomes were then applied to the whole globe, and the final global GPP estimation was compared to GPP_{MTE}. Two standard statistical measures were employed to assess the regression relationships: the coefficient of determination (R^2) and the root mean squared error (RMSE).

$$R^2 = 1 - \frac{\sum_i (x_i - y_i)^2}{\sum_i (x_i - \bar{x})^2} \quad (5.3)$$

$$RMSE = \sqrt{\frac{\sum_i (x_i - y_i)^2}{n}} \quad (5.4)$$

where x_i denotes the observed data, y_i the modeled data, n the number of observations.

R^2 represents the proportion of total variation of observed data explained by the model.

RMSE measures the bias between modeled and observed data.

3.3 Results

3.3.1 The overall relationship between GPP and iEVI without biomes categorization

The significant logarithmic-logarithmic regression ($R^2 = 0.67$, $p < 0.001$, Figure 3.2, inset) between GPP_{EC} and iEVI at the annual scale shows that there was a good general correspondence between GPP_{EC} and iEVI across all biomes (Figure 3.2). The leave-one-out cross-validation based performance measures ($CV R^2 = 0.66$, Table 3.2) further demonstrated the effectiveness of the logarithmic model (log-log) in regressing GPP against iEVI. The estimated GPP_{iEVI} using the global GPP-iEVI relationship also showed reasonable agreement with GPP_{EC} ($R^2 = 0.62$, $p < 0.001$), although GPP_{iEVI} was consistently underestimated relative to field (EC) measurements. However, the point distribution in the relationship was much more scattered at medium to high production biomes (approximately $GPP > 800 \text{ g C m}^{-2} \text{ yr}^{-1}$). The global relationship was unable to satisfactorily estimate GPP accurately for some of the biomes, such as evergreen broadleaf forest and woody savannas, although the data from these biomes still occurred within the overall distribution (Figure 3.2). Consequently, it was

necessary to further investigate the individual GPP-iEVI relationship within each biome.

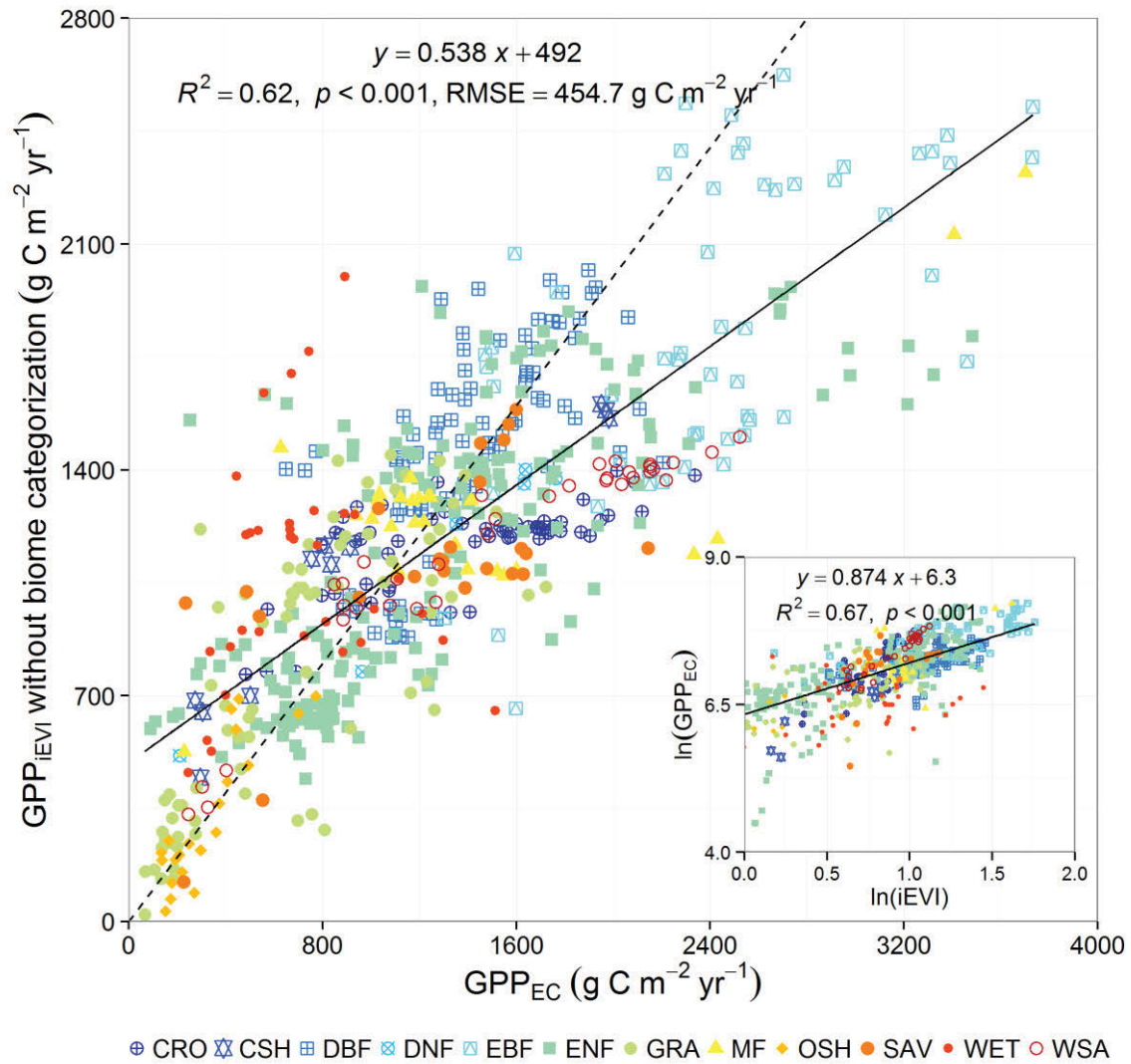


Figure 3.2. Relationship between derived annual GPP from iEVI (GPP_{iEVI}) and eddy covariance tower measured GPP (GPP_{EC}) since 2000 based on all sites and across 12 different biomes. The inset shows \ln -transformed annual GPP_{EC} and annual iEVI for all site-years. The solid line represents the least squares regression line. The dashed line represents the 1:1 line.

3.3.2 Biome-specific relationships between GPP and iEVI

There was considerable variation among the 12 individual biome types in the regression relationships between GPP_{EC} and iEVI (Figure 3.3). The poorest performance of iEVI in

estimating GPP_{EC} was observed in wetlands in raw regression ($R^2 = 0.11$, $p < 0.05$, $RMSE = 297.2 \text{ g C m}^{-2} \text{ yr}^{-1}$) and in cross validations (Table 3.2). The correlation was strongest in woody savannas, closed shrublands, deciduous needle-leaf forests, grasslands, and open shrublands; and moderate in croplands, evergreen needle-leaf forests, savannas, mixed forests, deciduous broadleaf forests, and evergreen broadleaf forests (Figure 3.3). Meanwhile, I calculated the anomalies (by subtracting the mean value) of GPP and iEVI within each biome and investigated correlations between GPP anomaly and iEVI anomaly using linear regressions. Except for the wetlands, GPP anomaly and iEVI anomaly showed moderate to strong correlations within biomes (Figure 3.4). This result was consistent with the non-linear models using GPP and iEVI themselves (Figure 3.3). Further, cross-validations revealed that the GPP-iEVI models within each biome (except wetlands) performed robustly and thus could be applied to the global scale. It is notable that the strength of the correlation within deciduous biomes was generally better (higher R^2 and lower RMSE) than those within evergreen vegetation, except deciduous broadleaf forest (still with better iEVI performance than evergreen broadleaf forest). The relationship for mixed forests had a similar R^2 to evergreen needle-leaf forest but was associated with the largest RMSE ($490.3 \text{ g C m}^{-2} \text{ yr}^{-1}$) across all biomes. There was also a wide range of values for the fitted slopes of the relationship between GPP_{EC} and iEVI. Croplands and deciduous needle-leaf forests occupied a similar and narrow iEVI spectrum, but GPP_{EC} of the former was more sensitive (larger slope) to iEVI. Among forested biomes, GPP_{EC} of evergreen broadleaf forest was less sensitive to iEVI than evergreen needle-leaf forests. Likewise, GPP_{EC} of deciduous broadleaf forests was less sensitive to iEVI than deciduous needle-leaf forests. GPP_{EC} of grasslands and savannas, both of which are grass-dominated biomes, exhibited similar responses to iEVI. Although the range of GPP_{EC} and iEVI values differed substantially among mixed forests and woody savannas, the biome-specific regression slopes were found to be close, whereas woody savannas had a

much smaller RMSE (Figure 3.3).

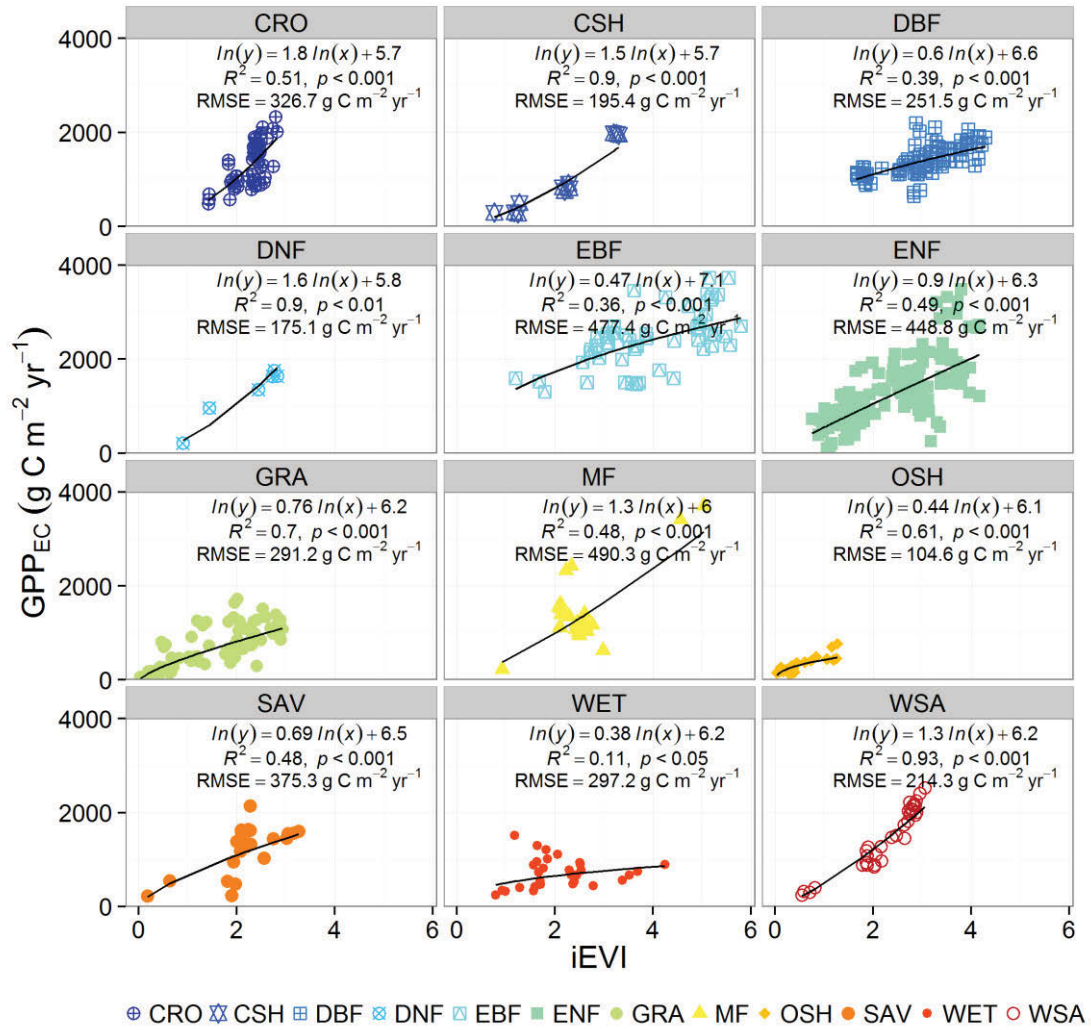


Figure 3.3. Biome-specific relationships between tower-estimated annual GPP (GPP_{EC}) and iEVI. Solid lines represent GPP-iEVI relationships derived from the $\ln(\text{GPP}_{\text{EC}}) \sim \ln(\text{iEVI})$ formulas within each biome. Coefficient of determination (R^2) represents the fit goodness of the $\ln(\text{GPP}_{\text{EC}}) \sim \ln(\text{iEVI})$ relationship, and the root mean squared error (RMSE) represents the bias between GPP estimated using iEVI and GPP_{EC} . All relationships are statistically significant.

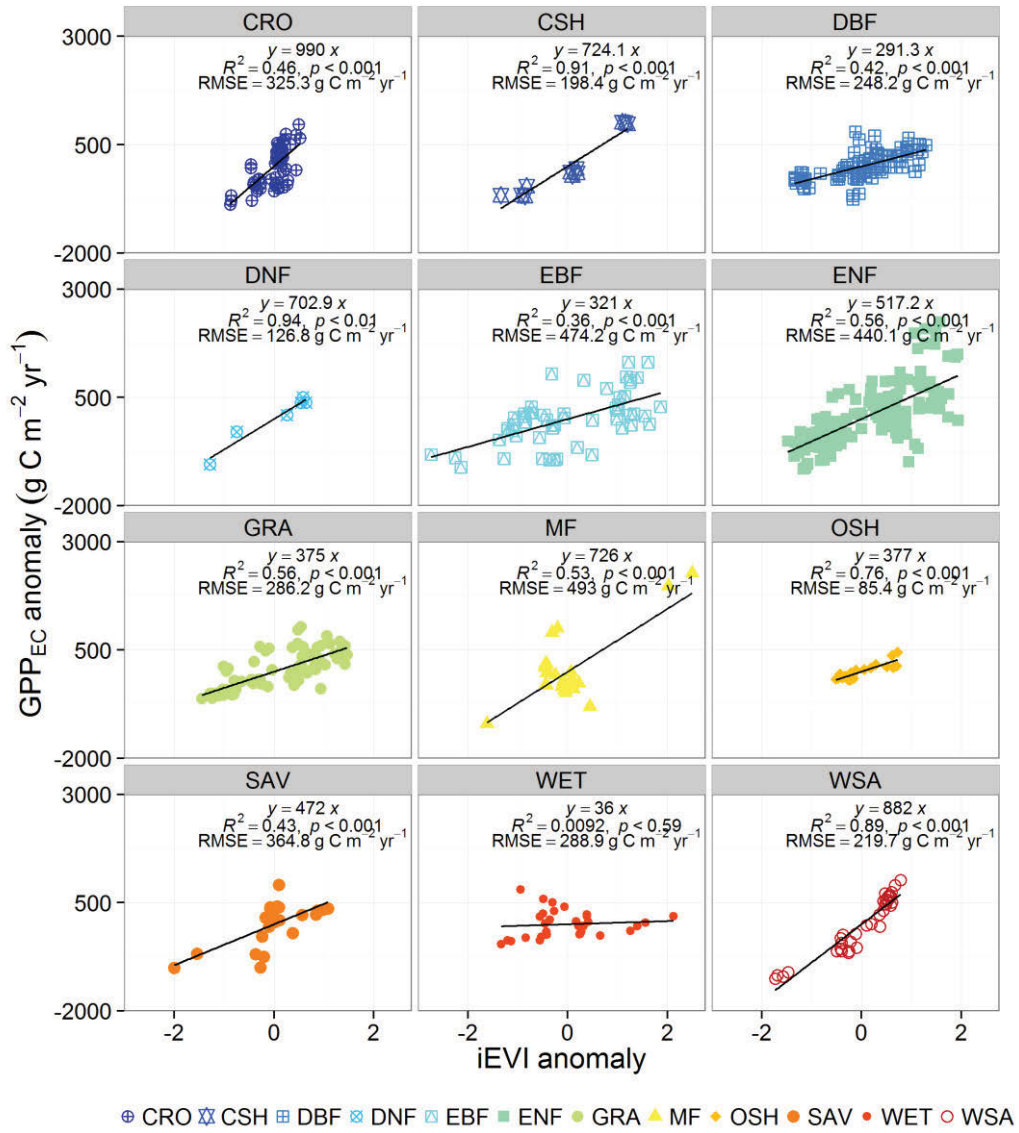


Figure 3.4. Linear correlations between observed GPP anomaly and iEVI anomaly within each biome. The anomaly is calculated as the variable values subtracting their mean.

Table 3.2. Summary of the raw and leave-one-out cross-validation (CV) performance measures (coefficients of determination, R^2 ; root mean squared error, RMSE) of $\ln(\text{GPP})$ - $\ln(\text{iEVI})$ models for all data points and each biome, respectively.

Biomes	Raw R^2	CV R^2	Raw RMSE	CV RMSE
All	0.67	0.66	454.7	455.8
CRO	0.51	0.48	326.7	335.9
CSH	0.90	0.81	195.4	239.6
DBF	0.39	0.36	251.5	256.0
DNF	0.90	0.51	175.1	284.9
EBF	0.36	0.32	477.4	492.1
ENF	0.49	0.48	448.8	454.2
GRA	0.70	0.67	291.2	296.2
MF	0.48	0.33	490.3	529.2
OSH	0.61	0.52	104.6	115.0
SAV	0.48	0.43	375.3	395.2
WET	0.11	0.01	297.2	311.9
WSA	0.93	0.93	214.3	222.8

Estimated GPP based on the biome-specific GPP-iEVI formulae at all sites were then compared with observed GPP_{EC} (Figure 3.5). The relationship between GPP_{iEVI} and GPP_{EC} was significantly strengthened relative to the regression obtained without biome partitioning (Figure 3.2) with increased R^2 (from 0.62 to 0.74), larger slope (from 0.538 to 0.723), decreased RMSE (from 454.7 to 368.2 $\text{g C m}^{-2} \text{ yr}^{-1}$) and smaller intercept (from 492 to 295). There was a large dispersion of points around the linearly fitted function, but these points were mainly obtained from high-GPP locations ($>$ approximately $2400 \text{ g C m}^{-2} \text{ yr}^{-1}$).

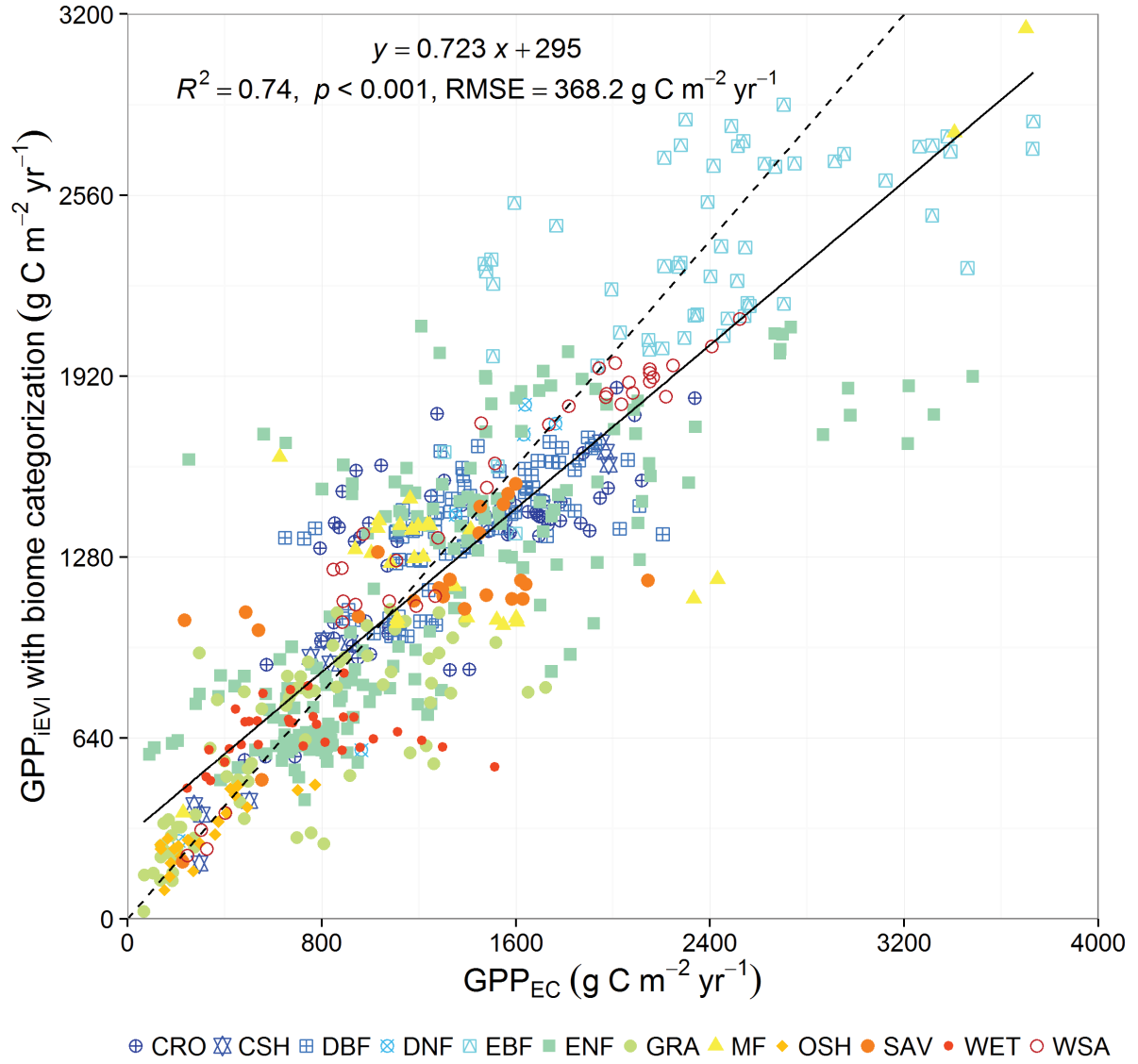


Figure 3.5. Comparison of modelled annual GPP (GPP_{iEVI}) using biome-specific GPP-iEVI relationships with eddy covariance tower measured GPP (GPP_{EC}). The solid line represents the linear regression line. The dashed line represents the 1:1 line.

3.3.3 Global application of biome-specific GPP-iEVI relationships

The set of biome-specific GPP-iEVI relationships were applied to the global data of iEVI and IGBP land cover types. Per-pixel comparison between GPP_{iEVI} and GPP_{MTE} demonstrated the

consistency of biome-specific GPP-iEVI models when up-scaling GPP from the site to global scales ($R^2 = 0.79$, $\text{RMSE} = 387.8 \text{ g C m}^{-2} \text{ yr}^{-1}$; Figure 3.6). The very high accuracy of global, multi-year, averaged GPP ($R^2 = 0.97$) within each biome was unexpected given that the number of flux towers was restricted and their distribution was not geographically uniform. Individual biomes for which annual GPP was larger than 10 Pg C yr^{-1} were scattered farther from the 1:1 line, resulting in underestimation of GPP by iEVI in EBF and overestimation in WSA, CRO and CNM in comparison with the benchmark dataset.

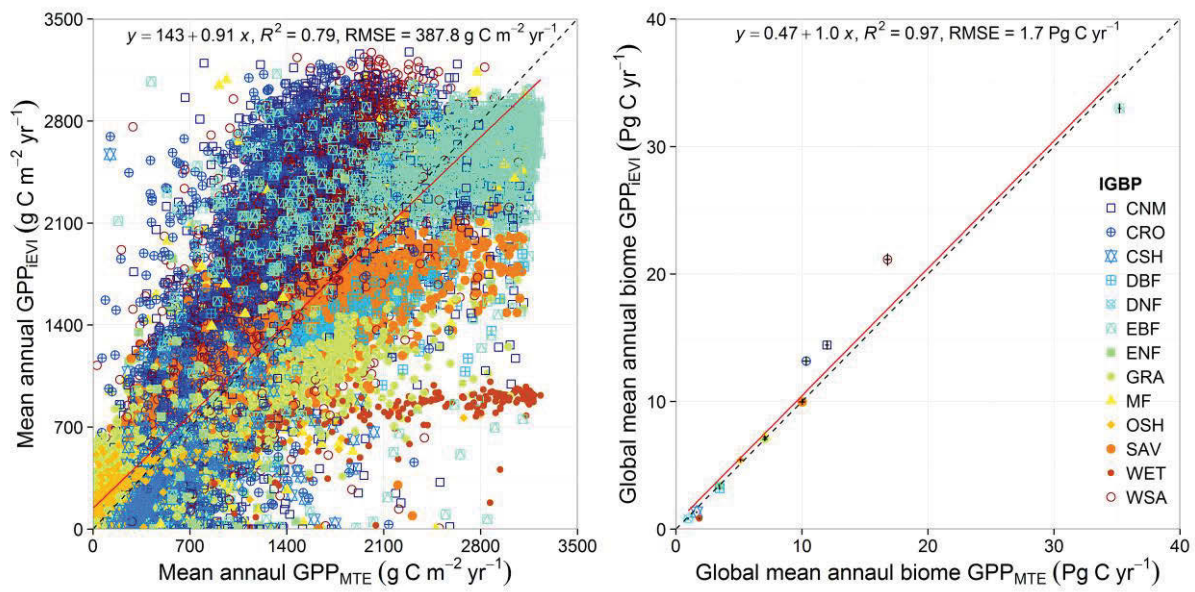


Figure 3.6. Comparison between modelled average annual GPP using iEVI (GPP_{iEVI}) (2000-2013) and the benchmark GPP (GPP_{MTE}) (1982-2008) at a grid level (left) and a biome level (right) across the globe. The red solid line represents the linear regression line and the black dashed line represents the 1:1 line. Horizontal and vertical error bars (right) indicate standard deviations of mean annual biome GPP_{iEVI} (2000-2013) and GPP_{MTE} (1982-2008), respectively.

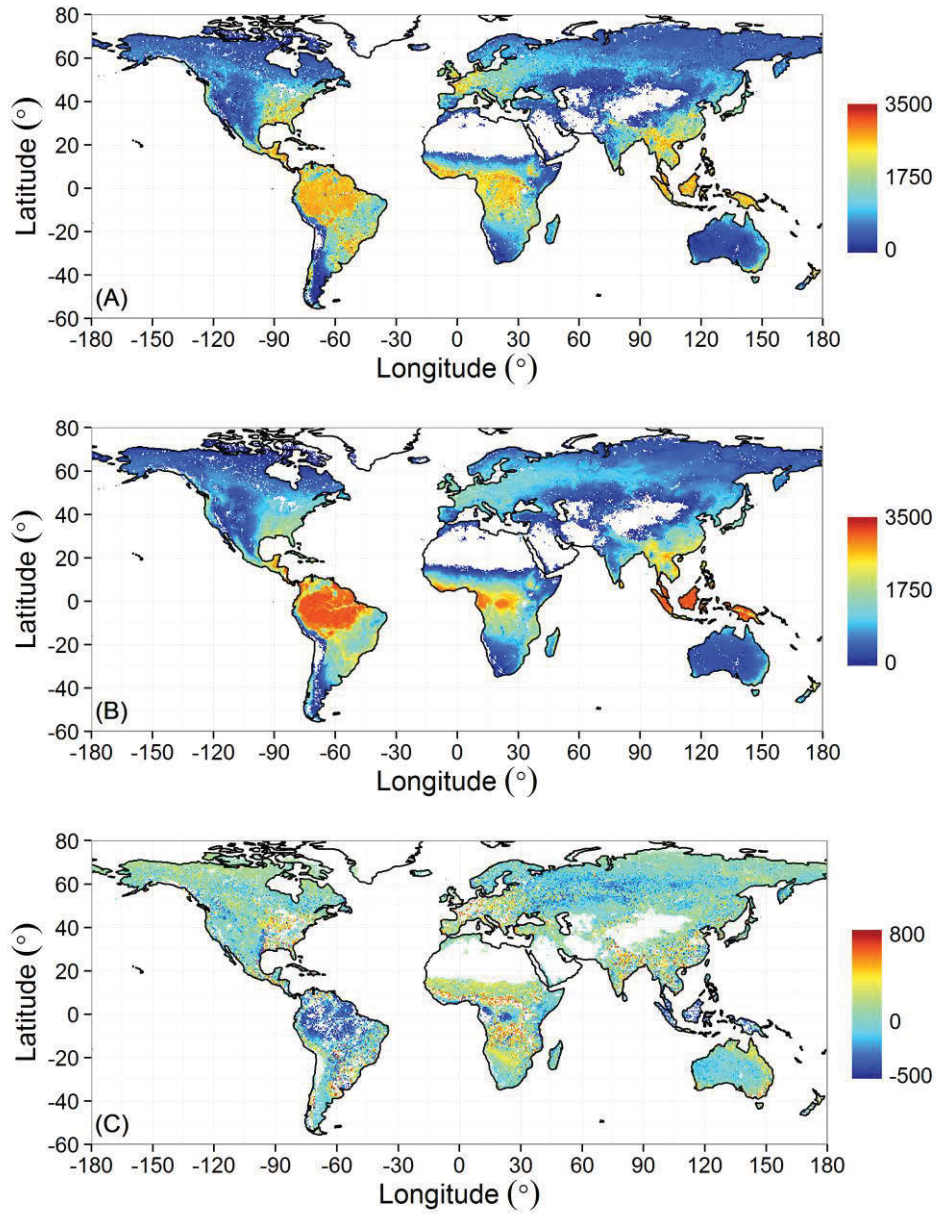


Figure 3.7. Spatial comparison of (A) the mean annual GPP from iEVI (GPP_{iEVI} , $\text{g C m}^{-2} \text{ yr}^{-1}$) (2000-2013) with (B) the benchmark GPP (GPP_{MTE} , $\text{g C m}^{-2} \text{ yr}^{-1}$) (1982-2008) and the distribution of (C) the residual ($\text{g C m}^{-2} \text{ yr}^{-1}$) between GPP_{iEVI} and GPP_{MTE} within the 5-95% quantile.

The mean spatial pattern of GPP was accurately reproduced by iEVI (Figure 3.7). However, GPP was primarily underestimated by iEVI in the tropics, western Russia and equatorial

Africa and was overestimated in Europe, eastern North America, the high-latitude tropics of Africa, southeastern South America, southeastern Australia, southeastern Asia, and parts of India and north China. In these regions, central Africa was dominated by tropical EBF (area around equator) and its north and south edges (area around 5° N and 5° S) were dominated by woody savannas; Europe, eastern North America, southeastern South America and Australia, India and north China were widely covered by cropland/natural vegetation mosaics or croplands (Figure 3.1), which were both parameterized as croplands when calculating GPP_{iEVI} . Latitudinal GPP derived from the iEVI showed positive biases from the benchmark in the regions 30°-38° S, 8°-15° N, 20°-28° N and 30°-55° N, and negative biases in the region 10° S-5° N (Figure 3.8).

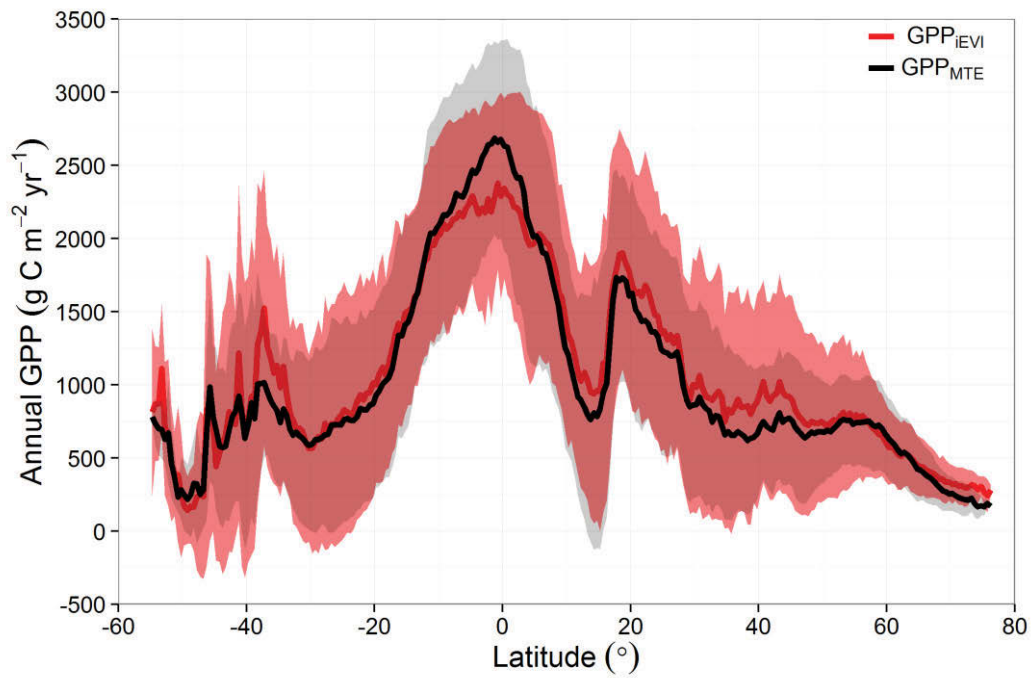


Figure 3.8. Latitudinal patterns (0.5° bands) of mean annual GPP by iEVI (GPP_{iEVI} , 2000-2013) and the benchmark (GPP_{MTE} , 1982-2008), respectively. The red shaded area represents the standard deviation of all GPP_{iEVI} values of cells along the latitude. The grey shaded area represents the standard deviation of all GPP_{MTE} values of cells along the latitude.

3.3.3 LAI and precipitation effects on biome-specific GPP-iEVI relationships

Among vegetation and climatic factors (mean annual maximal LAI, temperature, precipitation and VPD), only LAI and precipitation influenced the regression between GPP and iEVI. The strength of the biome-specific correlations between GPP and iEVI decreased with increasing mean annual LAI ($R^2 = 0.37$, $p < 0.05$) (Figure 3.9). The strength of biome-specific GPP-iEVI relationships with mean annual precipitation followed the same negative trend, but the R^2 was only marginally statistically significant ($R^2 = 0.33$, $p = 0.051$; Figure 3.9 inset). The slopes of relationships between GPP_{EC} and iEVI (i.e., the sensitivity of GPP to EVI) across 12 biomes increased at small values of maximal LAI and then decreased across larger values of maximal LAI (LAI breakpoint was estimated to be $1.98 \text{ m}^2 \text{ m}^{-2}$, Figure 3.9).

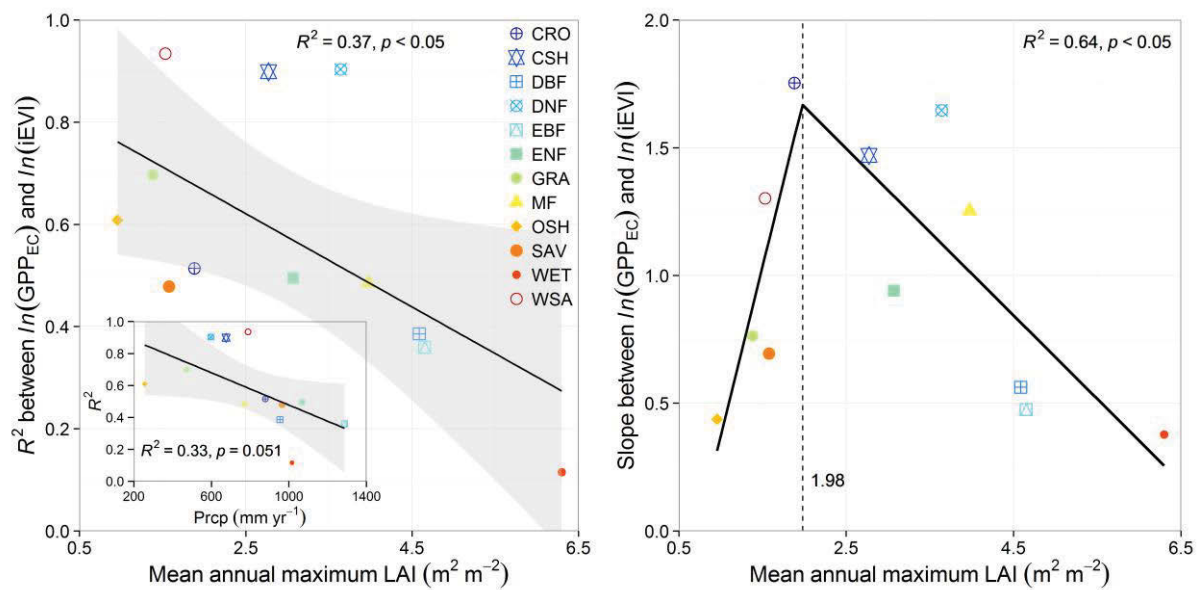


Figure 3.9. Strength (R^2) and slopes of relationships between $\ln(GPP_{EC})$ and $\ln(iEVI)$ for each biome as a function of either mean annual precipitation (Prpc, inset) or mean annual maximum LAI in each biome. Black lines represent the segmented linear regression line. The dashed vertical line indicates the breakpoint of the segmented linear relationship. The shaded area represents 95% confidence band.

3.4 Discussion

3.4.1 Uncertainty analysis

3.4.1.1 Gap-filling and partitioning of eddy covariance carbon fluxes

Two major concerns in up-scaling of eddy covariance measurements of fluxes are (1) the associated propagation of uncertainty within the source datasets, and (2) the up-scaling method itself. Systematic and random errors in measurement, gap-filling and partitioning procedures can result in uncertainty for estimates of GPP [Papale, 2006]. Flux measurements can be subject to substantial random errors, which can be modelled as a double exponential distribution [Hollinger and Richardson, 2005]. To minimize gap-filling errors in this study, only site-years without large gaps (fewer than 5% missing data) were included. A short-term empirical temperature function was used to model ecosystem respiration in the MDS method and the robustness of this function depends on the noisiness of the flux data and the range of temperatures during the short period [Reichstein *et al.*, 2005]. Therefore, at sites with stable temperatures and noisy eddy covariance data, it can be difficult to establish a reliable relationship between ecosystem respiration and temperature [Reichstein *et al.*, 2005]. Consequently, datasets from the FLUXNET ANN product were preferred above the MDS product. The total annual error in eddy fluxes has been conservatively estimated to be below $200 \text{ g C m}^{-2} \text{ yr}^{-1}$ [Reichstein *et al.*, 2007] and the products from these standard methodologies are widely used in up-scaling and benchmarking models [e.g., Beer *et al.*, 2010; Bonan *et al.*, 2011; Jung *et al.*, 2009; Rahman *et al.*, 2005]. However, it is noteworthy that neither the ANN nor the MDS method may be the best option in all flux sites.

3.4.1.2 Ecosystem heterogeneity

A further source of error is introduced when scaling EVI to global GPP. To match the spatial

resolution of GPP_{MTE} , MODIS EVI (1 km resolution) and IGBP classification maps (500 m resolution) were resampled into 0.5° , thereby simplifying prediction of GPP at the global scale. However, resampling unavoidably introduced error in areas with mixed land cover types. The loss of information concerning landscape heterogeneity within larger pixels can cause misuse of the biome-specific GPP-iEVI formulae at the sub-pixel level. The incongruence between GPP_{iEVI} and GPP_{MTE} in WSA, CNM and CRO could be due to varying proportions of vegetation components within a grid cell. For WSA, the eddy covariance measured flux data were mostly from Australia, where the woody and herbaceous components of woody savannas are substantially heterogeneous [Hirota *et al.*, 2011]. Even within a single continent (e.g., Africa or Australia), woody savannas display significant variation in structural and phenological patterns [Kutsch *et al.*, 2008; Sjöström *et al.*, 2011; Sjöström *et al.*, 2013]. However, EVI only has a moderate capacity to predict ecosystem structural and functional attributes such as basal cover of vegetated patches, perennial plants species richness and retention of nutrients [Gaitán *et al.*, 2013]. Similar situations (e.g., different species, cultivars and fragments of croplands) can be encountered in CNM and CRO, besides the fact that the CRO specific GPP-iEVI formula was applied in CNM. In addition, crops are generally intensely managed (e.g., irrigation, fertilization, sowing and harvest), which constrains the reflectance-based greenness indices to accurately estimate GPP of crops [Guanter *et al.*, 2014]. Consequently, the benchmark dataset GPP_{MTE} underestimates cropland GPP in large agricultural regions such as the US Corn Belt, the Indo-Gangetic Plain and the North China Plain but tends to moderately overestimate cropland GPP in South America [Guanter *et al.*, 2014]. Thus, the overestimation of GPP_{iEVI} in comparison with GPP_{MTE} in croplands of North America, north India and north China (Figure 3.7) seems reasonable but is still biased in other agricultural areas. Limitations arising from global scaling can be overcome using the original relatively high-spatial resolution satellite data [Sjöström *et al.*, 2011; Zhao *et al.*, 2005].

However, using these fine resolution data will inevitably increase modeling complexity. Furthermore, the 500 m resolution MODIS IGBP map has its own weakness and uncertainty [Friedl *et al.*, 2010]. Errors due to global scaling were similar in GPP_{iEVI} and GPP_{MTE} and consequently were comparable in this study (Figure 3.6).

3.4.2 Relationships between EVI and GPP

Vegetation greenness indices (VIs) associated GPP models are generally based on one of the following two hypothetical relationships between either LUE or GPP and VIs. The first holds that VIs provide proxy information for parameterizing LUE or fAPAR [Gitelson *et al.*, 2006; Inoue *et al.*, 2008; Sims *et al.*, 2006a; Sims *et al.*, 2006b; Wu *et al.*, 2012] in photosynthetic (as opposed to non-photosynthetic) tissues [Xiao *et al.*, 2005; Xiao *et al.*, 2004a; Xiao *et al.*, 2004b]. Following the logic of classical LUE theory, various LUE models have been developed based on eddy covariance observation and satellite data [Gitelson *et al.*, 2006; Peng *et al.*, 2011; Running *et al.*, 2004; Sims *et al.*, 2008; Yuan *et al.*, 2010]. Each of these models includes a combination of equations that are scaled by environmental regulation of GPP [Beer *et al.*, 2010]. The second is that VIs can estimate GPP alone. Values of EVI follow changes in the greenness and structure of vegetation regardless of the cause of those variations [Huete *et al.*, 2002], resulting in a stronger correlation between tower-estimated GPP and EVI than the correlations between tower-estimated GPP and MODIS GPP or between tower LUE and EVI during the photosynthetic period [Sims *et al.*, 2006b]. The assumption that EVI can be taken as a proxy of LUE results in curvilinear relationships between GPP and EVI [Sims *et al.*, 2006a]. This strongly supports the results presented here (Figure 3.3), suggesting the two hypotheses are essentially consistent, and it is therefore reasonable to assume a strong correlation between GPP and EVI. However, EVI does not perform satisfactorily across all vegetation types, particularly at evergreen forest sites [Rahman *et al.*, 2005; Sims *et al.*, 2006b;

Wu et al., 2010]. Furthermore, EVI is not able to capture GPP variations at short time-scales because short-term fluctuations in photosynthetic capacity are not reflected by variations in canopy greenness over physiological timescales [*Sims et al.*, 2006a]. For example, low temperature can significantly and rapidly reduce GPP whilst having little effect on canopy greenness [*Wu et al.*, 2010].

3.4.3 Environmental constraints on the ability of EVI to estimate GPP

3.4.3.1 LAI affects covariation (R^2) of GPP with iEVI

The performance of EVI in estimating GPP is constrained by environmental conditions, including features of both climate and vegetation structure. The covariation between GPP and EVI is often better in deciduous sites than evergreen sites [*Rahman et al.*, 2005; *Sims et al.*, 2006b; *Wu et al.*, 2010]. Deciduous sites experience a large range between maximal and minimal EVI (as a result of large seasonal variation in canopy cover) and among sites the range is significantly correlated with mean summer rainfall (positive correlation) or mean summer VPD (negative correlation) [*Sims et al.*, 2006b]. The results presented here showed that the strength of the correlation between GPP and iEVI in deciduous biomes was generally better than in evergreen biomes, although the strength of the correlation in DBF was only slightly better than in EBF. Evergreen biomes show smaller seasonal variation in EVI than deciduous biomes. Observable seasonal variation in vegetation greenness may be a prerequisite for successful use of VIs to estimate vegetation production. Deciduous biomes demonstrate distinct seasonal dynamics of leaf greenness, thus satellite data can accurately capture these large seasonal changes in greenness [*Ma et al.*, 2013; *Verma et al.*, 2014]. In contrast, it is difficult to achieve the same level of accuracy within evergreen biomes. This presumably explains the poor performance of iEVI in estimating GPP of EBF, either in wet tropical areas (Figures 3.5, 3.6 and 3.7) or in semi-arid evergreen forests, where

photosynthetic capacity can vary independently of EVI and LAI in response to dry conditions [Maseyk *et al.*, 2008]. However, either the seasonal change of EVI or LAI cannot effectively explain the weak correlation between iEVI and GPP in DBF. Nagai *et al.* [2010] found EVI to increase earlier than GPP during the leaf-expansion period in DBF, and this caused systematic variability in the GPP-EVI relationship [Richardson *et al.*, 2012; Verma *et al.*, 2014]. To address the asynchronicity between GPP and EVI in DBF, a phenological scalar may be needed in GPP-iEVI equations, as has been applied in the vegetation photosynthesis model of Xiao *et al.* [2004b]. This suggests that large seasonal variance of EVI does not necessarily imply a good correlation of EVI and GPP and thus EVI variance is not appropriate to explain the covariation of iEVI-GPP across biomes. My result also showed that iEVI variance across biomes can be greatly divergent while R^2 of iEVI-GPP correlations can be close. For example, iEVI standard deviations for CRO and ENF are 0.44 and 0.94, whereas R^2 are 0.51 and 0.49, respectively (Figure 3.3). In contrast, peak LAI can be as a metric of the complexity of canopy structures of a biome and thus is appropriate to indicate the covariation strength of iEVI-GPP relationships. As peak LAI increases, the iEVI-GPP relationship is weakened (Figure 3.9) by the increased structural complexity due to either small seasonal EVI variations in a biome such as EBF or the asynchronicity between GPP and EVI in a biome such as DBF.

Another possible factor contributing to the poor correlation between GPP and iEVI in vegetation with high LAI that are most located in wet regions may be the extensive cloudy conditions that reduce the quality of EVI retrievals [Nagai *et al.*, 2010]. In arid and semi-arid areas where cloud cover is minimal, precipitation is a controlling factor of vegetation phenology and productivity [Bradley *et al.*, 2011; Cleverly *et al.*, 2013; Huxman *et al.*, 2004; Jolly and Running, 2004; Ma *et al.*, 2013; Schwinning and Sala, 2004]. Moreover, peak LAI is typically limited by water availability in arid and semi-arid regions [Eamus and Prior, 2001; Sjöström *et al.*, 2011]. Consequently, the correlation between the strength of GPP-iEVI

relationships with mean annual precipitation showed the same trend as that for LAI_{max} (Figure 3.9 inset). The correlation between the strength of GPP-iEVI relationships and LAI_{max} may help identifying the regions where iEVI is most likely to be a good predictor of GPP. Globally, underestimation of GPP in some locations was compensated by overestimation in other locations within the same biome type (Figures 3.5 and 3.6), with a consequential minimisation of biases on the estimation of GPP due to global patterns of LAI.

3.4.3.2 LAI scales the sensitivity (fitted slopes) of GPP to iEVI

Lindroth et al. [2008] proposed that LAI is the principal scaling parameter for GPP in northern deciduous and coniferous forests. In biomes with a relatively small peak LAI (e.g., less than $2.5 \text{ m}^2 \text{ m}^{-2}$), the sensitivity of GPP to EVI increases with LAI [*Sjöström et al.*, 2011], although there were too few arid vegetation classes in the study to identify a statistically significant trend in sensitivity across small values of LAI (less than $1.98 \text{ m}^2 \text{ m}^{-2}$, Figure 3.9). Conversely, as vegetation becomes less water limited, the sensitivity of GPP to EVI tended to decrease across large values of LAI (larger than $1.98 \text{ m}^2 \text{ m}^{-2}$, Figure 3.9), which has not previously been found at a global scale. Degradation of the GPP-iEVI relationship at large LAI is due to (1) decreased sensitivity of variation in EVI to changes in canopy structure, including LAI and canopy type, of dense forests [*Gao et al.*, 2000] and (2) biased or decreased seasonality of variations in EVI.

3.5 Conclusions

I comprehensively evaluated the ability of MODIS EVI to estimate annual GPP across 12 land cover types based on GPP from eddy covariance. iEVI does not require calculation of the duration of the growing season, which significantly simplifies the estimation of annual GPP

by EVI at the global scale. Cross validations demonstrated the robustness of biome-specific $\ln(\text{GPP}) \sim \ln(\text{iEVI})$ models. In comparison to a global benchmarking dataset of mean annual GPP, I showed that the performance of iEVI was consistent from site-to-global scales. Compared to GPP_{MTE} , GPP_{iEVI} performed better in croplands of high productivity but poorer mainly in forests. The strength of the GPP-iEVI relationships across biomes was correlated with peak LAI, by which the slope was also scaled. These findings suggest that vegetation structure is an important factor regulating the accuracy and sensitivity of EVI in estimating spatial patterns of annual GPP across multiple biomes. While LUE models, data-driven models and terrestrial biosphere models are usually difficult to parameterize or are limited by coarse resolution meteorological inputs, this study provides a promising and very convenient approach to estimate global spatial patterns of GPP at either a fine or coarse resolution. Nevertheless, the use of EVI in estimating GPP requires further study, especially in deciduous broadleaf forest and evergreen biomes. My findings on impacts of vegetation structure provide valuable information for such efforts in improving EVI-based models of GPP.

Acknowledgements

This research was supported by an Australian Research Council Discovery Early Career Research Award (project number DE120103022). X.T. was supported by one of National Basic Research Program of China (grant number 2013CB733404) and the National Natural Science Foundation of China (grant number 41101379). This work used eddy covariance data acquired by the FLUXNET community and in particular by the following networks: AmeriFlux (U.S. Department of Energy, Biological and Environmental Research, Terrestrial Carbon Program (DE-FG02-04ER63917 and DE-FG02-04ER63911)), AfriFlux, AsiaFlux, CarboAfrica, CarboEuropeIP, CarboItaly, CarboMont, ChinaFlux, FLUXNET Canada (supported by CFCAS, NSERC, BIOCAP, Environment Canada, and NRCan), GreenGrass,

KoFlux, LBA, NECC, OzFlux, TCOS-Siberia, USCCC. I acknowledge the financial support to the eddy covariance data harmonization provided by CarboEuropeIP, FAO-GTOS-TCO, iLEAPS, Max Planck Institute for Biogeochemistry, National Science Foundation, University of Tuscia, Université Laval, Environment Canada and U.S. Department of Energy and the database development and technical support from Berkeley Water Center, Lawrence Berkeley National Laboratory, Microsoft Research eScience, Oak Ridge National Laboratory, University of California Berkeley, University of Virginia.

References

- Alexandrov, T. (2009), A method of trend extraction using singular spectrum analysis, *RevStat*, 7, 1-22.
- Asner, G. P., J. M. Scurlock, and J. A. Hicke (2003), Global synthesis of leaf area index observations: implications for ecological and remote sensing studies, *Global Ecology and Biogeography*, 12(3), 191-205.
- Aubinet, M., A. Grelle, A. Ibrom, Ü. Rannik, J. Moncrieff, T. Foken, A. Kowalski, P. Martin, P. Berbigier, and C. Bernhofer (2000), Estimates of the annual net carbon and water exchange of forests: the EUROFLUX methodology, *Advances in ecological research*, 30, 113-175.
- Baldocchi, D. (2008), 'Breathing' of the terrestrial biosphere: lessons learned from a global network of carbon dioxide flux measurement systems, *Australian Journal of Botany*, 56(1), 1-26.
- Baldocchi, D., E. Falge, L. Gu, R. Olson, D. Hollinger, S. Running, P. Anthoni, C. Bernhofer, K. Davis, and R. Evans (2001), FLUXNET: A new tool to study the temporal and spatial variability of ecosystem-scale carbon dioxide, water vapor, and energy flux densities, *Bulletin of the American Meteorological Society*, 82(11), 2415-2434.

- Beer, C., M. Reichstein, E. Tomelleri, P. Ciais, M. Jung, N. Carvalhais, C. Rödenbeck, M. A. Arain, D. Baldocchi, and G. B. Bonan (2010), Terrestrial gross carbon dioxide uptake: global distribution and covariation with climate, *Science*, 329(5993), 834-838.
- Bonan, G. B., P. J. Lawrence, K. W. Oleson, S. Levis, M. Jung, M. Reichstein, D. M. Lawrence, and S. C. Swenson (2011), Improving canopy processes in the Community Land Model version 4 (CLM4) using global flux fields empirically inferred from FLUXNET data, *Journal of Geophysical Research: Biogeosciences* (2005–2012), 116(G2).
- Bradley, A. V., F. F. Gerard, N. Barbier, G. P. Weedon, L. O. Anderson, C. Huntingford, L. E. Aragao, P. Zelazowski, and E. Arai (2011), Relationships between phenology, radiation and precipitation in the Amazon region, *Global Change Biology*, 17(6), 2245-2260.
- Campos, G. E. P., M. S. Moran, A. Huete, Y. Zhang, C. Bresloff, T. E. Huxman, D. Eamus, D. D. Bosch, A. R. Buda, and S. A. Gunter (2013), Ecosystem resilience despite large-scale altered hydroclimatic conditions, *Nature*, 494(7437), 349-352.
- Cescatti, A., B. Marcolla, S. K. Santhana Vannan, J. Y. Pan, M. O. Román, X. Yang, P. Ciais, R. B. Cook, B. E. Law, and G. Matteucci (2012), Intercomparison of MODIS albedo retrievals and in situ measurements across the global FLUXNET network, *Remote sensing of environment*, 121, 323-334.
- Ciais, P., M. Reichstein, N. Viovy, A. Granier, J. Ogée, V. Allard, M. Aubinet, N. Buchmann, C. Bernhofer, and A. Carrara (2005), Europe-wide reduction in primary productivity caused by the heat and drought in 2003, *Nature*, 437(7058), 529-533.
- Cleverly, J., N. Boulain, R. Villalobos-Vega, N. Grant, R. Faux, C. Wood, P. G. Cook, Q. Yu, A. Leigh, and D. Eamus (2013), Dynamics of component carbon fluxes in a semi-arid *Acacia* woodland, central Australia, *Journal of Geophysical Research: Biogeosciences*, 118, 1168–1185.

- Eamus, D., and L. Prior (2001), Ecophysiology of trees of seasonally dry tropics: Comparisons among phenologies, in *Advances in ecological research*, edited, pp. 113-197, Academic Press.
- Friedl, M. A., D. Sulla-Menashe, B. Tan, A. Schneider, N. Ramankutty, A. Sibley, and X. Huang (2010), MODIS Collection 5 global land cover: Algorithm refinements and characterization of new datasets, *Remote Sensing of Environment*, 114(1), 168-182.
- Gaitán, J. J., et al. (2013), Evaluating the performance of multiple remote sensing indices to predict the spatial variability of ecosystem structure and functioning in Patagonian steppes, *Ecological Indicators*, 34, 181-191.
- Gao, X., A. R. Huete, W. Ni, and T. Miura (2000), Optical–biophysical relationships of vegetation spectra without background contamination, *Remote Sensing of Environment*, 74(3), 609-620.
- Gitelson, A. A., A. Viña, S. B. Verma, D. C. Rundquist, T. J. Arkebauer, G. Keydan, B. Leavitt, V. Ciganda, G. G. Burba, and A. E. Suyker (2006), Relationship between gross primary production and chlorophyll content in crops: Implications for the synoptic monitoring of vegetation productivity, *Journal of Geophysical Research: Atmospheres (1984–2012)*, 111(D8).
- Goward, S. N., and K. F. Huemmrich (1992), Vegetation canopy PAR absorptance and the normalized difference vegetation index: an assessment using the SAIL model, *Remote Sensing of Environment*, 39(2), 119-140.
- Guanter, L., Y. Zhang, M. Jung, J. Joiner, M. Voigt, J. A. Berry, C. Frankenberg, A. R. Huete, P. Zarco-Tejada, and J.-E. Lee (2014), Global and time-resolved monitoring of crop photosynthesis with chlorophyll fluorescence, *Proceedings of the National Academy of Sciences*, 111(14), E1327-E1333.
- Hassani, H. (2007), Singular spectrum analysis: methodology and comparison.

- Heinsch, F. A., M. Zhao, S. W. Running, J. S. Kimball, R. R. Nemani, K. J. Davis, P. V. Bolstad, B. D. Cook, A. R. Desai, and D. M. Ricciuto (2006), Evaluation of remote sensing based terrestrial productivity from MODIS using regional tower eddy flux network observations, *Geoscience and Remote Sensing, IEEE Transactions on*, 44(7), 1908-1925.
- Hirota, M., M. Holmgren, E. H. Van Nes, and M. Scheffer (2011), Global resilience of tropical forest and savanna to critical transitions, *Science*, 334(6053), 232-235.
- Hollinger, D., and A. Richardson (2005), Uncertainty in eddy covariance measurements and its application to physiological models, *Tree Physiology*, 25(7), 873-885.
- Huete, A., H. Liu, K. Batchily, and W. Van Leeuwen (1997), A comparison of vegetation indices over a global set of TM images for EOS-MODIS, *Remote sensing of environment*, 59(3), 440-451.
- Huete, A., K. Didan, T. Miura, E. P. Rodriguez, X. Gao, and L. G. Ferreira (2002), Overview of the radiometric and biophysical performance of the MODIS vegetation indices, *Remote Sensing of Environment*, 83(1), 195-213.
- Huxman, T. E., K. A. Snyder, D. Tissue, A. J. Leffler, K. Ogle, W. T. Pockman, D. R. Sandquist, D. L. Potts, and S. Schwinning (2004), Precipitation pulses and carbon fluxes in semiarid and arid ecosystems, *Oecologia*, 141(2), 254–268.
- Inoue, Y., J. Peñuelas, A. Miyata, and M. Mano (2008), Normalized difference spectral indices for estimating photosynthetic efficiency and capacity at a canopy scale derived from hyperspectral and CO₂ flux measurements in rice, *Remote Sensing of Environment*, 112(1), 156-172.
- Jolly, W. M., and S. W. Running (2004), Effects of precipitation and soil water potential on drought deciduous phenology in the Kalahari, *Global Change Biology*, 10(3), 303-308.
- Jung, M., M. Reichstein, and A. Bondeau (2009), Towards global empirical upscaling of

- FLUXNET eddy covariance observations: validation of a model tree ensemble approach using a biosphere model, *Biogeosciences*, 6(10).
- Jung, M., M. Verstraete, N. Gobron, M. Reichstein, D. Papale, A. Bondeau, M. Robustelli, and B. Pinty (2008), Diagnostic assessment of European gross primary production, *Global Change Biology*, 14(10), 2349-2364.
- Jung, M., M. Reichstein, H. A. Margolis, A. Cescatti, A. D. Richardson, M. A. Arain, A. Arneth, C. Bernhofer, D. Bonal, and J. Chen (2011), Global patterns of land-atmosphere fluxes of carbon dioxide, latent heat, and sensible heat derived from eddy covariance, satellite, and meteorological observations, *Journal of Geophysical Research: Biogeosciences (2005–2012)*, 116(G3).
- Knyazikhin, Y., J. Martonchik, R. Myneni, D. Diner, and S. Running (1998), Synergistic algorithm for estimating vegetation canopy leaf area index and fraction of absorbed photosynthetically active radiation from MODIS and MISR data, *Journal of Geophysical Research: Atmospheres (1984–2012)*, 103(D24), 32257-32275.
- Kondrashov, D., and M. Ghil (2006), Spatio-temporal filling of missing points in geophysical data sets, *Nonlinear Processes in Geophysics*, 13(2), 151-159.
- Kutsch, W., N. Hanan, R. Scholes, I. McHugh, W. Kubheka, H. Eckhardt, and C. Williams (2008), Response of carbon fluxes to water relations in a savanna ecosystem in South Africa, *Biogeosciences Discussions*, 5(3).
- Lindroth, A., F. Lagergren, M. Aurela, B. Bjarnadottir, T. Christensen, E. Dellwik, A. Grelle, A. Ibrom, T. Johansson, and H. Lankreijer (2008), Leaf area index is the principal scaling parameter for both gross photosynthesis and ecosystem respiration of Northern deciduous and coniferous forests, *Tellus B*, 60(2), 129-142.
- Ma, X., A. Huete, Q. Yu, N. R. Coupe, K. Davies, M. Broich, P. Ratana, J. Beringer, L. B. Hutley, and J. Cleverly (2013), Spatial patterns and temporal dynamics in savanna

- vegetation phenology across the North Australian Tropical Transect, *Remote Sensing of Environment*, 139, 97-115.
- Mao, D., Z. Wang, L. Li, and W. Ma (2014), Spatiotemporal dynamics of grassland aboveground net primary productivity and its association with climatic pattern and changes in Northern China, *Ecological Indicators*, 41, 40-48.
- Maseyk, K. S., T. Lin, E. Rotenberg, J. M. Grünzweig, A. Schwartz, and D. Yakir (2008), Physiology–phenology interactions in a productive semi-arid pine forest, *New Phytologist*, 178(3), 603-616.
- Melillo, J. M., A. D. McGuire, D. W. Kicklighter, B. Moore, C. J. Vorosmarty, and A. L. Schloss (1993), Global climate change and terrestrial net primary production, *Nature*, 363(6426), 234-240.
- Monteith, J. (1972), Solar radiation and productivity in tropical ecosystems, *Journal of applied ecology*, 9(3), 747-766.
- Nagai, S., N. Saigusa, H. Muraoka, and K. N. Nasahara (2010), What makes the satellite-based EVI–GPP relationship unclear in a deciduous broad-leaved forest?, *Ecological Research*, 25(2), 359-365.
- Papale, D. (2006), Towards a standardized processing of Net Ecosystem Exchange measured with eddy covariance technique: algorithms and uncertainty estimation.
- Papale, D., and R. Valentini (2003), A new assessment of European forests carbon exchanges by eddy fluxes and artificial neural network spatialization, *Global Change Biology*, 9(4), 525-535.
- Peng, Y., A. A. Gitelson, G. Keydan, D. C. Rundquist, and W. Moses (2011), Remote estimation of gross primary production in maize and support for a new paradigm based on total crop chlorophyll content, *Remote Sensing of Environment*, 115(4), 978-989.
- Rahman, A., D. Sims, V. Cordova, and B. El-Masri (2005), Potential of MODIS EVI and

- surface temperature for directly estimating per-pixel ecosystem C fluxes, *Geophysical Research Letters*, 32(19), L19404.
- Reichstein, M., E. Falge, D. Baldocchi, D. Papale, M. Aubinet, P. Berbigier, C. Bernhofer, N. Buchmann, T. Gilmanov, and A. Granier (2005), On the separation of net ecosystem exchange into assimilation and ecosystem respiration: review and improved algorithm, *Global Change Biology*, 11(9), 1424-1439.
- Reichstein, M., D. Papale, R. Valentini, M. Aubinet, C. Bernhofer, A. Knohl, T. Laurila, A. Lindroth, E. Moors, and K. Pilegaard (2007), Determinants of terrestrial ecosystem carbon balance inferred from European eddy covariance flux sites, *Geophysical Research Letters*, 34(1).
- Richardson, A. D., R. S. Anderson, M. A. Arain, A. G. Barr, G. Bohrer, G. Chen, J. M. Chen, P. Ciais, K. J. Davis, and A. R. Desai (2012), Terrestrial biosphere models need better representation of vegetation phenology: results from the North American Carbon Program Site Synthesis, *Global Change Biology*, 18(2), 566-584.
- Running, S. W., R. R. Nemani, F. A. Heinsch, M. Zhao, M. Reeves, and H. Hashimoto (2004), A continuous satellite-derived measure of global terrestrial primary production, *Bioscience*, 54(6), 547-560.
- Schwinning, S., and O. E. Sala (2004), Hierarchy of responses to resource pulses in arid and semi-arid ecosystems, *Oecologia*, 141(2), 211-220.
- Sims, D. A., H. Luo, S. Hastings, W. C. Oechel, A. F. Rahman, and J. A. Gamon (2006a), Parallel adjustments in vegetation greenness and ecosystem CO₂ exchange in response to drought in a Southern California chaparral ecosystem, *Remote Sensing of Environment*, 103(3), 289-303.
- Sims, D. A., A. F. Rahman, V. D. Cordova, B. Z. El-Masri, D. D. Baldocchi, P. V. Bolstad, L. B. Flanagan, A. H. Goldstein, D. Y. Hollinger, and L. Misson (2008), A new model of

- gross primary productivity for North American ecosystems based solely on the enhanced vegetation index and land surface temperature from MODIS, *Remote Sensing of Environment*, 112(4), 1633-1646.
- Sims, D. A., et al. (2006b), On the use of MODIS EVI to assess gross primary productivity of North American ecosystems, *Journal of Geophysical Research: Biogeosciences*, 111(G4), G04015.
- Sjöström, M., J. Ardö, A. Arneth, N. Boulain, B. Cappelaere, L. Eklundh, A. De Grandcourt, W. Kutsch, L. Merbold, and Y. Nouvellon (2011), Exploring the potential of MODIS EVI for modeling gross primary production across African ecosystems, *Remote Sensing of Environment*, 115(4), 1081-1089.
- Sjöström, M., M. Zhao, S. Archibald, A. Arneth, B. Cappelaere, U. Falk, A. De Grandcourt, N. Hanan, L. Kergoat, and W. Kutsch (2013), Evaluation of MODIS gross primary productivity for Africa using eddy covariance data, *Remote sensing of environment*, 131, 275-286.
- Tan, B., J. T. Morisette, R. E. Wolfe, F. Gao, G. A. Ederer, J. Nightingale, and J. A. Pedelty (2011), An enhanced TIMESAT algorithm for estimating vegetation phenology metrics from MODIS data, *Selected Topics in Applied Earth Observations and Remote Sensing, IEEE Journal of*, 4(2), 361-371.
- Verma, M., et al. (2014), Remote sensing of annual terrestrial gross primary productivity from MODIS: an assessment using the FLUXNET La Thuile data set, *Biogeosciences*, 11(8), 2185-2200.
- Wang, D., and S. Liang (2008), Singular Spectrum Analysis for Filling Gaps and Reducing Uncertainties of MODIS Land Products, paper presented at Geoscience and Remote Sensing Symposium, 2008. IGARSS 2008. IEEE International, IEEE.
- Wang, K., and R. E. Dickinson (2012), A review of global terrestrial evapotranspiration:

- Observation, modeling, climatology, and climatic variability, *Reviews of Geophysics*, 50(2), RG2005.
- Wu, C., Z. Niu, and S. Gao (2012), The potential of the satellite derived green chlorophyll index for estimating midday light use efficiency in maize, coniferous forest and grassland, *Ecological Indicators*, 14(1), 66-73.
- Wu, C., J. W. Munger, Z. Niu, and D. Kuang (2010), Comparison of multiple models for estimating gross primary production using MODIS and eddy covariance data in Harvard Forest, *Remote Sensing of Environment*, 114(12), 2925-2939.
- Wylie, B. K., D. A. Johnson, E. Laca, N. Z. Saliendra, T. G. Gilmanov, B. C. Reed, L. L. Tieszen, and B. B. Worstell (2003), Calibration of remotely sensed, coarse resolution NDVI to CO₂ fluxes in a sagebrush–steppe ecosystem, *Remote Sensing of Environment*, 85(2), 243-255.
- Xiao, X., Q. Zhang, D. Hollinger, J. Aber, and B. Moore III (2005), Modeling gross primary production of an evergreen needleleaf forest using MODIS and climate data, *Ecological Applications*, 15(3), 954-969.
- Xiao, X., D. Hollinger, J. Aber, M. Goltz, E. A. Davidson, Q. Zhang, and B. Moore III (2004a), Satellite-based modeling of gross primary production in an evergreen needleleaf forest, *Remote sensing of environment*, 89(4), 519-534.
- Xiao, X., Q. Zhang, B. Braswell, S. Urbanski, S. Boles, S. Wofsy, B. Moore III, and D. Ojima (2004b), Modeling gross primary production of temperate deciduous broadleaf forest using satellite images and climate data, *Remote Sensing of Environment*, 91(2), 256-270.
- Yang, F., K. Ichii, M. A. White, H. Hashimoto, A. R. Michaelis, P. Votava, A. Zhu, A. Huete, S. W. Running, and R. R. Nemani (2007), Developing a continental-scale measure of gross primary production by combining MODIS and AmeriFlux data through Support Vector Machine approach, *Remote Sensing of Environment*, 110(1), 109-122.

- Yuan, W., S. Liu, G. Yu, J.-M. Bonnefond, J. Chen, K. Davis, A. R. Desai, A. H. Goldstein, D. Gianelle, and F. Rossi (2010), Global estimates of evapotranspiration and gross primary production based on MODIS and global meteorology data, *Remote Sensing of Environment*, 114(7), 1416-1431.
- Zhang, Q., X. Xiao, B. Braswell, E. Linder, F. Baret, and B. Moore III (2005), Estimating light absorption by chlorophyll, leaf and canopy in a deciduous broadleaf forest using MODIS data and a radiative transfer model, *Remote Sensing of Environment*, 99(3), 357-371.
- Zhang, X., M. A. Friedl, C. B. Schaaf, and A. H. Strahler (2004), Climate controls on vegetation phenological patterns in northern mid-and high latitudes inferred from MODIS data, *Global Change Biology*, 10(7), 1133-1145.
- Zhao, M., F. A. Heinsch, R. R. Nemani, and S. W. Running (2005), Improvements of the MODIS terrestrial gross and net primary production global data set, *Remote sensing of Environment*, 95(2), 164-176.

Appendix

Table A3.1. ID, code, coordinates, and IGBP of 155 flux sites used in this study. CRO: croplands; CSH: closed shrublands; DBF: deciduous broadleaf forest; DNF: deciduous needle-leaf forest; EBF: evergreen broadleaf forest; ENF: evergreen needle-leaf forest; GRA: grasslands; MF: mixed forest; OSH: open shrublands; SAV: savannas; WET: permanent wetlands; WSA: woody savannas.

ID	Code	Lat	Long	startYear	endYear	IGBP
1	AU-Ade	-13.0769	131.1178	2007	2008	SAV
2	AU-Asm	-22.28	133.25	2011	2012	SAV
3	AU-Cap	-34.0027	140.5877	2010	2012	OSH
4	AU-Da1	-14.0633	131.3181	2007	2012	SAV
5	AU-Da2	-14.1592	131.3881	2007	2012	SAV
6	AU-Dry	-15.2588	132.3706	2008	2012	SAV
7	AU-Fog	-12.5452	131.3072	2007	2008	WET
8	AU-How	-12.4952	131.15	2001	2012	WSA

9	AU-JXA	-34.9878	146.2908	2012	2012	CRO
10	AU-RDM	-14.5636	132.4776	2012	2012	SAV
11	AU-Rig	-36.6499	145.576	2011	2012	GRA
12	AU-Stp	-17.1507	133.3502	2008	2012	GRA
13	AU-Tum	-35.6566	148.1517	2001	2012	EBF
14	AU-Wac	-37.4262	145.1873	2006	2011	EBF
15	AU-Whr	-36.6731	145.0262	2012	2012	EBF
16	AU-Wom	-37.4222	144.0944	2010	2012	EBF
17	BR-Sa1	-2.85667	-54.9589	2002	2005	EBF
18	BR-Sa3	-3.01803	-54.9714	2001	2003	EBF
19	CA-Ca1	49.86725	-125.334	2000	2010	ENF
20	CA-Ca2	49.87048	-125.291	2001	2010	ENF
21	CA-Ca3	49.53462	-124.9	2002	2010	ENF
22	CA-Man	55.8796	-98.4808	2007	2008	ENF
23	CA-Mer	45.4094	-75.5186	2000	2010	WET
24	CA-NS1	55.8792	-98.4839	2003	2004	ENF
25	CA-NS2	55.9058	-98.5247	2002	2002	ENF
26	CA-NS3	55.9117	-98.3822	2002	2004	ENF
27	CA-NS5	55.8631	-98.485	2002	2004	ENF
28	CA-NS6	55.9167	-98.9644	2002	2004	OSH
29	CA-NS7	56.6358	-99.9483	2003	2004	OSH
30	CA-Oas	53.62889	-106.198	2000	2010	DBF
31	CA-Obs	53.98717	-105.118	2000	2010	ENF
32	CA-Ojp	53.91634	-104.692	2000	2010	ENF
33	CA-Qc2	49.75984	-74.5711	2008	2010	ENF
34	CA-Qcu	49.26708	-74.0365	2002	2010	ENF
35	CA-Qfo	49.69247	-74.342	2004	2010	ENF
36	CA-SJ2	53.94474	-104.649	2003	2007	ENF
37	CA-SJ3	53.87581	-104.645	2004	2006	ENF
38	CA-TP4	42.7098	-80.3574	2003	2010	ENF
39	CA-WP1	54.95384	-112.467	2004	2008	WET
40	CN-Bed	39.5306	116.2519	2006	2006	EBF
41	CN-Cha	42.4025	128.0958	2003	2007	MF
42	CN-Dan	30.41	91.08	2004	2007	GRA
43	CN-Din	23.16667	112.53	2003	2007	EBF
44	CN-Do2	31.58	121.9	2005	2005	WET
45	CN-Hab	37.66	101.33	2003	2007	GRA
46	CN-Hui	26.83	109.75	2008	2008	ENF
47	CN-Huz	51.47	123.01	2010	2010	DNF
48	CN-Ku2	40.3808	108.5486	2006	2006	OSH
49	CN-Lao	45.2786	127.5784	2004	2004	DNF
50	CN-Mao	45.38	127.53	2004	2004	DBF
51	CN-Pa1	41.14	121.9117	2005	2005	WET
52	CN-Qia	26.7333	115.0667	2003	2007	ENF
53	CN-Sa2	47.58	133.52	2005	2005	CRO
54	CN-Sa3	47.58	133.52	2005	2005	CRO
55	CN-San	34.35	100.55	2006	2006	GRA
56	CN-Tao	28.92	111.45	2003	2003	CRO
57	CN-Xgl	44.13	116.32	2004	2006	GRA
58	CN-Xi1	43.5544	16.2797	2006	2006	GRA
59	CN-Xi2	43.5528	116.6714	2006	2006	GRA
60	CN-Xip	33.35	113.91	2010	2010	DBF
61	CN-Xsh	21.95	101.2	2003	2007	EBF
62	CN-Yuc	36.83333	116.5667	2003	2007	CRO
63	CZ-BK1	49.5021	18.5368	2009	2011	ENF
64	CZ-BK2	49.4944	18.5429	2009	2011	GRA
65	CZ-wet	49.025	14.7722	2008	2009	WET
66	FR-Hes	48.6742	7.0656	2001	2006	DBF
67	FR-Mau	43.38528	1.292222	2008	2009	GRA
68	ID-Pag	-2.345	114.0364	2002	2005	EBF

69	IL-Yat	31.345	35.0515	2007	2009	ENF
70	IT-BCi	40.52375	14.95744	2008	2009	CRO
71	JP-HEF	42.98	141.38	2000	2000	ENF
72	JP-Mas	36.05397	140.0269	2001	2005	CRO
73	JP-MBF	44.38417	142.3186	2005	2005	DBF
74	JP-MMF	44.32194	142.2614	2004	2005	MF
75	JP-Tef	45.05	142.1	2002	2004	MF
76	JP-Tom	42.73697	141.5186	2001	2003	DNF
77	KR-Hnm	34.55	126.57	2004	2008	CRO
78	KR-Kw2	37.75	127.15	2006	2007	DBF
79	MA-PSO	2.966667	102.3	2003	2009	EBF
80	MN-Kbu	47.21	108.74	2003	2007	GRA
81	RU-Che	68.62	161.34	2003	2003	MF
82	RU-Tur	64.2	100.45	2004	2004	DNF
83	Th-Mae	14.57628	98.84389	2003	2004	MF
84	Th-Sak	14.49236	101.9163	2002	2003	EBF
85	TW-Chn	24.58333	121.4	2008	2008	ENF
86	UK-AMo	55.79167	-3.23889	2007	2010	WET
87	UK-Ham	51.15353	-0.8583	2011	2012	DBF
88	US-AR1	36.4267	-99.42	2010	2010	GRA
89	US-AR2	36.6358	-99.5975	2010	2010	GRA
90	US-ARM	36.6058	-97.4888	2007	2012	CRO
91	US-Bar	44.0646	-71.2881	2004	2006	DBF
92	US-Blo	38.8952	-120.633	2000	2006	ENF
93	US-Ced	39.8379	-74.3791	2008	2009	ENF
94	US-Cop	38.09	-109.39	2002	2007	GRA
95	US-Dia	37.6773	-121.53	2012	2012	GRA
96	US-Dix	39.9712	-74.4346	2007	2007	MF
97	US-Dk2	35.9736	-79.1004	2004	2005	DBF
98	US-Elm	25.5519	-80.7826	2009	2012	WET
99	US-Esm	25.4379	-80.5946	2009	2012	WET
100	US-Fmf	35.1426	-111.727	2006	2010	ENF
101	US-FR2	29.9495	-97.9962	2005	2005	WSA
102	US-FR3	29.94	-97.99	2005	2012	WSA
103	US-Fuf	35.089	-111.762	2007	2010	ENF
104	US-Fwf	35.4454	-111.772	2007	2010	GRA
105	US-GLE	41.3644	-106.239	2005	2012	ENF
106	US-Ha1	42.5378	-72.1715	2000	2011	DBF
107	US-Ho1	45.2041	-68.7402	2000	2008	ENF
108	US-Ho2	45.2091	-68.747	2005	2009	ENF
109	US-IB1	41.8593	-88.2227	2006	2008	CRO
110	US-IB2	41.8406	-88.241	2005	2007	GRA
111	US-KFS	39.0561	-95.1907	2008	2012	GRA
112	US-Kon	39.0824	-96.5603	2011	2012	GRA
113	US-KS2	28.6086	-80.6715	2004	2006	CSH
114	US-Los	46.0827	-89.9792	2006	2010	CSH
115	US-LPH	42.5419	-72.185	2003	2004	DBF
116	US-Me2	44.4523	-121.557	2002	2012	ENF
117	US-Me3	44.3154	-121.608	2004	2008	ENF
118	US-Me4	44.4992	-121.622	2000	2000	ENF
119	US-Me5	44.4372	-121.567	2001	2002	ENF
120	US-Me6	44.3232	-121.604	2011	2012	ENF
121	US-MMS	39.3231	-86.4131	2000	2010	DBF
122	US-MOz	38.7441	-92.2	2005	2009	DBF
123	US-MRf	44.6465	-123.552	2006	2010	ENF
124	US-NC1	35.8115	-76.7115	2005	2009	ENF
125	US-NC2	35.8031	-76.6679	2005	2010	ENF
126	US-Ne1	41.1651	-96.4766	2002	2012	CRO
127	US-Ne2	41.1649	-96.4701	2003	2012	CRO
128	US-Ne3	41.1797	-96.4397	2002	2012	CRO

129	US-NR1	40.0329	-105.546	2006	2012	ENF
130	US-Oho	41.5545	-83.8438	2005	2005	DBF
131	US-PFa	45.9459	-90.2723	2000	2012	MF
132	US-Ro1	44.7143	-93.0898	2007	2007	CRO
133	US-Ro3	44.7217	-93.0893	2007	2007	CRO
134	US-SdH	42.0693	-101.407	2005	2008	GRA
135	US-Seg	34.3623	-106.702	2007	2010	GRA
136	US-Ses	34.3349	-106.744	2007	2010	OSH
137	US-Skr	25.3646	-81.0779	2004	2009	EBF
138	US-Slt	39.9138	-74.596	2005	2011	DBF
139	US-Snd	38.0373	-121.754	2008	2010	GRA
140	US-SO2	33.3739	-116.623	2006	2006	CSH
141	US-SO4	33.3844	-116.64	2004	2006	CSH
142	US-SP1	29.7381	-82.2188	2008	2009	ENF
143	US-SRC	31.9083	-110.84	2009	2011	OSH
144	US-SRM	31.8214	-110.866	2004	2007	WSA
145	US-Syv	46.242	-89.3477	2002	2006	MF
146	US-Ton	38.4316	-120.966	2002	2011	WSA
147	US-Twt	38.1055	-121.652	2010	2010	CRO
148	US-UMB	45.5598	-84.7138	2004	2012	DBF
149	US-UMd	45.5625	-84.6975	2008	2012	DBF
150	US-Var	38.4133	-120.951	2001	2011	GRA
151	US-WCr	45.8059	-90.0799	2000	2012	DBF
152	US-Whs	31.7438	-110.052	2008	2012	OSH
153	US-Wkg	31.7365	-109.942	2005	2009	GRA
154	US-Wrc	45.8205	-121.952	2003	2011	ENF
155	ZA-Kru	-25.0197	31.4969	2007	2008	SAV

Chapter 4: Remote estimation of evapotranspiration for Australian seasonally water-limited ecosystems within an evapotranspiration-vegetation index framework

Abstract

Vegetation function, available energy and soil moisture (SM) availability are the principle controls for evapotranspiration (ET) from vegetated land surface. This is particularly pronounced at seasonally water-limited ecosystems in Australia. Using data from eight Australian seasonally water-limited ecosystems, I propose an ET-vegetation index framework, within which satellite retrieved land surface temperature (LST, serving as a proxy of available energy), together with MODIS EVI (Greenness index) and microwave SM (TG-SM), was used to estimate ET. At the site scale, TG-SM was evaluated against measured ET (R^2 : 0.59 ~ 0.90) and outperformed a land surface model and MODIS ET product. At the regional scale, TG-SM proved better than MODIS estimated ET by comparing to a global ET benchmark (R^2 = 0.87). These results show that the TG-SM model, as a purely remote sensing tool, can effectively contribute to diagnosing water consumption of Australian seasonally water-limited ecosystems due to climate variability.

4.1 Introduction

Evapotranspiration (ET) is a key component of water and energy exchange between terrestrial ecosystems and the atmosphere, which can account for as much as 60%, or more, of precipitation on land [*Oki and Kanae, 2006*]. Remote sensing is a promising tool to provide reasonable estimates of ET over large spatial scales [*Mu et al., 2011; Wang et al., 2007*].

Remote sensing methods can be grouped into: (1) thermal temperature-based surface energy balance models [e.g., *Nishida et al.*, 2003; *Yang and Shang*, 2013], and (2) models based upon vegetation indices (VIs) [e.g., *Mu et al.*, 2011; *Wang et al.*, 2007]. Thermal models are often very sensitive to the accuracy of remotely sensed surface temperature [*Wang and Dickinson*, 2012] whereas VI-based models can effectively avoid this problem by alleviating dependence on thermal imagery, although VI-based models can be limited by coarse resolution of meteorological inputs over large spatial scales [*Wang et al.*, 2007; *Yang et al.*, 2013]. VI-based models can further be grouped into: (1) empirical models employing VIs (e.g., enhanced vegetation index, EVI), land surface temperature (LST) or meteorological observations [*Glenn et al.*, 2010; *Wang et al.*, 2007] and (2) physical models based on the Penman-Monteith [*Leuning et al.*, 2008; *Mu et al.*, 2011] or Priestley-Taylor equations [e.g., *Guerschman et al.*, 2009] in which equation terms are parameterized using remotely sensed data. Empirical models are much simpler than physical ones which often require complex parametrization. However, empirical models can lack a theoretical framework, limiting their general applicability outside the locations where the models were developed and tested. Therefore, it is essential to propose a generic ET regimes framework as a function of VIs, which could help identify how VIs succeed or fail in estimating ET.

Classical hydrology defines energy-limited and water-limited ET regimes as a function of soil moisture (SM, inset in Figure 4.2). In the energy-limited ET regime (i.e., soil moisture is above a critical value θ_{crit}), water availability is not a limiting factor for ET; below the soil moisture content at the wilting point (θ_{wilt}), ET tends to zero; in the transitional interval between θ_{wilt} and θ_{crit} , water availability is the primary constraint on ET [*Salvucci*, 1997; *Seneviratne et al.*, 2010]. As vegetation indices are closely correlated with soil moisture [*Eamus et al.*, 2015; *Schnur et al.*, 2010; *Yang et al.*, 2014], it is natural to expect a similar framework between ET and VIs. Specifically, I hypothesize that ET will shift from extremely

water-limited to a transitional state and then to energy-limited as VI increases. Since EVI performs best amongst the various vegetation indexes in estimating ET [Yebra *et al.*, 2013], hereafter I will focus on EVI only.

Australia is largely arid to semi-arid and retains large areas of seasonally water limited ecosystems. Eddy covariance observations over these ecosystems provide a unique opportunity to verify the above hypothesis. Therefore, the main objectives of this research were (1) to develop an ET-EVI framework in seasonally water-limited ecosystems of Australia; (2) to develop a new VI model to estimate monthly ET based solely on remote sensing data; and (3) to evaluate this new model both across- and within-sites and at the regional scale, respectively, in comparison with a land surface model, the MOD16A2 ET product and a widely used global data-driven benchmark.

4.2 Data and Methods

4.2.1 Data

4.2.1.1 Flux Sites and Data Processing

Eight eddy covariance sites from the OzFlux network (<http://www.ozflux.org.au/>) were used in this study (Figure 4.1). These sites cover a spectrum of biomes across a range of climates in Australia, including savannas, grasslands, open shrublands and woody savannas (Figure 4.1, Figure 4.1) in temperate, sub-tropical and tropical climates. Climate regimes at these sites result in periodical seasonal oscillations between water and energy limitations [Shi *et al.*, 2014; Whitley *et al.*, 2011]. During the period of analysis, mean annual temperatures ranged from 17.4 °C at AU-Cap to 26.8 °C at AU-Ade and AU-Dry, and mean annual precipitation ranged between 1857 mm yr⁻¹ at AU-Ade and 346 mm yr⁻¹ at AU-Asm (Figure 4.1). The uneven temporal (intra-annual) distribution of precipitation leads to distinctive dry and wet seasons.

Although trees at AU-How can access to deep soil water [Cook *et al.*, 1998] and thus are mainly limited by light interception [Whitley *et al.*, 2011] in dry seasons, understory grasses do not persist during the dry season because of their annual habit [Whitley *et al.*, 2011] and some limitation on tree's stomatal conductance occurs in the dry season. Therefore, the AU-How site is still defined as a water-limited ecosystem. Gap-filling of carbon and water fluxes and meteorological forcing was performed using the dynamic integrated gap filling and partitioning for OzFlux (DINGO) system based on a feed-forward artificial neural network algorithm [Beringer *et al.*, 2007; Beringer *et al.*, 2016]. ET data in January, February and March 2008 at AU-Dry and ET data in November 2003 and October and November 2006 at AU-How were removed due to energy imbalance.

Table 4.1. Brief description of the eight flux tower sites used to develop and validate the TG-SM model, including site identifier (ID), site name (Site), latitude (Lat, °S), longitude (Long, °E), biome type (IGBP), data period, mean annual temperature (MAT, °C), mean annual precipitation (MAP, mm yr⁻¹) and mean annual radiation (Rad, W m⁻² s⁻¹). SAV denotes savannas; OSH denotes open shrublands; WSA denotes woody savannas; and GRA denotes grasslands.

ID	Site	Lat	Long	IGBP	Data period	MAT	MAP	Rad
AU-Ade	Adelaide River	-13.08	131.12	SAV	2007-2008	26.8	1857	503
AU-Asm	Alice Springs	-22.28	133.25	OSH	2011-2012	21.9	346	522
AU-Cap	Calperum	-34.00	140.59	OSH	2010-2012	17.4	363	422
AU-Da1	Daly Pasture	-14.06	131.32	GRA	2007-2012	25.4	1279	514
AU-Da2	Daly Uncleared	-14.16	131.39	SAV	2007-2012	26.3	1132	495
AU-Dry	Dry River	-15.26	132.37	SAV	2008-2012	26.8	1029	525
AU-How	Howard Springs	-12.50	131.15	WSA	2001-2012	26.6	1397	487
AU-Stp	Sturt Plains	-17.15	133.35	GRA	2008-2012	25.7	695	531

4.2.1.2 Remote Sensing Data

Seasonally water-limited ecosystems were classified using the Moderate Resolution Imaging Spectroradiometer (MODIS) land cover product (MCD12C1) in 2012 with a spatial resolution of 0.05° (Figure 4.1). Monthly EVI data were obtained from the MODIS vegetation index product (MOD13A3) at a 1 km spatial resolution [Huete *et al.*, 2002]. A central 3×3 km window was applied to extract EVI values around the flux tower following [Rahman *et al.*, 2005] and [Sims *et al.*, 2008]. Only EVI pixels with usefulness values not larger than 12, aerosol values less than 3 and cloud free were used to calculate the average. A value of 0.08 was subtracted from EVI values (scaled EVI) to remove soil background contamination [Ma *et al.*, 2013]. LST data were acquired from the monthly MOD11C3 product at a spatial resolution of 0.05° [Wan and Li, 1997]. A 3×3 km window was also applied to the readily available MOD16A2 ET product (8-day time-step, 1×1 km, <ftp://ftp.ntsg.umd.edu/pub/MODIS>). The extracted MODIS ET values were aggregated to a monthly time-step and then compared against the performance of the new model at the site level as a benchmark representative of physical remote sensing models. The yearly aggregation of the MOD16A2 product at a spatial resolution of $0.5 \times 0.5^\circ$ was also used to compare with the new model at the regional scale. The MODIS ET algorithm employs a remotely sensed model based on the Penman-Monteith approach and requires MODIS derived vegetation land cover, leaf area index, EVI and daily meteorological reanalysis data as inputs [Mu *et al.*, 2011; Mu *et al.*, 2007].

The daily Essential Climate Variable (ECV) soil moisture product ($0.25 \times 0.25^\circ$) from the European Space Agency's Water Cycle Multi-mission Observation Strategy and Climate Change Initiative projects was aggregated to a monthly time-step. The ECV soil moisture product is a new merged product combining soil moisture retrievals from both passive and active coarse resolution microwave sensors [Liu *et al.*, 2011; Liu *et al.*, 2012; Wagner *et al.*,

2012]. The ECV soil moisture product is also the first satellite-retrieved soil moisture product at the decade time-scale spanning from 1978 to 2013. The sensing depth of ECV soil moisture data is the top few centimeters on average [Dorigo *et al.*, 2015] but surface moisture can be closely related to the soil moisture in the upper ten centimeters because both are impacted by the weather during the preceding few days to weeks [Albergel *et al.*, 2008; Brocca *et al.*, 2011].

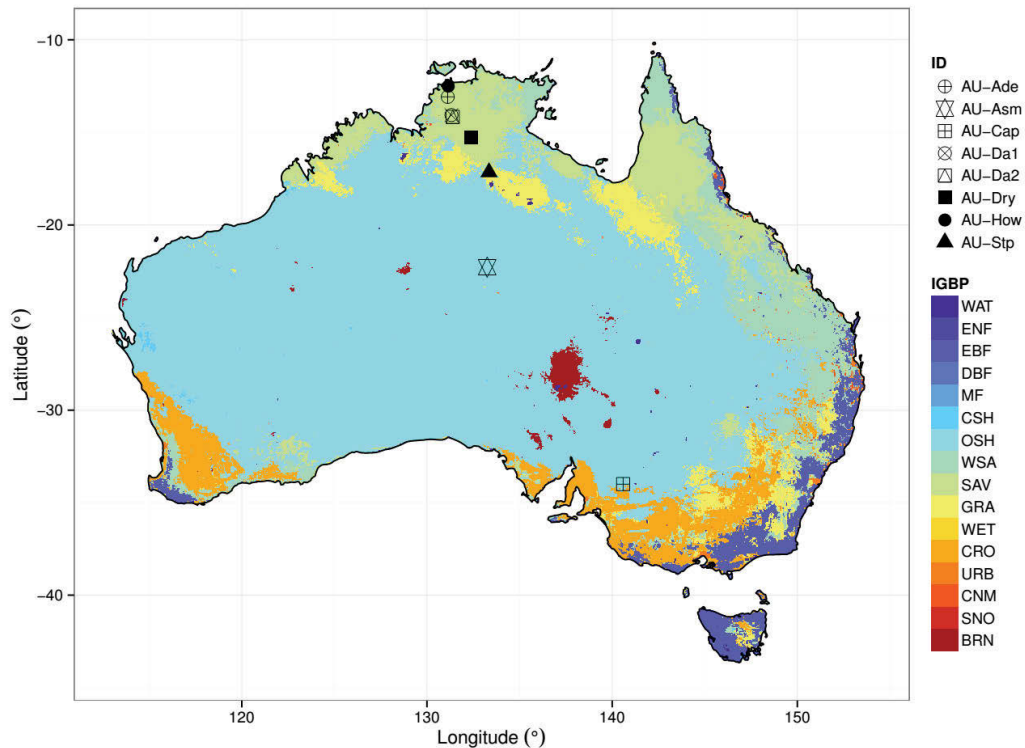


Figure 4.1. Spatial distribution of eight OzFlux sites. The IGBP land cover types in Australia are also shown. The acronyms WAT, ENF, EBF, DBF, MF, CSH, OSH, WSA, SAV, GRA, WET, CRO, URB, CNM, SNO and BRN denote water, evergreen needleleaf forest, evergreen broadleaf forest, deciduous broadleaf forest, mixed forest, closed shrublands, open shrublands, woody savannas, savannas, grasslands, wetlands, croplands, urban and built-up, cropland/natural vegetation mosaic, snow and ice and barren or sparsely vegetated, respectively.

4.2.1.3 Estimated ET from a Land Surface Model

A modified version [Haverd *et al.*, 2013] of the Community Atmosphere-Biosphere-Land Exchange (CABLE) model was used in the DINGO system [Beringer *et al.*, 2016] to simulate ET at these eight flux sites. The default soil module in CABLE v1.4 was replaced by the Soil-Litter-Iso model [Haverd and Cuntz, 2010] and the default carbon module was integrated with the CASA-CNP biogeochemical model [Wang *et al.*, 2010]. The modified CABLE was forced with prescribed LAI and disabled the nitrogen and phosphorous cycles [Haverd *et al.*, 2013]. The CABLE model calculates canopy transpiration as a linear combination of the water fluxes from the dry and wet portions of the canopy [Wang *et al.*, 2011], and transpiration is modelled using a coupled stomatal conductance-photosynthesis model [Leuning, 1990]. Soil evaporation in CABLE is calculated as a fraction of potential evaporation derived from a Penman-Monteith combination equation [Wang *et al.*, 2011]. The half-hourly CABLE ET outputs were further accumulated to a monthly time-step as a benchmark representative of complex biogeophysical models to evaluate the new model.

4.2.1.4 Global Benchmark Dataset

The global ET benchmark dataset was up-scaled from FLUXNET measurements using the model tree ensemble approach (MTE, Jung *et al.* [2009]). Input environmental variables for MTE consist of meteorological forcing, remotely sensed biophysical states of vegetation and biome types. This dataset is at a $0.5^\circ \times 0.5^\circ$ spatial resolution and has been widely used in evaluating land surface models and in climate change studies [e.g., Beer *et al.*, 2010; Bonan *et al.*, 2011]. Here I used the dataset from 2001 to 2011 to benchmark the performance of the new model at the regional scale.

4.2.2 Development of the ET-EVI Framework

By applying a three-segmented regression approach to investigate the ET-EVI relationship across the eight flux sites, two important EVI thresholds were determined that partitioned ET-EVI into three regimes (Figure 4.2), which correspond to the classical ET-soil moisture framework (inset in Figure 4.2). Below the lower threshold (scaled EVI = 0.09), vegetation was sparse with high radiation but low precipitation; conversely, above the higher threshold (scaled EVI = 0.27), dense vegetation was accompanied by high precipitation but low radiation (Figure 4.2). Linear regressions in the stage 1 of water-limited regime and the energy-limited regime interval showed that EVI could not significantly explain variations in ET. However, the reasons that EVI fails in estimating ET in these two intervals are different for each interval. In dry conditions (stage 1 in water-limited regime), soil evaporation tends to dominate ET when the surface is wet due to occurrences of light rain [Gong *et al.*, 2007], whereas EVI indicates canopy water content and thus can represent only transpiration effectively [Glenn *et al.*, 2010]. In energy-limited conditions, though transpiration comprises the major component of ET, lack of energy constrains the increase of ET and thus undermines the linear relationship between ET and EVI that characterized the transient interval (Figure 4.2). Therefore, an energy constraint was imposed on EVI and included a soil evaporation module in the EVI model to improve the accuracy of estimations of ET.

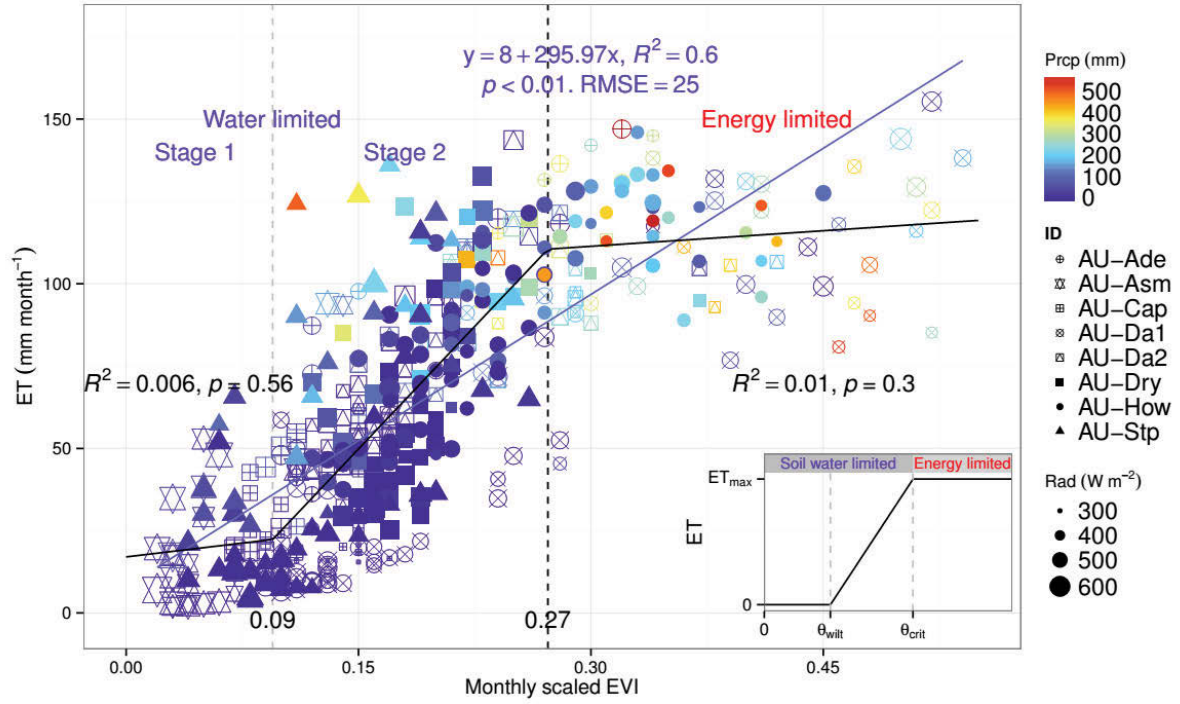


Figure 4.2. Scatterplots of measured monthly ET versus scaled monthly EVI across eight seasonally water- limited ecosystems in Australia. The inset is a conceptual diagram [Feddes *et al.*, 1978; Seneviratne *et al.*, 2010] defining energy-limited and water-limited ET regimes as a function of soil moisture (θ). θ_{wilt} is the “soil wilting point” and θ_{crit} is a critical soil moisture value. The black line represents a three-segment regression line. The coefficients of determination (R^2) and the significance values (p) for the stage 1 in water-limited domain and energy-limited domain are shown in black. The blue line is the linear regression line between ET and scaled EVI. The related regression equation and statistical values are shown in blue color.

4.2.3 A Simple EVI-Based ET Model

Based on the above analysis, ET can be given as a function of EVI:

$$ET = f(scaled_EVI, e) + E \quad (8.1)$$

where $scaled_EVI = EVI - 0.08$, e is the energy constraint factor, $f(scaled_EVI, e)$ indicates transpiration and E indicates soil evaporation. This equation takes the same form as the Penman-Monteith-Leuning (PML) model that calculates ET as the sum of canopy transpiration and soil evaporation [Leuning *et al.*, 2008]. Soil evaporation in the PML model occurs as a fraction of the equilibrium evaporation rate derived from the energy available at the soil surface [Leuning *et al.*, 2008]. Thus the form of soil evaporation in the model was:

$$E = f(A_s, f) \quad (8.2)$$

where A_s indicates the available energy at the soil surface and f indicates a fraction constraint on A_s . An advantage of this form is that it allows use of separate but unique variables to represent the energy constraint on transpiration and at the soil surface. LST was chosen to represent energy availability because LST reflects partitioning of surface energy [Price, 1990] and contains significant information about land surface evaporation [Caparrini *et al.*, 2004]. LST was directly used to represent A_s and investigated the relationship between ET and LST to determine e . Figure 4.3a shows the constraining effect of LST on ET, from which e can be defined as:

$$e = \min \left[\left(\frac{LST}{30} \right), (2.5 - 0.05 \times LST) \right] \quad (8.3)$$

where e obtains a maximum value of 1 at 30 °C and minimum value of 0 at 0 °C and 50 °C. This formula is the same as the LST scalar used in Sims *et al.* [2008] to estimate ecosystem gross primary productivity (GPP). Because carbon and water cycles are strongly coupled, it is thus not surprising that LST shows similar effects on ET and GPP.

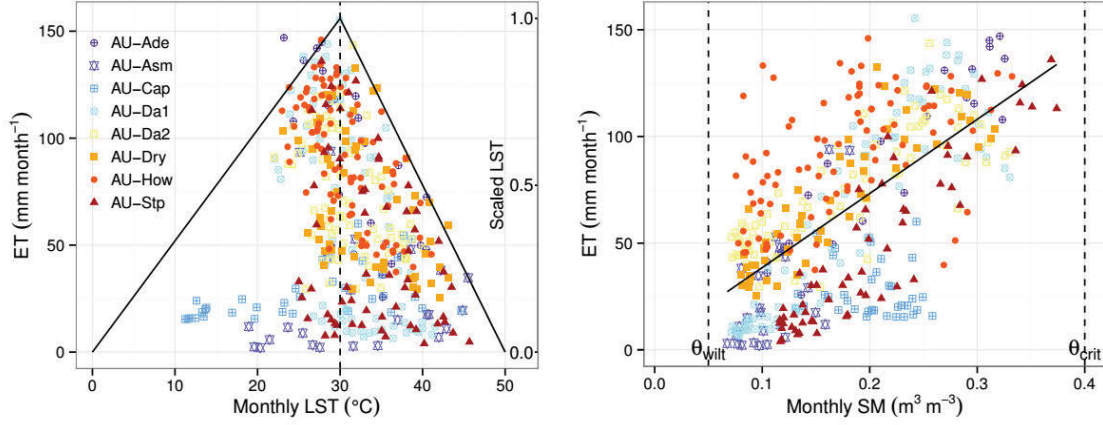


Figure 4.3. Regulation effects of land surface temperature (LST, a) and soil moisture (SM, b) on ecosystem observed ET across eight Australian seasonally water-limited sites.

The two-stage theory of bare soil evaporation suggests that, between soil wetting events, soil evaporation is governed mainly by energy availability in the first stage and then is limited by soil moisture [Salvucci, 1997]. Therefore, soil moisture was employed to define f . According to the linear regulating effect of soil moisture on ET between θ_{wilt} and θ_{crit} (Figure 4.3b), f is defined as

$$f = \begin{cases} 0, & \theta < \theta_{wilt} \\ \frac{\theta - \theta_{wilt}}{\theta_{crit} - \theta_{wilt}}, & \theta_{wilt} < \theta < \theta_{crit} \\ 1, & \theta > \theta_{crit} \end{cases} \quad (8.4)$$

where θ indicates microwave soil moisture, $\theta_{wilt} = 0.05 \text{ m}^3 \text{m}^{-3}$ and $\theta_{crit} = 0.40 \text{ m}^3 \text{m}^{-3}$. θ was scaled to $0 \sim 1$ where it is between θ_{wilt} and θ_{crit} .

Combining Equations 4.1-4.4 forms an ET model as a function of monthly LST, EVI (Greenness index) and SM data (TG-SM) which are all obtained from remote sensing measurements:

$$ET = \max(0, a \times scaled_EVI \times e + b \times LST \times f + \varepsilon) \quad (8.5)$$

where a (mm, transpiration per unit EVI) and b (mm, soil evaporation per degree LST) are coefficients and accounts for regression intercept. The TG-SM model was then regressed against observed ET across and within eight sites, respectively. The TG-SM model was also parametrized using data from only stage 1 of water-limited domain or energy-limited domain, respectively, to investigate its performance under hydrothermal limiting conditions. Further, the parametrized TG-SM models within biomes were used to estimate ET in seasonally water-limited ecosystems across Australia.

4.3 Results

4.3.1 Performance of the TG-SM Model across Sites

Compared with the linear regression between measured ET and EVI ($ET = 295.97 \times scaled_EVI + 8.0$, $R^2 = 0.60$ and $RMSE = 25.0 \text{ mm month}^{-1}$, Figure 4.2), the TG-SM model ($ET = \max(0, 240.4 \times scaled_EVI \times e + 6.9 \times LST \times f + 0.1)$) improved the estimation accuracy considerably ($R^2 = 0.72$ and $RMSE = 20.9 \text{ mm month}^{-1}$, Figure 4.5a). Larger improvements were achieved in the energy-limited regime and stage 1 in the water-limited regime and the predicted ET was significantly correlated with tower observed ET with R^2 values of 0.06 and 0.46 and RMSE of $19.3 \text{ mm month}^{-1}$ and $11.1 \text{ mm month}^{-1}$ (Figures 4.5b and 4.3c), respectively. In contrast, there was no significant relationship between ET and EVI in neither the energy-limited domain nor stage 1 in the water-limited domain (Figure 4.2). When TG-SM was parameterized independently at each site, modelled ET were better correlated to measured ET, with R^2 values of 0.87 across all three intervals, 0.32 in the energy-limited domain and 0.50 in the lower water-limited domain (Figure 4.4).

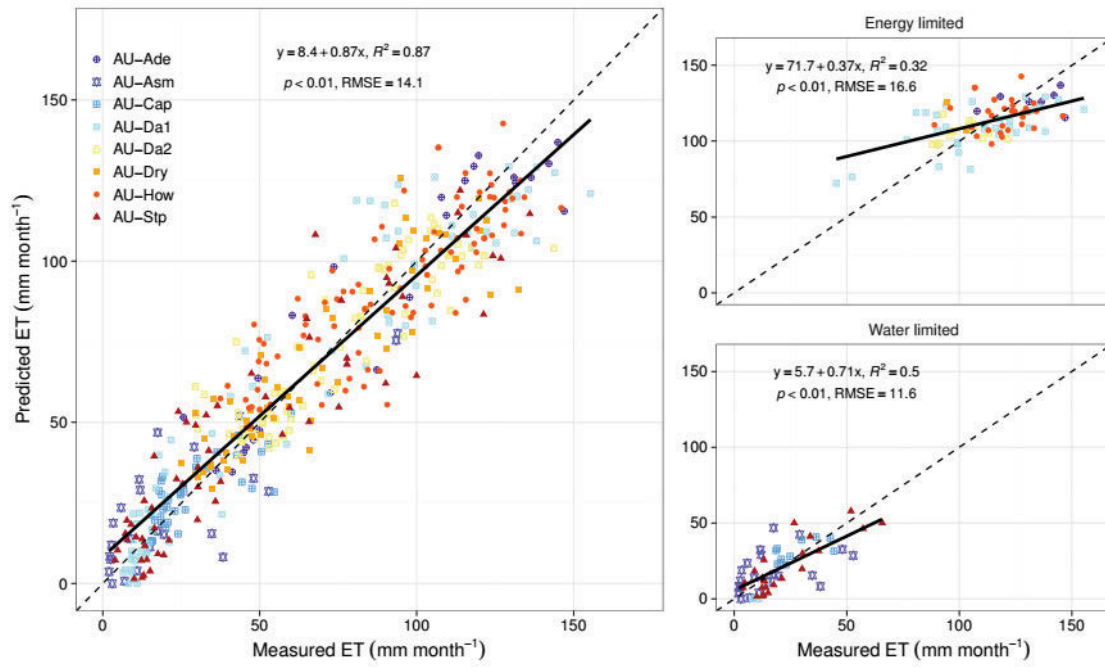


Figure 4.4. Comparison of predicted ET by TG-SM models fitted within each site with in-situ measured ET across all eight sites in Australia on a monthly basis.

4.3.2 Performance of the TG-SM Model within Sites

The TG-SM model successfully estimated monthly ET both at the arid sites (e.g., AU-Asm) and at relatively humid sites (e.g., AU-Da1). The only relatively poor performance was found at the AU-Cap site ($R^2 = 0.59$, $RMSE = 8.2 \text{ mm month}^{-1}$, $p < 0.01$). Compared to the CABLE simulation and the MOD16A2 product (Figures 4.5d, 4.5e and 4.5f, 4.6 and 4.7) the TG-SM model showed generally better performance. At the AU-Cap site, the R^2 value of the TG-SM model was slightly smaller than that of the CABLE model, but the RMSE value of the CABLE model was larger. Similarly, at the AU-How site, though the R^2 value of the MOD16A2 ET product was slightly larger than that of the TG-SM model, the RMSE value was almost two times larger than the RMSE of TG-SM. At other sites, the TG-SM model performed equally to or much better than the CABLE model and the MOD16A2 ET product (Figures 4.5d, 4.5e and 4.5f). However, the TG-SM model tended to underestimate ET when

ET was large but tended to overestimate ET when ET was small (Figures 4.5a, 4.5b, 4.5c and 4.5f). Systematic bias (shown as the slopes of the linear regressions in Figure 4.5f) ranged from 0.59 at AU-Cap to 0.92 at AU-Da1 and was 0.73 across all sites (Figure 4.5a).

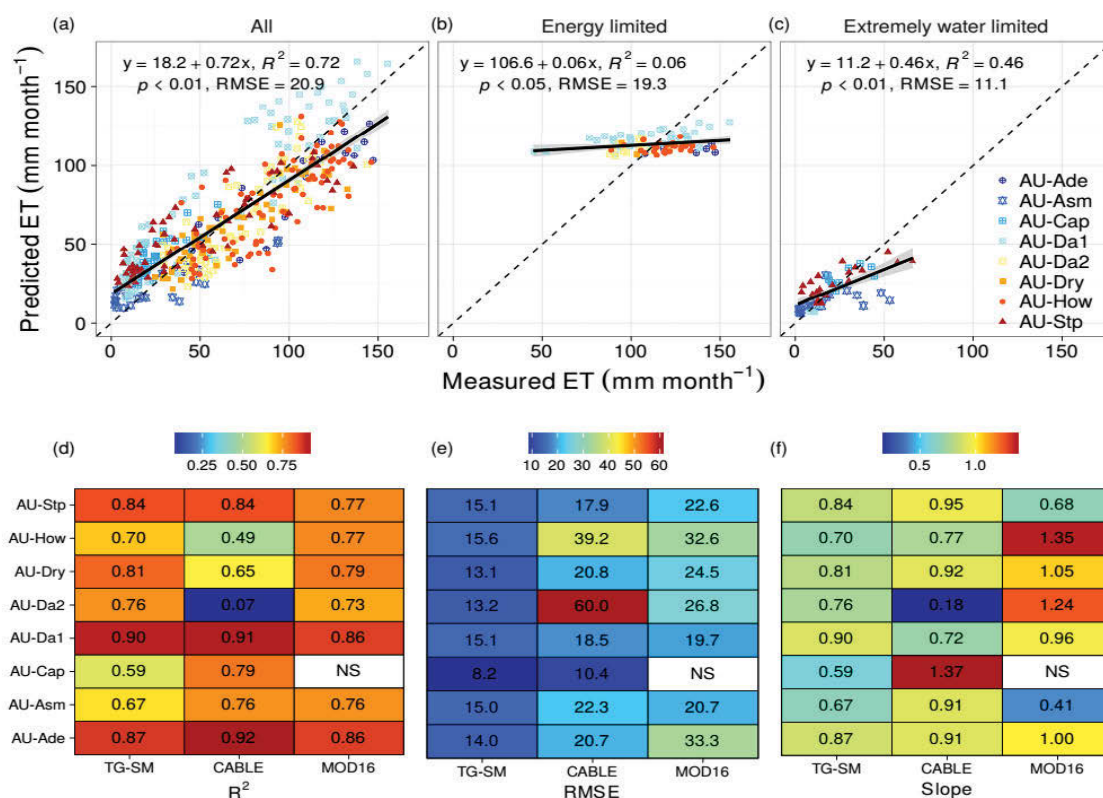


Figure 4.5. Comparison of predicted ET and measured ET across (top) and within (bottom) eight sites. (a) Performance of the model parametrized across all sites, (b) performance of the model parametrized in only the energy-limited domain, (c) performance of the model parametrized in only the extremely water-limited domain, and (d, e and f) coefficients of determination (R^2), RMSE (mm month⁻¹) and fitted slopes of TG-SM, CABLE or MOD16A2 predicted ET against measured ET at each site on a monthly time-scale. At AU-Cap, MOD16A2 ET was not significantly correlated with observed ET. At AU-Da2, CABLE ET was correlated with observed ET at a significant level of $p < 0.05$. All correlations between estimated and observed ET were significant with $p < 0.01$ except for the CABLE model at AU-Da2 ($p < 0.05$).

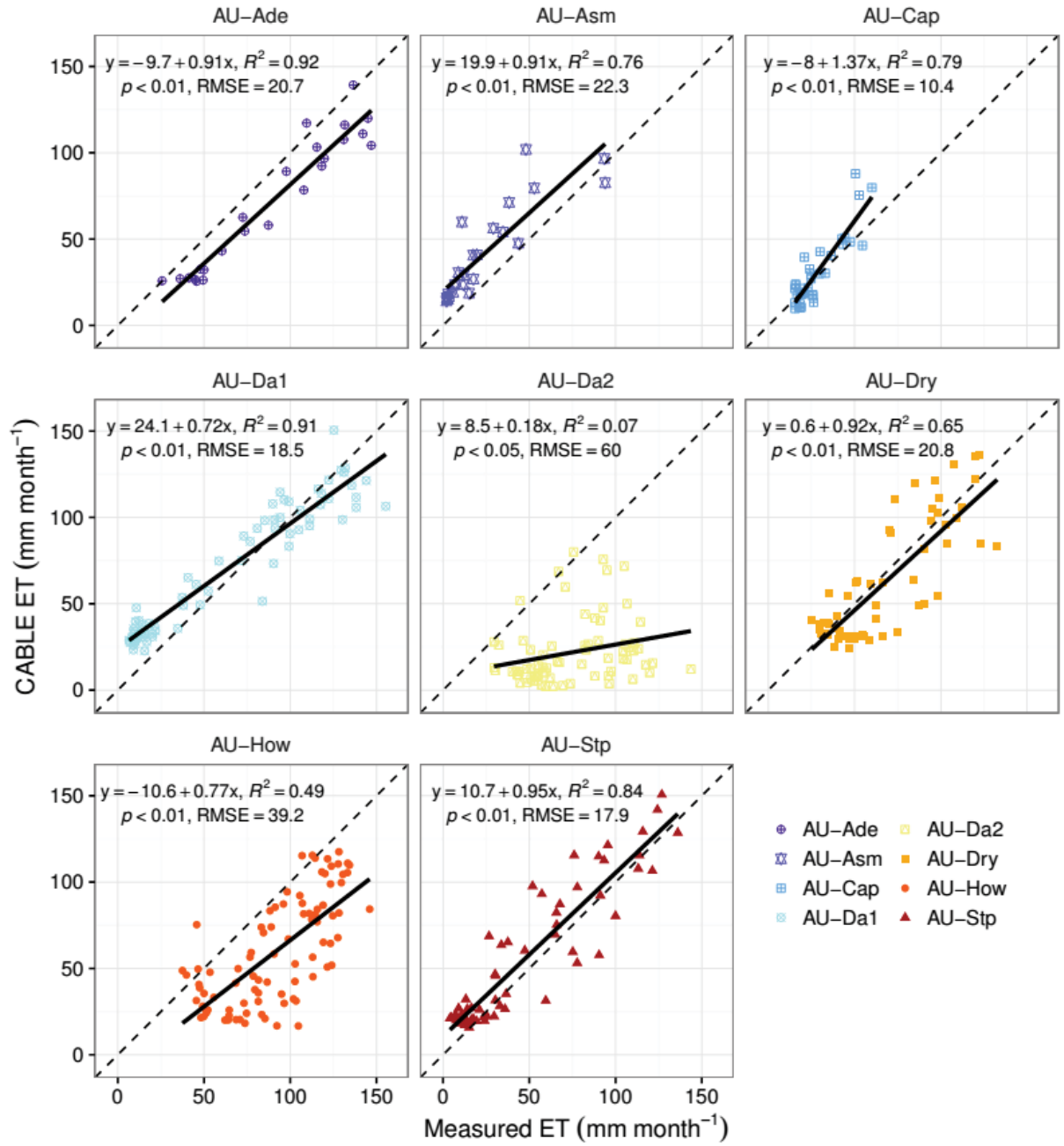


Figure 4.6. The performance of the CABLE model at each of the eight flux sites at a monthly time-scale.

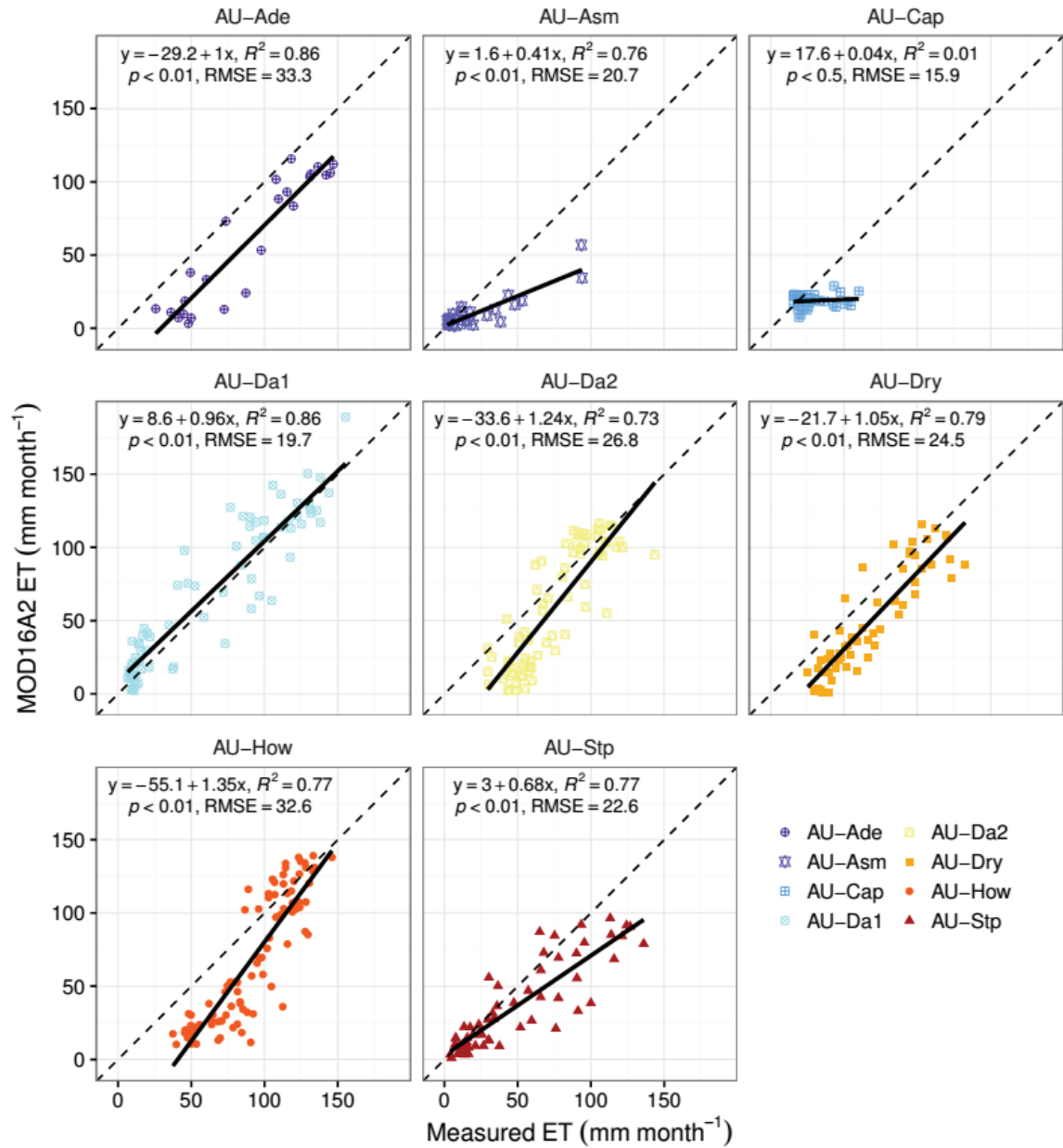


Figure 4.7. The performance of MOD16A2 ET product at each of the eight flux sites at a monthly timescale.

4.3.3 Performance of the TG-SM Model at the Regional Scale

The TG-SM model showed moderate agreement with ET-MTE in the mean annual spatial pattern of ET in Australian seasonally water-limited ecosystems during 2001-2011 (Figures 4.8a, 4.8c and 4.8d). The correlation analysis across all pixels resulted in a RMSE of 101.4

mm yr⁻¹ and R² of 0.87. Although MOD16A2 product obtained a slightly larger R² of 0.94, it obtained a larger RMSE of 111.7 mm yr⁻¹ against ET-MTE than TG-SM. Furthermore, MOD16A2 product systematically underestimated ET with a spatial annual mean bias of -100.3 mm yr⁻¹ (Figure 4.8). In contrast, the spatial annual mean for TG-SM (297.4 mm yr⁻¹) was close to that of ET-MTE (327.3 mm yr⁻¹) (Figure 4.8d). Overestimation of ET by TG-SM occurred mainly along the coast and some inland regions whereas for transition regions from coast to inland the TG-SM model slightly underestimated ET in contrast to ET-MTE (Figures 4.8a and 4.8c).

Temporally, ET estimated by the TG-SM model correlated with ET-MTE at almost all pixels with a p value less than 0.01 (Figure 4.8g). The strongest correlation occurred in North and East Australia whereas the correlation was moderate or weak in inland Australia (Figure 4.8e) and the mean R² value of all pixels was 0.55 (Figure 4.8h). The majority of RMSE values between TG-SM ET and ET-MTE were around 12 mm month⁻¹ (Figure 4.8f). The performance of the TG-SM model generally surpassed the MOD16A2 product, which failed to capture the temporal variation of ET-MTE in southern Australia (Figures 4.8i and 4.8k). The mean R² value (0.44, Figure 4.8l) of all pixels between MOD16A2 and ET-MTE was also smaller than that between TG-SM and ET-MTE.

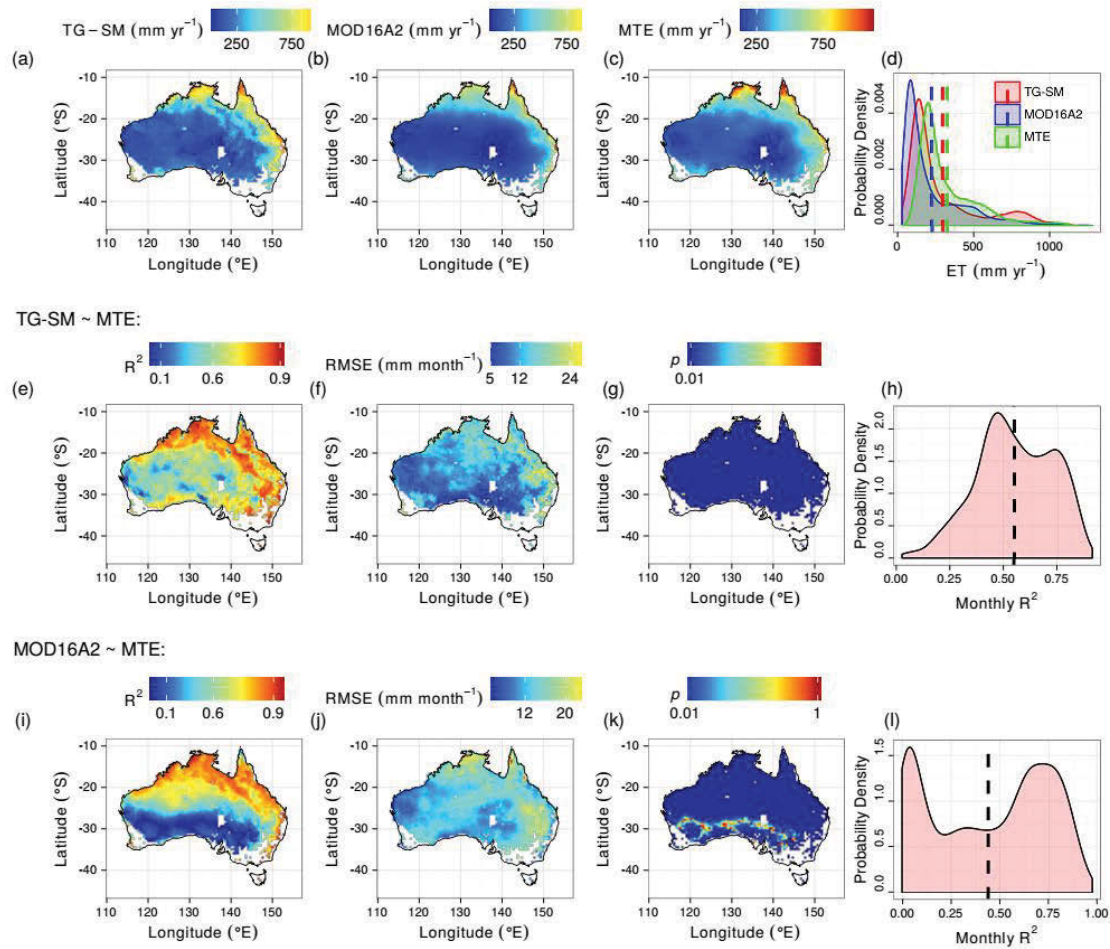


Figure 4.8. Spatial comparisons of mean annual TG-SM ET (a) and mean annual MOD16A2 ET (b) against mean annual ET-MTE (c) during 2001-2011. Figure 4.8d is the probability density distributions of spatial mean values. The red, blue and green dashed lines indicate spatial mean annual values for TG-SM, MOD16A2 and ET-MTE, respectively. Figures 4.8e, 4.8f and 4.8g are determination coefficients (R^2), RMSE and significant values of monthly TG-SM ET against monthly ET-MTE at the pixel level and Figure 4.8h is the probability density distribution of R^2 between TG-SM ET and ET-MTE. Figures 4.8i, 4.8j and 4.8k are determination coefficients, RMSE and significant values of monthly MOD16A2 ET against monthly ET-MTE at the pixel level and Figure 4.8i is the probability density distribution of R^2 between MOD16A2 ET and ET-MTE. Black dashed lines in Figures 4.8h and 4.8l indicate mean values of R^2 .

4.4 Discussion and conclusions

The parametrized TG-SM model at only eight flux sites worked well at the regional scale on a monthly time-step in comparison with ET-MTE and the complex physical model-based MOD16A2 product, suggesting the TG-SM model was both robust and contained a reasonable representation of the process of ET. However, one limitation of the framework is that it cannot apply over short time-scales (e.g., seconds to hourly), because changes in EVI are not rapid enough to capture short-term fluctuations in vegetation function and structure.

The application of LST as a proxy for available energy is necessary for scaling EVI as transpiration and for calculating soil evaporation. Variations in LST can be positively correlated with variations in vegetation and soil fractions in vegetated regions [*Sims et al.*, 2008], which will affect partitioning of ET from transpiration and soil evaporation. Furthermore, LST significantly correlates with air temperature, photosynthetically active radiation and vapor pressure deficit over a wide diversity of natural vegetation and thus is a good proxy for several important environmental variables [*Sims et al.*, 2008]. Although *Wu et al.* [2010] reported that air temperature instead of LST provided the best regulating effect on EVI in a vegetation index based carbon model [*Sims et al.*, 2008], LST cannot be substituted by air temperature because LST is available as continuous observations over large spatial scales but air temperatures are not.

Soil moisture provides an important constraint on ET because both evaporation and transpiration respond to variation in soil moisture [*Seneviratne et al.*, 2010]. Satellite retrieved soil moisture can sensitively respond to atmospheric forcing such as radiation and precipitation because the shallow sensing soil surface layer is directly exposed to air [*Wagner et al.*, 2007]. This characteristic makes satellite retrieved soil moisture appropriate to estimate soil evaporation because deeper soil layers are largely disconnected from shallow layers near

the surface in dry periods [Wang and Dickinson, 2012]. The ECV soil moisture data used in this study show moderate correlation with *in-situ* observations from global monitoring networks [Dorigo *et al.*, 2015]. Satellite retrievals of soil moisture can be a poor representation of measured soil water content (i) in densely vegetated regions due to attenuation of the satellite signal and radiation at the soil surface [Liu *et al.*, 2012] and (ii) because of gaps due to the interference of snow or frozen soil. However, over sparsely-to-moderately vegetated regions, the ECV soil moisture product is expected to provide reasonable estimates of upper soil moisture content [Liu *et al.*, 2012].

The lack of joint observations of both transpiration and soil evaporation introduces uncertainty in scaling LST and soil moisture, which potentially limits the applicability of the TG-SM model. The systematic bias of the TG-SM model was identified by overestimation of energy limitations when ET was high and by under-estimation of water stress when ET was low. Failure to partition trees and grasses at those sites where both trees and grasses grow also introduces uncertainty due to their distinct access to soil moisture reserves and differential contribution to fluctuations in leaf area [Whitley *et al.*, 2011]. Trees and grasses have different vegetation traits and display different responses to environmental changes which can affect their respective patterns of water use. All trees are C3 but some grasses, especially in central and northern Australia are C4, and these behave differently. Several studies reported that grasses consume water more aggressively [Bond, 2008], have larger maximum transpiration rates and more rapid depletion of available soil moisture than coexistent trees [Holdo and Brocato, 2015]. Even within different species of savanna trees, stomatal conductance shows differential response to watering [Holdo and Brocato, 2015]. These facts imply that using the same coefficient for EVI to represent transpiration of trees and grasses can significantly contribute to systematic bias in the TG-SM model. It is therefore important to understand how trees and grasses individually and jointly contribute to ET and observations of overstory and

understory canopy transpiration will help achieve this goal.

Although the TG-SM model was developed using seasonally water-limited sites, it has potential to be applied in non-water limited ecosystems of other types, such as forests and crops, assuming there is access to accurate soil moisture inputs. Since a separate soil evaporation item is explicitly incorporated, the TG-SM model theoretically can be applied to estimate ET of irrigated crops, as previously shown by *Wang et al.* [2007], who used a combination of net radiation, VI and temperature data. However, the application of the TG-SM model still needs testing and validation in ecosystems with various vegetation types and climate regimes in future.

By linking EVI to a classical ET-soil moisture framework, a similar ET-EVI framework was proposed. This framework provided insights into the behaviors of vegetation under contrasting energy and water conditions and thus can be used to guide the development of vegetation index based models for not only ET but also vegetation productivity. The TG-SM model in this study puts the ET-EVI framework into a practical outcome. Using a combination of EVI, LST and microwave soil moisture, the TG-SM model was proven better than the MODIS ET product in comparison to ET-MTE at seasonally water-limited ecosystems in Australia. Therefore, the TG-SM model can serve as a tool for estimating regional ET by using satellite images only, and contribute to diagnosing the vulnerability of seasonally water-limited ecosystems in Australia to climate variability.

Acknowledgments

This research was supported by an Australian Research Council Discovery Early Career Research Award (project number DE120103022). This work used eddy co- variance data acquired by the OzFlux community.

References

- Albergel, C., C. Rüdiger, T. Pellarin, J.-C. Calvet, N. Fritz, F. Froissard, D. Suquia, A. Petitpa, B. Piguet, and E. Martin (2008), From near-surface to root-zone soil moisture using an exponential filter: an assessment of the method based on in-situ observations and model simulations, *Hydrology and Earth System Sciences*, 12(6), 1323-1337.
- Beer, C., et al. (2010), Terrestrial Gross Carbon Dioxide Uptake: Global Distribution and Covariation with Climate, *Science*, 329(5993), 834-838.
- Beringer, J., L. B. Hutley, N. J. Tapper, and L. A. Cernusak (2007), Savanna fires and their impact on net ecosystem productivity in North Australia, *Global Change Biology*, 13(5), 990-1004.
- Beringer, J., I. Mchugh, L. B. Hutley, P. Isaac, and N. Kljun (2016), Dynamic INtegrated Gap-filling and partitioning for OzFlux (DINGO), *Biogeosciences Discussions*, 1-36.
- Bonan, G. B., P. J. Lawrence, K. W. Oleson, S. Levis, M. Jung, M. Reichstein, D. M. Lawrence, and S. C. Swenson (2011), Improving canopy processes in the Community Land Model version 4 (CLM4) using global flux fields empirically inferred from FLUXNET data, *Journal of Geophysical Research: Biogeosciences*, 116(G2).
- Bond, W. J. (2008), What Limits Trees in C4 Grasslands and Savannas?, *Annual Review of Ecology, Evolution, and Systematics*, 39(1), 641-659.
- Brocca, L., et al. (2011), Soil moisture estimation through ASCAT and AMSR-E sensors: An intercomparison and validation study across Europe, *Remote Sensing of Environment*, 115(12), 3390-3408.
- Caparrini, F., F. Castelli, and D. Entekhabi (2004), Estimation of surface turbulent fluxes through assimilation of radiometric surface temperature sequences, *Journal of Hydrometeorology*, 5(1), 145-159.
- Cook, P. G., T. J. Hatton, D. Pidsley, A. L. Herczeg, A. Held, A. O'Grady, and D. Eamus

- (1998), Water balance of a tropical woodland ecosystem, Northern Australia: A combination of micro-meteorological, soil physical and groundwater chemical approaches, *Journal of Hydrology*, 210(1&“4), 161-177.
- Dorigo, W. A., et al. (2015), Evaluation of the ESA CCI soil moisture product using ground-based observations, *Remote Sensing of Environment*, 162, 380-395.
- Eamus, D., S. Zolfaghar, R. Villalobos-Vega, J. Cleverly, and A. Huete (2015), Groundwater-dependent ecosystems: recent insights from satellite and field-based studies, *Hydrology and Earth System Sciences*, 19(10), 4229-4256.
- Feddes, R. A., P. J. Kowalik, and H. Zaradny (1978), *Simulation of field water use and crop yield*, Centre for Agricultural Publishing and Documentation.
- Glenn, E. P., P. L. Nagler, and A. R. Huete (2010), Vegetation Index Methods for Estimating Evapotranspiration by Remote Sensing, *Surveys in Geophysics*, 31(6), 531-555.
- Gong, D., S. Kang, L. Yao, and L. Zhang (2007), Estimation of evapotranspiration and its components from an apple orchard in northwest China using sap flow and water balance methods, *Hydrological Processes*, 21(7), 931-938.
- Guerschman, J. P., A. I. J. M. V. Dijk, G. Mattersdorf, J. Beringer, L. B. Hutley, R. Leuning, R. C. Pipunic, and B. S. Sherman (2009), Scaling of potential evapotranspiration with MODIS data reproduces flux observations and catchment water balance observations across Australia, *Journal of Hydrology*, 369(1&“2), 107-119.
- Haverd, V., and M. Cuntz (2010), Soil–Litter–Iso: A one-dimensional model for coupled transport of heat, water and stable isotopes in soil with a litter layer and root extraction, *Journal of Hydrology*, 388(3), 438-455.
- Haverd, V., M. R. Raupach, P. R. Briggs, J. G. Canadell, P. Isaac, C. Pickettheaps, S. H. Roxburgh, E. V. Goresl, R. A. V. Rossel, and Z. Wang (2013), Multiple observation types reduce uncertainty in Australia's terrestrial carbon and water cycles, *Biogeosciences*,

10(3), 2011-2040.

- Holdo, R. M., and E. R. Brocato (2015), Tree–grass competition varies across select savanna tree species: a potential role for rooting depth, *Plant Ecology*, 216(4), 577-588.
- Huete, A., K. Didan, T. Miura, E. P. Rodriguez, X. Gao, and L. G. Ferreira (2002), Overview of the radiometric and biophysical performance of the MODIS vegetation indices, *Remote Sensing of Environment*, 83(1), 195-213.
- Jung, M., M. Reichstein, and A. Bondeau (2009), Towards global empirical upscaling of FLUXNET eddy covariance observations: validation of a model tree ensemble approach using a biosphere model, *Biogeosciences*, 6(10), 2001-2013.
- Leuning, R. (1990), Modelling stomatal behaviour and and photosynthesis of *Eucalyptus grandis*, *Functional Plant Biology*, 17(2), 159-175.
- Leuning, R., Y. Q. Zhang, A. Rajaud, H. Cleugh, and K. Tu (2008), A simple surface conductance model to estimate regional evaporation using MODIS leaf area index and the Penman-Monteith equation, *Water Resources Research*, 44(10), W10419.
- Liu, Y. Y., R. M. Parinussa, W. A. Dorigo, R. A. M. De Jeu, W. Wagner, A. I. J. M. van Dijk, M. F. McCabe, and J. P. Evans (2011), Developing an improved soil moisture dataset by blending passive and active microwave satellite-based retrievals, *Hydrology and Earth System Sciences*, 15(2), 425-436.
- Liu, Y. Y., W. A. Dorigo, R. M. Parinussa, R. A. M. de Jeu, W. Wagner, M. F. McCabe, J. P. Evans, and A. I. J. M. van Dijk (2012), Trend-preserving blending of passive and active microwave soil moisture retrievals, *Remote Sensing of Environment*, 123, 280-297.
- Ma, X., A. Huete, Q. Yu, N. R. Coupe, K. Davies, M. Broich, P. Ratana, J. Beringer, L. Hutley, and J. Cleverly (2013), Spatial patterns and temporal dynamics in savanna vegetation phenology across the North Australian Tropical Transect, *Remote Sensing of Environment*, 139, 97-115.

- Mu, Q., M. Zhao, and S. W. Running (2011), Improvements to a MODIS global terrestrial evapotranspiration algorithm, *Remote Sensing of Environment*, 115(8), 1781-1800.
- Mu, Q., F. A. Heinsch, M. Zhao, and S. W. Running (2007), Development of a global evapotranspiration algorithm based on MODIS and global meteorology data, *Remote Sensing of Environment*, 111(4), 519-536.
- Nishida, K., R. R. Nemani, J. M. Glassy, and S. W. Running (2003), Development of an evapotranspiration index from Aqua/MODIS for monitoring surface moisture status, *Geoscience and Remote Sensing, IEEE Transactions on*, 41(2), 493-501.
- Oki, T., and S. Kanae (2006), Global hydrological cycles and world water resources, *science*, 313(5790), 1068-1072.
- Price, J. C. (1990), Using spatial context in satellite data to infer regional scale evapotranspiration, *Geoscience and Remote Sensing, IEEE Transactions on*, 28(5), 940-948.
- Rahman, A. F., D. A. Sims, V. D. Cordova, and B. Z. El-Masri (2005), Potential of MODIS EVI and surface temperature for directly estimating per-pixel ecosystem C fluxes, *Geophysical Research Letters*, 32(19).
- Salvucci, G. D. (1997), Soil and moisture independent estimation of stage-two evaporation from potential evaporation and albedo or surface temperature, *Water Resources Research*, 33(1), 111-122.
- Schnur, M. T., H. Xie, and X. Wang (2010), Estimating root zone soil moisture at distant sites using MODIS NDVI and EVI in a semi-arid region of southwestern USA, *Ecological Informatics*, 5(5), 400-409.
- Seneviratne, S. I., T. Corti, E. L. Davin, M. Hirschi, E. B. Jaeger, I. Lehner, B. Orlowsky, and A. J. Teuling (2010), Investigating soil moisture–climate interactions in a changing climate: A review, *Earth-Science Reviews*, 99(3–4), 125-161.

- Shi, H., L. Li, D. Eamus, J. Cleverly, A. Huete, J. Beringer, Q. Yu, E. v. Gorsel, and L. Hutley (2014), Intrinsic climate dependency of ecosystem light and water-use-efficiencies across Australian biomes, *Environmental Research Letters*, 9(10), 104002.
- Sims, D. A., et al. (2008), A new model of gross primary productivity for North American ecosystems based solely on the enhanced vegetation index and land surface temperature from MODIS, *Remote Sensing of Environment*, 112(4), 1633-1646.
- Wagner, W., V. Naeimi, K. Scipal, R. de Jeu, and J. Mart?nez-Fern??ndez (2007), Soil moisture from operational meteorological satellites, *Hydrogeology Journal*, 15(1), 121-131.
- Wagner, W., W. Dorigo, R. de Jeu, D. Fernandez, J. Benveniste, E. Haas, and M. Ertl (2012), Fusion of Active and Passive Microwave Observations to Create AN Essential Climate Variable Data Record on Soil Moisture, *ISPRS Annals of Photogrammetry, Remote Sensing and Spatial Information Sciences*, 315-321.
- Wan, Z., and Z.-L. Li (1997), A physics-based algorithm for retrieving land-surface emissivity and temperature from EOS/MODIS data, *Geoscience and Remote Sensing, IEEE Transactions on*, 35(4), 980-996.
- Wang, K., and R. E. Dickinson (2012), A review of global terrestrial evapotranspiration: Observation, modeling, climatology, and climatic variability, *Reviews of Geophysics*, 50(2).
- Wang, K., P. Wang, Z. Li, M. Cribb, and M. Sparrow (2007), A simple method to estimate actual evapotranspiration from a combination of net radiation, vegetation index, and temperature, *Journal of Geophysical Research: Atmospheres*, 112(D15), D15107.
- Wang, Y. P., R. M. Law, and B. Pak (2010), A global model of carbon, nitrogen and phosphorus cycles for the terrestrial biosphere, *Biogeosciences*, 7(7), 9891-9944.
- Wang, Y. P., E. Kowalczyk, R. Leuning, G. Abramowitz, M. R. Raupach, B. Pak, E. van

- Gorsel, and A. Luhar (2011), Diagnosing errors in a land surface model (CABLE) in the time and frequency domains, *Journal of Geophysical Research: Biogeosciences*, *116*(G1), G01034.
- Whitley, R. J., C. A. T. R. I. O. N. A. M. O. Macinnis-NG, L. B. Hutley, J. Beringer, M. Zeppel, M. Williams, D. Taylor, and D. Eamus (2011), Is productivity of mesic savannas light limited or water limited?: Results of a simulation study, *Global Change Biology*, *17*(10), 3130-3149.
- Wu, C., J. W. Munger, Z. Niu, and D. Kuang (2010), Comparison of multiple models for estimating gross primary production using MODIS and eddy covariance data in Harvard Forest, *Remote Sensing of Environment*, *114*(12), 2925-2939.
- Yang, Y., and S. Shang (2013), A hybrid dual-source scheme and trapezoid framework-based evapotranspiration model (HTEM) using satellite images: Algorithm and model test, *Journal of Geophysical Research: Atmospheres*, *118*(5), 2284-2300.
- Yang, Y., D. Long, and S. Shang (2013), Remote estimation of terrestrial evapotranspiration without using meteorological data, *Geophysical Research Letters*, *40*(12), 3026-3030.
- Yang, Y., D. Long, H. Guan, B. R. Scanlon, C. T. Simmons, L. Jiang, and X. Xu (2014), GRACE satellite observed hydrological controls on interannual and seasonal variability in surface greenness over mainland Australia, *Journal of Geophysical Research: Biogeosciences*, *119*(12), 2014JG002670.
- Yebra, M., A. Van Dijk, R. Leuning, A. Huete, and J. P. Guerschman (2013), Evaluation of optical remote sensing to estimate actual evapotranspiration and canopy conductance, *Remote Sensing of Environment*, *129*, 250-261.

Chapter 5. Identifying and optimizing key above- and below-ground processes for carbon assimilation and evapotranspiration in the CABLE model across Australian vegetation types

Abstract

Land surface models, as a critical component of global climate models, provide estimates of carbon, water and energy fluxes as the lower boundary conditions for climate prediction. Here I combined a global sensitive analysis method and a generic optimization framework to investigate key parameters and associated processes in an improved version (v2.0b, with dynamic root water uptake function and hydrological redistribution, HR) of the Australian Community Atmosphere-Biosphere Land Exchange (CABLE) model. My results showed that biochemical process (V_{max}) and the process of HR were most important for carbon assimilation across 10 OzFlux sites while HR as well as root depth were key determinants of evapotranspiration (ET). When optimized values of both above- and below-ground parameters were used, model performance was significantly improved, particularly during dry periods. In contrast there was very limited improvement if only optimized aboveground parameters were used. Further, I investigated effects of optimization at various time-scales and found a decrease of model performance from mesic to xeric sites at hourly to daily time-scales but not at the monthly timescale. However, soil water content was still poorly modeled even if the GPP and ET were reasonably estimated. These results suggest that below-ground processes such as HR and root water uptake are critical for LSMs in correctly capture vegetation responses to droughts and also highlights the challenges for LSMs to characterize variations of soil water content.

5.1 Introduction

After decades of evolution, current land surface models (LSMs) represent interactions between land surface and the atmosphere through a coupling of biophysical and biogeochemical processes with explicit partitions of vegetation and soil types [Pitman, 2003; Wang *et al.*, 2011]. As a key component of global climate models, LSMs provide the lower boundary conditions for climate and weather predictions, i.e., calculate available energy at the surface and its partitioning between sensible and latent heat (Q_{le}) fluxes, balance incoming water between evapotranspiration (ET, calculated by Q_{le} times a transform coefficient), runoff and soil water content (SWC), and estimate net ecosystem exchange (NEE) of CO_2 , which is critical to the development of our understanding of the future climate [Pitman, 2003]. Of these turbulent fluxes outputted by LSMs, most important are likely to be NEE and Q_{le} [Abramowitz *et al.*, 2008; Reichstein *et al.*, 2003] while SWC can be of central importance among slowly varying state variables of LSMs because it can have strong impacts on carbon uptake [Poulter *et al.*, 2014], Q_{le} and precipitation [Koster *et al.*, 2004]. It is important to note that NEE is calculated as the difference between gross primary productivity (GPP) and ecosystem respiration (RE, equal to nighttime NEE) in LSMs and GPP is tightly coupled with ET at the ecosystem scale [Beer *et al.*, 2009]. Therefore, for the purpose of identifying key processes in LSMs, I focus on GPP, Q_{le} , NEE and SWC. By convention, I use Q_{le} at hourly time-scale but use ET over daily to annual time-scales hereafter.

LSMs have been extensively evaluated [Li *et al.*, 2012; Ukkola *et al.*, 2016; Wang *et al.*, 2001], inter-compared [Boone *et al.*, 2009; Dirmeyer *et al.*, 2006] and benchmarked [Abramowitz *et al.*, 2008; Best *et al.*, 2015] for carbon, water and energy fluxes. Significant problems are identified as remaining within LSMs, including sub-grid-scale heterogeneity, biogeochemical cycles [Pitman, 2003] and particularly their limited ability to replicate the impacts of water stress [De Kauwe *et al.*, 2015; Egea *et al.*, 2011; Powell *et al.*, 2013]. Thus, improving the

performance of LSMs in circumstances of low water availability has been a priority task and this is gaining growing interest within the land modeling community, especially since droughts are widely expected to increase in both frequency and intensity [Allen *et al.*, 2010; Dai, 2013]. Efforts have been done in parametrizing both above- and below-ground component processes using either alternative model structures or parameter sets. Reichstein *et al.* [2003] applied an inverse modeling method to estimate drought effects on leaf stomatal conductance and ensuing changes in leaf photosynthetic capacities in three Mediterranean ecosystems. De Kauwe *et al.* [2015] incorporated drought sensitivities of different species to constrain stomatal conductance and photosynthetic biochemistry parameters (V_{cmax} and J_{max}). Ukkola *et al.* [2016] compared effects of alternative hydrological processes, leaf area index and soil properties on simulated Q_{le} and found that a more physically consistent parametrization of hydrology [Decker, 2015] could better capture responses of Q_{le} during precipitation deficits. While above efforts are of significant importance, the majority examine above- and below-ground processes separately and few attempt to revise bias induced by root water uptake functions [Li *et al.*, 2012] and associated SWC changes in LSMs. These problems result from the large number of parameters (typically 20-60 for each vegetation type) [Lu *et al.*, 2013; Wang *et al.*, 2011], lack of or difficulties in direct measurements of parameters involved in fine-scale processes (e.g., V_{cmax} and root density distribution, Reichstein *et al.* [2003]), and non-linearity between surface fluxes and model parameters [Wang *et al.*, 2001]. However, interactions between roots and soil water are important because plants take up water from soil in the root zone [De Kauwe *et al.*, 2015; Li *et al.*, 2012].

Model-data fusion techniques provide a systematic and rigorously analytical framework for identifying the best or most probable values and associated uncertainties of model parameters [Keenan *et al.*, 2011; Raupach *et al.*, 2005; Wang *et al.*, 2009]. The principle of model-data

fusion is iterative comparisons of model outputs using proposed parameter sets at each step with observed data. The objective is to minimize the cost function which is usually a metric of mismatch between a model and measurements [Raupach *et al.*, 2005; Wang *et al.*, 2009]. Model-data fusion methods have been successfully applied to estimate soil organic carbon pools [Ahrens *et al.*, 2014; Hararuk *et al.*, 2014], vegetation properties [Keenan *et al.*, 2012; Reichstein *et al.*, 2003; Richardson *et al.*, 2010], and propagation of model and data uncertainties [Keenan *et al.*, 2011]. These applications show that model-data fusion is a powerful tool to investigate critical parameters and processes in LSMs.

Here I use an adaptive Bayesian Markov-chain Monte Carlo framework to optimize both above- and below-ground parameters in an improved version of the Australian Community Atmosphere-Biosphere Land Exchange (CABLE, Wang *et al.* [2011]) model, which performs comparably with other major LSMs [Abramowitz *et al.*, 2007; Best *et al.*, 2015]. Different from the standard version, Li *et al.* [2012] incorporated a dynamic root water uptake function [Lai and Katul, 2000] and a hydraulic redistribution (HR) function [Ryel *et al.*, 2002], which significantly improved estimation of NEE, Q_{le} and SWC during dry seasons in three forest ecosystems. I select 23 parameters (Table 5.2) involved in vegetation photosynthesis and evapotranspiration processes. As not all these parameters can be well constrained by observed turbulent fluxes, I first use a global sensitivity analysis method to screen out parameters that are relatively insensitive. This filtering step can effectively avoid ill-conditioning [Tarantola, 2005] and decrease dimensions of parameter space in optimization [Lu *et al.*, 2013]. Then I conducted optimization at ten OzFlux sites, covering a diversity of vegetation types from xeric to mesic environments. Three simulations using default parameters (S-Def), above-ground parameters only (S-Abv) and all optimized parameters (S-Opt) were performed to identify effects of above- and belowground processes on GPP and Q_{le} . Therefore, the objectives of this study are to (1) identify both above- and below-ground key parameters and processes for

GPP and Q in LSMs, (2) optimize key parameters across different vegetation types, (3) gain insights about the coupling of GPP and ET, and (4) evaluate performance of optimization at different time-scales.

5.2 Data and Methods

5.2.1 Sites and Measurements

Ten sites from the OzFlux network (<http://www.ozflux.org.au>) were used in this study (Table 5.1). These sites cover a variety of biomes across a spectrum of climates in Australia, including savannas (SAV), woody savannas (WSA), open shrublands (OSH), crops (CRO), grasslands (GRA) and evergreen broad-leaf forests (EBF). Three savannas sites, Adelaide River (AU-Ade), Daly Uncleared (AU-Da2) and Dry River (AU-Dry), are located in northern Australia with a tropical climate. The dominant species are *Eucalyptus tectifica* and *Planchonia careya* in AU-Ade, Eucalypts and tussock in AU-Da2 and *Eucalyptus tetradonta*, *Eucalyptus terminalis* and *Eucalyptus dichromophloia* in AU-Dry [Beringer et al., 2011]. Howard Springs (AU-How) is the woody savanna site dominated by tree species *Eucalyptus miniata* and *Eucalyptus tentrodonata* and Sorghum tall grass [Eamus et al., 2001]. Two open shrublands sites are Alice Springs (AU-Asm) located in central Australia and Calperum (AU-Cap) in southeastern Australia. The AU-Asm site is a Mulga woodland [Cleverly et al., 2013] and the AU-Cap site is dominated by mallee trees and various shrubs [Meyer et al., 2015]. The crop site, Yanco (AU-JXA), is located in the western plains of southeastern Australia [Smith et al., 2012]. The Sturt Plains (AU-Stp) site lies in a low plain dominated by Mitchell grass [Beringer et al., 2011]. Two evergreen broad-leaf forests, Tumbarumba (AU-Tum) and Wombat (AU-Wom) are both located in southeastern Australia. The Forest at AU-Tum is classified as wet sclerophyll dominated by *Eucalyptus delegatensis* [van Gorsel et

al., 2013] and the Wombat site (AU-Wom) is a secondary regrowth forest dominated by *Eucalyptus obliqua*, *Eucalyptus radiata* and *Eucalyptus rubida* [Griebel *et al.*, 2016].

Table 5.1. Eddy covariance data used in this study. Information includes site name (Site), latitude (Lat), longitude (Lon), vegetation type (IGBP), data observed period, mean annual temperature (MAT, °C), mean annual radiation (MAR, $W m^{-2}$), mean annual precipitation (MAP, $mm y^{-1}$) and reference citation

Site	Lat	Lon	IGBP	Period	MAT	MAR	MAP	Reference
Adelaide River (AU-Ade)	-13.08	131.12	SAV	2007-2008	26.8	239.7	1852	<i>Beringer et al. [2011]</i>
Alice Springs (AU-Asm)	-22.28	133.25	OSH	2011-2012	21.9	255.2	335	<i>Cleverly et al. [2013]</i>
Calperum (AU-Cap)	-34.00	140.59	OSH	2010-2012	17.4	210.6	335	<i>Meyer et al. [2015]</i>
Daly Uncleared (AU-Da2)	-14.16	131.39	SAV	2007-2009	26.4	246.2	882	<i>Beringer et al. [2011]</i>
Dry River (AU-Dry)	-15.26	132.37	SAV	2009-2010	28.1	254.4	935	<i>Beringer et al. [2011]</i>
Howard Springs (AU-How)	-12.50	131.15	WSA	2001-2002	26.5	232.2	1193	<i>Eamus et al. [2001]</i>
Yanco (AU-JXA)	-35.00	146.29	CRO	2012	16.4	203.0	301	<i>Smith et al. [2012]</i>
Sturt Plains (AU-Stp)	-17.15	133.35	GRA	2008-2010	26.3	256.2	623	<i>Beringer et al. [2011]</i>
Tumbarumba (AU-Tum)	-35.66	148.15	EBF	2001-2003	8.2	192.1	1013	<i>van Gorsel et al. [2013]</i>
Wombat (AU-Wom)	-37.42	144.09	EBF	2010-2012	11.1	181.2	1059	<i>Griebel et al. [2016]</i>

Half-hourly eddy covariance measurements of carbon, water and energy fluxes and auxiliary observations of meteorological and soil variables at these ten sites were collected and processed using the dynamic integrated gap filling and partitioning for OzFlux (DINGO) system based on a feed-forward artificial neural network algorithm [Beringer *et al.*, 2007; Shi *et al.*, 2014]. MOD15A2 leaf area index (LAI, at 8-day time-step and 1 km resolution) at ten sites during the study periods were interpolated into half-hourly time-step as inputs.

5.2.2 The CABLE Model

The CABLE (version 2.0b) model is a global land surface model that allows for interactions between micro-climate, plant physiology and hydrology [Kowalczyk *et al.*, 2006]. It can simulate momentum, heat, water and carbon exchange between the land surface and the lower atmosphere [Kowalczyk *et al.*, 2006; Wang *et al.*, 2011]. Here key processes are described for GPP and ET in an improved version of the CABLE model incorporating a root water uptake function, assuming root water uptake efficiency as a function of rooting depth, and a hydraulic redistribution function [Li *et al.*, 2012]. A one-layered, two-leaf (sunlit and shaded) canopy model is used to calculate canopy carbon assimilation and transpiration through coupling of stomatal conductance, photosynthesis and transpiration [Wang and Leuning, 1998; Wang *et al.*, 2011]. Potential transpiration ($E_{c,i}^*$) without soil moisture limit for the sunlit leaf ($i = 1$) or the shaded leaf ($i = 2$) is modelled as:

$$\lambda E_{c,i}^* = \frac{s R n_{c,i} + c_p \rho_a D_a (G_{h,i} + G_{r,i})}{s + \gamma (G_{h,i} + G_{r,i}) / G_{w,i}} \quad (12.1)$$

photosynthesis-gas diffusion and photosynthesis-biochemistry are calculated as:

$$A_{c,i} = b_{sc} G_{s,i} (C_{s,i} - C_i) = G_{c,i} (C_a - C_i) \quad (12.2)$$

$$A_{c,i} = \min(V_{J,i}, V_{c,i}, V_{p,i}) - R_{d,i} \quad (12.3)$$

and stomatal conductance is represented as:

$$G_{s,i} = G_{0,i} + \frac{a_1 f_w A_{c,i}}{(C_{s,i} - \Gamma)(1 + D_{s,i} / D_0)} \quad (12.4)$$

where λ is the latent heat of vaporization ($J kg^{-1}$), $R n_{c,i}$ is the net available energy partitioned into latent and sensible heat fluxes, s is the slope of the curve relating saturation water vapor to temperature, γ is the psychrometric constant, c_p is the specific heat, and ρ_a is the air density.

D_a and $D_{s,i}$ are vapor pressure deficit in the ambient air and at the leaf surface, respectively. $G_{w,i}$, $G_{h,i}$ and $G_{r,i}$ are conductances for water, heat and radiation, respectively. $A_{c,i}$ is the net photosynthesis rate, b_{sc} is the ratio of diffusivity of CO₂ and H₂O through the stomata, $G_{s,i}$ and $G_{0,i}$ ($G_{s,i}$, when $A_{c,i} = 0$) are the bulk stomatal and residual conductance for water vapor, and $G_{c,i}$ is the total conductance from the inter-cellular space of the leaves to the reference height above the canopy for CO₂. $C_{s,i}$, C_a and C_i are CO₂ mole fractions at the leaf surface, in the ambient air and leaf inter-cellular spaces, respectively. $\min(V_{J,i}, V_{c,i}, V_{p,i})$ and $R_{d,i}$ indicate net carboxylation rate and day respiration rate, respectively, where $V_{J,i}$, $V_{c,i}$ and $V_{p,i}$ are the RuBP-limited, Rubisco-limited and sink-limited carboxylation rates. a_1 and D_0 are two empirical constants, and Γ is the CO₂ compensation point of photosynthesis. f_w is an empirical parameter describing soil water stress on stomatal conductance and is calculated, in the improved version of CABLE, as:

$$f_w = \min(1.0, \max(1.0e-4, \alpha_{2,m})) \quad (12.5)$$

where $m = 1, \dots, 6$ is the number of soil layer and $\alpha_{2,m}$ is calculated as:

$$\alpha_{2,m} = \max \left(1.0e-4, \left(\frac{\theta_m - \theta_{wilt}}{\theta_s} \right)^{\gamma_r / \max(1.0e-3, \theta_m - \theta_{wilt})} \right) \quad (12.6)$$

where θ_m , θ_{wilt} and θ_s are soil water content in soil layer i , soil water content at wilting point and saturated soil moisture content, respectively, and γ_r is an empirical constant.

The actual evapotranspiration (λE) is calculated as the sum of transpiration from both dry (λE_{dry}) and wet (λE_{wet}) canopy and evaporation (E_s) from the soil:

$$\lambda E = (1 - f_{wet}) \lambda E_{dry} + f_{wet} \lambda E_{wet} + \lambda E_s \quad (12.7)$$

where $f_{wet} \in [0, 1]$ is used to indicate the canopy wet fraction. E_{wet} , E_s , and E_{dry} are all based on

Equation 5.1 while the calculation of E_{dry} needs considering root water uptake from soil layers.

That is:

$$E_{dry} = \sum_{m=1}^n \min((1 - f_{wet})\eta_m E_{dry}^*, 1000(\theta_m - \theta_{wilt})\Delta z / \Delta t) \quad (12.8)$$

where E_{dry}^* is the potential transpiration of dry canopy calculated using Equation 5.1, Δz is the thickness of soil layer m , Δt is the time step of CABLE, and η_m is the fraction of E_{dry}^* extracted from soil layer m . In the improved version of CABLE, η_m is calculated using root water uptake function by *Lai and Katul* [2000] as:

$$\eta_m = \frac{f_{root,m} \alpha_{1,m} \alpha_{2,m}}{\sum_{m=1}^n f_{root,m} \alpha_{1,m} \alpha_{2,m}} \quad (12.9)$$

where $f_{root,m}$ is the fraction of root mass in soil layer m and is formulated according to *Gale and Grigal* [1987] and *Jackson et al.* [1996] as:

$$\sum_{m=1}^n f_{root,m} = 1 - \beta_r^{z_n} \quad (12.10)$$

where $\sum_{m=1}^n f_{root,m}$ indicates the cumulative root fraction from soil layer 1 to soil layer n , β_r is the “extinction coefficient” for vertical root biomass distribution, and z_n is the depth of soil layer n . $\alpha_{1,m}$ is calculated as:

$$\alpha_{1,m} = \max(1.0e - 4, \frac{\theta_m}{\theta_s - \theta_{wilt}}) \quad (12.11)$$

Soil water content at each layer (θ_m) is modelled as:

$$\frac{\partial \theta}{\partial t} = -\frac{\partial q}{\partial z} - E_{dry} - E_s + H \quad (12.12)$$

where q is the kinematic moisture flux between soil layers and H is water flux from hydraulic redistribution. q is represented as:

$$q = -D \frac{\partial \theta}{\partial z} + K \quad (12.13)$$

$$D = \frac{K \partial \psi}{\partial \theta} \quad (12.14)$$

$$K = K_{sat} \sqrt{\frac{\theta_m - \theta_r}{\theta_s - \theta_r}} \left(1 - \left(1 - \left(\frac{\theta_m - \theta_r}{\theta_s - \theta_r} \right)^{\frac{\nu-1}{\nu}} \right)^{\frac{\nu-1}{\nu}} \right)^2 \quad (12.15)$$

$$\psi = -\frac{1}{\alpha} \left(\left(\frac{\theta_m - \theta_r}{\theta_s - \theta_r} \right)^{\frac{\nu}{\nu-1}} - 1 \right)^{\frac{1}{\nu}} \quad (12.16)$$

and H_m for soil layer m redistributed from soil layer k ($k \neq m$) is represented as:

$$H_m = C_{RT} \sum_{k=1}^n (\psi_m - \psi_k) \max(c_m, c_k) \frac{f_{root,m} f_{root,k}}{1 - f_{root,x}} \delta_T \quad (12.17)$$

$$c_m = \frac{1}{1 + \left(\frac{\psi_m}{\psi_{50}} \right)^b} \quad (12.18)$$

where D is soil moisture diffusivity, K is hydraulic conductivity, ψ is soil matrix potential, ψ_{50} is the soil water potential when soil-root conductance decreases by 50%, and θ_r is the residual soil water content. C_{RT} is the maximum radial soil-root water conductance of the entire active root system, c_m represents the constraint of soil water potential on soil-root conductance, and $\delta_T = 0$ during day time and $\delta_T = 1$ during nighttime. $f_{root,x}$ is equal to $f_{root,m}$ when $\theta_m > \theta_k$, otherwise $f_{root,x}$ is equal to $f_{root,k}$. α, ν and b are empirical parameters.

Equations 5.1 – 5.18 describe the key processes for GPP, ET and root water uptake in the CABLE model. In this study, I tested a total of 23 parameters involved in these equations (Table 5.2). Because C_3 and C_4 plants have different photosynthetic pathways, parameters for

both C_3 and C_4 were denoted separately. For example, G_0 was denoted as G_{03} for C_3 plant and G_{04} for C_4 plant, respectively (Table 5.2). All CABLE runs were forced with prescribed LAI and without activation of nitrogen and phosphorus cycles.

5.2.3 Sensitivity Analysis

Land surface models generally have several hundred parameters, of which many are not well constrained by current measurements [Lu *et al.*, 2013] and thus a variety of optimization methods are used to tune them [e.g., Beven and Freer, 2001; Keenan *et al.*, 2012; Wang *et al.*, 2001]. However, the efficiency of optimization algorithms can decrease exponentially with the increasing number of parameters [Zhang *et al.*, 2015]. Taking the long simulation of land surface models into account, the computational cost of optimization will be extremely high or even unacceptable in high-dimension parametric space. This cost is particularly uneconomical for those inherently serial algorithms in which the current model state depends on the previous one. In addition, limited measurements cannot provide effective boundary conditions for all parameters and those poorly constrained parameters will not converge or will be ill-conditioned in the optimization [Beven and Freer, 2001; Keenan *et al.*, 2012; Tarantola, 2005; Wang *et al.*, 2001]. Therefore, it is essential to reduce the parameter dimension and identify parameters sensitive to available measurements.

I used the Morris method [Campolongo *et al.*, 2007; Morris, 1991], a global sensitivity analysis approach, to screen out the sensitive parameters. Assuming a k -dimension parameter input X_i , $i = 1, \dots, k$, the Morris method partitions the range of each parameter into p levels and thus produces a k -dimensional p -level grid, Ω . Each dimension of Ω is normalized into $0 \sim 1$ and then transformed to the actual distribution when input into the model [Campolongo *et al.*, 2007]. For a given \mathbf{X} , the Morris method varies one factor at a time (OAT) by a predetermined

multiple of $1/(p-1)$ to calculate the impact of that factor on output. This impact is called elementary effect and can be represented as:

$$d_i(\mathbf{X}) = \frac{y(X_1, X_2, \dots, X_{i-1}, X_i + \Delta, X_{i+1}, \dots, X_k) - y(\mathbf{X})}{\Delta} \quad (12.19)$$

where $\mathbf{X} \in \Omega$, $X_i \leq 1-\Delta$ and $\Delta = p/[2(p-1)]$ when p is even [Morris, 1991]. In OAT based experiment design, the Morris method first randomly samples a start parameter set $S_0(\mathbf{X})$ from Ω and then generates another parameter set $S_i(\mathbf{X})$ by increasing the i th parameter by Δ until all parameters are varied once. In doing so, the procedure produces $k+1$ parameter sets $S_i(\mathbf{X})$, $i = 0, 1, \dots, k$ and can yield k elementary effects, one per parameter. The combination of these $k+1$ parameter sets constitutes a trajectory. To determine which parameter has effects that are negligible, linear and additive, nonlinear, or involved in interactions with other inputs, r (generally $10 \sim 50$) trajectories are suggested to calculate the mean (μ) and the standard deviation (σ) of the elementary effects of each parameter [Campolongo et al., 2007; Morris, 1991]. Because elementary effects of a parameter can have different signs, the absolute value of μ is recommended [Campolongo et al., 2007] and thus the following can be defined:

$$\mu_i^* = \sum_{j=1}^r \frac{|d_{ij}(\mathbf{X})|}{r} \quad (12.20)$$

$$\sigma_i = \sqrt{\frac{\sum_{j=1}^r (d_{ij}(\mathbf{X}) - \mu_i)^2}{r}} \quad (12.21)$$

where $d_{ij}(\mathbf{X})$ indicates the elementary effect of the i th parameter in the j th trajectory, μ_i is the mean of $d_{ij}(\mathbf{X})$, μ_i^* is the mean of the absolute values of $d_{ij}(\mathbf{X})$, and σ_i is the standard deviation of $d_{ij}(\mathbf{X})$. Furthermore, a sensitivity index s_i using μ_i^* and σ_i is defined as:

$$s_i = \sqrt{\mu_i^{*2} + \sigma_i^2} \quad (12.22)$$

The Morris method provides a good compromise between accuracy and efficiency [Campolongo *et al.*, 2007; Lu *et al.*, 2013]. Employing this method, I assessed sensitivities of GPP and ET to 23 parameters (Table 5.2) in CABLE at ten sites, respectively. At all sites, p was set to 6 and $y(\mathbf{X})$ was equal to mean values of GPP or ET during the simulation period. Meanwhile, a generic Ω (ranges of parameters in Table 5.2) was used at all sites. Using the mean values of GPP or ET as $y(\mathbf{X})$ and the same *priori* can enable direct comparisons of parameter sensitivities at different sites with differed number of observations. 200 trajectories were sampled to obtain enough effective elementary effects because some trajectories were not valid to make the simulation converge, and the first 30 effective elementary effects were used to calculate the sensitivity index of each parameter. At each site, an arbitrary threshold of 80% quantile was used to rank all sensitivity indices and only parameters above the threshold were considered to be important.

Table 5.2. Definitions and ranges of CABLE parameters in sensitivity analysis

Parameter	Definition	Min	Max
X	A parameter in the leaf inclination angle distribution (dimensionless)	-1.0	0.50
V_{cmax}	Maximum RuBP carboxylation rate at canopy top at a leaf temperature of 25 °C ($\mu mol\ m^{-2}\ s^{-1}$)	5.0e-6	1.8e-4
a_{13}	An empirical parameter in C3 leaf stomatal model (dimensionless)	3.0	50.0
a_{14}	An empirical parameter in C4 leaf stomatal model (dimensionless)	0.8	50.0
D_{03}	An empirical parameter in C3 leaf stomatal model (Pa)	750	2600
D_{04}	An empirical parameter in C3 leaf stomatal model (Pa)	750	2600
r_{d3}	The ratio of C3 leaf day respiration to maximal carboxylation rate (dimensionless)	7.5e-3	2.5e-2
r_{d4}	The ratio of C4 leaf day respiration to maximal carboxylation rate (dimensionless)	1.25e-2	3.75e-2
G_{03}	The stomatal conductance for H ₂ O when C3 leaf net photosynthesis is 0 ($H_2O\ m^{-2}\ s^{-1}$)	0.005	0.015
G_{04}	The stomatal conductance for H ₂ O when C4 leaf net photosynthesis is 0 ($H_2O\ m^{-2}\ s^{-1}$)	0.020	0.060
α_3	Initial slope of the C3 response curve of potential electron transport rate to absorbed quantum flux ($mol\ mol^{-1}$)	0.10	0.40
α_4	Initial slope of the C4 response curve of potential electron transport rate to absorbed quantum flux ($mol\ mol^{-1}$)	0.60	0.99
Θ_3	Convexity of the C3 response curve of potential electron transport rate to absorbed quantum flux (dimensionless)	0.001	0.99
Θ_4	Convexity of the C4 response curve of potential electron transport rate to absorbed quantum flux (dimensionless)	0.60	0.99
β_r	A parameter for estimating vertical root mass distribution in soil (m^{-1})	0.7	1.0
CRT	Maximum radial soil-root conductance of the entire active root system for water ($m\ MPa^{-1}\ s^{-1}$)	0.01	110
γ_r	A parameter in the function of root water extraction (dimensionless)	0.001	0.030
K_{sat}	Soil hydraulic conductivity at saturation ($m\ s^{-1}$)	5.0e-7	3.0e-3
θ_r	Soil residual volumetric water content ($m^3\ m^{-3}$)	0.01	0.10
v	An empirical parameter in hydraulic conductivity function (dimensionless)	1.0	3.0
a	An empirical parameter in soil matrix potential function (dimensionless)	0.005	0.040
ψ_{50}	The soil water potential (MPa) where the relative soil-root conductance is reduced by 50%	-2.0	-0.3
b	An empirical parameter in formula for the relative soil-root conductance (dimensionless)	1.5	3.22

5.2.4 Parameter Optimization

The Bayesian inference method using an adaptive Markov chain Monte Carlo (MCMC)

algorithm was employed to optimize parameters. Instead of searching a unique best parameter set, the Bayesian approach is to estimate the probability distribution of acceptable parameter values. This stochastic strategy can effectively avoid an overconfident fit of complex non-linear models [Ahrens *et al.*, 2014; Van Oijen *et al.*, 2005] by acknowledging alternative model parametrizations and their probabilities [Harrison *et al.*, 2012]. According to the Bayes' rule, the prior probability ($p(\theta)$) of a parameter can be updated to the posterior probability ($p(\theta|y)$) using the data likelihood function as:

$$p(\theta|y) \propto p(y|\theta) \cdot p(\theta) \quad (12.23)$$

where $p(y|\theta)$, assuming a Gaussian distribution of residuals between modelled values and observations, can be calculated as:

$$p(y|\theta) = \prod_{i=1}^N \exp\left(-\frac{(y_i - \hat{y}_i)^2}{2\sigma_i^2}\right) \quad (12.24)$$

where N is the number of observation values, y_i is the i th observation value, \hat{y}_i is the i th simulation value, and σ_i is the standard deviation of the i th observation.

An adaptive MCMC algorithm based on the random walk Metropolis-Hastings (MH) sampling strategy [Haario *et al.*, 2001; 2005] was used to approximate the posterior distributions of model parameters. I first assume for all parameters non-informative uniform distributions over the ranges in Table 5.2 and then used a proposal distribution ($q_t(\cdot|X_0, \dots, X_{t-1})$) to generate a candidate parameter set (X_t^*) from the previous accepted parameter set (X_{t-1}). The acceptance probability ($r(X_t^*|X_{t-1})$) of X_t^* relative to X_{t-1} can be calculated as:

$$a(X_t^*|X_{t-1}) = \min\left(1, \frac{p(X_t^*|y)}{p(X_{t-1}|y)}\right) \quad (12.25)$$

and according to the MH strategy, the probability of accepting X_t^* is determined by:

$$X_t = \begin{cases} X_t^*, r < a(X_t^* | X_{t-1}) \\ X_{t-1}, r \geq a(X_t^* | X_{t-1}) \end{cases} \quad (12.26)$$

where r is a random number from a uniform distribution $U(0,1)$. Through iterations, we can get a Markov chain $\{X_0, \dots, X_t\}$, in which the current state only depends on the previous state. The proposal distribution $q_t(\cdot | X_0, \dots, X_{t-1})$ is critical for effectively searching candidate parameters and thus the convergence of the chain. $q_t(\cdot | X_0, \dots, X_{t-1})$ in the adaptive MCMC is Gaussian with X_{t-1} as mean and C_t as covariance, which adapts as:

$$X_t^* = N(X_{t-1}, C_t) \quad (12.27)$$

$$C_t = \begin{cases} C_0, t \leq U \\ s_k \text{cov}(X_{t-H}, \dots, X_{t-1}) + s_k \varepsilon I_k, (t-1) \% U = 0 \end{cases} \quad (12.28)$$

where C_0 is the initial covariance, U and H are constant integers, k is the dimension of parameter space, s_k is the scaling parameter and generally $s_k = (2.4)^2/k$ [Gelman *et al.*, 1996], ε is a very small value to ensure that C_t will not become singular, and I_k is a k -dimensional identity matrix.

In this study, I used the joint vector of GPP, Q_{le} and NEE as a multi-objective constraint on the model, i.e., $y = \{GPP, Q_{le}, NEE\}$, which is proved to be highly effective [Reichstein *et al.*, 2003; Wang *et al.*, 2001]. The start parameter values in chains at each site were set as the default values in CABLE, and C_0 was set as the square of 1/8 of the range of each parameter. U and H were both equal to 100. I ran 5000 iterations at each site and judged the convergence of the chains according to trace plots [Andrieu and Thoms, 2008; Das *et al.*, 2008] of parameters and the acceptance rate, which is the fraction of proposed samples that is accepted in the whole chain. Only the last 1000 values were used to approximate the posterior distributions of parameters and the first 4000 values were as burn-in samples.

5.2.5 Statistical Metrics

I used two statistical metrics to compare the modelled and observed fluxes of NEE, GPP and ET (Q_{le}) and also SWC. They are coefficient of determination (R^2) and agreement index (d).

R^2 is calculated as:

$$R^2 = \frac{\left(\sum_{n=1}^N (O_n - \bar{O})(P_n - \bar{P})\right)^2}{\sum_{n=1}^N (O_n - \bar{O})^2 \sum_{n=1}^N (P_n - \bar{P})^2} \quad (12.29)$$

where \bar{O} and \bar{P} are means of observed and modeled fluxes, O_n and P_n are the observed and modeled fluxes at the time step n , and N is the total number of observations. d is calculated following *Willmott* [1981] as:

$$d = 1 - \frac{\sum_{n=1}^N (P_n - O_n)^2}{\sum_{n=1}^N (|P_n - \bar{O}| + |O_n - \bar{O}|)^2} \quad (12.30)$$

where d varies between 0 (no agreement) and 1 (perfect match) and is sensitive to the difference between observed and modeled means.

5.3 Results

5.3.1 Important Parameters for GPP and Q_{le}

Figure 5.1 shows sensitivities (accounted by elementary effects) of annual GPP and Q_{le} at each site to those important parameters. The number of identified important parameters was five for both GPP and Q_{le} at each site. However, the total sensitivity of Q_{le} to its selected parameters was much higher than that of GPP within all sites. For the same parameter, GPP and Q_{le} could also show different responses. For example, in EBF sites constituted by C3 tree species, parametrization of a_{13} (the empirical parameter in C3 leaf stomatal model) was more

important for Q_{le} than GPP. In these parameters, the above-ground parameter V_{cmax} and the below-ground parameter ν (an empirical parameter in hydraulic conductivity function) were common to all sites for annual GPP while γ_r and β_r showed importance in sites with herbaceous species (excluding EBF sites, Figure 5.1a). In addition, a_1 (including a_{13} and a_{14} for C3 and C4 plants, respectively) also showed importance across sites among above-ground parameters. In contrast to GPP, Q_{le} was more influenced by below-ground parameters including ν , θ_r and β_r in the majority of sites (Figure 5.1b). V_{cmax} was the most important parameter for annual GPP (Figure 5.1a) but only asserted very limited influence on Q_{le} (Figure 5.1b) whereas a_{13} was of significant importance at six out of the ten sites, particularly within EBF (Figure 5.1b). Within each vegetation type, sites occupied a similar set of important parameters. Across all vegetation types, the total sensitivity of GPP for woody savannas and savannas were highest while evergreen forests was ranked the first in the total sensitivity of Q_{le} to selected parameters.

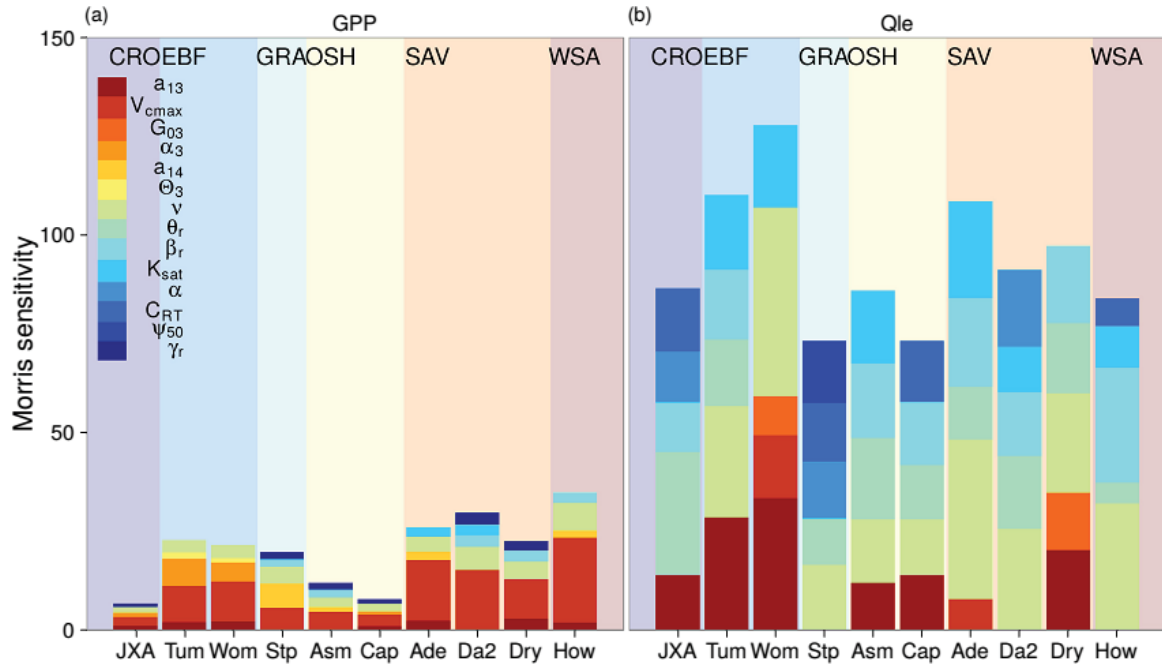


Figure 5.1. Sensitivities of key parameters identified by the Morris method for gross primary productivity (GPP, Figure 5.1a) and latent heat (Q_{le} , Figure 5.1b) over the study periods across ten flux sites, covering crops (CRO), evergreen broad-leaf forests (EBF), C4 grasslands (GRA), open shrublands (OSH), savannas (SAV) and woody savannas (WSA). Bars tending to be red indicate parameters involved in above-ground processes whereas bars tending to be blue indicate parameters involved in below-ground processes.

5.3.2 Distribution of Optimized Parameters

The majority of parameters, including those below-ground ones which are difficult to measure (Figures 5.2g-5.2n), were well constrained by the joint of GPP, Q_{le} and NEE at the hourly time-scale with low uncertainty (Figure 5.2). The acceptance rate was lowest at the Cap site (0.18) with all other sites between 0.22 (AU-Dry) and 0.27 (AU-Ade). In contrast to the default parameters that were vegetation type specific, optimized parameters were quite site specific (Figure 5.2). For V_{cmax} , optimized values were larger than the default values in open

shrublands, savannas and woody savannas whereas they were smaller in crops and evergreen forests (Figure 5.2a). For sites with C3 species, the optimized a_{13} were close to or smaller than the default values except for the AU-Asm site. Within the open shrublands, the AU-Asm site showed different vegetation properties from the AU-Cap site for both above (Figures 5.2a and 5.2b) and below-ground processes (Figures 5.2g and 5.2h). In contrast, EBF sites obtained similar optimized values for vegetation parameters (Figures 5.2a, 5.2b, 5.2d, 5.2f, 5.2g, and 5.2j). Of all parameters, ψ_{50} (soil water potential when soil-root conductance is reduced by 50%) showed the highest uncertainty, suggesting some limitation of joint constraints of turbulent fluxes on the hydraulic redistribution process (Equations 5.17 and 5.18).

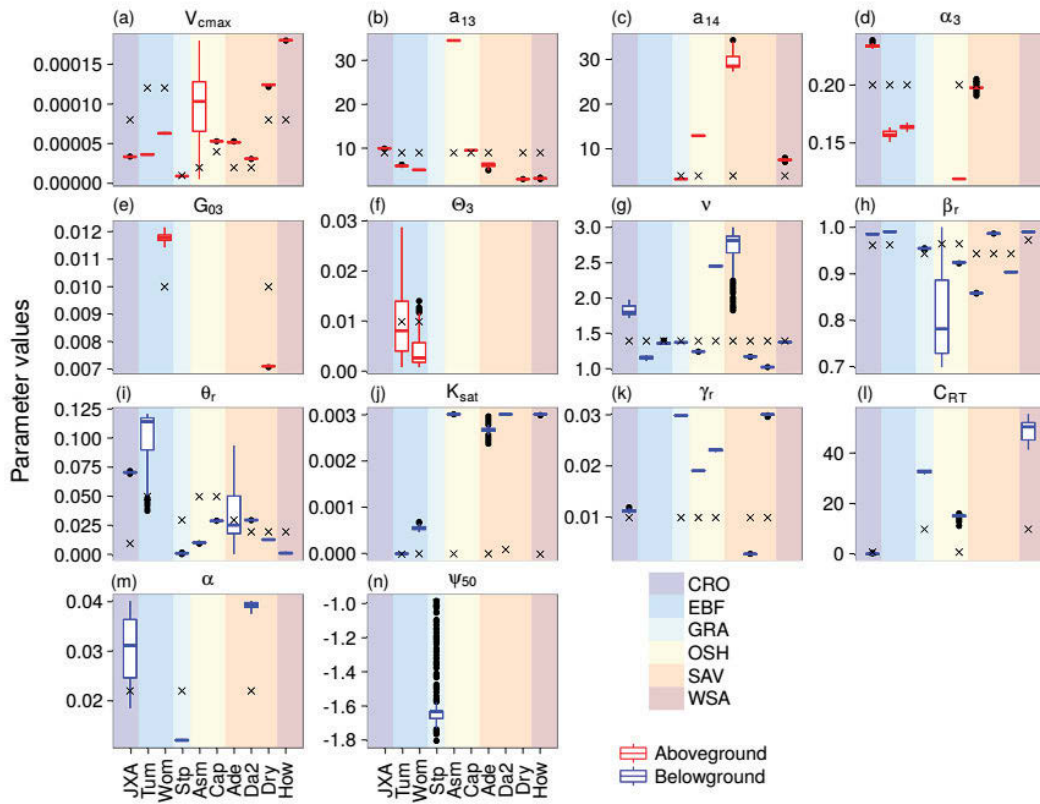


Figure 5.2. Boxplots of optimized values of key above-ground (red) and below-ground (blue) parameters at ten flux sites. Black cross symbols represent default values of parameters. Boxplots show first quartile, median and third quartile (box) as well as the total range of values.

5.3.3 Performance of Optimization at the Hourly Time-scale

The responses of mean diurnal NEE, GPP and Q_{le} simulated from S-Def, S-Abv and S-Opt were compared to quantify effects of above- and below-ground processes on carbon assimilation and evapotranspiration. All three simulations successfully captured the time of peak NEE values, which was around 12:00 AM in EBF (Figures 5.3i and 5.3j) but 10:00 AM in other vegetation types (Figures 5.3a-5.3h). Across sites, S-Def showed the poorest covariation with observed NEE, especially at the AU-Tum, AU-Stp and AU-Dry sites (Figure 5.6b). Figure 5.6e also indicates S-Def was in lower agreement with observations. Compared to SDef, S-Abv mainly improved model performance in estimating daytime NEE but remained the same as S-Def during night-time except at the AU-How site, suggesting minor influence of above-ground processes on nocturnal ecosystem respiration. S-Opt improved model performance for both daytime and night-time NEE with best covariation (Figure 5.6b) and agreement (Figure 5.6e) with observations. However, all three simulations tended to underestimate night-time NEE at the AU-Ade, AU-Da2, AU-Dry and AU-Stp sites and performed poorest at the only C4 grassland site AU-Stp (Figures 5.3h, 5.6b and 5.6e).

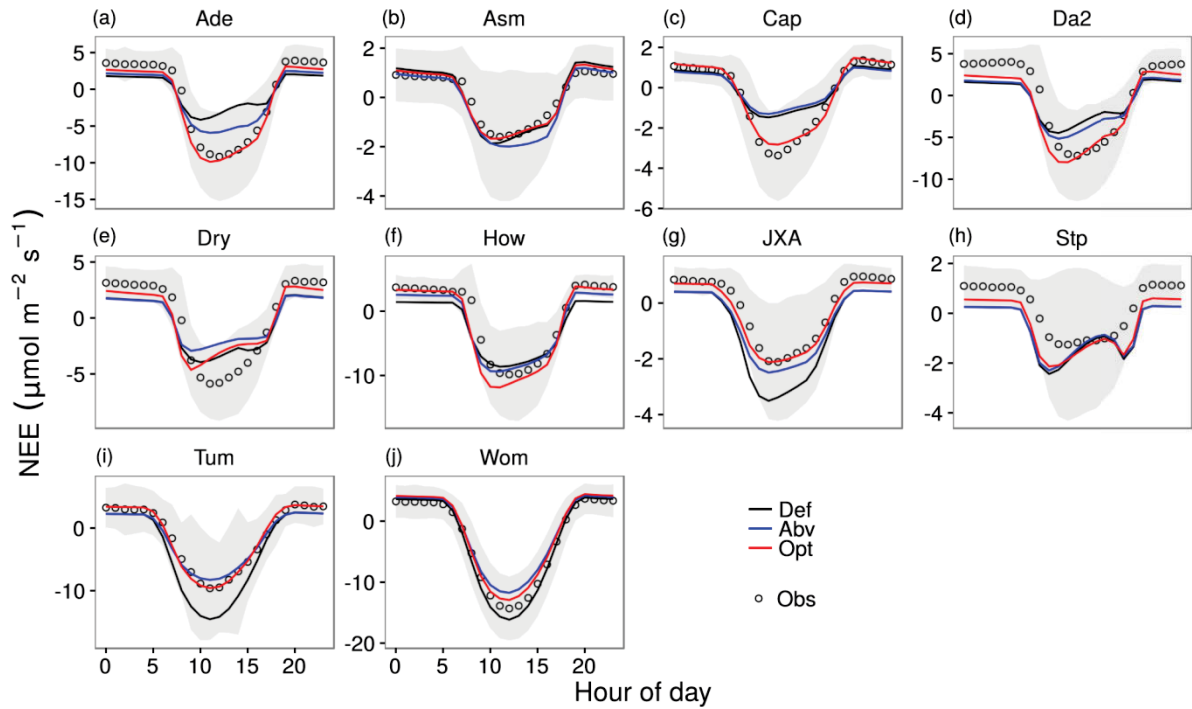


Figure 5.3. Average diurnal cycles for net ecosystem carbon exchange (NEE) as calculated from the observations (Obs, open circles) and modeled by CABLE using default parameters (Def, black line), optimized above-ground parameters alone (Abv, blue line) and optimized parameters (Opt, red line), respectively. The shaded area represents standard deviation of the mean observed NEE.

Similar to NEE, observed GPP reached peak values at around 10:00 AM (Figures 5.4a and 5.4h) in non-forests but 12:00 AM (Figures 5.4i and 5.4j) in forest sites. However, all three simulations failed to capture the peak time of GPP at AU-Dry and AU-How sites. S-Abv was slightly better than S-Def but was outperformed by the latter at an open shrublands site AU-Cap and the C4 grassland site AU-Stp (Figures 5.6a and 5.6d). Compared to S-Abv and S-Def, SOpt improved the model performance considerably especially in agreement with observed GPP (Figure 5.6d), whereas it still underestimated mid-day GPP at the AU-Dry and AU-Stp site (Figures 5.4e and 5.4h). Across all sites, S-Opt still performed poorest in estimating GPP at the only C4 grassland site AU-Stp, just like its performance in estimating NEE.

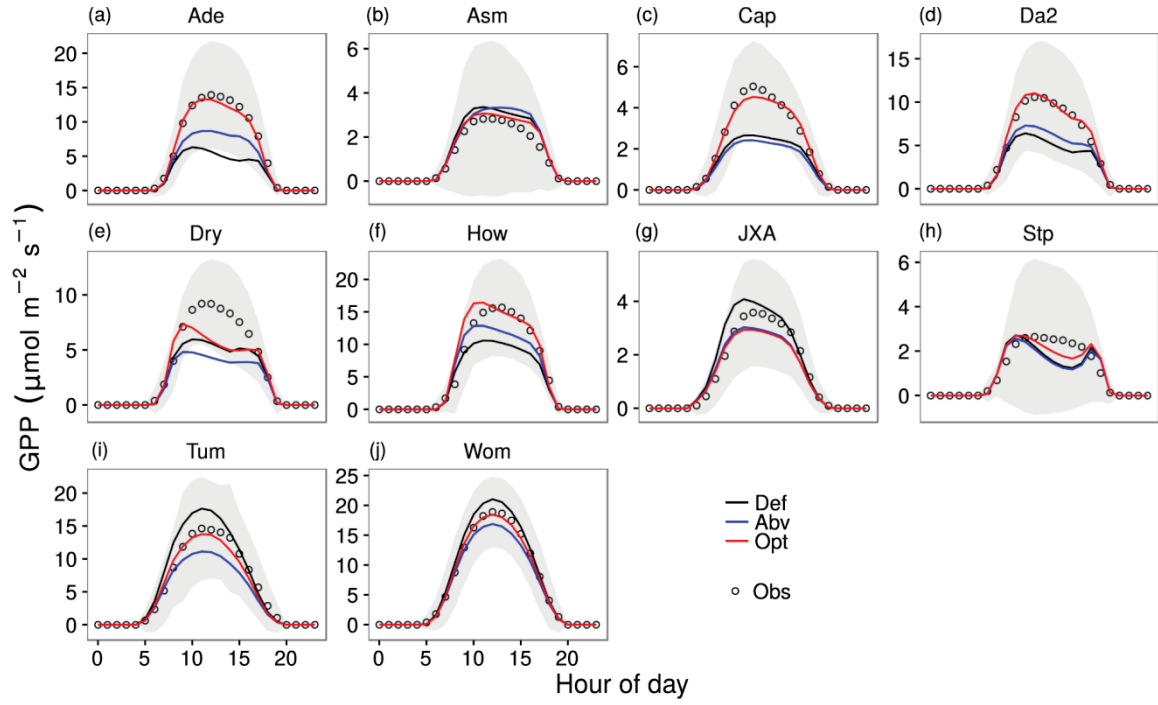


Figure 5.4. Average diurnal cycles for gross primary productivity (GPP) as calculated from the observations (Obs, open circles) and modeled by CABLE using default parameters (Def, black line), optimized above-ground parameters alone (Abv, blue line) and optimized parameters (Opt, red line), respectively. The shaded area represents standard deviation of the mean observed GPP.

Although Q_{le} is tightly coupled with GPP, observed Q_{le} reached its peak values at around 12:00 AM across all sites (Figure 5.5), showing diurnal asynchrony of Q_{le} and GPP in response to environmental changes. S-Abv showed no significant improvement over S-Def in vegetation types excluding EBF and WSA, indicating limited influence of above-ground vegetation parameters on evapotranspiration process in these vegetation types. S-Opt significantly improved model performance across all sites except the only crop site AU-JXA and one open shrublands site AU-Cap (Figures 5.6c and 5.6f), particularly in EBF and WSA sites. Improvements of S-Opt over the other two simulations mainly occurred during daytime while at night-time all three simulations tended to slightly overestimate Q_{le} (Figure 5.5).

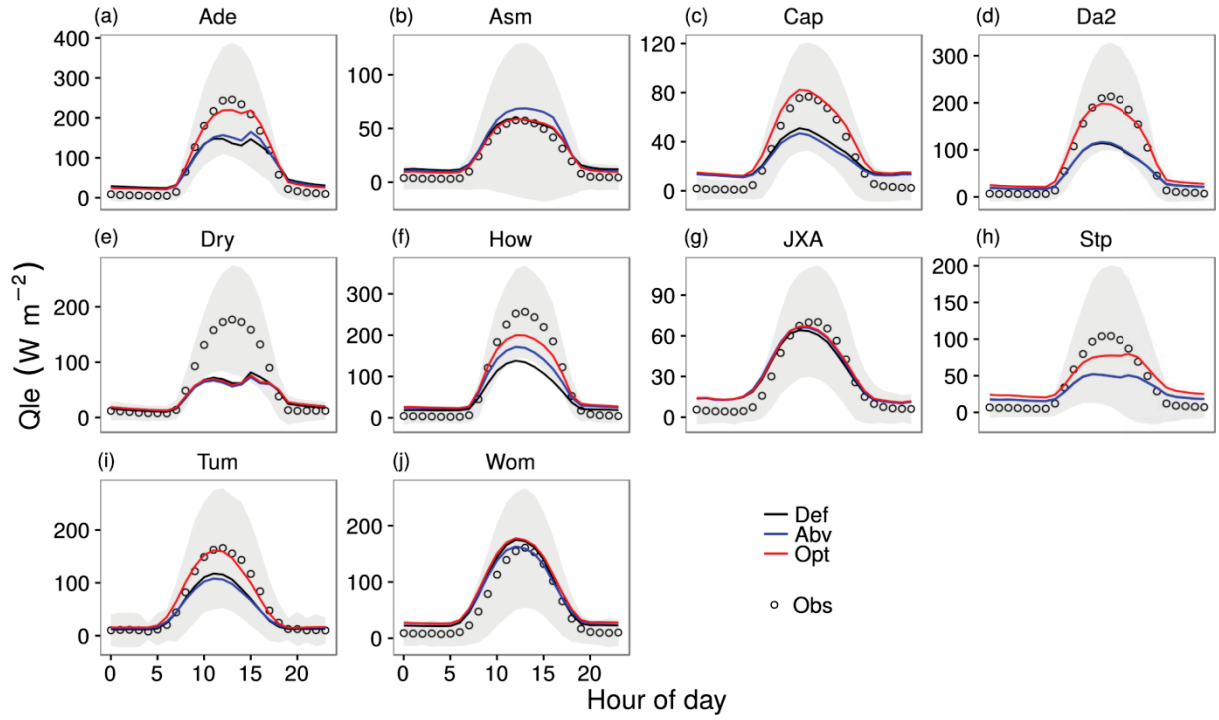


Figure 5.5. Average diurnal cycles for latent heat (GPP) as calculated from the observations (Obs, open circles) and modeled by CABLE using default parameters (Def, black line), optimized above-ground parameters alone (Abv, blue line) and optimized parameters (Opt, red line), respectively. The shaded area represents standard deviation of the mean observed Q_{le} .

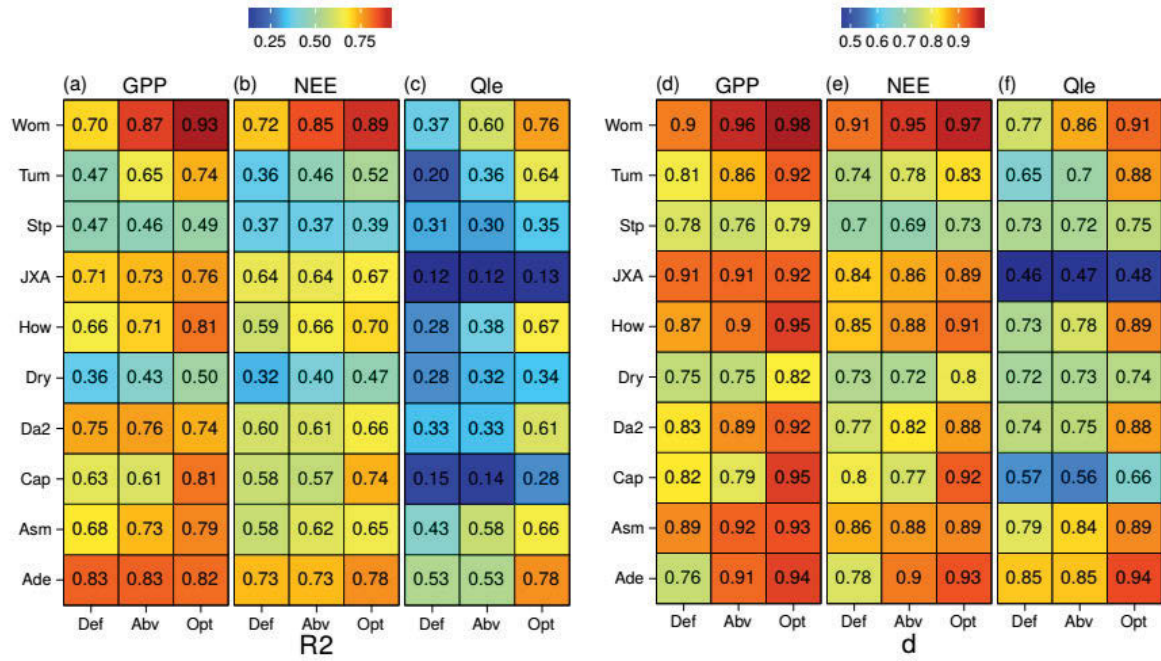


Figure 5.6. Statistical metrics for CABLE performance at the hourly time-scale using default parameters (Def), optimized above-ground parameters alone (Abv) and optimized parameters (Opt) at ten sites. Figures 5.6a, 5.6b and 5.6c indicate coefficient of determination (R^2) and Figures 5.6d, 5.6e and 5.6f indicate agreement index (d).

5.3.4 Simulated SWC, GPP and ET at the Daily Time-scale

Mean daily SWC was also simulated because SWC is the key state variable constraining GPP and ET. The observed SWC was measured at the soil depth 5 cm while the simulated SWC was calculated at the soil depth 5.8 cm. Figure 5.7 shows that S-Abv and S-Def obtained similar results. S-Opt was in better agreement with observations across the majority of sites but failed to outperform S-Def or S-Abv at the AU-Ade, AU-Asm and AU-Wom sites (Figures 5.7a, 5.7b, and 5.7j). This phenomenon is normal because the optimization targeted the combination of GPP, Q_{le} and NEE but not SWC alone. A major reason for biases of S-Def and S-Abv was excessive water consumption in the early stages of the development of low soil

water availability (e.g., Figures 5.7a, 5.7f, 5.7g and 5.7i). In contrast, at the AU-Cap site, which occupied the lowest SWC across sites, all three simulations overestimated the responses of SWC to precipitation events (Figures 5.7c). This bias between model and observation at a site such as AU-Cap showed excess sensitivity of model parametrization in extremely water-limited environment.

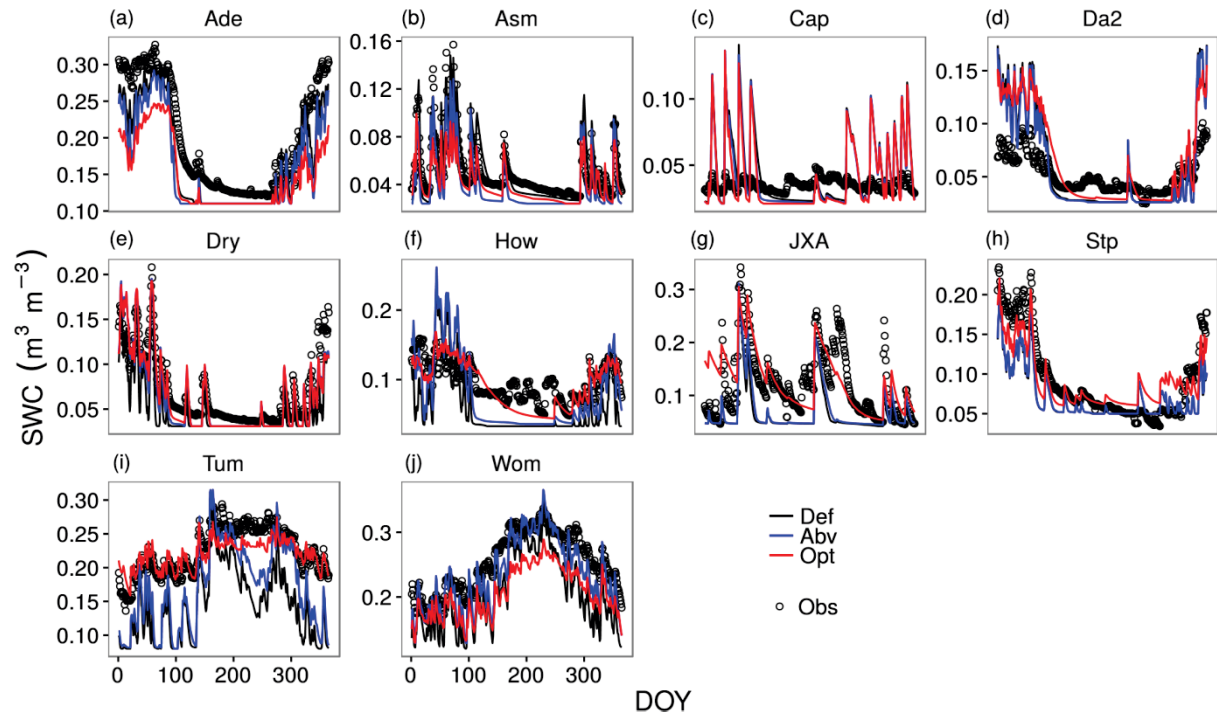


Figure 5.7. Mean daily soil water content (SWC) at depth 5 cm as calculated from the observations (Obs, open circles) and modeled by CABLE at depth 5.8 cm using default parameters (Def, black line), optimized above-ground parameters alone (Abv, blue line) and optimized parameters (Opt, red line), respectively.

In contrast to the results obtained in simulating SWC, S-Opt generally surpassed S-Def and S-Abv in modelling GPP (Figure 5.8) except at the only C4 grassland site, AU-Stp, where the three simulations performed equally (Figure 5.8h). S-Abv obtained significant improvement in only EBF sites in comparison with S-Def (Figures 5.8i and 5.8j). Contrary to simulations of SWC, S-Opt tended to underestimate environmental constraints on GPP during periods of low

SWC (Figures 5.8a, 5.8b, 5.8d, 5.8e, 5.8f and 5.8h). At the AU-Cap site with lowest SWC, S-Opt agreed quite well with observed GPP ($R^2 = 0.55$ and $d = 0.85$) though S-Opt overestimated SWC during precipitation days.

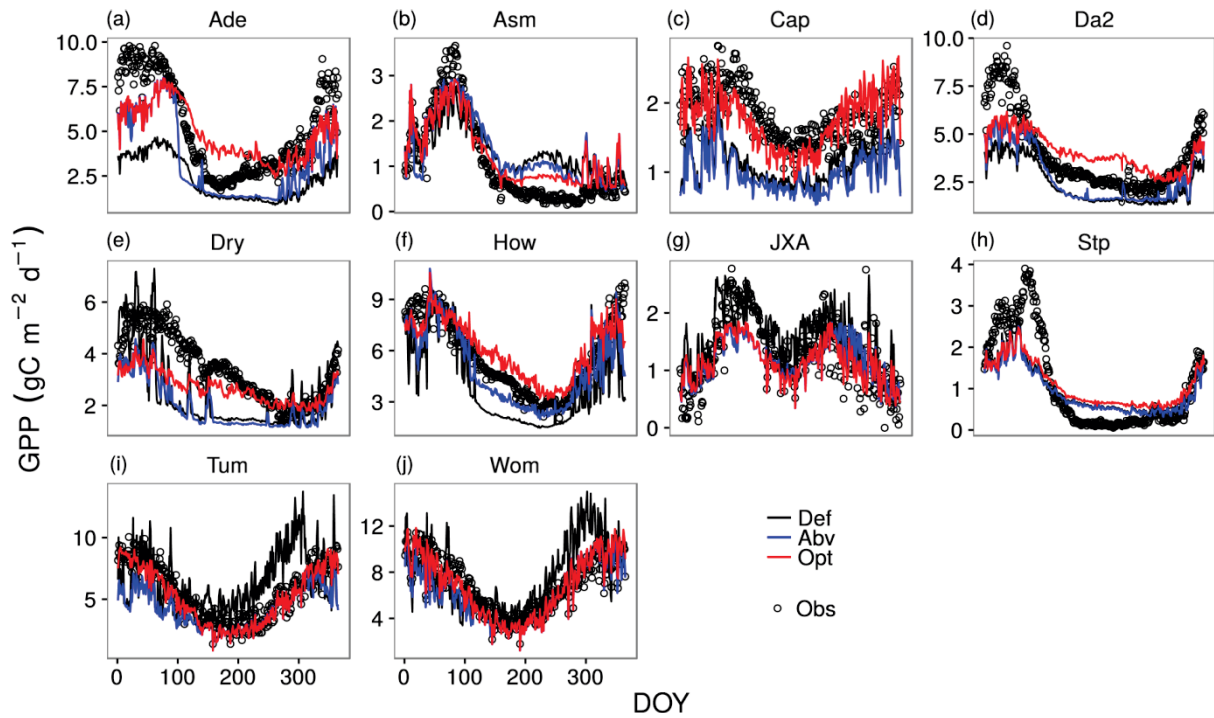


Figure 5.8. Mean daily gross primary productivity (GPP) as calculated from the observations (Obs, open circles) and modeled by CABLE using default parameters (Def, black line), optimized above-ground parameters alone (Abv, blue line) and optimized parameters (Opt, red line), respectively.

For daily ET, S-Abv showed limited improvement over S-Def whereas S-Opt improved model performance, particularly when ET was low, across the majority of sites except at the AU-Cap, AU-Dry and AU-JXA sites (Figures 5.9c, 5.9e and 5.9g). The major bias was induced by overestimation of ET at all above three sites during precipitation days and underestimation of ET at AU-Dry when SWC was low.

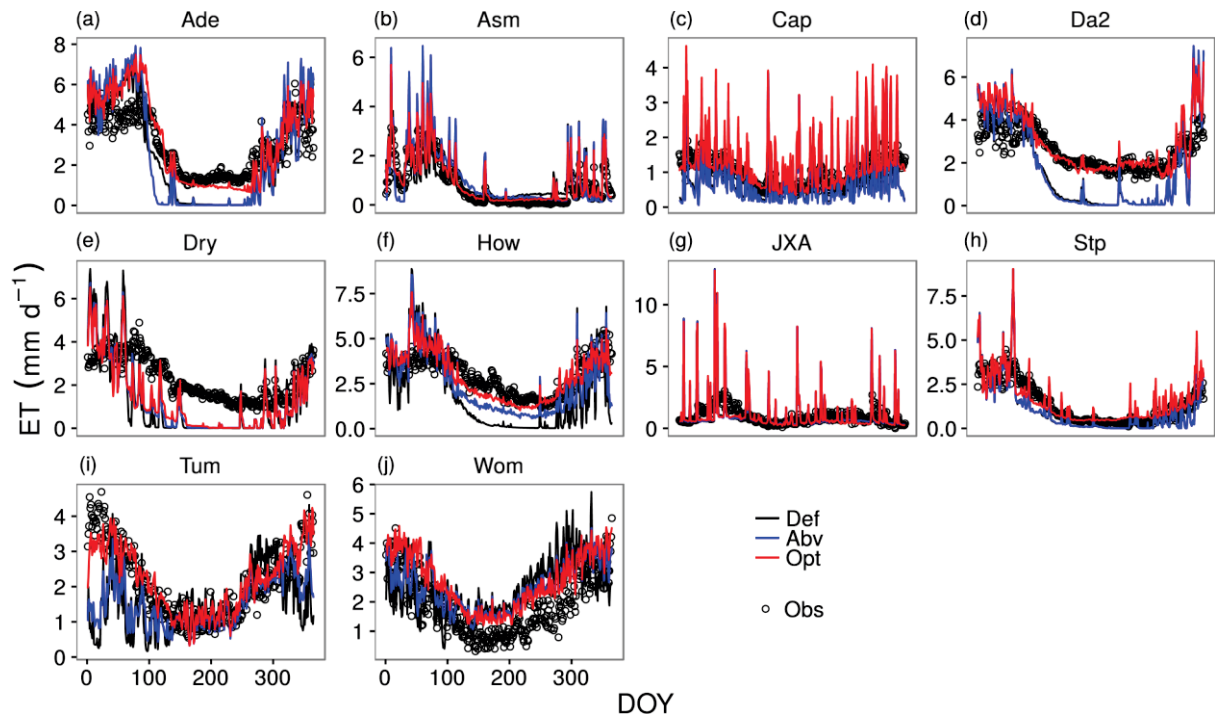


Figure 5.9. Mean daily evapotranspiration (ET) as calculated from the observations (Obs, open circles) and modeled by CABLE using default parameters (Def, black line), optimized aboveground parameters alone (Abv, blue line) and optimized parameters (Opt, red line), respectively.

5.3.5 Seasonal Responses of Simulated GPP and Qle to Water Deficits

Figure 5.10 shows comparison of three simulations in modelling monthly GPP. At savannas and woody savannas sites where ecosystems experience pronounced wet and dry seasons, S-Opt tended to underestimate water constraints on GPP whereas the other models showed a tendency to overestimate water limitation leading to considerable underestimation of GPP during dry seasons (Figures 5.10a, 5.10d, 5.10e and 5.10f). At EBF sites, S-Def predicted a short duration of low water availability resulting in an early timing of spring growth (Figures 5.10i and 5.10j). S-Abv significantly improved modelling performance during periods of low water availability but slightly underestimated GPP during wet seasons at EBF sites whereas

S-Opt successfully resolved the issue with S-Abv (Figures 5.10i and 5.10j).

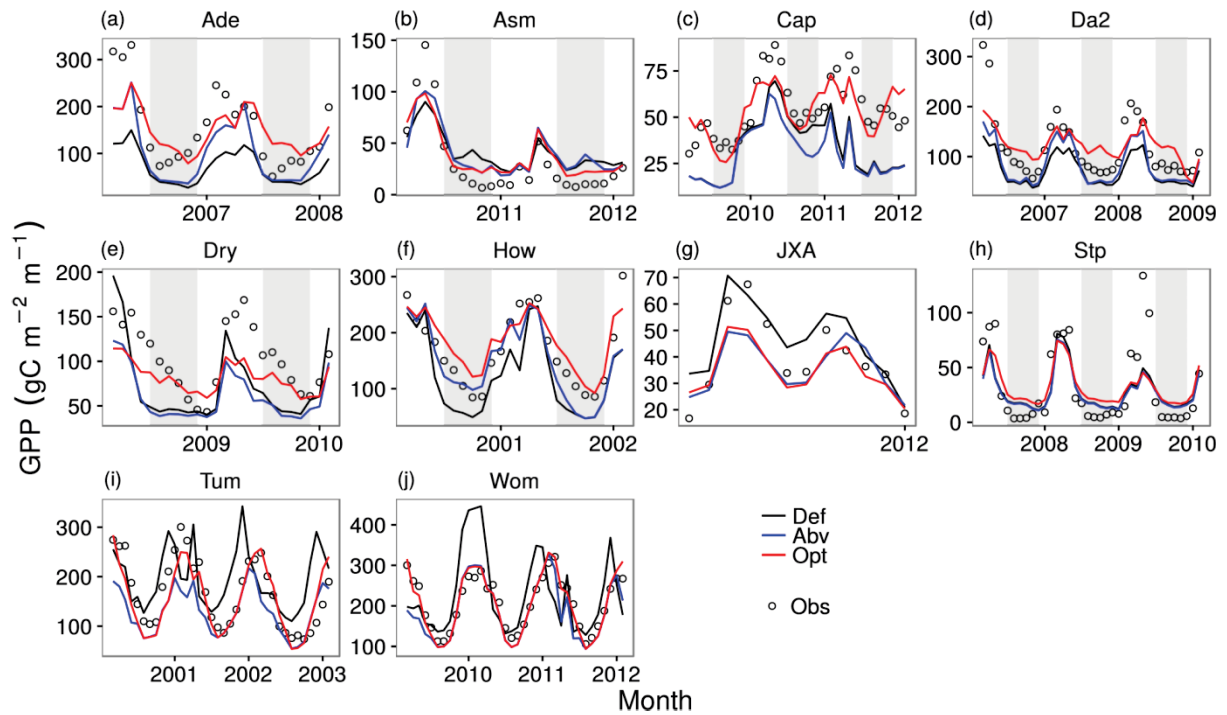


Figure 5.10. Monthly gross primary productivity (GPP) as calculated from the observations (Obs, open circles) and modeled by CABLE using default parameters (Def, black line), optimized above-ground parameters alone (Abv, blue line) and optimized parameters (Opt, red line), respectively. The shaded area denotes the dry season.

For monthly ET, both S-Def and S-Abv overestimated rates of water use at the majority of sites within savannas, woody savannas, C4 grasslands and open shrublands (Figures 5.11a, 5.11c, 5.11d, 5.11e, 5.11f and 5.11h), which caused a sharp depletion of SWC early in the dry season (Figure 7). At EBF sites, S-Def and S-Abv showed similar performance for estimating ET to GPP. S-Opt significantly improved model performance mainly during dry seasons across non-forest sites except at the AU-Dry site (Figure 5.11e).

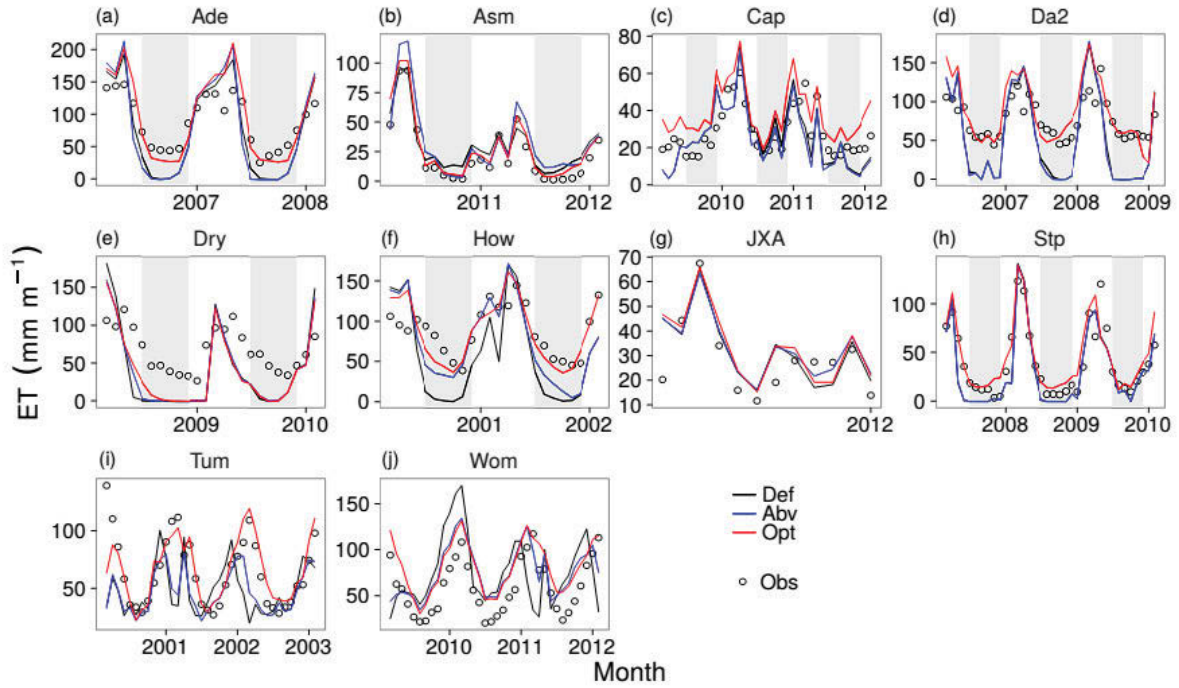


Figure 5.11. Monthly evapotranspiration (ET) as calculated from the observations (Obs, open circles) and modeled by CABLE using default parameters (Def, black line), optimized aboveground parameters alone (Abv, blue line) and optimized parameters (Opt, red line), respectively. The shaded area denotes the dry season.

5.3.6 Effects of Optimization on GPP and ET at Different Time-scales

From the results shown above, it is apparent that S-Opt could better estimate temporal variations of GPP and ET at each site. However, the effects of optimization varied not only between GPP and ET but also over hourly to monthly time-scales. Figure 5.12 shows that improvements through optimization conducted at short-term scale were not necessarily transferred to longer time-scales. For example, both R^2 and d for hourly GPP at the AU-Stp site were smaller than those at the AU-Da2 site but they became larger at the monthly time-scale (Figure 5.12a). Meanwhile, effects of optimization were clearly affected by water availability across sites. Both R^2 and d for GPP and ET at hourly and daily time-scales

increased as sites became increasingly mesic. However, at the monthly time-scale, this influence became weak. Instead, sites located between xeric and mesic showed the poorest effects of optimization.

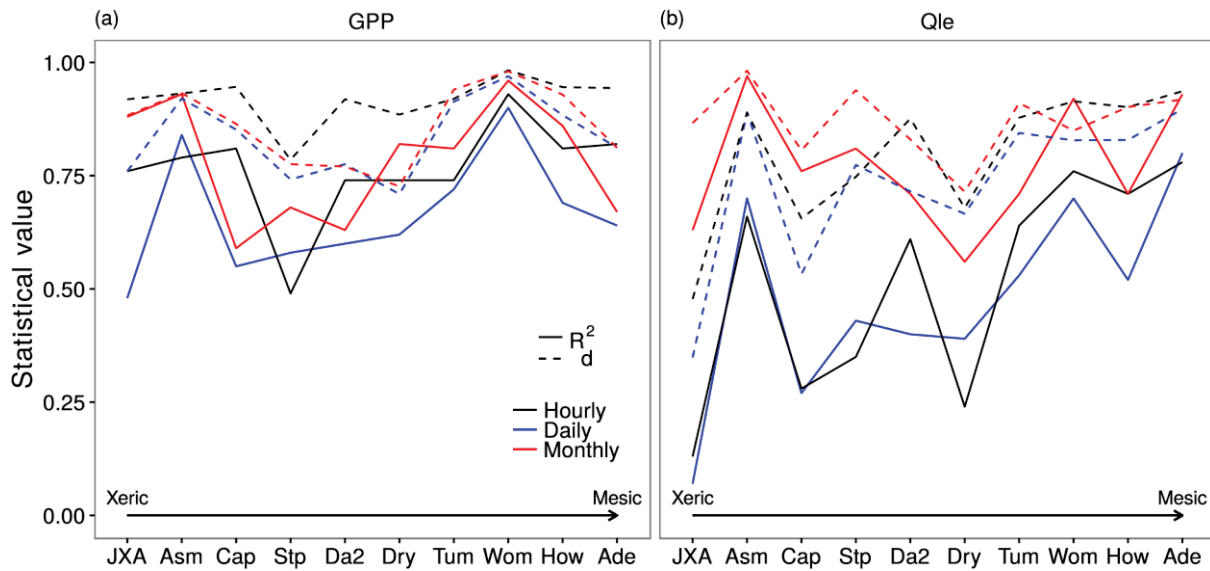


Figure 5.12. Performance of the optimized CABLE at different time-scales. Model parameters are optimized targeted at observed hourly GPP, Q_{le} and NEE. Coefficient of determination (R^2 , solid line) and agreement index (d , dashed line) are shown at hourly (black), daily (blue) and monthly (red) time-scales. Both GPP (Figure 5.12a) and Q_{le} (Figure 5.12b) are ordered by mean annual precipitation across the ten sites.

I further investigated the effects of optimization on the spatio-temporal coupling between GPP and ET (Figure 5.13) at the annual time-scale. S-Def weakened the covariation ($R^2 = 0.42$) between GPP and ET mainly by overestimating their ratios (i.e., water use efficiency, WUE) for EBF sites (Figure 5.13b). In contrast, S-Abv overestimated the covariation ($R^2 = 0.70$) between GPP and ET mainly by underestimating WUE for OSH sites (Figure 5.13c). S-Opt also over-predicted the coupling ($R^2 = 0.67$) of GPP and ET but obtained closest WUE to the observed value. In addition, S-Opt systematically overestimated annual ET.

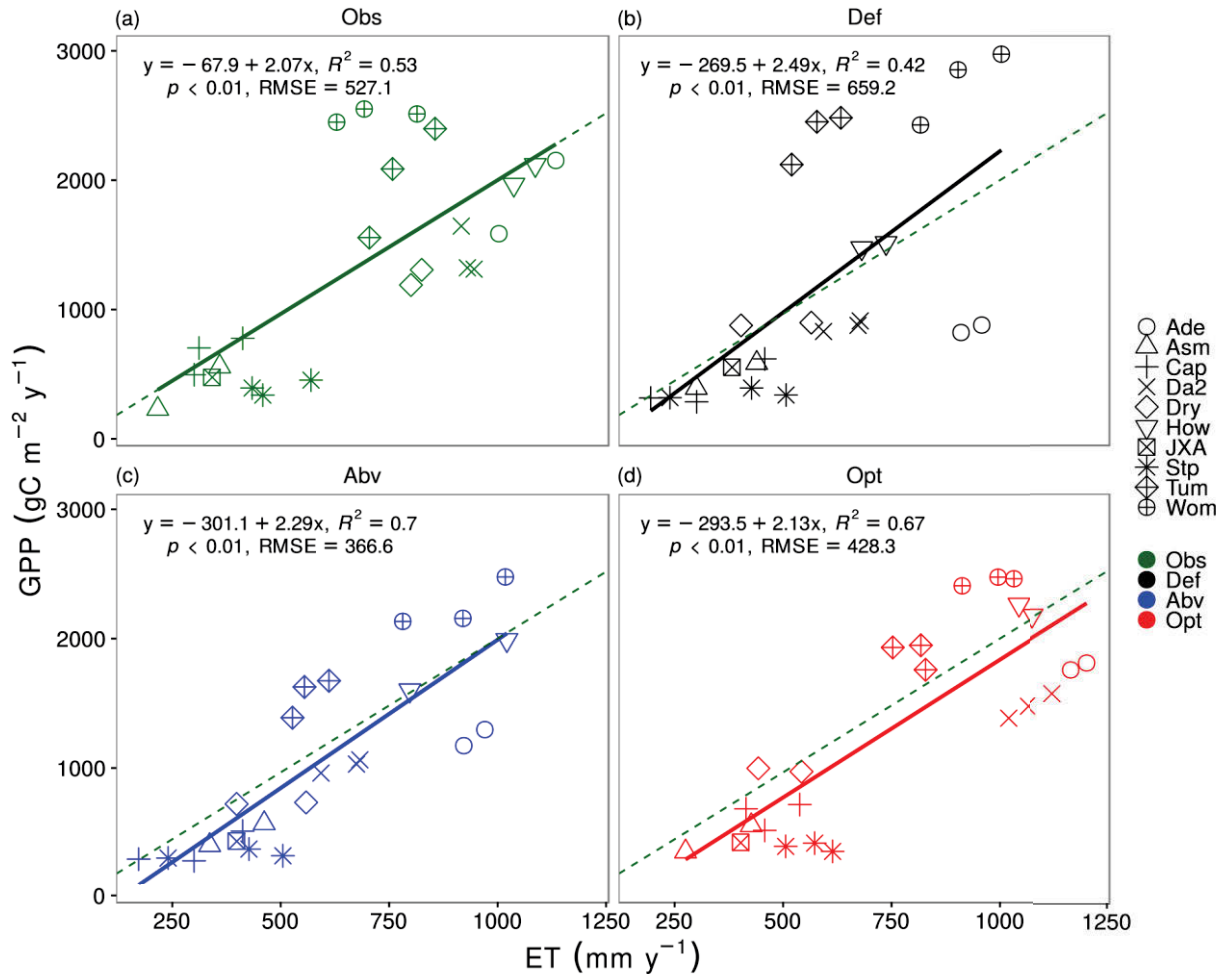


Figure 5.13. Coupling of gross primary productivity (GPP) and evapotranspiration (ET) at the annual time-scale across ten sites as calculated from the observations (Obs, dark green) and modeled by CABLE using default parameters (Def, black line), optimized above-ground parameters alone (Abv, blue line) and optimized parameters (Opt, red line), respectively. The solid line represents the linear regression and the dashed line indicates the linear regression using observation data.

5.4 Discussion

5.4.1 Key Parameters and Processes for GPP and ET

Sensitivity analysis shows that V_{cmax} and v are the primary parameters influencing carbon

assimilation across a wide range of vegetation types. Corresponding to these two parameters are the biochemical process of photosynthesis (Equations 5.2 and 5.3) and hydraulic redistribution of soil water (Equations 5.15-5.18). The extreme importance of V_{cmax} in estimating GPP has long been recognized. *Wang et al.* [2001] used a non-linear parameter estimation method to optimize J_{max} (maximum potential electron transport rate, usually defined as proportional to V_{cmax}) over six grazing/pasture sites. *Reichstein et al.* [2003] tuned leaf photosynthetic capacity to address seasonal drought effects on carbon and water fluxes by inverse estimation of V_{cmax} . The optimization results presented herein also suggest that tuned V_{cmax} only can improve model performance on GPP and Q_{le} (Figure 5.6) during either wet (e.g., Figure 5.10a) or dry seasons (e.g., Figure 5.10f). However, these improvements are very limited and in some circumstances tuned V_{cmax} gave no better GPP estimates than default V_{cmax} values (e.g., dry season in 2001 in Figure 5.10c). Furthermore, optimized V_{cmax} exerted only a minor improvement on SWC modelling (Figure 5.7). These results underline two points: (1) there is indeed a need to include environmental constraints on V_{cmax} to get dynamic parametrization instead of a presumed static value, and (2) improvements on SWC modelling are critical for CABLE LSM to consent to reality. *De Kauwe et al.* [2015] tested variable data-driven drought sensitivities [*Zhou et al.*, 2013] of V_{cmax} in CABLE and found little effect if simulations of SWC were not improved because of the rapid depletion of SWC in the early stage of dry periods. Such “on-off” [*De Kauwe et al.*, 2015] behavior in response to droughts was also revealed in the current study and others [e.g., *Ukkola et al.*, 2016] using CABLE and also other LSMs, such as CLM (Community Land Model, *Powell et al.* [2013]) and VIC+ (Variable Infiltration Capacity Model, *Luo et al.* [2013]). Including optimized below-ground parameters greatly lessens the water constraint on vegetation photosynthesis (e.g., Figures 5.10a, 5.10b, and 5.10d). The side effect of including HR optimization (also optimization of root water uptake process at some sites) is the tendency of underestimating drought impacts

on GPP (see the same examples, Figures 5.10a, 5.10b, and 5.10d), which is not expected. This side effect may be amended by dynamic parametrization of V_{cmax} or other below-ground processes, such as changes in rooting depth and ground water table, which is discussed later.

Estimation of ET is significantly affected by parametrization of a_{13} , β_r , v and θ_r . These parameters relate to the biophysical process of canopy stomatal conductance (Equation 5.4), dynamic root water uptake (Equations 5.9 and 5.10), and the process of HR (Equations 5.15-5.18). a_{13} , as the slope of the relationship between A_c and G_s (Equation 5.4), is reduced by a factor of water stress (f_w in Equation 5.4) to down-regulate A_c . However, our results suggest that ET rather than GPP is more sensitive to a_{13} (Figure 5.1), possibly because of the predominantly biophysical nature of ET. β_r is the unique parameter to determine the vertical distribution of root biomass (Equation 5.10), which is used to weight the contribution of SWC from different soil layers (Equation 5.9). The standard CABLE and LSMs such as CLM also applies this root biomass based weighting method to calculate water stress. However, this approach is criticized by *De Kauwe et al.* [2015] based on evidences that it performs poorly in response to droughts in the standard CABLE and shows no significant improvement even using alternative root water uptake functions (i.e., the version of CABLE used in this study, *Li et al.* [2012]) without HR inclusion. However, our optimization results show that this approach can work well for ET at the majority of sites experiencing dry seasons (e.g., Figures 5.11a, 5.11b, 5.11d, 5.11f and 5.11h) although some bias was still apparent. This bias can be induced by the parametrization of β_r , which determines root depth. *Luo et al.* [2013] applied the same root biomass based weighting method in the VIC+ model and evaluated the impact of root depth. They found that increase of root depth effectively improved soil water availability for ET in dry seasons [*Luo et al.*, 2013]. Meanwhile, our optimized values for β_r (Figure 5.1h) also suggest that current soil depth (287.2 cm) used in CABLE LSM is inappropriate. For example, at the woody savannas site AU-How, the mean value of optimized

β_r is 0.99, meaning a 94.4% cumulative root fraction at soil depth 287.2 cm and a 99.8% cumulative root fraction at soil depth 600 cm according to Equation 5.10. *Cook et al.* [1998] found that trees at the AU-How site have deep roots to absorb water at soil depth 6 m, which is consistent with our optimized β_r . Therefore, if a larger rooting depth is included in CABLE, the additional 5.4% of deep roots can contribute to water uptake and further reduce the bias between ET by S-Opt and observations at the AU-How site (Figure 5.9f). Furthermore, *Decker* [2015] realized an alternative hydrological scheme allowing larger soil depth and changing groundwater depth and effectively improved the performance of CABLE in dry periods [*Decker*, 2015; *Ukkola et al.*, 2016]. These findings indicate that a larger rooting depth is favorable for ET estimation in dry seasons. However, note that improvement on ET estimation does not mean the same to modelled SWC (Figures 5.9a vs. 5.7a). This contrast gives two possible hints: (1) optimization targeted at turbulent fluxes only cannot ensure the success in estimating state variables simultaneously, and (2) including HR process alone in LSMs may not fully resolve the issue of the response to droughts. *Luo et al.* [2013] in VIC+ model demonstrated that HR, increase of root depth and the rise of the water table can interactively contribute to improvement in modelling ET during dry periods at a forest site. Therefore, realizing a changing ground water table along with HR and a larger root depth should be an option in the future development of CABLE.

Given the important impacts of below-ground processes on both GPP and ET, it is not surprising that the coupling relationship between GPP and ET was best captured across sites (Figure 5.13). This suggests that across a diversity of vegetation types, the representation of below-ground processes in CABLE LSM should receive further attention in the modelling community.

5.4.2 Applications of the Model-data Fusion Framework

The model-data fusion framework has a large potential in calibration of complex process-based models [Reichstein *et al.*, 2003]. The adaptive Bayesian MCMC method used in this study demonstrates its advantages on inverse estimation of parameters without enough prior information and investigation of deficits of model structures. Prentice *et al.* [2015] suggest that model-data fusion should be a standard part of model development because only when a model fails after optimization, can the model be judged as incorrectly structured. The results of the current study strongly support this opinion as the model performance was considerably improved after optimization. However, some problems still exist with model-data fusion before it can be generally applied. First, the computation efficiency is quite low for generic optimization algorithms such as Bayesian MCMC [Prentice *et al.*, 2015; Wang *et al.*, 2009]. Although the gradient-based approaches are more efficient, they can get trapped into a local optimum [Wang *et al.*, 2009]. Therefore, a global sensitivity such as the Morris method should be conducted before optimization to reduce the dimensions of parameter space. Second, there are still no general specifications on selections of multiple datasets to constrain optimization. The results presented here show that only hourly turbulent fluxes could not provide enough information to obtain better modelled SWC (e.g., Figures 5.9a vs. 5.7a) and some parameters (e.g., Figure 5.2h), underlining the necessity of including SWC into the joint constraint. However, introducing more datasets as constrain conditions can bring new problems. Although more constraints can usually reduce the model's degrees of freedom, they are accompanied by more uncertainties with different spatio-temporal scales [Prentice *et al.*, 2015]. Additionally, optimization on short-term time-scales cannot necessarily ensure positive effects at longer time-scales and *vice versa* because many details during short terms can be hidden when optimized at longer time-scales. Wang *et al.* [2011] proposed to minimize cost functions at different frequencies separately. Here I suggest that the coupling of GPP and ET

over various time-scales could be included to constrain optimization without introducing additional datasets but providing more information. The results presented here on the ratios of annual GPP over ET (Figure 5.13) show that there is still considerable bias between optimized and observed data, which can be used as an effective constraint over both spatial and temporal scales.

5.4.3 Further Model Uncertainties

Besides the above key parameters and processes, there are other factors contributing to model uncertainties. (1) Soil properties, such as K_{sat} and θ_r , could significantly impact ET (Figure at some sites 1). *Ukkola et al.* [2016] also found that effects of soil properties on ET are highly site-specific in CABLE. Thus, accurate soil maps are necessary to improve model performance. (2) As well as soil properties, LAI is another factor influencing ET estimation [*Ukkola et al.*, 2016], because LAI is used to upscale leaf-scale fluxes to the canopy scale. It is noteworthy that in ecosystems with trees and grasses coexisting such as savannas and woody savannas, dynamic tree-grass partitioning of LAI can improve model performance at such sites [*Haverd et al.*, 2016], implying a favored vegetation dynamics over a fixed tree-grass ratio in CABLE. (3) The results presented here show that optimized parameters are quite site-specific rather than vegetation type-specific which is popular in modern LSMs. *Alton* [2011] systematically investigated the effect of the simplification of dividing plants into discrete vegetation types and found about 15% difference for global vegetation net primary production between simulations using vegetation-specific parameters and those using varying parameters. However, varying site-specific parameters are generally not accessible, particularly over large regions or for below-ground processes. Thus the simplification of vegetation types is still commonly accepted though it has obvious limitations. (4) The results presented here revealed the underestimation of nocturnal NEE and the overestimation of ET

during night-time or rainfall days at some sites. These issues are out of the range of this study but worth attentions in future. (5) CABLE with optimized parameters should be benchmarked by those data driven models to further assess its deficits in model structures [Abramowitz *et al.*, 2007; Best *et al.*, 2015; Keenan *et al.*, 2012]. Optimized CABLE performed better at mesic sites than at xeric sites (Figure 5.12), implying the possibility of differing mechanisms for ecosystems with different water stress. Benchmarking with data-driven models can effectively help to identify the sources of errors.

5.5 Conclusions

I used the Morris sensitivity method to identify the critical parameters for carbon assimilation and evapotranspiration in the CABLE LSM across 10 Australian sites, covering major several Australian vegetation types. Then I optimized these parameters using the adaptive Bayesian MCMC method targeting the joint of NEE, GPP and Q_{le} at an hourly time-scale. These results revealed that biochemical process (V_{cmax}) and hydrological redistribution were most important for GPP while stomatal parameterization as well as HR process were key for ET. Only when optimized parameters for both above- and belowground processes were used was the model's performance, including the coupling relationship of GPP and ET, considerably improved, particularly during dry periods. I also investigated the effects of optimization at different time-scales and found that the model's performance decreased from mesic sites to xeric sites at short-time scales (hourly and daily) but showed no significant trend at the monthly time-scale. This phenomenon implies that possibly there are differences in mechanisms to respond to water stress between vegetation in a wet environment and that in a dry environment. It is important to note that soil water content could be poorly estimated even if GPP and ET were reasonably modeled, featuring the necessity of introducing SWC as

constraint in optimization. However, more target datasets can bring more uncertainties with different time-scales. Thus, efforts are needed in selecting parsimonious datasets but with containing enough information to constrain optimization. Furthermore, I discussed other issues contributing to model uncertainties such as soil properties, leaf area index inputs and vegetation type-specific parameters, effects of which can be quite site-specific. This study highlights the importance of correct representation of below-ground processes in the CABLE LSM, especially in the context of more intensified and frequent droughts in future.

Acknowledgments. This research was supported by an Australian Research Council Discovery Early Career Research Award (project number DE120103022). This work used eddy covariance data acquired by the OzFlux community.

References

- Abramowitz, G., R. Leuning, M. Clark, and A. Pitman (2008), Evaluating the performance of land surface models, *Journal of Climate*, 21(21), 5468-5481.
- Abramowitz, G., A. Pitman, H. Gupta, E. Kowalczyk, and Y. Wang (2007), Systematic bias in land surface models, *Journal of Hydrometeorology*, 8(5), 989-1001.
- Ahrens, B., M. Reichstein, W. Borken, J. Muhr, S. E. Trumbore, and T. Wutzler (2014), Bayesian calibration of a soil organic carbon model using $\Delta^{14}\text{C}$ measurements of soil organic carbon and heterotrophic respiration as joint constraints, *Biogeosciences*, 11(8), 2147-2168.
- Allen, C. D., et al. (2010), A global overview of drought and heat-induced tree mortality reveals emerging climate change risks for forests, *Forest ecology and management*, 259(4), 660-684.

- Alton, P. B. (2011), How useful are plant functional types in global simulations of the carbon, water, and energy cycles?, *Journal of Geophysical Research: Biogeosciences*, 116(G1).
- Andrieu, C., and J. Thoms (2008), A tutorial on adaptive MCMC, *Statistics and Computing*, 18(4), 343-373.
- Beer, C., et al. (2009), Temporal and among-site variability of inherent water use efficiency at the ecosystem level, *Global biogeochemical cycles*, 23(2).
- Beringer, J., L. B. Hutley, N. J. Tapper, and L. A. Cernusak (2007), Savanna fires and their impact on net ecosystem productivity in North Australia, *Global Change Biology*, 13(5), 990-1004.
- Beringer, J., L. B. Hutley, J. M. Hacker, B. Neininger, and U. Kyaw Tha Paw (2011), Patterns and processes of carbon, water and energy cycles across northern Australian landscapes: From point to region, *Agricultural and Forest Meteorology*, 151(11), 1409 - 1416.
- Best, M. J., et al. (2015), The plumbing of land surface models: benchmarking model performance, *Journal of Hydrometeorology*, 16(3), 1425-1442.
- Beven, K., and J. Freer (2001), Equifinality, data assimilation, and uncertainty estimation in mechanistic modelling of complex environmental systems using the GLUE methodology, *Journal of Hydrology*, 249(1&4), 11-29.
- Boone, A., et al. (2009), The AMMA land surface model intercomparison project (ALMIP), *Bulletin of the American Meteorological Society*, 90(12), 1865.
- Campolongo, F., J. Cariboni, and A. Saltelli (2007), An effective screening design for sensitivity analysis of large models, *Environmental Modelling & Software*, 22(10), 1509 - 1518.
- Cleverly, J., N. Boulain, R. Villalobos-Vega, N. Grant, R. Faux, C. Wood, P. G. Cook, Q. Yu, A. Leigh, and D. Eamus (2013), Dynamics of component carbon fluxes in a semi-arid Acacia woodland, central Australia, *Journal of Geophysical Research: Biogeosciences*,

118(3), 1168-1185.

- Cook, P. G., T. J. Hatton, D. Pidsley, A. L. Herczeg, A. Held, A. O'Grady, and D. Eamus (1998), Water balance of a tropical woodland ecosystem, Northern Australia: a combination of micro-meteorological, soil physical and groundwater chemical approaches, *Journal of Hydrology*, 210(1), 161-177.
- Dai, A. (2013), Increasing drought under global warming in observations and models, *Nature Climate Change*, 3(1), 52-58.
- Das, N. N., B. P. Mohanty, and E. G. Njoku (2008), A Markov chain Monte Carlo algorithm for upscaled soil-vegetation-atmosphere-transfer modeling to evaluate satellite-based soil moisture measurements, *Water Resources Research*, 44(5).
- De Kauwe, M. G., S.-X. Zhou, B. E. Medlyn, A. J. Pitman, Y.-P. Wang, R. A. Duursma, and I. C. Prentice (2015), Do land surface models need to include differential plant species responses to drought? Examining model predictions across a mesic-xeric gradient in Europe, *Biogeosciences*, 12(24), 7503-7518.
- Decker, M. (2015), Development and evaluation of a new soil moisture and runoff parameterization for the CABLE LSM including subgrid-scale processes, *Journal of Advances in Modeling Earth Systems*, 7(4), 1788-1809.
- Dirmeyer, P. A., R. D. Koster, and Z. Guo (2006), Do global models properly represent the feedback between land and atmosphere?, *Journal of Hydrometeorology*, 7(6), 1177-1198.
- Eamus, D., L. B. Hutley, and A. P. O'Grady (2001), Daily and seasonal patterns of carbon and water fluxes above a north Australian savanna, *Tree Physiology*, 21(12-13), 977-988.
- Egea, G., A. Verhoef, and P. L. Vidale (2011), Towards an improved and more flexible representation of water stress in coupled photosynthesis--stomatal conductance models, *Agricultural and Forest Meteorology*, 151(10), 1370-1384.
- Gale, M. R., and D. F. Grigal (1987), Vertical root distributions of northern tree species in

- relation to successional status, *Canadian Journal of Forest Research*, 17(8), 829-834.
- Gelman, A., G. Roberts, and W. Gilks (1996), Efficient metropolis jumping hules, *Bayesian statistics*, 5(599-608), 42.
- Griebel, A., L. T. Bennett, D. Metzen, J. Cleverly, G. Burba, and S. K. Arndt (2016), Effects of inhomogeneities within the flux footprint on the interpretation of seasonal, annual, and interannual ecosystem carbon exchange, *Agricultural and Forest Meteorology*, 221, 50-60.
- Haario, H., E. Saksman, and J. Tamminen (2001), An adaptive Metropolis algorithm, *Bernoulli*, 223-242.
- Haario, H., E. Saksman, and J. Tamminen (2005), Componentwise adaptation for high dimensional MCMC, *Computational Statistics*, 20(2), 265-273.
- Hararuk, O., J. Xia, and Y. Luo (2014), Evaluation and improvement of a global land model against soil carbon data using a Bayesian Markov chain Monte Carlo method, *Journal of Geophysical Research: Biogeosciences*, 119(3), 403-417.
- Harrison, K. W., S. V. Kumar, C. D. Peters-Lidard, and J. A. Santanello (2012), Quantifying the change in soil moisture modeling uncertainty from remote sensing observations using Bayesian inference techniques, *Water Resources Research*, 48(11).
- Haverd, V., B. Smith, M. Raupach, P. Briggs, L. Nieradzik, J. Beringer, L. Hutley, C. M. Trudinger, and J. Cleverly (2016), Coupling carbon allocation with leaf and root phenology predicts tree--grass partitioning along a savanna rainfall gradient, *Biogeosciences*, 13(3), 761-779.
- Jackson, R. B., J. Canadell, J. R. Ehleringer, H. A. Mooney, O. E. Sala, and E. D. Schulze (1996), A global analysis of root distributions for terrestrial biomes, *Oecologia*, 108(3), 389-411.
- Keenan, T. F., M. S. Carbone, M. Reichstein, and A. D. Richardson (2011), The model--data

- fusion pitfall: assuming certainty in an uncertain world, *Oecologia*, 167(3), 587-597.
- Keenan, T. F., E. Davidson, A. M. Moffat, W. Munger, and A. D. Richardson (2012), Using model-data fusion to interpret past trends, and quantify uncertainties in future projections, of terrestrial ecosystem carbon cycling, *Global Change Biology*, 18(8), 2555-2569.
- Koster, R. D., et al. (2004), Regions of strong coupling between soil moisture and precipitation, *Science*, 305(5687), 1138-1140.
- Kowalczyk, E. A., Y. P. Wang, and E. M. Law (2006), The CSIRO Atmospheric Biosphere Land Exchnage (CABLE) model for use in climate models and as an offline model, *Tech. Pap. 013, CSIRO Mar. and Atmos. Res., Aspendale, Vic., Australia*.
- Lai, C.-T., and G. Katul (2000), The dynamic role of root-water uptake in coupling potential to actual transpiration, *Advances in Water Resources*, 23(4), 427-439.
- Li, L., Y.-P. Wang, Q. Yu, B. Pak, D. Eamus, J. Yan, E. van Gorsel, and I. T. Baker (2012), Improving the responses of the Australian community land surface model (CABLE) to seasonal drought, *Journal of Geophysical Research: Biogeosciences*, 117(G4), n/a-n/a.
- Lu, X., Y.-P. Wang, T. Ziehn, and Y. Dai (2013), An efficient method for global parameter sensitivity analysis and its applications to the Australian community land surface model (CABLE), *Agricultural and Forest Meteorology*, 182–183, 292 - 303.
- Luo, X., X. Liang, and H. R. McCarthy (2013), VIC+ for water-limited conditions: A study of biological and hydrological processes and their interactions in soil-plant-atmosphere continuum, *Water Resources Research*, 49(11), 7711-7732.
- Meyer, W. S., E. Kondrlovà, and G. R. Koerber (2015), Evaporation of perennial semi-arid woodland in southeastern Australia is adapted for irregular but common dry periods, *Hydrological Processes*, 29(17), 3714-3726.
- Morris, M. D. (1991), Factorial Sampling Plans for Preliminary Computational Experiments, *Technometrics*, 33(2), 161-174.

- Pitman, A. J. (2003), The evolution of, and revolution in, land surface schemes designed for climate models, *International Journal of Climatology*, 23(5), 479-510.
- Poulter, B., et al. (2014), Contribution of semi-arid ecosystems to interannual variability of the global carbon cycle, *Nature*, 509(7502), 600-603.
- Powell, T. L., et al. (2013), Confronting model predictions of carbon fluxes with measurements of Amazon forests subjected to experimental drought, *New Phytologist*, 200(2), 350-365.
- Prentice, I. C., X. Liang, B. E. Medlyn, and Y.-P. Wang (2015), Reliable, robust and realistic: the three R's of next-generation land-surface modelling, *Atmospheric Chemistry and Physics*, 15(10), 5987-6005.
- Raupach, M. R., P. J. Rayner, D. J. Barrett, R. S. DeFries, M. Heimann, D. S. Ojima, S. Quegan, and C. C. Schmullius (2005), Model--data synthesis in terrestrial carbon observation: methods, data requirements and data uncertainty specifications, *Global Change Biology*, 11(3), 378-397.
- Reichstein, M., J. Tenhunen, O. Roupsard, J.-M. Ourcival, S. Rambal, F. Miglietta, A. Peressotti, M. Pecchiari, G. Tirone, and R. Valentini (2003), Inverse modeling of seasonal drought effects on canopy CO₂/H₂O exchange in three Mediterranean ecosystems, *Journal of Geophysical Research: Atmospheres*, 108(D23).
- Richardson, A. D., et al. (2010), Estimating parameters of a forest ecosystem C model with measurements of stocks and fluxes as joint constraints, *Oecologia*, 164(1), 25-40.
- Ryel, R., M. Caldwell, C. Yoder, D. Or, and A. Leffler (2002), Hydraulic redistribution in a stand of *Artemisia tridentata*: evaluation of benefits to transpiration assessed with a simulation model, *Oecologia*, 130(2), 173-184.
- Shi, H., L. Li, D. Eamus, J. Cleverly, A. Huete, J. Beringer, Q. Yu, E. van Gorsel, and L. Hutley (2014), Intrinsic climate dependency of ecosystem light and water-use-efficiencies

- across Australian biomes, *Environmental Research Letters*, 9(10), 104002.
- Smith, A. B., J. P. Walker, A. W. Western, R. I. Young, K. M. Ellett, R. C. Pipunic, R. B. Grayson, L. Siriwardena, F. H. S. Chiew, and H. Richter (2012), The Murrumbidgee soil moisture monitoring network data set, *Water Resources Research*, 48(7).
- Tarantola, A. (2005), *Inverse problem theory and methods for model parameter estimation*, siam.
- Ukkola, A. M., A. J. Pitman, and M. G. De Kauwe (2016), Modelling evapotranspiration during precipitation deficits: identifying critical processes in a land surface model, *Hydrology and Earth System Sciences*, 20(6), 2403.
- van Gorsel, E., et al. (2013), Primary and secondary effects of climate variability on net ecosystem carbon exchange in an evergreen Eucalyptus forest, *Agricultural and Forest Meteorology*, 182–183, 248 - 256.
- Van Oijen, M., J. Rougier, and R. Smith (2005), Bayesian calibration of process-based forest models: bridging the gap between models and data, *Tree Physiology*, 25(7), 915-927.
- Wang, Y. P., and R. Leuning (1998), A two-leaf model for canopy conductance, photosynthesis and partitioning of available energy I: Model description and comparison with a multi-layered model, *Agricultural and Forest Meteorology*, 91(1–2), 89 - 111.
- Wang, Y. P., C. M. Trudinger, and I. G. Enting (2009), A review of applications of model--data fusion to studies of terrestrial carbon fluxes at different scales, *Agricultural and Forest Meteorology*, 149(11), 1829-1842.
- Wang, Y. P., R. Leuning, H. A. Cleugh, and P. A. Coppin (2001), Parameter estimation in surface exchange models using nonlinear inversion: how many parameters can we estimate and which measurements are most useful?, *Global Change Biology*, 7(5), 495-510.
- Wang, Y. P., E. Kowalczyk, R. Leuning, G. Abramowitz, M. R. Raupach, B. Pak, E. van

- Gorsel, and A. Luhar (2011), Diagnosing errors in a land surface model (CABLE) in the time and frequency domains, *Journal of Geophysical Research: Biogeosciences*, 116(G1).
- Willmott, C. J. (1981), ON THE VALIDATION OF MODELS, *Physical Geography*, 2(2), 184-194.
- Zhang, T., L. Li, Y. Lin, W. Xue, F. Xie, H. Xu, and X. Huang (2015), An automatic and effective parameter optimization method for model tuning, *Geoscientific Model Development*, 8(11), 3579-3591.
- Zhou, S., R. A. Duursma, B. E. Medlyn, J. W. G. Kelly, and I. C. Prentice (2013), How should we model plant responses to drought? An analysis of stomatal and non-stomatal responses to water stress, *Agricultural and forest meteorology*, 182, 204-214.

Chapter 6. Benchmarking the CABLE model using remote sensing GPP and ET products across Australia

Abstract

Land surface models (LSMs) provide lower boundary conditions for general circulation models. Both leaf area index (LAI) and soil water content (SWC) play a key role in the carbon, water and energy budgets. Therefore, reasonable representation of these two variables is central for prognostic LSMs to capture the variations of gross primary production (GPP) and evapotranspiration (ET) spatially and temporally. Here, I used two simple remote sensing GPP models and two remote sensing ET models, together with a data-driven product, to benchmark the performance of the CABLE model in a prognostic mode across Australia. CABLE greatly overestimated GPP and moderately overestimated ET in evergreen broad-leaf forests, savannas/woody savannas/C4 grasslands and the peripheral shrublands. Inappropriate prediction of photosynthetic capacity or LAI could cause the biased estimation of GPP and ET, featuring the joint control of physiological properties and canopy structures. CABLE failed to outperform the simplest EVI-based GPP model, implying the critical importance of correct representation of vegetation information, whereas the surpass of CABLE and the other remote sensing ET model over the MODIS ET product suggests information on soil water content or precipitation is important in accurate prediction of ET. CABLE could not well capture the temporal variations of LAI in the majority of arid and semi-arid regions but performed well in estimating soil water content in uppermost surface soil layer. More number of PFTs and realistic parametrization are needed to accurately estimate LAI and land surface data assimilation can help to achieve this aim.

6.1 Introduction

Land surface models (LSMs) are a key component of general circulation models, serving as a lower boundary constraining the carbon, water and energy fluxes between atmosphere and the land surface [Thornton and Zimmermann, 2007]. The presence of vegetation and root zone soil water content (SWC) is of primary importance for the partitioning of water and energy budgets [Shukla and Mintz, 1982] and the natural carbon exchanges [Tucker *et al.*, 1986]. Vegetation conditions generally include physiological parameters and leaf area index (LAI). The previous are incorporated into LSMs based on the partitioning of plant function types (PFTs), whereas LAI can be either prescribed based on field or satellite observations [Kala *et al.*, 2014] or predicted according to the prognostic leaf carbon pools and PFT-specific thresholds [Murray-Tortarolo *et al.*, 2013; Thornton and Zimmermann, 2007]. This difference divides LSMs running into diagnostic type and prognostic type [Thornton and Zimmermann, 2007].

The variation of LAI is critical for accurately estimating carbon assimilation [Kala *et al.*, 2014; Puma *et al.*, 2013], evapotranspiration (ET) [Jarlan *et al.*, 2008; van den Hurk *et al.*, 2003] and radiation [Parton *et al.*, 1996]. LAI can also influence precipitation variability through a change of the local hydrological cycle and a change of the general circulation patterns [van den Hurk *et al.*, 2003], forming a feedback from vegetation to atmosphere. In the diagnostic running, observed LAI has a strong positive correlation with gross primary production (GPP) across the PFTs [Duursma *et al.*, 2009; Keith *et al.*, 2012]. However, in the prognostic running, LAI is calculated using the leaf carbon pool depending on GPP, which in turn depends on LAI [Thornton and Zimmermann, 2007]. Therefore, accurate estimation of LAI is central to the success of prognostic LSMs.

Soil water content, particularly root zone SWC, provides key constraint on plant transpiration

and soil evaporation [Seneviratne *et al.*, 2010], and thus the energy partitioning between latent and sensible heat. Previous studies have shown that SWC can significantly impact near-surface climate, including temperature [Koster *et al.*, 2006; Seneviratne *et al.*, 2006; Zhang *et al.*, 2009] and precipitation [Koster *et al.*, 2006; Santanello Jr *et al.*, 2009], through direct and indirect interactions with atmosphere [Seneviratne *et al.*, 2010]. Soil water content is also a key variable controlling the growth of vegetation because plants take up water from soil in the root zone [De Kauwe *et al.*, 2015]. Therefore, there exists a SWC-LAI feedback, co-determining the vegetation response to environmental stress.

The Australian Community Atmosphere Biosphere Land Exchange Model (CABLE, [Kowalczyk *et al.*, 2006; Wang *et al.*, 2010; Wang *et al.*, 2011]) is a widely used land surface model, shares common features in some representation of photosynthesis and evapotranspiration processes and performs comparably with other major LSMs [Wang *et al.*, 2011]. Recently Kala *et al.* [2014] examined the effects of prescribed LAI on GPP and ET using CABLE in a diagnostic running across Australia. This research is of significant importance but perturbed prescribed LAI cannot reflect the capacity of CABLE in predicting LAI and thus its ability to estimate GPP and ET in future. Hence, here I investigate the effects of LAI and SWC on GPP and ET using CABLE in a prognostic mode. Instead of simply comparing with observations or inter-comparison of multiple LSMs, I use remote sensing models with simple empirical structures and remote sensing retrieved LAI and SWC products to benchmark the prognostic CABLE across Australia. This benchmark method can well inform us how an LSM utilizes available information including in input variables and how well an LSM should perform [Abramowitz *et al.*, 2007; Best *et al.*, 2015] both spatially and temporally. Because the most significant time-scale for vegetation of different PFTs is the seasonal variation [Wilson and Henderson-Sellers, 1985], my analysis focuses on a monthly time-step.

6.2 Data and Methods

6.2.1 Flux sites

Eddy covariance observations at 13 sites from the OzFlux network (<http://www.ozflux.org.au>) were used in this study (Table 6.1). These sites, according to the MODIS IGBP classifications (Figure 6.1a), consist of major biomes in Australia, namely savannas (SAV), woody savannas (WSA), grasslands (GRA), open shrublands (OSH), crop lands (CRO), evergreen broad-leaf forests (EBF) and wetlands (WET). Their distribution covers a variety of climate regimes, from tropical in the north to temperate in the south. Half-hourly measurements of carbon, water and energy fluxes and auxiliary meteorological and soil variables were processed using

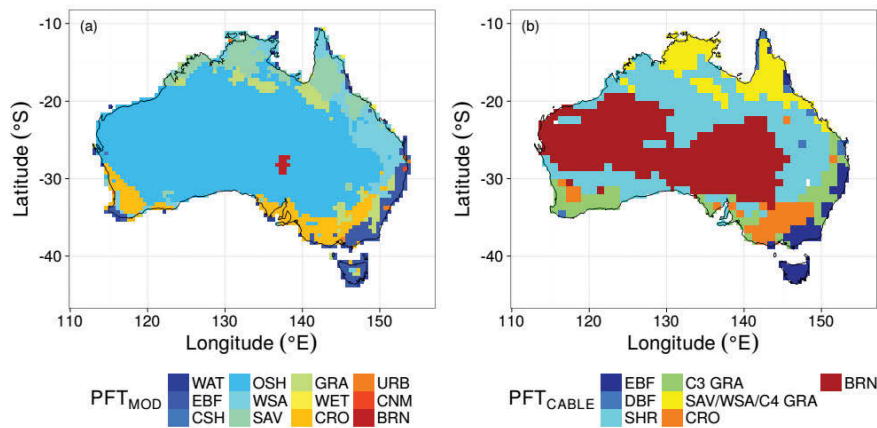


Figure 6.1. Comparison of MCD12C1 biomes and the CABLE biomes. Acronyms WAT, ENF, EBF, DBF, MF, CSH, OSH, WSA, SAV, GRA, WET, CRO, URB, CNM, SNO and BRN denote water, evergreen needleleaf forest, evergreen broadleaf forest, deciduous broadleaf forest, mixed forest, closed shrublands, open shrublands, woody savannas, savannas, grasslands, wetlands, croplands, urban and built-up, cropland/natural vegetation mosaic, snow and ice and barren or sparsely vegetated, respectively.

the dynamic integrated gap filling and partitioning for OzFlux (DINGO) system using a feed-forward artificial neural network algorithm [Beringer *et al.*, 2007]. Half-hourly GPP, ET

and associated meteorological data were aggregated into the monthly time-scale to fit the following remote sensing models.

Table 6.1. Eddy covariance data used in this study. Information includes site name (Site), latitude (Lat), longitude (Lon), vegetation type (IGBP), data observed period and reference citation

Site	Lat	Lon	IGBP	Period	Reference
Adelaide River (AU-Ade)	-13.08	131.12	SAV	2007-2008	<i>Beringer et al. [2011]</i>
Alice Springs (AU-Asm)	-22.28	133.25	OSH	2011-2012	<i>Cleverly et al. [2013]</i>
Calperum (AU-Cap)	-34.00	140.59	OSH	2010-2012	<i>Meyer et al. [2015]</i>
DalyPasture (AU-Da1)	-14.06	131.32	GRA	2007-2012	<i>Beringer et al. [2011]</i>
Daly Uncleared (AU-Da2)	-14.16	131.39	SAV	2007-2012	<i>Beringer et al. [2011]</i>
Dry River (AU-Dry)	-15.26	132.37	SAV	2008-2012	<i>Beringer et al. [2011]</i>
Fogg Dam (AU-Fog)	-12.55	131.31	WET	2007-2008	<i>Beringer et al. [2013]</i>
Howard Springs (AU-How)	-12.50	131.15	WSA	2001-2012	<i>Eamus et al. [2001]</i>
Yanco (AU-JXA)	-35.00	146.29	CRO	2012	<i>Smith et al. [2012]</i>
Sturt Plains (AU-Stp)	-17.15	133.35	GRA	2008-2012	<i>Beringer et al. [2011]</i>
Tumbarumba (AU-Tum)	-35.66	148.15	EBF	2001-2012	<i>van Gorsel et al. [2013]</i>
Wallaby Creek (AU-Wac)	-37.43	145.19	EBF	2006-2008	<i>Martin et al. [2007]</i>
Wombat (AU-Wom)	-37.42	144.09	EBF	2010-2012	<i>Griebel et al. [2016]</i>

6.2.2 Spatial data

The Moderate Resolution Imaging Spectroradiometer (MODIS) land cover product (MCD12C1, $0.05 \times 0.05^\circ$) in 2012 was used in parametrizing all the remote sensing models for estimation of GPP and ET across different biomes (Table 6.2). MOD13C2 EVI (monthly, $0.05 \times 0.05^\circ$) and MOD11C3 LST (monthly, $0.05 \times 0.05^\circ$) were also used. A value of 0.08 was subtracted from EVI to remove soil background contamination. MOD15A2 LAI (8-day, 1

$\times 1$ km) data were aggregated into the monthly time-scale. Microwave soil water content data were from the Essential Climate Variable (ECV) soil moisture product ($0.25 \times 0.25^\circ$, [Liu *et al.*, 2012; Wagner *et al.*, 2012]). The sensing depth of ECV product is the top few centimeters on average [Dorigo *et al.*, 2015] and thus it was used to compare with modelled SWC in soil layer 1 (2.8 cm depth) by the CABLE model. All the remote sensing data were resampled into a spatial resolution of $0.5 \times 0.5^\circ$.

The meteorological forcing for the CABLE model is a fusion of products by the Climate Research Unit (CRU) and the National Center for Environmental Prediction (NCEP)/National Center for Atmospheric Research (NCAR) with a sub-daily temporal resolution and a $0.5 \times 0.5^\circ$ spatial resolution [Wei *et al.*, 2014]. This CRU-NCEP dataset includes air temperature, surface pressure, air specific humidity, wind speed, downward longwave and shortwave radiations, and precipitation. The land use change map for CABLE was from Hurtt *et al.* [2011] also with a spatial resolution of $0.5 \times 0.5^\circ$ (Figure 6.1b). The major difference of this land use map from the MODIS product is that it partitions open shrublands into shrublands and barren (Figure 6.1b).

Table 6.2. Comparison of input data for various GPP and ET models. FAPAR indicates the fraction of absorbed photosynthetic active radiation (APAR), LWDown and SWDown indicate downward long- and short-wave radiation, respectively

Variable	GPP-EVI	GPP-TG	ET-TGSM	ET-MOD	CABLE	MTE
Air temperature				×	×	×
Precipitation					×	×
Potential evaporation						×
Climatic water balance						×
Sunshine hours						×
Number of wet days						×
Air humidity				×	×	×
Potential radiation						×
Net radiation				×		
Cloudiness						×
FAPAR				×		×
Albedo				×		×
Potential APAR						×
Land cover	×	×	×	×	×	×
LWDown					×	
SWDown					×	
Surface pressure				×	×	
Wind speed					×	
Land surface temperature		×	×			
Soil water content			×			
Enhanced vegetation index	×	×	×			
Leaf area index				×		

6.2.3 Remote sensing GPP models

Two remote sensing based GPP models using EVI only (GPP-EVI) and a combination of EVI and LST (GPP-TG [Sims *et al.*, 2008]) were used. Instead of the log-log relationships established in Chapter 3 of this thesis, GPP-EVI here is defined as a simple linear function:

$$GPP = a \times EVI + b \quad (18.1)$$

where a and b are empirical coefficients. GPP-TG is defined as:

$$GPP = m \times EVI \times scaled_LST \quad (18.2)$$

where m is an empirical coefficient and $scaled_LST = \min[(LST/30), (2.5 - 0.05 \times LST)]$.

6.2.4 Remote sensing ET models

The 8-day MOD16A2 ET product (1×1 km [Mu *et al.*, 2011]) was aggregated and resampled into the monthly time-scale at a spatial resolution of $0.5 \times 0.5^\circ$. The MODIS ET algorithm (ET-MOD) is based the Penman-Monteith equation [Monteith, 1964] and partitions ET into daytime soil evaporation, canopy transpiration, canopy interception and nighttime ET. Besides the MODIS ET product, the TG-SM model (ET-TGSM) developed in Chapter 4 of this thesis was also used to provide estimate of ET across Australia. Specifically, ET-TGSM is calculated as:

$$ET = \max(0, a \times EVI \times e + b \times LST \times f + \varepsilon) \quad (18.3)$$

$$e = \min\left[\left(\frac{LST}{30}\right), (2.5 - 0.05 \times LST)\right] \quad (18.4)$$

$$f = \begin{cases} 0, & \theta < \theta_{wilt} \\ \frac{\theta - \theta_{wilt}}{\theta_{crit} - \theta_{wilt}}, & \theta_{wilt} < \theta < \theta_{crit} \\ 1, & \theta > \theta_{crit} \end{cases} \quad (18.5)$$

where a , b and ε are empirical coefficients, θ is soil water content, $\theta_{wilt} = 0.05 \text{ m}^3 \text{ m}^{-3}$ and $\theta_{crit} = 0.40 \text{ m}^3 \text{ m}^{-3}$. θ was scaled to $0 \sim 1$ where it is between θ_{wilt} and θ_{crit} .

6.2.5 The CABLE Model

The CABLE (v2.0b) model is a global land surface model capable of simulating momentum, heat, water and carbon exchange between the land surface and the lower atmosphere [Kowalczyk *et al.*, 2006; Wang *et al.*, 2011]. Wang *et al.* [2010] incorporated nitrogen and phosphorus cycles into the CABLE while Li *et al.* [2012] included a dynamic root water uptake function [Lai and Katul, 2000] and a hydrological redistribution function [Ryel *et al.*, 2002] to improve model performance in response to water stress. In this study, I used this improved version of CABLE with optimized parameters (Table 6.3) obtained in Chapter 5. The CABLE model calculates GPP using a one-layered, two-leaf canopy model through coupling of stomatal conductance and photosynthesis [Wang and Leuning, 1998; Wang *et al.*, 2011]. ET is modeled based on the Penman-Monteith equation. Hourly CABLE outputs were aggregated into a monthly time-step. Hereafter, GPP and ET estimated by CABLE are written as GPP-CABLE and ET-CABLE, respectively. Different from Chapter 5 in which observed MODIS LAI was input at the site level, this study used prognostic LAI estimated by CABLE at the regional scale. LAI is predicted through specific leaf area varying among PFTs and a carbon-nitrogen cycling model that can simulate leaf carbon. Besides, LAI is regulated by prescribed PFT-specific maximum and minimum LAI thresholds, and also modelled phenology status. LAI is important as it is used to upscale leaf photosynthesis and transpiration to canopy level and intercepts considerable precipitation. The meteorological inputs for CABLE can be seen in Table 6.2.

6.2.6 Data-driven product

Jung et al. [2009] upscaled FLUXNET measurements into global products (monthly, $0.5 \times 0.5^\circ$) using the model tree ensemble (MTE) approach, which have been widely used in land surface modeling and climate change research [Beer et al., 2010; Bonan et al., 2011]. The MTE method took advantage of a large number of input variables, including meteorological forcing, vegetation states and biome types. Table 6.2 shows comparisons of input variables for above remote sensing models, the CABLE model and MTE products. The MTE estimated GPP (GPP-MTE) and ET (ET-MTE) during the period from 2001 to 2011 were taken as “true” values to serve as the standard to assess other models.

6.2.7 Statistical metrics

Two statistical metrics were used to analyze the performance of models. They are coefficient of determination (R^2) and root mean squared error (RMSE). R^2 is calculated as:

$$R^2 = \frac{(\sum_{n=1}^N (O_n - \bar{O})(P_n - \bar{P}))^2}{\sum_{n=1}^N (O_n - \bar{O})^2 \sum_{n=1}^N (P_n - \bar{P})^2} \quad (6)$$

where \bar{O} and \bar{P} are means of observed and modeled variables, O_n and P_n are the observed and modeled fluxes at the time step n , and N is the total number of observations. RMSE is calculated as:

$$RMSE = \sqrt{\frac{\sum_{n=1}^N (P_n - O_n)^2}{N}} \quad (7)$$

Table 6.3. Key parameters used in CABLE for evergreen broad-leaf forests (EBF), open shrublands (OSH), C4 grasslands/savannas/woody savannas (C4 GRA/SAV/WSA), C3 croplands (C3 CRO), C3 grasslands (C3 GRA) and barren soils (BRN). Soil 1 is coarse sand/loamy sand, soil 2 is medium clay loam/silty clay loam/silt loam, and soil 3 is coarse-medium sandy loam/loam. V_{cmax} is the maximum RuBP carboxylation rate at canopy top at a leaf temperature of 25 °C, a_1 is an empirical parameter in leaf stomatal model, α is the initial slope of leaf response curve of potential electron transport rate to absorbed quantum flux, G_0 is the stomatal conductance for water when leaf net photosynthesis is 0, β_r is a parameter for estimating vertical root mass distribution in soil, and v is an empirical parameter in hydraulic conductivity function

Vegetation	EBF	OSH	C4 GRA/SAV/WSA	C3 CRO	C3 GRA	BRN
V_{cmax}	4.96e-5	3.90e-5	5.40e-5	3.35e-5	3.35e-5	5.31e-5
a_1	5.54	9.52	4.6	9.97	9.97	9.52
A	0.16	0.12	0.20	0.23	0.23	0.12
G_0	1.18e-2	0.01	7.13e-3	0.01	0.01	0.01
β_r	0.99	0.92	0.93	0.98	0.98	0.92
Soil	Soil 1	Soil 2	Soil 3	Others		
N	1.51	1.46	1.89	2.06		

6.3 Results

6.3.1 Temporal benchmarking

Figure 6.2 shows comparisons of monthly GPP, LAI and PC by different models across Australia from 2001 to 2011. Remote sensing models and CABLE all overestimated monthly GPP, particularly CABLE (Figure 6.2a). The simplest model GPP-EVI correlated best ($R^2 =$

0.46) with GPP-MTE. Inclusion of LST in GPP-TG further decreased RMSE at the cost of a slight decrease of R^2 (Table 6.4). This improvement benefited mainly from effective constraint of LST on EVI when GPP was low (Figure 6.2a). In contrast, the most complex CABLE model performed poorest using metrics of both R^2 and RMSE (Table 6.4, Figure 6.2a). However, all models could capture the exceptional large carbon assimilation during 2011 [Poulter et al., 2014; Ahlström et al., 2015]. Since the difference of land cover maps for remote sensing models and the CABLE model was basically consistent (Figure 6.1), land use change could not explain the poor performance of CABLE in estimating temporal monthly GPP. To investigate the reason, I compared LAI-CABLE with LAI-MOD and also the photosynthetic capacities (ratio of GPP over LAI) of all GPP models. The LAI-CABLE was nearly twice of the LAI-MOD (Figure 6.2b) whereas PC-CABLE (also RMSE) was intermediate between PC-EVI and PC-TG (Figure 6.2c) and correlated best with PC-MTE (Table 6.4), suggesting the overestimation of LAI was the major cause of the large RMSE between GPP-CABLE and GPP-MTE (Table 6.4). The product of PC-CABLE and LAI-MOD greatly decreased the bias (Figure 6.2a), further implying the inappropriate prediction of LAI in CABLE.

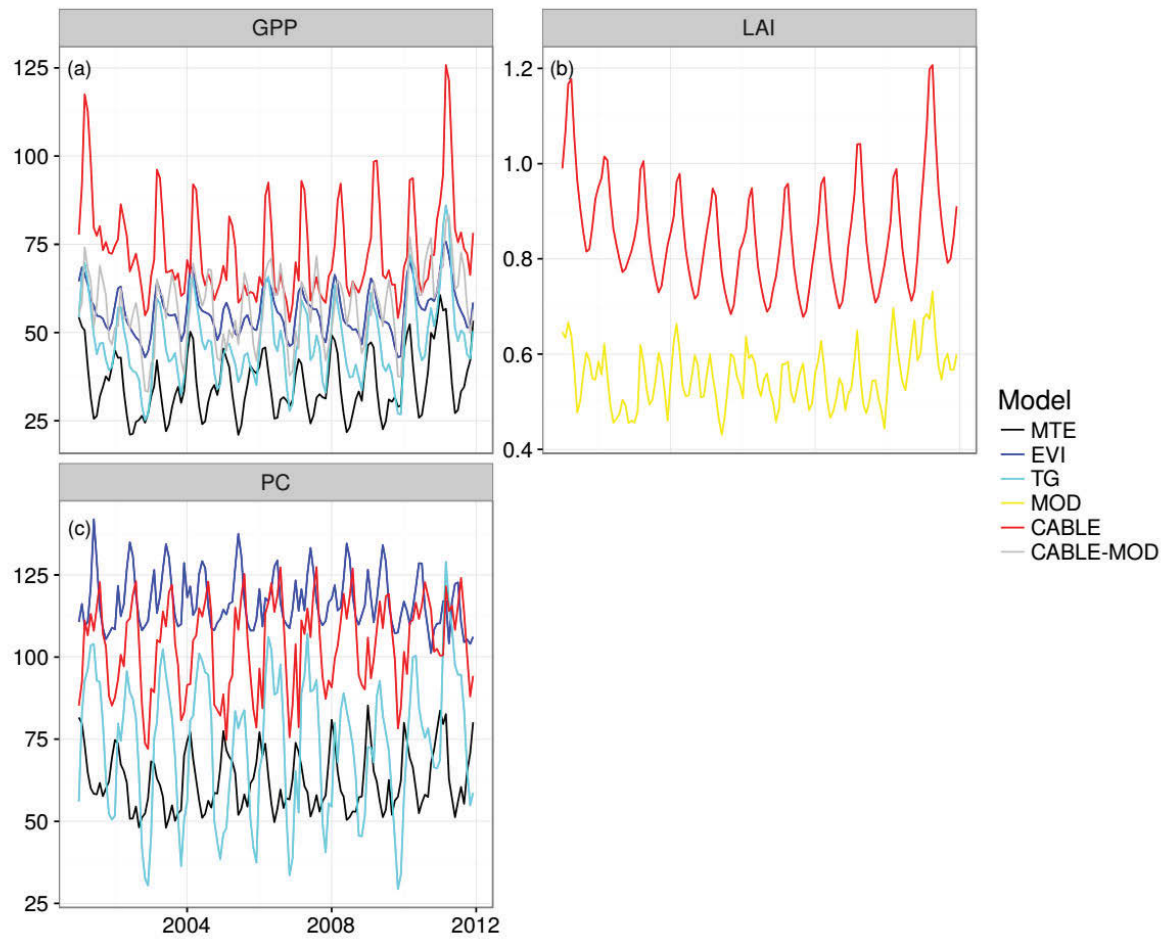


Figure 6.2. Monthly gross primary production (GPP), leaf area index (LAI) and photosynthetic capacity (PC, the ratio of GPP over LAI) of different models across Australia from 2001 to 2011. The gray line indicates the product of PC-CABLE and LAI-MOD.

Table 6.4. Statistical metrics for the performance of models on estimating GPP, ET, LAI and SWC. For spatial statistics, the significance level is calculated as the percent of pixels with significant correlations against object data at a p level of 0.05

Model	Temporal			Spatial			“True”
	R^2	RMSE	p	R^2	RMSE	Sig %	
GPP-EVI	0.46	21.9	0.001	0.51	26.2	93.0%	GPP-MTE
GPP-TG	0.42	15.1	0.001	0.47	23.5	93.5%	GPP-MTE
GPP-CABLE	0.23	39.9	0.001	0.12	60.7	56.9%	GPP-MTE
PC-EVI	0.07	56.5	0.01	0.17	63.7	57.5%	GPP-MTE/LAI-MOD
PC-TG	0.01	26.7	NS	0.15	43.0	57.7%	GPP-MTE/LAI-MOD
PC-CABLE	0.13	45.5	0.001	0.11	50.9	46.8%	GPP-MTE/LAI-MOD
ET-TGSM	0.83	5.1	0.001	0.57	13.8	100.0%	ET-MTE
ET-MOD	0.62	10.3	0.001	0.46	14.1	84.7%	ET-MTE
ET-CABLE	0.87	17.7	0.001	0.59	24.7	99.6%	ET-MTE
LAI-CABLE	0.27	0.3	0.001	0.12	0.7	54.5%	LAI-MOD
SWC-CABLE	0.62	0.04	0.001	0.51	0.05	99.6%	SWC-ECV

Similar to GPP, CABLE overestimated ET but mainly during the periods when ET was high (Figure 6.3a). In contrast to GPP, ET-CABLE correlated best with ET-MTE ($R^2 = 0.87$) but with the largest RMSE (Table 6.4). ET-TGSM performed much better than ET-MOD featuring including SWC information is important in estimating ET. Compared to satellite retrieved SWC-ECV, CABLE modelled SWC performed well in both R^2 and RMSE (Table 6.4, Figure 6.3b). Compared to ET-MOD with similar algorithms and meteorological inputs (Table 6.2), ET-CABLE performed better when ET was low (Figure 6.3a), further showing the significant constraint of SWC on ET estimation.

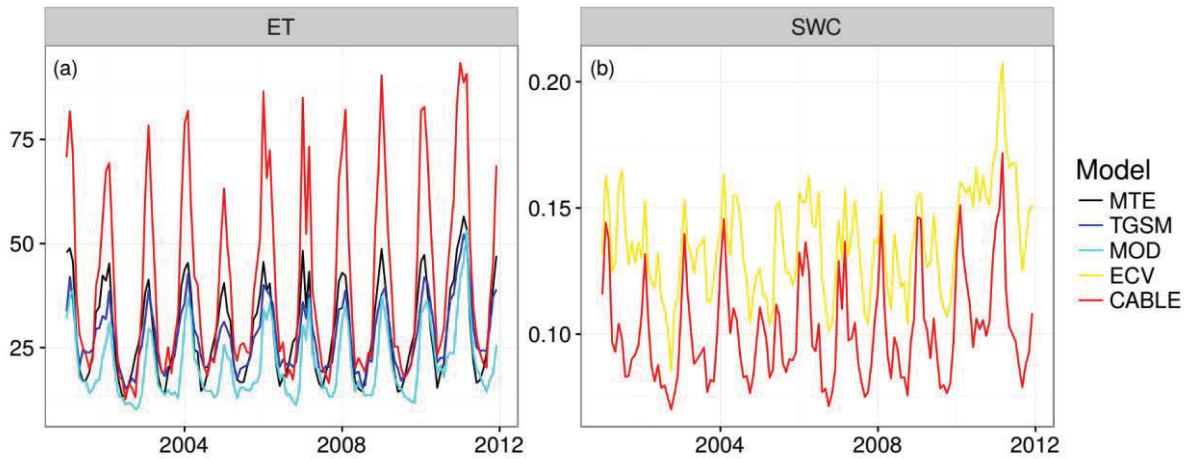


Figure 6.3. Monthly evapotranspiration (ET) and surface soil water content (SWC) of different models across Australia from 2001 to 2011.

6.3.2 Spatial benchmarking

Figure 6.4 shows the spatial patterns of average monthly GPP by all models. Compared with GPP-MTE, both GPP-EVI and GPP-TG overestimated GPP along the east and north coasts and transition regions from coast to inland (Figures 6.4b and 6.4c), where EBF and savannas/woody savannas/C4 grasslands dominate. GPP-EVI also slightly overestimated GPP in inland area. GPP-CABLE showed the largest bias in comparison with GPP-MTE (Figure 6.4d). The major bias occurred in EBF and peripheral areas of shrublands classified according to the CABLE land use map (Figure 6.1b). The spatial statistical analysis showed that GPP-CABLE performed poorest with mean R^2 of 0.12 and only 56.9% significant pixels (Table 6.4, Figure 6.5c). The insignificant pixels were mostly shrublands and barren regions, featuring the deficit of CABLE in arid and semi-arid environments. However, large RMSE also occurred for EBF and SAV/WSA/C4 GRA (Figure 6.5f). The two remote sensing GPP models failed mainly in the west and south central open shrublands (Figures 6.5a and 6.5b) according to the MODIS IGBP classifications (Figure 6.1a), suggesting the challenge for both

remote sensing models and LSMs in estimating GPP in context of water stress.

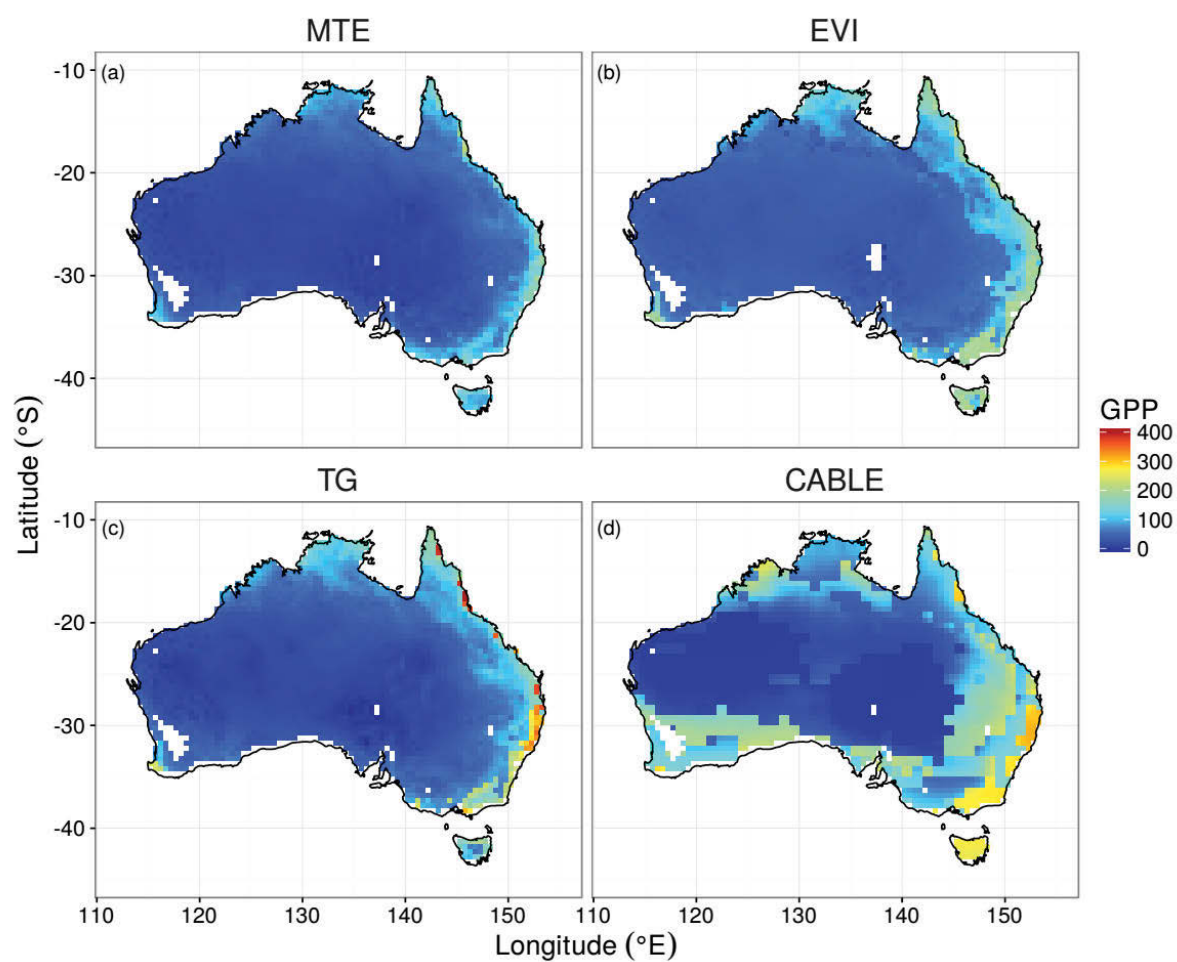


Figure 6.4. Average monthly gross primary production (GPP) calculated from different models from 2001 to 2011. The unit is $\text{gC m}^{-2} \text{ month}^{-1}$.

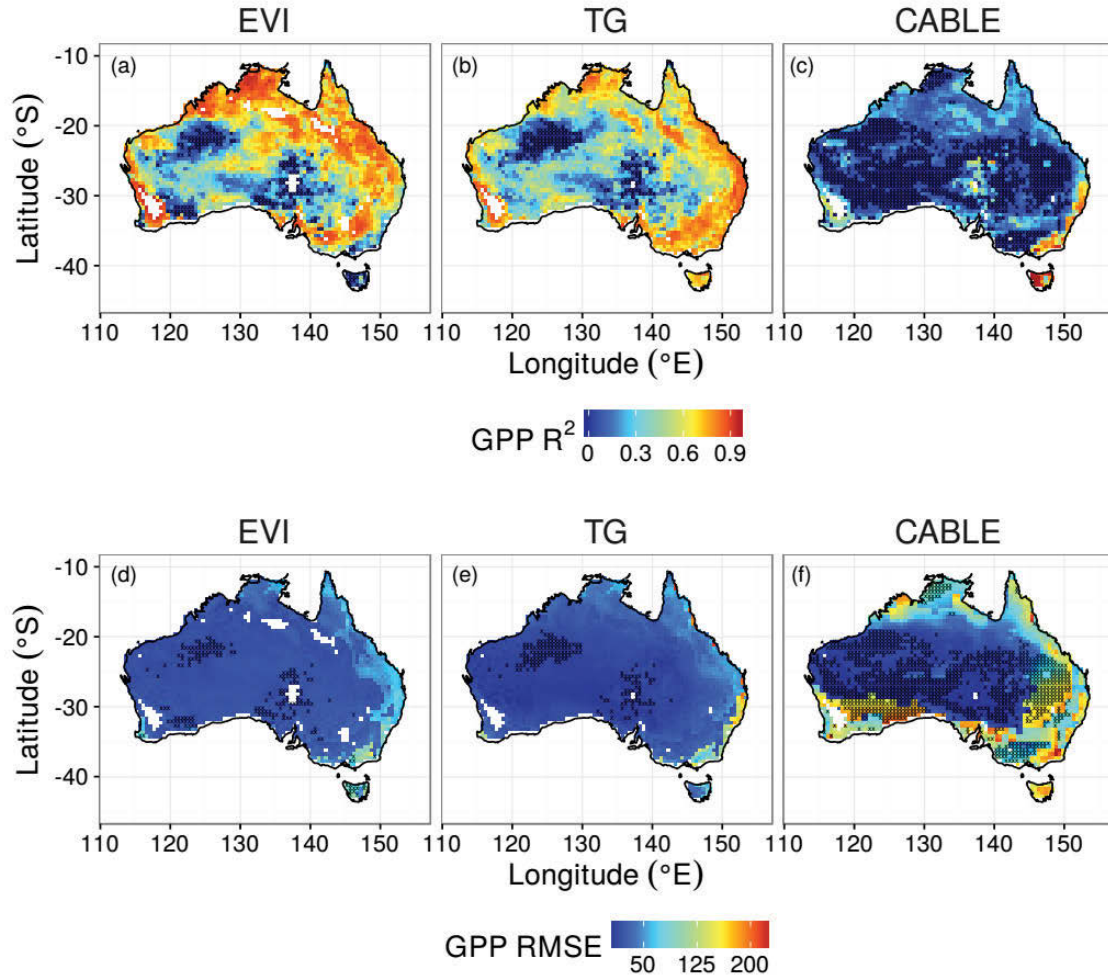


Figure 6.5. The spatial distribution of per-pixel correlations and RMSE between GPP-EVI, GPP-TG, GPP-CABLE and GPP-MTE. The cross symbols indicate the correlation is not statistically significant at a p level of 0.05.

Both remote sensing models and CABLE failed to capture the variation of photosynthetic capacity in inland regions (Figures 6.6 and 6.7). In contrast to remote sensing models, CABLE also showed poor performance in SAV/WSA/C4 GRA located in the north using metrics of both R^2 and RMSE (Figures 6.6d, 6.7c and 6.7f). However, both PC-CABLE and PC-TG obtained a smaller RMSE than PC-EVI across Australia (Table 6.4, Figure 6.7), showing the effect of LST or temperature on limiting PC.

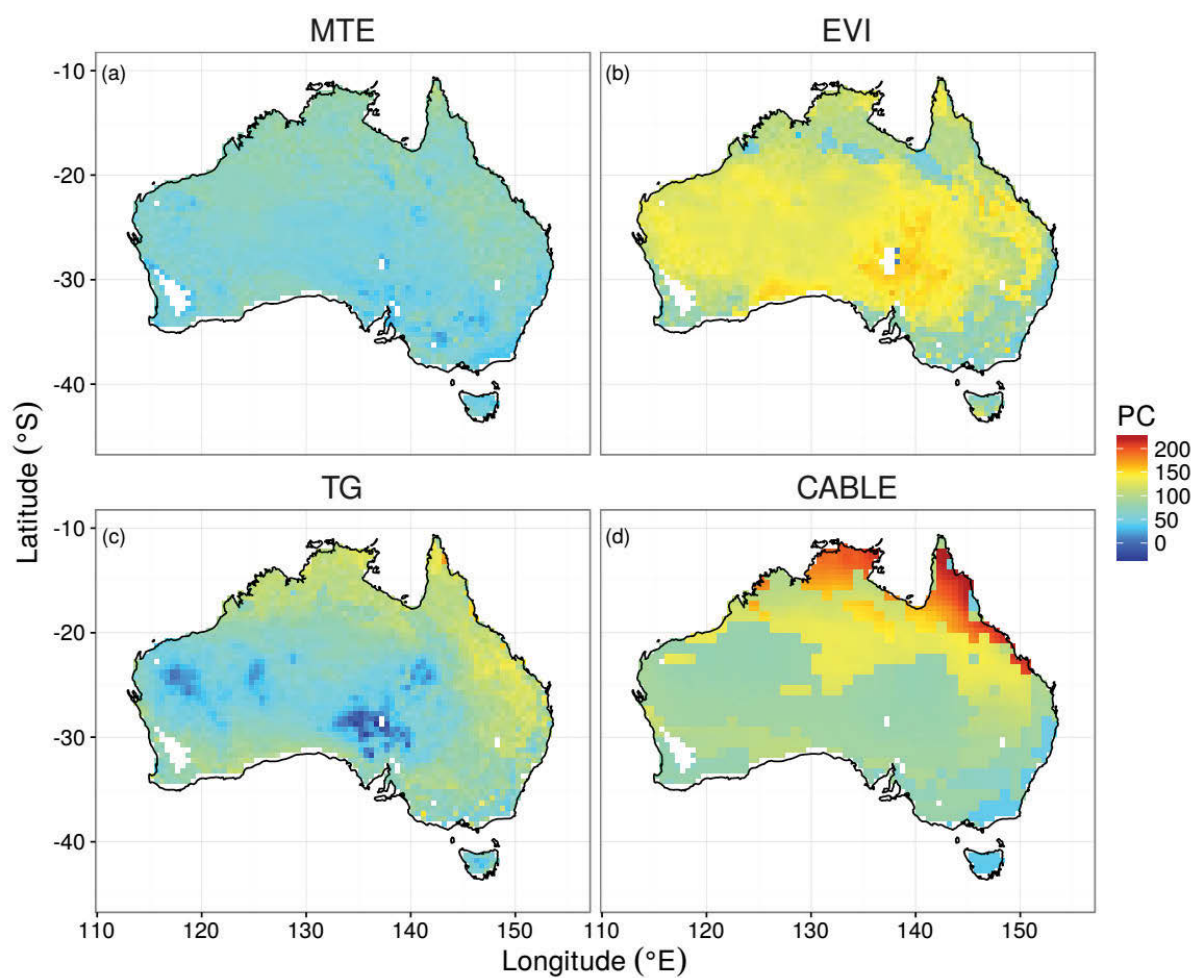


Figure 6.6. Average monthly photosynthetic capacity (GPP/LAI) calculated from different models from 2001 to 2011. The unit is $\text{gC LAI}^{-1} \text{ month}^{-1}$.

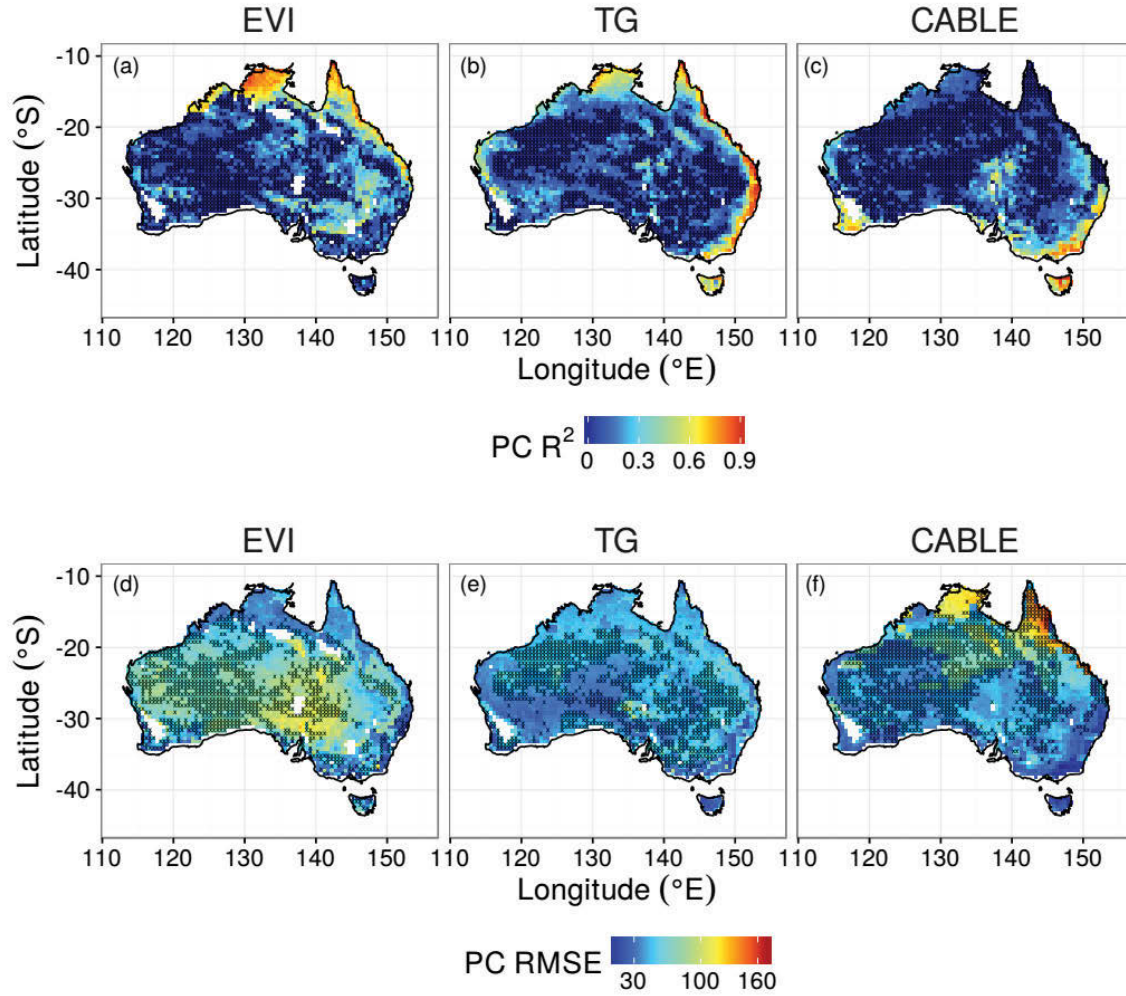


Figure 6.7. The spatial distribution of per-pixel correlations and RMSE between PC-EVI, PCTG, PC-CABLE and PC-MTE. The cross symbols indicate the correlation is not statistically significant at a p level of 0.05.

The reasons for bias between GPP-CABLE and GPP-MTE were different. For EBF, CABLE overestimated LAI (Figure 6.8b) but with a small bias of PC (Figure 6.7f). For peripheral areas of shrublands, CABLE both overestimated LAI (Figure 6.8b) and PC (Figure 6.6d). For SAV/WSA/C4 GRA, LAI-CABLE was underestimated (Figure 6.8b) while PC-CABLE had largest positive bias compared to PC-MTE (Figures 6.6d and 6.7f), leading to considerable RMSE of GPP (Figure 6.5f) though the effects of LAI and PC counteracted (Figure 6.5f). The

spatial statistical analysis showed that CABLE failed to capture the temporal variations of LAI in the majority of shrublands and barren regions (Figure 6.9a) though the RMSE was relatively small (Figure 6.9c). The largest bias (9a) between LAI-CABLE and LAI-MOD occurred in EBF whereas the best correlation were in SAV/WSA/C4 GRA regions (Figure 6.9c).

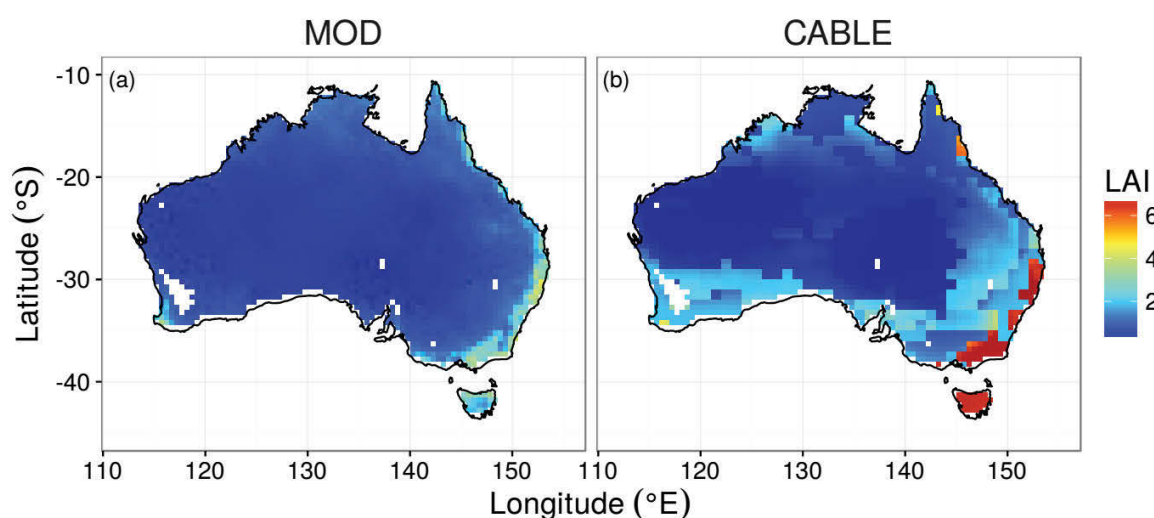


Figure 6.8. Average monthly leaf area index (LAI) calculated from the MCD12C1 product and the CABLE estimation during the period of 2001 to 2011.

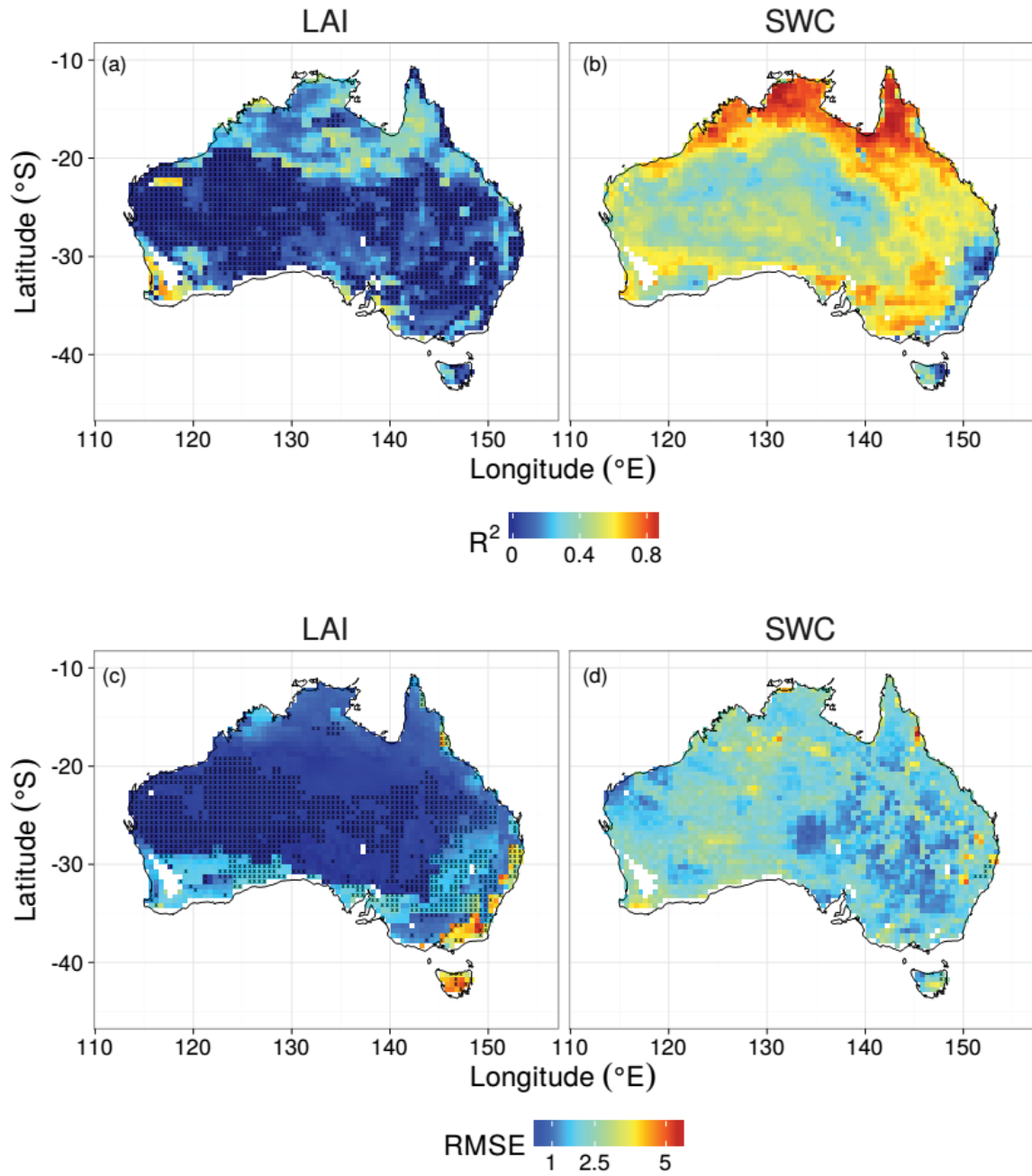


Figure 6.9. The spatial distribution of per-pixel correlations and RMSE between estimated LAI and SWC by the CABLE model with LAI-MOD and SWC-ECV products. The RMSE between SWC-CABLE and SWC-ECV is multiplied by 40. The cross symbols indicate the correlation is not statistically significant at a p level of 0.05.

Both remote sensing models and CABLE performed much better in estimating ET than GPP.

Figure 6.10 shows that ET-TGSM, ET-MOD and CABLE could capture the gradual decrease of ET from coast to inland. ET-CABLE correlated best with ET-MTE across Australia ($R^2 = 0.59$, Figure 6.11c) but with the largest RMSE (Table 6.4, Figure 6.11f). The bias between ET-CABLE and ET-MTE mainly occurred in EBF and northern regions (Figures 6.10d and 6.11f), where LAI-CABLE (Figure 6.8b) and PC-CABLE (Figure 6.6d) were largely overestimated, respectively. ET-TGSM obtained a slightly lower R^2 than ETCABLE but with only half of the RMSE of the latter (Table 6.4), featuring the importance of including vegetation information (EVI in ET-TGSM) in estimating ET according to the comparison of inputs into these two models (Table 6.2). Compared to SWC-ECV, CABLE underestimated SWC mainly in inland regions (Figures 6.9d and 6.12b). Compared to ETTGSM with SWC as input and ET-CABLE with precipitation as input, ET-MOD had no variable related to soil water status as input (Table 6.2). This resulted in the failure of ET-MOD to capture the temporal variations of ET in the southern part of shrublands and barren regions (15.3% of the total pixels, Figure 6.11b) and further its poorest correlation with ET-MTE. But ET-MOD still obtained a much smaller RMSE than ET-CABLE (Table 6.4), featuring the deficit of CABLE in estimating LAI.

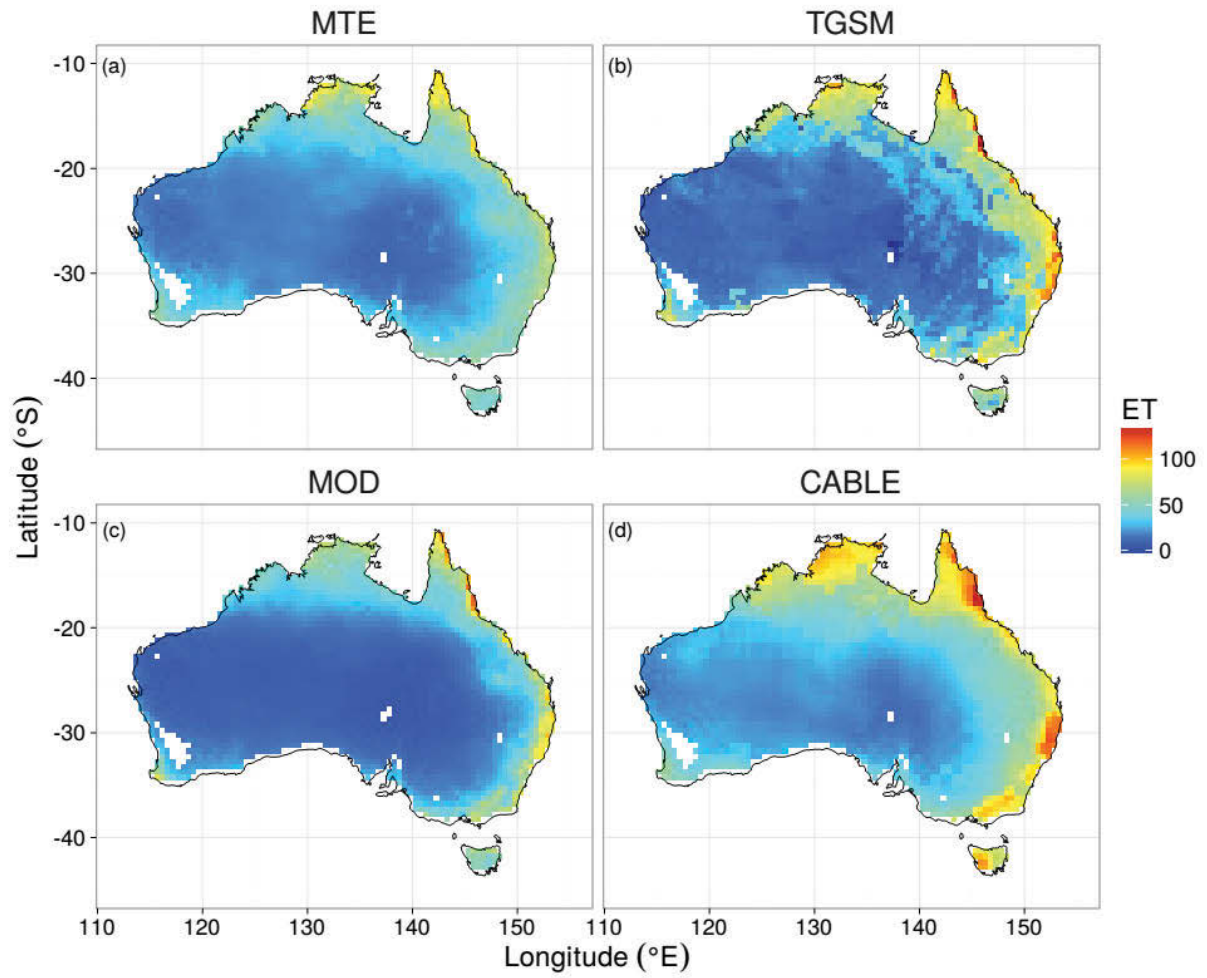


Figure 6.10. Average monthly evapotranspiration (ET) calculated from different models from 2001 to 2011. The unit is mm month⁻¹.

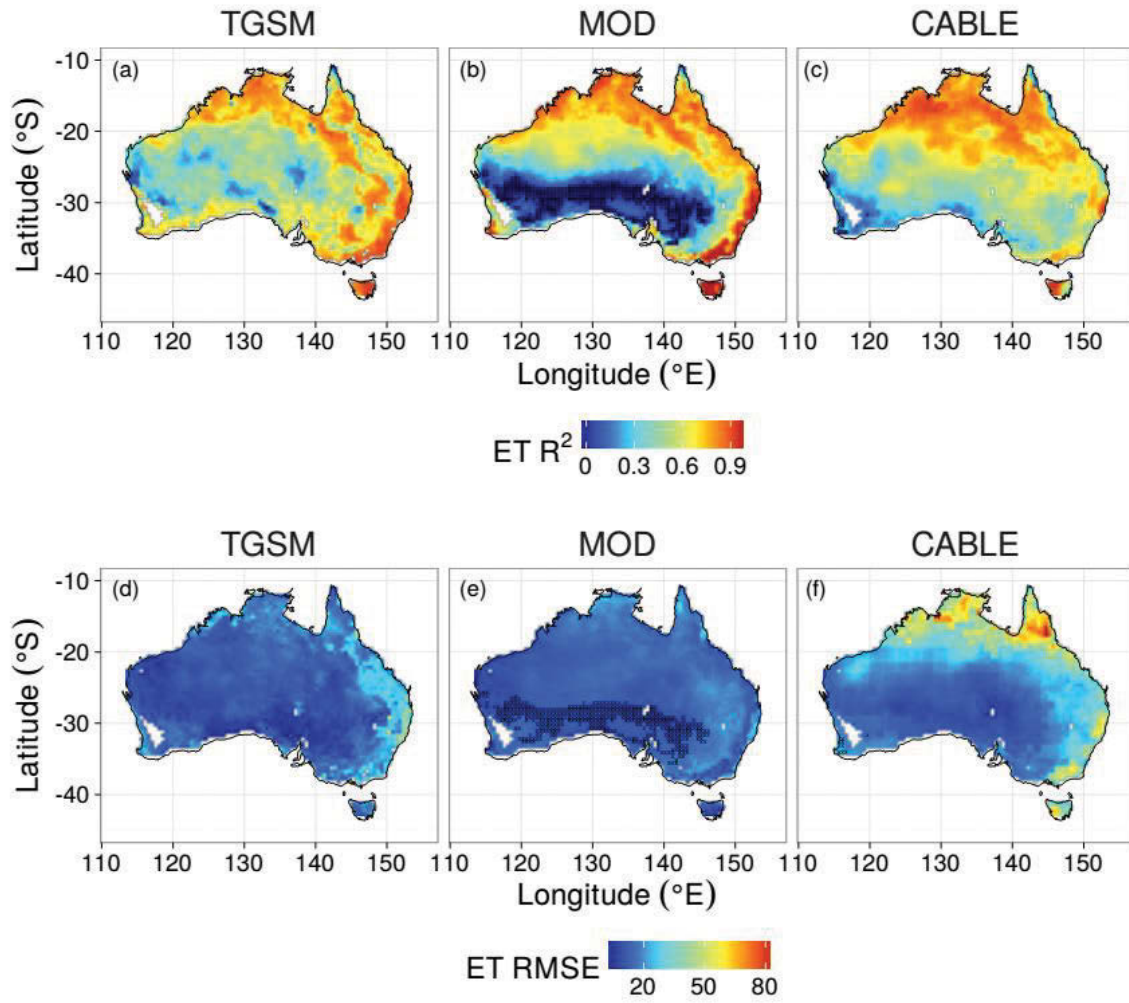


Figure 6.11. The spatial distribution of per-pixel correlations and RMSE between ET-TGSM, ET-MOD, ET-CABLE and ET-MTE. The cross symbols indicate the correlation is not statistically significant at a p level of 0.05.

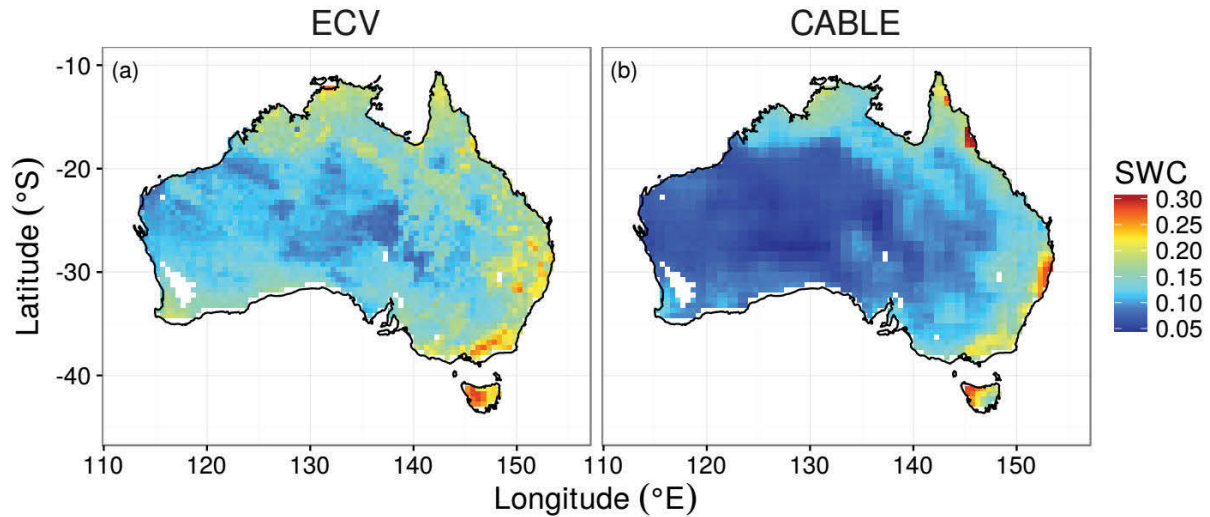


Figure 6.12. Average monthly soil water content (SWC) at soil surface layer calculated from the ECV product and the CABLE estimation during the period of 2001 to 2011.

6.4 Discussion

The result that the CABLE model, with complex structures and a large number of meteorological inputs, failed to outperform the simplest EVI-based remote sensing model in estimating GPP is not expected. The unrealistic LAI estimation in EBF (Figure 6.8b), photosynthetic capacity estimation in SAV/WSA/C4 GRA (Figure 6.6d), and both in peripheral areas of shrublands (Figures 6.6d and 6.8b) were the main causes. High photosynthetic capacity means high canopy conductance per LAI while high LAI is correlated to high total canopy conductance [van den Hurk *et al.*, 2003]. Therefore, they are strongly positively correlated with GPP consistent with both observational [Keith *et al.*, 2012; Wong *et al.*, 1979] and modelling [Duursma *et al.*, 2009; Kala *et al.*, 2014; Lu *et al.*, 2013; Puma *et al.*, 2013] evidences. However, the underlying mechanisms of PC and LAI influencing GPP are different in LSMs. PC is mostly regulated by maximum RuBP carboxylation rate (V_{cmax}), the initial slope of the leaf response curve of potential electron transport rate to absorbed quantum

flux (α), an empirical parameter in leaf stomatal model (a_1) and the minimum stomatal conductance when net photosynthesis is 0 (G_0) in CABLE [Wang *et al.*, 2011], whereas LAI determines the absorbed amount of photosynthetically active radiation [Kala *et al.*, 2014]. A sensitivity analysis of CABLE at the global scale also proved the primary importance of above physiological parameters for PC and LAI across various PFTs [Lu *et al.*, 2013], further implying the correct representation of vegetation information is vital for LSMs to simulate the carbon assimilation.

Because of the tight coupling between ET and GPP [Beer *et al.*, 2009], ET-CABLE was also affected by the biased estimation of LAI and PC. However, the impacts of LAI and PC on ET were much more moderate than that on GPP, consistent with previous studies in west Africa [Jarlan *et al.*, 2008] and Australia [Kala *et al.*, 2014]. LAI plays a vital role in the partitioning of surface energy into latent and sensible heat fluxes [Barbu *et al.*, 2011; Bonan *et al.*, 1993; van den Hurk *et al.*, 2003] through controlling canopy transpiration and precipitation interception. High LAI can result in a relatively large portion of the available energy for transpiration in wet conditions but favors soil evaporation in dry conditions [van den Hurk *et al.*, 2003]. This is the reason that the same changes in LAI could not induce a large variation of ET as well as GPP in Australia, of which a large portion is arid and semi-arid. Kala *et al.* [2014] reported a similar result with perturbed prescribed LAI as input for a diagnostic version of CABLE. In addition, LAI can influence surface albedo and thus the amount of available energy for ET [Kala *et al.*, 2014]. Apart from LAI, root zone soil moisture is also vital for partitioning of water and energy through root water uptake process for plant transpiration [Shukla and Mintz, 1982]. As surface soil water content can be well correlated with that in soil profile under specific conditions, it is reasonable to infer that CABLE well modelled deep soil water as well as its performance in the uppermost surface soil layer (Figure 6.9b and 9d). The overestimation of ET in inland regions (Figure 6.10d) was

compensated by underestimated soil water content (Figure 6.12b), implying a significant ET-SWC feedback in Australia. This result strongly supports the finding that over half of the water in Australia is lost through soil evaporation instead of plant transpiration [Haverd *et al.*, 2013]. Furthermore, the better performance of CABLE and TG-SM than the MODIS ET product features that soil water or precipitation information is critically important for ET estimation.

Similar to GPP, CABLE performed poor in estimating LAI, in particular in arid and semi-arid regions (Figures 6.9a and 6.9c). This result features the deficits of CABLE in response to water stress and the LAI prediction needs incorporating various environmental stress in future. Previous studies also found that the majority of land surface models overestimate LAI in the high-latitude northern hemisphere either running offline using observed meteorological forcing [Murray-Tortarolo *et al.*, 2013] or running offline with self-generated climatology by the coupled climate model [Anav *et al.*, 2013]. Both studies pointed out that inappropriate parametrization of PFTs is the major reason for biased LAI and LSMs need to incorporate more accurate PFTs. For example, temperate EBF is different from tropical EBF and thus current parametrization of a unique EBF PFT across the globe is incorrect. Actually, current LSMs are built around the concept of PFTs although the simple partitioning of a diversity of vegetation has long been criticized [Alton, 2011]. But as I explained in Chapter 5 of this thesis, large-scale varying site-specific parameters are generally not accessible and thus the simplification into limited PFTs is still necessary. Increase of the number of PFTs is a reasonable compromise between limited PFTs and site-specific parametrization. However, this approach can increase a large number of parameters and bring new uncertainties, though it is towards a more realistic representation of different PFTs. Land surface data assimilation as used in Chapter 5 of this thesis, originating from the numerical weather prediction [Jarlan *et al.*, 2008], can effectively address this concern. Barbu *et al.* [2011] assimilated soil wetness

index and LAI into an LSM at a grassland site and obtained an improvement of 13% of the root zone soil water content and corrected low LAI values in the senescence phase. In another example, [Jarlan *et al.* [2008]] assimilated LAI in modeling carbon and water processes in west Africa and compared simulations with MODIS products, concluding that a LAI data assimilation is essential for carbon prediction at seasonal and inter-annual time-scales while it may be sufficient for climatology only to predict ET in the light of the moderate effect of LAI on ET.

6.5 Conclusions

In this study, two remote sensing GPP models and two remote sensing ET models, together with a data-driven product, were used to benchmark the CABLE model in estimating GPP and ET. CABLE failed to outperform the simplest EVI-based GPP model, implying the critical importance of correct representation of vegetation information. Both inappropriate prediction of photosynthetic capacity (characterized by physiological parameters) and LAI could cause the biased estimation of GPP and ET, featuring the joint control of physiological properties and canopy structures. However, their impacts on ET were much more moderate than that on GPP. The surpassing of CABLE and the TG-SM model over the MODIS product suggests that information on soil water content or precipitation is important in accurate prediction of ET. Spatially, the biased GPP and ET were mainly induced by the overestimation of LAI in evergreen broad-leaf forests, by the overestimation of photosynthetic capacity in savannas/woody savannas/C4 grasslands, and biased estimation of both in shrublands. CABLE failed to capture the temporal variations of LAI in the majority of arid and semi-arid regions but performed well in estimating soil water content in uppermost surface soil layer. More number of PFTs and associated parameters are needed to accurately estimate LAI and

land surface data assimilation can help to achieve this aim.

Acknowledgments. This research was supported by an Australian Research Council Discovery Early Career Research Award (project number DE120103022). This work used eddy covariance data acquired by the OzFlux community.

References

- Abramowitz, G., A. Pitman, H. Gupta, E. Kowalczyk, and Y. Wang (2007), Systematic bias in land surface models, *Journal of Hydrometeorology*, 8(5), 989-1001.
- Alton, P. B. (2011), How useful are plant functional types in global simulations of the carbon, water, and energy cycles?, *Journal of Geophysical Research: Biogeosciences*, 116(G1).
- Anav, A., G. Murray-Tortarolo, P. Friedlingstein, S. Sitch, S. Piao, and Z. Zhu (2013), Evaluation of land surface models in reproducing satellite Derived leaf area index over the high-latitude northern hemisphere. Part II: Earth system models, *Remote Sensing*, 5(8), 3637-3661.
- Barbu, A. L., J.-C. Calvet, J.-F. Mahfouf, C. Albergel, and S. Lafont (2011), Assimilation of Soil Wetness Index and Leaf Area Index into the ISBA-A-gs land surface model: grassland case study, *Biogeosciences*, 8(7), 1971-1986.
- Beer, C., et al. (2009), Temporal and among-site variability of inherent water use efficiency at the ecosystem level, *Global biogeochemical cycles*, 23(2).
- Beringer, J., L. B. Hutley, N. J. Tapper, and L. A. Cernusak (2007), Savanna fires and their impact on net ecosystem productivity in North Australia, *Global Change Biology*, 13(5), 990-1004.
- Beringer, J., S. J. Livesley, J. Randle, and L. B. Hutley (2013), Carbon dioxide fluxes dominate the greenhouse gas exchanges of a seasonal wetland in the wet-tropics of

- northern Australia, *Agricultural and Forest Meteorology*, 182, 239-247.
- Beringer, J., et al. (2011), SPECIAL—Savanna Patterns of Energy and Carbon Integrated across the Landscape, *Bulletin of the American Meteorological Society*, 92(11), 1467-1485.
- Best, M. J., et al. (2015), The plumbing of land surface models: benchmarking model performance, *Journal of Hydrometeorology*, 16(3), 1425-1442.
- Bonan, G. B., D. Pollard, and S. L. Thompson (1993), Influence of subgrid-scale heterogeneity in leaf area index, stomatal resistance, and soil moisture on grid-scale land-atmosphere interactions, *Journal of Climate*, 6(10), 1882-1897.
- Cleverly, J., N. Boulain, R. Villalobos-Vega, N. Grant, R. Faux, C. Wood, P. G. Cook, Q. Yu, A. Leigh, and D. Eamus (2013), Dynamics of component carbon fluxes in a semi-arid Acacia woodland, central Australia, *Journal of Geophysical Research: Biogeosciences*, 118(3), 1168-1185.
- De Kauwe, M. G., S.-X. Zhou, B. E. Medlyn, A. J. Pitman, Y.-P. Wang, R. A. Duursma, and I. C. Prentice (2015), Do land surface models need to include differential plant species responses to drought?: Examining model predictions across a mesic-xeric gradient in Europe, *Biogeosciences*, 12(24), 7503-7518.
- Dorigo, W. A., et al. (2015), Evaluation of the ESA CCI soil moisture product using ground-based observations, *Remote Sensing of Environment*, 162, 380-395.
- Duursma, R. A., et al. (2009), Contributions of climate, leaf area index and leaf physiology to variation in gross primary production of six coniferous forests across Europe: a model-based analysis, *Tree physiology*, 29(5), 621-639.
- Eamus, D., L. B. Hutley, and A. P. O'Grady (2001), Daily and seasonal patterns of carbon and water fluxes above a north Australian savanna, *Tree Physiology*, 21(12-13), 977-988.
- Griebel, A., L. T. Bennett, D. Metzen, J. Cleverly, G. Burba, and S. K. Arndt (2016), Effects

- of inhomogeneities within the flux footprint on the interpretation of seasonal, annual, and interannual ecosystem carbon exchange, *Agricultural and Forest Meteorology*, 221, 50-60.
- Haverd, V., M. Raupach, P. Briggs, J. Canadell, P. Isaac, C. Pickett-Heaps, S. Roxburgh, E. v. Gorsel, R. Viscarra Rossel, and Z. Wang (2013), Multiple observation types reduce uncertainty in Australia's terrestrial carbon and water cycles, *Biogeosciences*, 10(3), 2011-2040.
- Hurt, G. C., et al. (2011), Harmonization of land-use scenarios for the period 1500-2100: 600 years of global gridded annual land-use transitions, wood harvest, and resulting secondary lands, *Climatic change*, 109(1-2), 117-161.
- Jarlan, L., G. Balsamo, S. Lafont, A. Beljaars, J.-C. Calvet, and E. Mougin (2008), Analysis of leaf area index in the ECMWF land surface model and impact on latent heat and carbon fluxes: Application to West Africa, *Journal of Geophysical Research: Atmospheres*, 113(D24).
- Kala, J., M. Decker, J.-F. Exbrayat, A. J. Pitman, C. Carouge, J. P. Evans, G. Abramowitz, and D. Mocko (2014), Influence of leaf area index prescriptions on simulations of heat, moisture, and carbon fluxes, *Journal of Hydrometeorology*, 15(1), 489-503.
- Keith, H., E. Van Gorsel, K. L. Jacobsen, and H. A. Cleugh (2012), Dynamics of carbon exchange in a Eucalyptus forest in response to interacting disturbance factors, *Agricultural and Forest Meteorology*, 153, 67-81.
- Koster, R. D., et al. (2006), GLACE: the global land-atmosphere coupling experiment. Part I: overview, *Journal of Hydrometeorology*, 7(4), 590-610.
- Kowalczyk, E. A., Y. P. Wang, and E. M. Law (2006), The CSIRO Atmospheric Biosphere Land Exchange (CABLE) model for use in climate models and as an offline model, *Tech. Pap. 013, CSIRO Mar. and Atmos. Res., Aspendale, Vic., Australia*.

- Lai, C.-T., and G. Katul (2000), The dynamic role of root-water uptake in coupling potential to actual transpiration, *Advances in Water Resources*, 23(4), 427-439.
- Li, L., Y.-P. Wang, Q. Yu, B. Pak, D. Eamus, J. Yan, E. van Gorsel, and I. T. Baker (2012), Improving the responses of the Australian community land surface model (CABLE) to seasonal drought, *J. Geophys. Res.*, 117(G4).
- Liu, Y. Y., W. A. Dorigo, R. M. Parinussa, R. A. M. d. Jeu, W. Wagner, M. F. McCabe, J. P. Evans, and A. I. J. M. v. Dijk (2012), Trend-preserving blending of passive and active microwave soil moisture retrievals, *Remote Sensing of Environment*, 123, 280-297.
- Lu, X., Y.-P. Wang, T. Ziehn, and Y. Dai (2013), An efficient method for global parameter sensitivity analysis and its applications to the Australian community land surface model (CABLE), *Agr. Forest Meteorol.*, 182–183(0), 292-303.
- Martin, D., J. Beringer, L. B. Hutley, and I. McHugh (2007), Carbon cycling in a mountain ash forest: Analysis of below ground respiration, *Agricultural and Forest Meteorology*, 147(1&2), 58-70.
- Meyer, W., E. Kondrlovà, and G. Koerber (2015), Evaporation of perennial semi-arid woodland in southeastern Australia is adapted for irregular but common dry periods, *Hydrological Processes*, 29(17), 3714-3726.
- Monteith, J. L. (1964), Evaporation and environment, paper presented at Symposia of the society for experimental biology.
- Mu, Q., M. Zhao, and S. W. Running (2011), Improvements to a MODIS global terrestrial evapotranspiration algorithm, *Remote Sensing of Environment*, 115(8), 1781-1800.
- Murray-Tortarolo, G., et al. (2013), Evaluation of land surface models in reproducing satellite-derived LAI over the high-latitude Northern Hemisphere. Part I: Uncoupled DGVMs, *Remote Sensing*, 5(10), 4819-4838.
- Parton, W. J., A. Haxeltine, P. Thornton, R. Anne, and M. Hartman (1996), Ecosystem

- sensitivity to land-surface models and leaf area index, *Global and Planetary Change*, 13(1), 89-98.
- Puma, M. J., R. D. Koster, and B. I. Cook (2013), Phenological versus meteorological controls on land-atmosphere water and carbon fluxes, *Journal of Geophysical Research: Biogeosciences*, 118(1), 14-29.
- Ryel, R., M. Caldwell, C. Yoder, D. Or, and A. Leffler (2002), Hydraulic redistribution in a stand of *Artemisia tridentata*: evaluation of benefits to transpiration assessed with a simulation model, *Oecologia*, 130(2), 173-184.
- Santanello Jr, J. A., C. D. Peters-Lidard, S. V. Kumar, C. Alonge, and W.-K. Tao (2009), A modeling and observational framework for diagnosing local land-atmosphere coupling on diurnal time scales, *Journal of Hydrometeorology*, 10(3), 577-599.
- Seneviratne, S. I., D. Lüthi, M. Litschi, and C. Schär (2006), Land-atmosphere coupling and climate change in Europe, *Nature*, 443(7108), 205-209.
- Seneviratne, S. I., T. Corti, E. L. Davin, M. Hirschi, E. B. Jaeger, I. Lehner, B. Orlowsky, and A. J. Teuling (2010), Investigating soil moisture–climate interactions in a changing climate: A review, *Earth-Science Reviews*, 99(3–4), 125-161.
- Shukla, J., and Y. Mintz (1982), Influence of land-surface evapotranspiration on the earth's climate, *Science*, 215(4539), 1498-1501.
- Sims, D. A., et al. (2008), A new model of gross primary productivity for North American ecosystems based solely on the enhanced vegetation index and land surface temperature from MODIS, *Remote Sensing of Environment*, 112(4), 1633-1646.
- Smith, A. B., J. P. Walker, A. W. Western, R. I. Young, K. M. Ellett, R. C. Pipunic, R. B. Grayson, L. Siriwardena, F. H. S. Chiew, and H. Richter (2012), The Murrumbidgee soil moisture monitoring network data set, *Water Resources Research*, 48(7).
- Thornton, P. E., and N. E. Zimmermann (2007), An improved canopy integration scheme for a

- land surface model with prognostic canopy structure, *Journal of Climate*, 20(15), 3902-3923.
- Tucker, C. J., I. Y. Fung, C. D. Keeling, and R. H. Gammon (1986), Relationship between atmospheric CO₂ variations and a satellite-derived vegetation index, *Nature*, 319, 195-199.
- van den Hurk, B. J., P. Viterbo, and S. O. Los (2003), Impact of leaf area index seasonality on the annual land surface evaporation in a global circulation model, *Journal of Geophysical Research: Atmospheres*, 108(D6).
- van Gorsel, E., et al. (2013), Primary and secondary effects of climate variability on net ecosystem carbon exchange in an evergreen Eucalyptus forest, *Agricultural and Forest Meteorology*, 182–183(0), 248-256.
- Wagner, W., W. Dorigo, R. de Jeu, D. Fernandez, J. Benveniste, E. Haas, and M. Ertl (2012), Fusion of Active and Passive Microwave Observations to Create AN Essential Climate Variable Data Record on Soil Moisture, *ISPRS Annals of Photogrammetry, Remote Sensing and Spatial Information Sciences*, 315-321.
- Wang, Y.-P., and R. Leuning (1998), A two-leaf model for canopy conductance, photosynthesis and partitioning of available energy I:: Model description and comparison with a multi-layered model, *Agricultural and Forest Meteorology*, 91(1&2), 89-111.
- Wang, Y. P., R. M. Law, and B. Pak (2010), A global model of carbon, nitrogen and phosphorus cycles for the terrestrial biosphere, *Biogeosciences*, 7(7), 2261-2282.
- Wang, Y. P., E. Kowalczyk, R. Leuning, G. Abramowitz, M. R. Raupach, B. Pak, E. van Gorsel, and A. Luhar (2011), Diagnosing errors in a land surface model (CABLE) in the time and frequency domains, *Journal of Geophysical Research: Biogeosciences*, 116(G1), G01034.
- Wei, Y., et al. (2014), The North American Carbon Program Multi-scale Synthesis and

Terrestrial Model Intercomparison Project?Part 2: Environmental driver data, *Geoscientific Model Development*, 7(6), 2875-2893.

Wilson, M. F., and A. Henderson-Sellers (1985), A global archive of land cover and soils data for use in general circulation climate models, *Journal of Climatology*, 5(2), 119-143.

Wong, S. C., I. R. Cowan, and G. D. Farquhar (1979), Stomatal conductance correlates with photosynthetic capacity.

Zhang, J., W.-C. Wang, and L. Wu (2009), Land-atmosphere coupling and diurnal temperature range over the contiguous United States, *Geophysical Research Letters*, 36(6).

Chapter 7. General discussion and conclusions

7.1 General discussion

7.1.1 Coupling of GPP and ET across Australian biomes

GPP and ET are tightly coupled and their ratio, water use efficiency (WUE) is proportional to the reciprocal of square root of vapor pressure deficit ($1/\sqrt{D}$) [Zhou *et al.*, 2014], the reciprocal of D [Beer *et al.*, 2009; Sinclair *et al.*, 1984] or leaf area index (LAI) [Hu *et al.*, 2008] within biomes. Huxman *et al.* [2004] and Campos *et al.* [2013] proved the convergence of rain use efficiency and WUE using above-ground productivity across biomes, respectively. I investigated WUE relationships with various climate and vegetation variables across seven Australian sites along a precipitation gradient (Chapter 2). These sites cover major Australian biomes such as savannas, C4 grasslands and evergreen broadleaf forests. Half-hourly GPP and ET were decomposed into daily, 8-day, monthly and annual frequencies. My results showed that WUE was strongly correlated with D over daily to annual time-scales across biomes. Simultaneously, I found that the ratio of GPP over radiation, light use efficiency (LUE), was also strongly correlated with D across biomes. These intrinsic climate dependency reveals the impacts of climate variability on ecosystem functioning. Meanwhile, WUE can act as an effective boundary condition to constrain optimization of land surface models (Chapter 5) because the intrinsic dependence of WUE on D allows WUE to rapidly reflect ecosystem responses to water stress.

7.1.2 EVI-based GPP model

Remote sensing models for estimating GPP are generally of LUE type, which down-regulates maximum LUE using various climate scalars and then multiplies absorbed photosynthetic

available radiation [Verma *et al.*, 2014; Xiao *et al.*, 2004; Zhao *et al.*, 2005]. However, these LUE models are not effective across all biomes and are often limited by coarse meteorological inputs at large spatial scales [Rahman *et al.*, 2005; Sims *et al.*, 2006; Sjöström *et al.*, 2011]. In chapter 3, I investigated the potential of EVI alone to estimate annual GPP within biomes. My results showed that EVI alone can well capture inter-annual variations of GPP within the majority of biomes. The accuracy of EVI-based GPP model was limited by the complexity of ecosystem structures across biomes. The EVI-based model provides a simple but robust tool for estimating GPP over large spatial scales and can serve as a metric to benchmark complex land surface models (Chapter 6).

7.1.3 TG-SM ET model

Remote sensing methods in estimation of ET include empirical models based on vegetation indices and meteorological inputs, thermal temperature-based surface energy balance models and physical models such as the Penman-Monteith [Leuning *et al.*, 2008; Mu *et al.*, 2011] type or Priestley-Taylor type [e.g., Guerschman *et al.*, 2009]. Thermal models are very sensitive to the accuracy of land surface temperature while physical models need complex parameterization and large amount of inputs data, which bring considerable uncertainty to these two types of models. Empirical models regressing ET against vegetation indices and meteorological inputs are generally location specific and lacks mechanistic explanation of each component in the fitted equations. Furthermore, over large spatial scales, empirical models can be limited by coarse meteorological inputs as well as physical models [Yang *et al.*, 2013]. Unlike GPP, EVI or other vegetation indices alone perform poorly in estimating ET [Yebra *et al.*, 2013] because ET consists of canopy transpiration, canopy interception and soil evaporation. Variations of the latter two items, particularly soil evaporation, cannot be well captured by vegetation greenness index. Therefore, a simple but robust remote sensing ET

model is needed. According to the classical energy-limited and water-limited ET regimes, I added an energy scalar to EVI and included a soil item to estimate ET, solely based on remote sensing EVI, LST and microwave soil moisture (TG-SM). This model showed good performance across Australian seasonally water-limited ecosystems (Chapter 4) and also other types of ecosystems such as forests (Chapter 6). The most important is that the model can provide both temperature and soil water information to benchmark complex land surface models to inform existing deficits in LSMs.

7.1.4 Optimization of the CABLE model

Two advantages of land surface models over remote sensing methods are that they can provide short-term predictions of GPP and ET and states of variables such as soil water table and vegetation carbon pools, which are usually not visible to observers (e.g., flux towers and satellites). Furthermore, LSMs can predict changes of ecosystem functioning in future. However, the prerequisite for LSMs performing as a positive role is that they are well parameterized and structured. Otherwise, model uncertainty existing in one time-step can be propagated into and amplified in following time-steps and leads to apparent “drifts” [Pijanowski *et al.*, 2011]. In chapter 5, I used the Bayesian Monte Carlo Markov Chain method to identify and optimize the key processes of GPP and ET in the CABLE model with eddy covariance observed carbon and water fluxes as constraints. My results featured the impacts of below-ground processes such as hydrological redistribution on modelling GPP and ET. Also I raised suggestions to improve CABLE model and strengthen the constraint conditions in optimization method.

7.1.5 Benchmarking CABLE using remote sensing products

Land surface models generally include complex processes and a number of inputs data, such as meteorological forcing, land cover map, soil map and also leaf area index in some occasions. This complexity of LSMs hinders distinguishing which process contributes most when the model performs poorly. In contrast, remote sensing models of GPP and ET have limited inputs and processes. Benchmarking the LSMs with remote sensing products can tell how effectively the complex LSMs utilize available information in the inputs and which process should be improved [Abramowitz, 2005; Best *et al.*, 2015; Luo *et al.*, 2012]. In Chapter 6, I calculated GPP using EVI alone (GPP-EVI, Chapter 3) and the TG model in combination of LST and EVI [Sims *et al.*, 2008], and calculated ET using the TG-SM model (Chapter 4) and resampled MOD16A2 ET product into a spatial resolution of $0.5^\circ \times 0.5^\circ$ in Australia. The widely used model tree ensemble based GPP (GPP-MTE) and ET (ET-MTE) products [Jung *et al.*, 2009] were taken as the “true” values. These remote sensing GPP and ET products were then used to benchmark CABLE GPP and ET. CABLE modeled LAI and SWC at surface soil layer (2.2 cm) were compared with MODIS LAI and microwave ECV soil moisture product, respectively. Further, the photosynthetic capacity (PC, GPP per LAI) of CABLE and remote sensing products (remote sensing GPP per MODIS LAI) were calculated to determine which of PC and LAI contributed mainly to the biases between CABLE GPP, remote sensing products and the “true” GPP values.

7.2 Future research

There have been over 850 flux towers around the world and these towers have collected a large volume of carbon, water, energy fluxes and meteorological data. Although the number of flux towers is still increasing, the more important task is how to fully utilize the information

included in current available datasets. One direction is to upscale tower flux observations into large spatial scales using process-based [e.g., *Desai et al.*, 2010] or data-driven approaches [e.g., *Jung et al.*, 2009]. However, there is still no available fine-scale (sub-hourly) product over large regions and issues that observed energy imbalance [*Foken*, 2008; *Stoy et al.*, 2013] and the mismatch between flux tower footprint and remote sensing or model grids are ignored. *Xu et al.* [2017] recently proposed that the environmental response function approach [*Metzger et al.*, 2013] combining process-based and data-driven methods can be used to upscale flux tower observations into grids at a sub-hourly resolution with explicit consideration of variations of flux footprints. This is an advance in up-scaling flux data but more efforts are needed to produce available global fine scale products. The other direction is to prove or uncover the underlying ecological mechanisms using flux datasets. There have been many studies in this aspect. For example, *Eamus et al.* [2013] analyzed seasonal responses of WUE to rainfall events in an arid savanna woodland. *Zhou et al.* [2014] used flux data from AmeriFlux to evidence the concept of underlying water use efficiency across biomes. Chapter 2 of this thesis is also of this kind. However, there are still many problems to elucidate on ecosystem responses to environmental drivers due to nonlinear feedbacks among vegetation, soil and atmosphere at multiple scales [*Katul et al.*, 2007; *Levin*, 1992; *Paschalis et al.*, 2015; *Thornton et al.*, 2014]. The transfer of impacts of short-term meteorological variability to long-term scales and vice versa is also worth further research [*Paschalis et al.*, 2015].

New available remote sensing data and methods are emerging. To be noted are the applications of sun-induced fluorescence (SIF) as a probe of photosynthesis and unmanned aerial systems (UAS) filling the gap between the plot/site scale and the regional scale. SIF, as a signal emitted by vegetation photosynthesis actively, effectively complements reflectance-based vegetation indices such as EVI [*Guanter et al.*, 2014]. UAS can get

hyperspectral imagery at a finer time resolution than satellites. How to effectively apply these new available data and methods into analysis of GPP and ET in joint with traditional remote sensing data (e.g., EVI and LST) is a priority in future research. Integrating various remote sensing data within sophisticated framework is an option just as Chapter 4 of this thesis.

Chapter 5 and Chapter 6 featured the deficit of LSMs in arid and sub-arid regions. The modelling community have achieved significant progress in improving the model performance in response to water stress induced by droughts, heatwaves or high temperature [De Kauwe *et al.*, 2015; Decker, 2015; Li *et al.*, 2012; Luo *et al.*, 2013]. However, further improvements of LSMs are still required in parametrizing interactions between biological and hydrological processes and below-ground root processes [Pitman, 2003; Prentice *et al.*, 2015]. Understanding the mechanisms underlying observed patterns at different scales is the key to achieve this goal [Levin, 1992]. Moreover, Prentice *et al.* [2015] proposed that benchmarking (Chapter 6) and optimization (Chapter 5) of LSMs should be as a standard step in developing LSMs to test accuracy of models' parameters and structures. To be noted is the idea of traits-based ecological models. Current LSMs are built on the concept of plant functional types [Lavorel *et al.*, 1997], within which vegetation traits are generally assumed to be constant. In contrast, traits-based models allow variations of vegetation traits to reflect vegetation acclimation and adaptation to the changing environment and feedback mechanisms between them [van Bodegom *et al.*, 2014]. There have been implementations of fully traits-based models independent of LSMs for analyzing ecosystem productivity [Fyllas *et al.*, 2014] and global vegetation distribution [van Bodegom *et al.*, 2014]. For LSMs, vegetation traits, such as leaf mass per area, leaf lifespan and leaf nitrogen concentration, can be used to constrain model predictions to reduce uncertainties [Wang *et al.*, 2012]. These studies show the large potential of vegetation traits in development of next-generation LSMs.

Besides the separate developments of eddy covariance (Chapter 2), remote sensing (Chapters

3 and 4) and LSMs (Chapter 5), joint use of these three approaches (Chapter 6) are extremely important to elucidate patterns and underlying mechanisms of GPP and ET at various scales of space and time and thus to guide field experiments [Medlyn *et al.*, 2016] or improve LSMs' performance [Beer *et al.*, 2010; Blyth *et al.*, 2010; Bonan *et al.*, 2011; Medlyn *et al.*, 2015; Stöckli *et al.*, 2008; Williams *et al.*, 2009]. My results provide an example and contribute new insights for resolving patterns of GPP and ET at various scales using the three approaches individually and jointly.

References

- Abramowitz, G. (2005), Towards a benchmark for land surface models, *Geophysical Research Letters*, 32(22).
- Beer, C., P. Ciais, M. Reichstein, D. Baldocchi, B. Law, D. Papale, J.-F. Soussana, C. Ammann, N. Buchmann, and D. Frank (2009), Temporal and among-site variability of inherent water use efficiency at the ecosystem level, *Global Biogeochemical Cycles*, 23(2), GB2018.
- Beer, C., M. Reichstein, E. Tomelleri, P. Ciais, M. Jung, N. Carvalhais, C. Rödenbeck, M. A. Arain, D. Baldocchi, and G. B. Bonan (2010), Terrestrial gross carbon dioxide uptake: global distribution and covariation with climate, *Science*, 329(5993), 834-838.
- Best, M., G. Abramowitz, H. Johnson, A. Pitman, G. Balsamo, A. Boone, M. Cuntz, B. Decharme, P. Dirmeyer, and J. Dong (2015), The plumbing of land surface models: benchmarking model performance, *Journal of Hydrometeorology*, 16(3), 1425-1442.
- Blyth, E., J. Gash, A. Lloyd, M. Pryor, G. P. Weedon, and J. Shuttleworth (2010), Evaluating the JULES land surface model energy fluxes using FLUXNET data, *Journal of Hydrometeorology*, 11(2), 509-519.
- Bonan, G. B., P. J. Lawrence, K. W. Oleson, S. Levis, M. Jung, M. Reichstein, D. M.

- Lawrence, and S. C. Swenson (2011), Improving canopy processes in the Community Land Model version 4 (CLM4) using global flux fields empirically inferred from FLUXNET data, *Journal of Geophysical Research: Biogeosciences*, 116(G2).
- Campos, G. E. P., M. S. Moran, A. Huete, Y. Zhang, C. Bresloff, T. E. Huxman, D. Eamus, D. D. Bosch, A. R. Buda, and S. A. Gunter (2013), Ecosystem resilience despite large-scale altered hydroclimatic conditions, *Nature*, 494(7437), 349-352.
- De Kauwe, M., S.-X. Zhou, B. Medlyn, A. Pitman, Y.-P. Wang, R. Duursma, and I. Prentice (2015), Do land surface models need to include differential plant species responses to drought? Examining model predictions across a mesic-xeric gradient in Europe, *Biogeosciences*, 12(24), 7503-7518.
- Decker, M. (2015), Development and evaluation of a new soil moisture and runoff parameterization for the CABLE LSM including subgrid-scale processes, *Journal of Advances in Modeling Earth Systems*, 7(4), 1788-1809.
- Desai, A. R., B. R. Helliker, P. R. Moorcroft, A. E. Andrews, and J. A. Berry (2010), Climatic controls of interannual variability in regional carbon fluxes from top-down and bottom-up perspectives, *Journal of Geophysical Research: Biogeosciences*, 115(G2).
- Eamus, D., J. Cleverly, N. Boulain, N. Grant, R. Faux, and R. Villalobos-Vega (2013), Carbon and water fluxes in an arid-zone *Acacia* savanna woodland: An analyses of seasonal patterns and responses to rainfall events, *Agricultural and Forest Meteorology*, 182–183(0), 225-238.
- Foken, T. (2008), The energy balance closure problem: an overview, *Ecological Applications*, 18(6), 1351-1367.
- Fyllas, N., E. Gloor, L. Mercado, S. Sitch, C. Quesada, T. Domingues, D. Galbraith, A. Torre-Lezama, E. Vilanova, and H. Ramírez-Angulo (2014), Analysing Amazonian forest productivity using a new individual and trait-based model (TFS v. 1), *Geoscientific Model*

Development, 7(4), 1251-1269.

- Guanter, L., Y. Zhang, M. Jung, J. Joiner, M. Voigt, J. A. Berry, C. Frankenberg, A. R. Huete, P. Zarco-Tejada, and J.-E. Lee (2014), Global and time-resolved monitoring of crop photosynthesis with chlorophyll fluorescence, *Proceedings of the National Academy of Sciences*, 111(14), E1327-E1333.
- Guerschman, J. P., A. I. J. M. V. Dijk, G. Mattersdorf, J. Beringer, L. B. Hutley, R. Leuning, R. C. Pipunic, and B. S. Sherman (2009), Scaling of potential evapotranspiration with MODIS data reproduces flux observations and catchment water balance observations across Australia, *Journal of Hydrology*, 369(1&2), 107-119.
- Hu, Z., G. Yu, Y. Fu, X. Sun, Y. Li, P. Shi, Y. Wang, and Z. Zheng (2008), Effects of vegetation control on ecosystem water use efficiency within and among four grassland ecosystems in China, *Global Change Biology*, 14(7), 1609-1619.
- Huxman, T. E., M. D. Smith, P. A. Fay, A. K. Knapp, M. R. Shaw, M. E. Loik, S. D. Smith, D. T. Tissue, J. C. Zak, and J. F. Weltzin (2004), Convergence across biomes to a common rain-use efficiency, *Nature*, 429(6992), 651-654.
- Jung, M., M. Reichstein, and A. Bondeau (2009), Towards global empirical upscaling of FLUXNET eddy covariance observations: validation of a model tree ensemble approach using a biosphere model, *Biogeosciences*, 6(10), 2001-2013.
- Katul, G., A. Porporato, and R. Oren (2007), Stochastic dynamics of plant-water interactions, *Annual review of ecology, evolution, and systematics*, 767-791.
- Lavorel, S., S. McIntyre, J. Landsberg, and T. Forbes (1997), Plant functional classifications: from general groups to specific groups based on response to disturbance, *Trends in Ecology & Evolution*, 12(12), 474-478.
- Leuning, R., Y. Q. Zhang, A. Rajaud, H. Cleugh, and K. Tu (2008), A simple surface conductance model to estimate regional evaporation using MODIS leaf area index and the

- Penman-Monteith equation, *Water Resources Research*, 44(10), W10419.
- Levin, S. A. (1992), The problem of pattern and scale in ecology: the Robert H. MacArthur award lecture, *Ecology*, 73(6), 1943-1967.
- Li, L., Y. P. Wang, Q. Yu, B. Pak, D. Eamus, J. Yan, E. Gorsel, and I. T. Baker (2012), Improving the responses of the Australian community land surface model (CABLE) to seasonal drought, *Journal of Geophysical Research: Biogeosciences*, 117(G4).
- Luo, X., X. Liang, and H. R. McCarthy (2013), VIC+ for water-limited conditions: A study of biological and hydrological processes and their interactions in soil-plant-atmosphere continuum, *Water Resources Research*, 49(11), 7711-7732.
- Luo, Y., J. T. Randerson, G. Abramowitz, C. Bacour, E. Blyth, N. Carvalhais, P. Ciais, D. Dalmonech, J. B. Fisher, and R. Fisher (2012), A framework for benchmarking land models, *Biogeosciences*, 9(10).
- Medlyn, B. E., S. Zaehle, M. G. De Kauwe, A. P. Walker, M. C. Dietze, P. J. Hanson, T. Hickler, A. K. Jain, Y. Luo, and W. Parton (2015), Using ecosystem experiments to improve vegetation models, *Nature Climate Change*, 5(6), 528-534.
- Medlyn, B. E., M. G. De Kauwe, S. Zaehle, A. P. Walker, R. A. Duursma, K. Luus, M. Mishurov, B. Pak, B. Smith, and Y. P. Wang (2016), Using models to guide field experiments: a priori predictions for the CO₂ response of a nutrient-and water-limited native Eucalypt woodland, *Global change biology*.
- Metzger, S., W. Junkermann, M. Mauder, K. Butterbach-Bahl, B. Trancón y Widemann, F. Neidl, K. Schäfer, S. Wieneke, X. Zheng, and H. Schmid (2013), Spatially explicit regionalization of airborne flux measurements using environmental response functions, *Biogeosciences*, 10(4), 2193-2217.
- Mu, Q., M. Zhao, and S. W. Running (2011), Improvements to a MODIS global terrestrial evapotranspiration algorithm, *Remote Sensing of Environment*, 115(8), 1781-1800.

- Paschalis, A., S. Fatichi, G. G. Katul, and V. Y. Ivanov (2015), Cross-scale impact of climate temporal variability on ecosystem water and carbon fluxes, *Journal of Geophysical Research: Biogeosciences*, *120*(9), 1716-1740.
- Pijanowski, B., N. Moore, D. Mauree, and D. Niyogi (2011), Evaluating error propagation in coupled land-atmosphere models, *Earth Interactions*, *15*(28), 1-25.
- Pitman, A. (2003), The evolution of, and revolution in, land surface schemes designed for climate models, *International Journal of Climatology*, *23*(5), 479-510.
- Prentice, I. C., X. Liang, B. Medlyn, and Y.-P. Wang (2015), Reliable, robust and realistic: the three R's of next-generation land-surface modelling, *Atmospheric Chemistry and Physics*, *15*(10), 5987-6005.
- Rahman, A., D. Sims, V. Cordova, and B. El-Masri (2005), Potential of MODIS EVI and surface temperature for directly estimating per-pixel ecosystem C fluxes, *Geophysical Research Letters*, *32*(19), L19404.
- Sims, D. A., A. F. Rahman, V. D. Cordova, B. Z. El-Masri, D. D. Baldocchi, P. V. Bolstad, L. B. Flanagan, A. H. Goldstein, D. Y. Hollinger, and L. Misson (2008), A new model of gross primary productivity for North American ecosystems based solely on the enhanced vegetation index and land surface temperature from MODIS, *Remote Sensing of Environment*, *112*(4), 1633-1646.
- Sims, D. A., et al. (2006), On the use of MODIS EVI to assess gross primary productivity of North American ecosystems, *Journal of Geophysical Research: Biogeosciences*, *111*(G4), G04015.
- Sinclair, T. R., C. Tanner, and J. Bennett (1984), Water-use efficiency in crop production, *BioScience*, *34*(1), 36-40.
- Sjöström, M., J. Ardö, A. Arneth, N. Boulain, B. Cappelaere, L. Eklundh, A. De Grandcourt, W. Kutsch, L. Merbold, and Y. Nouvellon (2011), Exploring the potential of MODIS EVI

- for modeling gross primary production across African ecosystems, *Remote Sensing of Environment*, 115(4), 1081-1089.
- Stöckli, R., D. Lawrence, G. Y. Niu, K. Oleson, P. Thornton, Z. L. Yang, G. Bonan, A. Denning, and S. Running (2008), Use of FLUXNET in the Community Land Model development, *Journal of Geophysical Research: Biogeosciences*, 113(G1).
- Stoy, P. C., M. Mauder, T. Foken, B. Marcolla, E. Boegh, A. Ibrom, M. A. Arain, A. Arneth, M. Aurela, and C. Bernhofer (2013), A data-driven analysis of energy balance closure across FLUXNET research sites: The role of landscape scale heterogeneity, *Agricultural and forest meteorology*, 171, 137-152.
- Thornton, P. K., P. J. Ericksen, M. Herrero, and A. J. Challinor (2014), Climate variability and vulnerability to climate change: a review, *Global change biology*, 20(11), 3313-3328.
- van Bodegom, P. M., J. C. Douma, and L. M. Verheijen (2014), A fully traits-based approach to modeling global vegetation distribution, *Proceedings of the National Academy of Sciences*, 111(38), 13733-13738.
- Verma, M., et al. (2014), Remote sensing of annual terrestrial gross primary productivity from MODIS: an assessment using the FLUXNET La Thuile data set, *Biogeosciences*, 11(8), 2185-2200.
- Wang, Y., X. Lu, I. Wright, Y. Dai, P. Rayner, and P. Reich (2012), Correlations among leaf traits provide a significant constraint on the estimate of global gross primary production, *Geophysical Research Letters*, 39(19).
- Williams, M., A. Richardson, M. Reichstein, P. Stoy, P. Peylin, H. Verbeeck, N. Carvalhais, M. Jung, D. Hollinger, and J. Kattge (2009), Improving land surface models with FLUXNET data, *Biogeosciences*, 6(7), 1341-1359.
- Xiao, X., D. Hollinger, J. Aber, M. Goltz, E. A. Davidson, Q. Zhang, and B. Moore III (2004), Satellite-based modeling of gross primary production in an evergreen needleleaf forest,

Remote sensing of environment, 89(4), 519-534.

- Xu, K., S. Metzger, and A. R. Desai (2017), Upscaling tower-observed turbulent exchange at fine spatio-temporal resolution using environmental response functions, *Agricultural and Forest Meteorology*, 232, 10-22.
- Yang, Y., D. Long, and S. Shang (2013), Remote estimation of terrestrial evapotranspiration without using meteorological data, *Geophysical Research Letters*, 40(12), 3026-3030.
- Yebra, M., A. Van Dijk, R. Leuning, A. Huete, and J. P. Guerschman (2013), Evaluation of optical remote sensing to estimate actual evapotranspiration and canopy conductance, *Remote Sensing of Environment*, 129, 250-261.
- Zhao, M., F. A. Heinsch, R. R. Nemani, and S. W. Running (2005), Improvements of the MODIS terrestrial gross and net primary production global data set, *Remote sensing of Environment*, 95(2), 164-176.
- Zhou, S., B. Yu, Y. Huang, and G. Wang (2014), The effect of vapor pressure deficit on water use efficiency at the subdaily time scale, *Geophysical Research Letters*, 41(14), 5005-5013.